

Internal dynamics of coalescing droplets

Thomas Craig Sykes

SUBMITTED IN ACCORDANCE WITH THE REQUIREMENTS FOR THE DEGREE OF
DOCTOR OF PHILOSOPHY

THE UNIVERSITY OF LEEDS

EPSRC CENTRE FOR DOCTORAL TRAINING IN FLUID DYNAMICS

SEPTEMBER 2020

Declaration

The candidate confirms that the work submitted is his own, except where work which has formed part of jointly authored publications has been included. The contribution of the candidate and the other authors to this work has been explicitly indicated below. The candidate confirms that appropriate credit has been given within the thesis where reference has been made to the work of others.

Chapters 3, 4 and 6 contain material from the following jointly authored publication:

Sykes, T.C., Harbottle, D., Khatir, Z., Thompson, H.M., and Wilson, M.C.T. 2020. Substrate wettability influences internal jet formation and mixing during droplet coalescence. *Langmuir*. **36**(32), pp. 9596–9607.

Chapters 1, 3 and 7 contain material from the following jointly authored publication:

Sykes, T.C., Castrejón-Pita, A.A., Castrejón-Pita, J.R., Harbottle, D., Khatir, Z., Thompson, H.M., and Wilson, M.C.T. 2020. Surface jets and internal mixing during the coalescence of impacting and sessile droplets. *Phys. Rev. Fluids*. **5**(2), pp. 023602.

The former publication was published under a Creative Commons CC-BY licence. Excerpts from the latter publication are reprinted with permission from Sykes et al. (2020a), Copyright (2020) by the American Physical Society.

All scientific research contained within both publications was undertaken by the candidate himself. The experiments contained within the latter were carried out during a visit to the Fluid Dynamics Laboratory at the Department of Engineering Science, University of Oxford – the experimental setup was constructed jointly by the candidate, A.A. Castrejón-Pita and J.R. Castrejón-Pita together; all experiments were conducted by the candidate himself, with the analysis and interpretation of the acquired data conducted by the candidate on returning to Leeds. For both publications, all co-authors (four supervisors, in addition to A.A. Castrejón-Pita and J.R. Castrejón-Pita for the latter publication) provided excellent direction/guidance and commented on the drafts. Only the candidate himself made direct edits to the text contained within these publications.

This copy has been supplied on the understanding that it is copyright material and that no quotation from the thesis may be published without proper acknowledgement.

The right of Thomas Craig Sykes to be identified as Author of this work has been asserted by Thomas Craig Sykes in accordance with the Copyright, Designs and Patents Act 1988.

Acknowledgements

I am fortunate to have benefited from an excellent team of supervisors (led by Mark C. T. Wilson), who I thank for their guidance, enthusiasm and good humour over the past three years. I am grateful to Mark for generously sharing his extensive knowledge of droplets, for all the opportunities he has given me and for his insightful suggestions about my work. I am equally grateful to my co-supervisors David Harbottle (especially for his boundless positivity about my work), Zinedine Khatir (especially for his encouragement of both my PhD work and career) and Harvey M. Thompson (especially for always ensuring that both my research and career were on track). I particularly appreciate my supervisors' willingness to allow me the freedom to develop and pursue my own research interests, with their unwavering support. I hope this work is not the last that we will do together.

My PhD was undertaken within the Engineering and Physical Sciences Research Council (EPSRC) Centre for Doctoral Training (CDT) in Fluid Dynamics, led by Peter K. Jimack. I thank Peter not only for giving me the opportunity to pursue a PhD, but also for showing me what it means to be a good researcher, academic and leader. I also wish to thank many of my fellow CDT PhD students (especially Andy, Colin, Craig, Eva, Khaled and Rob).

A special thanks goes to my unofficial adopted supervisors Alfonso A. Castrejón-Pita and J. Rafael Castrejón-Pita, with whom I carried out much of the experimental work presented in this thesis. I very much appreciate all of the invaluable help and advice Alfonso and Rafa have given me throughout the last three years, whilst welcoming me into their groups as if I were their PhD student. I hope this collaboration will be the first of many we have together. Furthermore, I would like to thank the Department of Engineering Science at the University of Oxford for hosting me during my research visit.

I am very grateful to Anne Juel for the excellent opportunity to work with her on droplet mixing experiments in Manchester, though the results of these experiments do not form part of this thesis. I hope that this is a collaboration that we can continue into the future. Moreover, I thank the Department of Physics and Astronomy at the University of Manchester for allowing me access to their labs.

I extend my thanks to Karrar H. Al-Dirawi, Colin D. Bain, Andrew E. Bayly, Ben Douglas, Jim Fraser, Chris S. Hodges, jh (John Hodrien), Oliver G. Harlen (especially for always thinking about my career), Claire Savy, Supraït (Mick) Tangparitkul and all those in the groups at Manchester, Oxford and Queen Mary. I thank my examiners for taking the time to carefully read and evaluate this thesis. I also acknowledge the useful comments of the four anonymous reviewers for the two already-published papers that appear in this thesis. Moreover, I appreciate the contributions of all who have helped me get to this point, whether they are named individually here or not.

I gratefully acknowledge the EPSRC for generously funding my PhD via the CDT in Fluid

Dynamics at the University of Leeds [grant number EP/L01615X/1]. I also appreciate the supplementary funding that I received from the EPSRC-funded UK Fluids Network (via a short research visit grant and several special interest groups) and a Leeds for Life Conference Award (to attend APS DFD 2019). The numerical work presented in this thesis was largely undertaken on ARC2, ARC3 and ARC4, all part of the High Performance Computing facilities at the University of Leeds.

Above all though, I am thankful to my parents and maternal grandparents, for everything.

Abstract

Internal flows determine the extent of advective mixing (stretching and folding of fluid interfaces) between coalescing droplets, effectively defining the initial condition for molecular diffusion to homogenise the fluid. Efficient mixing is essential in applications from inkjet printing to microfluidic devices, especially where a chemical reaction or biological process occurs between the droplet fluids. In emerging technologies, coalescing droplets often have different fluid properties, are in contact with a substrate and are surrounded by gas. An improved fundamental understanding of the internal dynamics in such cases, as contributed by this work, is both of significant physical interest and essential for improving mixing efficiency in applications.

This combined numerical and experimental work considers surface-tension-dominated coalescing droplets in two primary configurations: initially-static free and sessile droplets; impacting and sessile droplets with varied lateral separation. Two high-speed imaging experimental setups were designed and constructed, including one featuring synchronised colour cameras yielding simultaneous front and bottom views. A quantitatively-validated customised numerical simulation code was developed within OpenFOAM, utilising the Kistler dynamic contact angle model (including contact angle hysteresis) to capture substrate wettability and a conserved passive scalar to assess advective mixing.

The conditions leading to the formation of internal and surface jets between coalescing droplets are determined, where jet formation can significantly improve mixing efficiency. In particular, the effect of substrate wettability (principally via capillary waves) and fluid properties on internal flows are systematically studied in tandem. A mechanism of internal jet formation between free and sessile coalescing droplets, at volume ratios very different from those accepted for free droplets, is identified. A mechanism of surface jet formation between impacting and sessile droplets with a large lateral separation is elucidated, in which jet formation and mixing is controlled via Marangoni flow for droplets of different surface tension. Moreover, it is shown that diffusive mixing can be passively assessed via colour-change reactions, which are in turn used to identify efficient mixing mechanisms.

Contents

List of Figures	x
List of Tables	xv
Nomenclature	xvii
1 Introduction	1
1.1 Internal and external dynamics	1
1.2 Mixing within coalescing droplets	2
1.3 Inkjet-based technologies	3
1.4 Contributions of this work	6
2 Review of key concepts and previous work	9
2.1 Surface tension and its effects	9
2.1.1 Molecular origin and definition	9
2.1.2 Capillary waves	10
2.1.3 Chemical modification	11
2.1.4 Marangoni flow	11
2.1.5 Laplace pressure	12
2.2 Wetting	13
2.2.1 Spreading coefficient	13
2.2.2 Young contact angle	14
2.2.3 Substrate properties	15
2.2.4 Contact angle hysteresis	15
2.2.5 Capillary length	17
2.2.6 Sessile droplet geometry	18
2.3 Droplet interactions and coalescence	20
2.4 Fluid mixing	21
2.5 Dimensionless numbers and time scales	25
2.6 Moving contact lines	27
2.6.1 The moving contact-line problem	27
2.6.2 Dynamic contact angle	28
2.6.3 Apparent contact angle	30
2.6.4 Empirical dynamic contact angle models	31
2.7 Experimental studies of internal flows	33
2.7.1 Flow visualisation techniques	33

2.7.2	Challenges and limitations	36
2.8	Fluid interfaces in numerical simulations	37
2.8.1	Finite element method	38
2.8.2	Marker methods	40
2.8.3	Volume-of-fluid method	40
2.8.4	Level-set method	41
2.8.5	Lattice Boltzmann method	41
2.8.6	Summary	42
3	Experimental design and methodology	43
3.1	Fluids and characterisation	43
3.1.1	Fluids, dyes and indicators	43
3.1.2	Density and viscosity	45
3.1.3	Surface tension	46
3.2	Substrate	50
3.2.1	Requirements and choice	50
3.2.2	Silanisation	51
3.2.3	Wettability	52
3.3	High-speed imaging	53
3.4	Initially-static free and sessile droplets setup	55
3.5	Impacting and sessile droplets setup	58
3.6	Image processing	62
4	Numerical methodology and development	69
4.1	Preliminary aspects	69
4.2	Mathematical model	71
4.3	Boundary conditions	75
4.4	Numerical framework	78
4.4.1	Finite volume method	78
4.4.2	Discretisation	79
4.4.3	Computational domain and mesh	80
4.4.4	Customised solver	84
4.4.5	Pressure-velocity calculation procedure	85
4.4.6	Bounded scalars	85
4.4.7	Iterative algorithms	90
4.4.8	Time marching	90
4.5	Initial condition	91
4.5.1	Volume fraction and passive scalar	91
4.5.2	Meniscus bridge	92
4.5.3	Velocity and modified pressure	95
4.6	Free droplet coalescence examples	96
4.7	Summary	98

5	Numerical verification for free and sessile droplet coalescence	99
5.1	Free and sessile droplet coalescence	99
5.1.1	Numerical setup	99
5.1.2	Initial coalescence dynamics	100
5.2	Sensitivity analyses	101
5.2.1	Mesh	101
5.2.2	Domain size	104
5.2.3	Initial meniscus bridge width	105
5.3	Effect of fluid properties	107
5.3.1	Matched Ohnesorge number	107
5.3.2	Surface tension	109
5.3.3	Outer fluid	110
5.4	Summary	111
6	Internal jets	113
6.1	Introduction	113
6.2	Experimental observations	115
6.2.1	Initial condition	115
6.2.2	Fluid properties	116
6.2.3	Droplet volume ratio	116
6.2.4	Revisiting the initial condition	118
6.3	Comparisons to numerical simulations	119
6.3.1	Substrate wettability	119
6.3.2	Qualitative assessment	120
6.3.3	Quantitative analysis	121
6.4	Modifying substrate wettability	124
6.4.1	Changing receding contact angle	124
6.4.2	Mechanism of jet formation	126
6.4.3	Droplet volume	134
6.4.4	Droplet viscosity	136
6.5	Discussion and summary	139
7	Surface jets	141
7.1	Introduction	141
7.2	Experimental details	143
7.3	Droplets with equal fluid properties	144
7.3.1	Modest lateral separation	144
7.3.2	Large lateral separation	147
7.3.3	Surface jet formation	148
7.3.4	Surface jet properties	153
7.4	Droplets of different surface tension	156
7.4.1	Surface flow control	156
7.4.2	Time scale analysis	158

7.4.3	Regime map	159
7.5	Long term dynamics and advective mixing	161
7.6	Discussion and summary	163
8	Droplet mixing	165
8.1	Introduction to colour-change reactions	165
8.2	Experimental details	168
8.3	Effect of colour-change reactions	169
8.3.1	Non-axisymmetric impact	169
8.3.2	Sodium hydroxide	171
8.3.3	Reassessment of colour-change reactions	172
8.4	Mixing in different droplet configurations	174
8.4.1	Axisymmetric impact and coalescence	174
8.4.2	Non-zero lateral separation	175
8.5	Discussion and summary	177
9	Conclusions	179
9.1	Summary of the work	179
9.2	Key results	180
9.3	Implications of the results	181
9.4	Contributions to the literature	182
9.5	Outlook for future work	183
	Appendices	185
A	Sessile droplet geometry derivations	187
A.1	Droplet height in terms of contact angle	187
A.2	Droplet volume in terms of contact angle	188
B	Contact angle implementation as a boundary condition within VOF	189
C	Iterative algorithms and parameters	193
	References	195

List of Figures

1.1	Axisymmetric impact of a dyed droplet onto a undyed droplet of the same fluid, from Castrejón-Pita et al. (2013).	6
2.1	Sketch of cohesive forces between fluid molecules within a sessile droplet, from Yuan and Lee (2013).	10
2.2	Schematic depicting Marangoni flow along a free surface of non-constant surface tension.	12
2.3	Sketch of three sessile droplets on different substrates (hydrophilic, hydrophobic, etc.), from Yuan and Lee (2013).	14
2.4	Sketch of a droplet sliding down an inclined non-zero-hysteresis substrate, from Yuan and Lee (2013).	16
2.5	Sketch depicting the pumping method used to measure θ_a and θ_r of a sessile droplet, from Yuan and Lee (2013).	17
2.6	The geometry of a sessile droplet in the form of a spherical cap.	19
2.7	Laminar vortex ring in a deep water pool, visualised using PLIF, from Olcay and Krueger (2008).	24
2.8	Internal jet formation between initially-static free droplets in oil, from Nowak et al. (2017).	25
2.9	Sketch of θ_d against u_{cl} , from Blake (2006).	30
2.10	θ_d , observed for advancing free surfaces in a glass capillary, plotted against contact line velocity, from Hoffman (1975).	32
3.1	Surface tension against ethanol mass proportion, for ethanol-water mixtures.	44
3.2	Schematics of various tensiometers, from Berry et al. (2015).	47
3.3	Time series for the measured surface tension of water, with various concentrations of Nigrosin dye.	48
3.4	Volume loss from sessile droplets of ethanol-water mixtures, due to evaporation, over time.	50
3.5	Apparent contact angle against duration of silanisation for a glass substrate.	52
3.6	Schematic diagram of the experimental setup for studying free-sessile droplet coalescence. Note the 5 mm acrylic blocks below the silanised glass substrate.	56
3.7	Pictures of the experimental setup for studying free-sessile droplet coalescence.	57
3.8	Schematic diagram of the experimental setup for studying impacting-sessile droplet coalescence.	59

3.9	Pictures of the experimental setup for studying impacting-sessile droplet coalescence.	60
3.10	Image-processed droplet radius time series, demonstrating how the impacting droplet radius, r_f is determined in this work.	65
3.11	Image-processed centre height of a falling droplet in time, with a quadratic polynomial used to determine the impact velocity fitted.	66
4.1	Sketches depicting the use of the volume fraction, α and passive scalar, β to assess advective mixing within coalescing droplets.	75
4.2	An example of the quarter domain and hexahedral adaptive mesh, with the initial condition for a typical free-sessile droplet coalescence simulation set.	81
4.3	Typical mesh structure for the numerical simulations in this work.	84
4.4	An free droplet coalescence simulation demonstrating the need to use a flux-corrected transport scheme for bounded scalars within OpenFOAM.	88
4.5	A free and sessile droplet coalescence simulation with massless particles initialised on the internal interface and advected along pathlines by the velocity field, to verify the implementation of the passive scalar.	89
4.6	Evolution of the adjustable time step over a typical free-sessile droplet coalescence simulation.	91
4.7	An example of the interface destabilisation that can occur on a hexahedral mesh due to vapour being trapped near mathematical singularities.	93
4.8	Meniscus bridge structure on the hexahedral mesh at $t = 0.0$ ms, i.e. the initial condition for α and β	94
4.9	Verification of accurate Laplace pressure recovery in the simulations.	95
4.10	Coalescence of two initially-static free toluene droplets in water.	96
4.11	Coalescence of two initially-static low-viscosity free droplets.	97
5.1	Pressure contours highlighting the capillary waves emitted due to meniscus bridge building between free and sessile coalescing droplets.	100
5.2	Mesh sensitivity analysis of spread length.	102
5.3	Mesh sensitivity analysis of internal interface height.	103
5.4	Mesh sensitivity analysis of total droplet height.	103
5.5	Emitted capillary wave and internal dynamics sensitivity to initial meniscus bridge form and width for initially-static free and sessile coalescing droplets.	106
5.6	Normalised droplet height and spread length plotted against normalised time for multiple inertial time scales but fixed Ohnesorge number.	108
5.7	Effect of varying surface tension on total droplet height and internal interface height, with respect to both dimensional and non-dimensional time.	109
5.8	Effect of varying vapour phase dynamic viscosity on spread length and internal interface height.	111
6.1	Experiment frames showing the bouncing dynamics that generate the effectively static initial condition for free-sessile droplet coalescence.	115

6.2	Experiment frames showing the coalescence of a dyed free droplet with an undyed sessile droplet of the same fluid, for four droplet volume ratios. . . .	117
6.3	Experiment frames showing the coalescence of a dyed free droplet with an undyed sessile droplet of the same fluid, for which the initial condition is <i>not</i> generated by bouncing.	118
6.4	Apparent contact angle against contact line velocity, image processed from experiments and the Kistler model with non-zero contact angle hysteresis. .	119
6.5	Qualitative validation: experiment and simulation frames showing the coalescence of a dyed free droplet with an undyed sessile droplet of the same fluid, for two different droplet volume ratios.	121
6.6	Quantitative validation: graphs of spread length, internal interface height and total droplet height for a free-sessile droplet coalescence experiment in which a jet is seen. Data from image-processed experiments and four simulations, the latter assuming a small range of values for θ_a and θ_r	122
6.7	Quantitative validation: graphs of spread length, internal interface height and total droplet height for a free-sessile droplet coalescence experiment in which a jet is <i>not</i> seen. Data from image-processed experiments and four simulations, the latter with θ_r varied whilst θ_a is fixed.	125
6.8	Velocity fields for two simulations of free-sessile droplet coalescence, assuming different values of θ_r such that a jet is only seen in one.	126
6.9	Pressure contours for two simulations of free-sessile droplet coalescence, assuming different values of θ_r such that a jet is only seen in one.	128
6.10	Simulation frames showing the coalescence of a free droplet with a sessile droplet of the same fluid, with the velocity zeroed within 1 mm of the substrate in two simulations at different times to assess the effect of reflected capillary waves.	129
6.11	Graphs of spread length, internal interface height and total droplet height, with the velocity zeroed within 1 mm of the substrate in four simulations at different times to assess the effect of reflected capillary waves.	130
6.12	Graphs of spread length and internal interface height, including simulations in which the velocity is zeroed within 1 mm of the substrate and θ_a is altered at different times to confirm the effect of reflected capillary waves.	132
6.13	Experiment frames showing the coalescence of a dyed free droplet with an undyed sessile droplet of the same fluid, for a droplet volume ratio such that pinch-off and satellite droplet formation arises.	133
6.14	Numerically-generated regime maps for jet dependence on droplet volume ratio and substrate wettability, plotted against both θ_r and $\theta_a - \theta_r$	134
6.15	Graphs of spread length and internal interface height for free-sessile droplet coalescence, with data from three simulations, in which only θ_a is varied. . .	135
6.16	Numerically-generated regime map for jet dependence on droplet viscosity and receding contact angle.	137

6.17	Simulation frames showing the coalescence of a free droplet with a sessile droplet of the same fluid, with the droplet viscosity, μ_d varied between panels.	138
7.1	Experiment frames showing the coalescence of a dyed impacting droplet with an undyed sessile droplet of the same fluid, in an axisymmetric configuration.	145
7.2	Experiment frames showing the coalescence of a dyed impacting droplet with an undyed sessile droplet of the same fluid, in a non-axisymmetric configuration.	146
7.3	Experiment frames showing the coalescence of a dyed impacting droplet with an undyed sessile droplet of the same fluid, where the impacting droplet spreads into the sessile droplet to initiate coalescence.	147
7.4	Sketch depicting a coalesced droplet, formed from non-axisymmetric impacting and sessile droplets, at its maximum spread length.	149
7.5	Free surface dynamics following the coalescence of impacting and sessile droplets in a non-axisymmetric configuration.	150
7.6	Evolution of free surface height following the coalescence of impacting and sessile droplets in a non-axisymmetric configuration.	151
7.7	Evolution of bulk and jet leading edge horizontal positions following the coalescence of impacting and sessile droplets of identical fluids, in a non-axisymmetric configuration.	154
7.8	Sensitivity of dynamics to lateral separation during the coalescence of a dyed impacting droplet with an undyed sessile droplet of the same fluid, where the impacting droplet spreads into the sessile droplet to initiate coalescence.	155
7.9	Experiment frames demonstrating surface jet and mixing control during the coalescence of impacting and sessile droplets of different surface tension. . .	157
7.10	Evolution of bulk and jet leading edges' horizontal position following the coalescence of impacting and sessile droplets of different surface tension, in a non-axisymmetric configuration.	158
7.11	Regime map for early-time flow structures seen during the coalescence of impacting and sessile droplets, with respect to lateral separation and (relative) fluid properties.	160
7.12	Experiment frames demonstrating the effect of relative fluid properties on long-term dynamics and mixing during the coalescence of impacting and sessile droplets.	162
8.1	Impact of a droplet onto a pool of different fluid properties, with mixing visualised using a colour-change reaction, from Tsuji and Müller (2012). . .	166
8.2	Coalescence of two sessile droplets, with mixing visualised both using a colour-change reaction and an inert dye, from Yeh et al. (2015).	167
8.3	Experiment frames showing the coalescence of an impacting droplet with a sessile droplet in a non-axisymmetric configuration, with mixing visualised both using a colour-change reaction and an inert dye.	169

8.4	Experiment frames showing the coalescence of an impacting droplet with a sessile droplet for two non-zero lateral separations, with mixing visualised using a colour-change reaction.	171
8.5	Experiment frames showing the coalescence of an impacting droplet with a sessile droplet in a non-axisymmetric configuration, which confirms the passive effect of NaOH and phph on the dynamics.	172
8.6	Sketch indicating mixing mechanisms during the impact of a droplet onto a pool of higher surface tension.	173
8.7	Experiment frames showing the coalescence of an impacting droplet with a sessile droplet in an axisymmetric configuration, with mixing visualised both using a colour-change reaction and an inert dye.	175
8.8	Experiment frames showing the coalescence of an impacting droplet with a sessile droplet at three different lateral separations, with mixing visualised using a colour-change reaction.	176

List of Tables

2.1	Summary of key numerical works concerning internal flows and mixing in coalescing droplets, with the numerical framework indicated.	39
3.1	Ethanol-water mixture fluid properties.	45
4.1	OpenFOAM discretisation schemes used in this work.	80
4.2	PISO algorithm controls specified in this work.	86
5.1	Details of meshes employed in the mesh sensitivity analysis.	102
5.2	Sensitivity of free-sessile droplet coalescence dynamics to domain size, with absolute differences scaled by the minimum value.	104
5.3	Sensitivity of free-sessile droplet coalescence dynamics to domain size, with absolute differences scaled by the mean value.	105
5.4	Fluid properties for five simulations with matched Ohnesorge number but varying inertial time scale.	108
7.1	Impacting droplet radius and velocity of the ethanol-water mixtures used in the study of surface jets, alongside the observed equilibrium contact angle of the precursor sessile droplet.	144
8.1	Impacting droplet radius and velocity of the ethanol-water mixtures used in the study of mixing.	168
C.1	OpenFOAM solver settings for α . Equivalent settings are used for β	193
C.2	OpenFOAM solver settings for <code>p_rgh</code> – the modified pressure, p'	194
C.3	OpenFOAM solver settings for <code>pcorr</code> – the pressure correction required for the adaptive mesh refinement algorithm.	194
C.4	OpenFOAM solver settings for <code>U</code> – the velocity, u_i	194

Nomenclature

Abbreviations

CFA	Colour Filter Array
CLSVOF	Coupled Level-Set Volume-Of-Fluid
EDR	Extreme Dynamic Range
FCT	Flux-Corrected Transport
FDM	Finite Difference Method
FEM	Finite Element Method
FPS	Frames Per Second
FVM	Finite Volume Method
(O)LED	(Organic) Light Emitting Diode
(P)LIF	(Planar) Laser-Induced Fluorescence
LBM	Lattice Boltzmann Method
LHS	Left-Hand Side
MAC	Marker-And-Cell
MULES	Multidimensional Universal Limiter for Explicit Solution
(μ)PIV	(Micro-)Particle Image Velocimetry
PCG	Preconditioned Conjugate Gradient (Method)
PDE	Partial Differential Equation
phph	Phenolphthalein
PISO	Pressure-Implicit with Splitting of Operators
PMMA	Polymethylmethacrylate (also known as acrylic)
RGB	Red Green Blue

RHS	Right-Hand Side
RIJ	Reactive Inkjet (Printing)
SLIPS	Slippery Liquid-Infused Porous Surfaces
TVD	Total Variation Diminishing
UV	Ultraviolet
VOF	Volume-Of-Fluid

Dimensionless numbers

Bo	Bond number, sometimes known as the Eötvös number (defined on page 18)
Ca _{cl}	Contact line capillary number (defined on page 29)
Co	Courant number (defined on page 90)
Oh	Ohnesorge number (defined on page 26)
Pe	Péclet number (defined on page 22)
Re	Reynolds number (defined on page 25)
We	Weber number (defined on page 25)
Wo	Worthington number (defined on page 47)

Greek symbols

α	Volume fraction
β	Passive scalar
γ	Interfacial tension (in general)
γ_{sl}	Solid-liquid (substrate-droplet) interfacial tension
γ_{sv}	Solid-vapour (substrate-air) interfacial tension
δ	Dirac delta function
δ_{ij}	Kronecker delta
ε_{ijk}	Levi-Civita symbol
θ	Contact angle (in general)
θ_a	Advancing contact angle
θ_d	Dynamic contact angle (see Section 2.6.2)
θ_{eq}	Equilibrium contact angle

θ_{\max}	Maximum contact angle
θ_{\min}	Minimum contact angle
θ_r	Receding contact angle
κ	(Free surface) curvature
λ	Blending factor (used in FCT)
μ	Dynamic viscosity
μ_d	Droplet dynamic viscosity
μ_m	Mixture dynamic viscosity
μ_o	Outer phase dynamic viscosity
ν	Kinematic viscosity
ν_d	Droplet kinematic viscosity
ν_m	Mixture kinematic viscosity
ν_o	Outer phase kinematic viscosity
ρ	Density
$\Delta\rho$	Density difference
ρ_d	Droplet density
ρ_m	Mixture density
ρ_o	Outer phase density
$\partial\Omega$	Boundary
σ	Surface tension (i.e. the liquid-vapour interfacial tension, γ_{lv})
τ_σ	Inertial time scale
τ_m	Marangoni time scale
τ_μ	Viscous time scale
τ_{ij}	Viscous stress tensor
ϕ	Cell-face flux
ω_i	Vorticity

Roman symbols

c	Concentration
-----	---------------

c_α	Compression term coefficient (in Equation (4.27))
D	Diffusivity
D_n	Dispensing tip outer diameter
E	Total cohesive energy of a molecule
\mathcal{F}	Fourier transform
F^C	Corrected cell-face flux
F^L	Cell-face flux computed using a low-order, bounded scheme
F^H	Cell-face flux computed using a high-order, potentially unbounded scheme
F_i	Body force
f	Cell face
f_H	Hoffman function
g	Gravity of Earth
g_i	Acceleration vector due to Earth's gravitational force
h	Sessile droplet height
l	Characteristic length scale
l_c	Capillary length (defined on page 18)
l_m	Microscopic length scale (in the Cox-Voinov law on page 29)
\log	Natural logarithm (base e)
\hat{n}	Unit normal vector to an interface (1D) – see Figure 2.2
N	Number of cells
\hat{n}_i	Unit normal vector to the interface
$\hat{n}_{0,i}$	Uncorrected free surface unit normal at the contact line
$\hat{n}_{c,i}$	Updated free surface unit normal at the contact line
$\hat{n}_{s,i}$	Unit normal to the substrate
p	Pressure
Δp	Pressure difference across an interface (typically Laplace pressure)
p'	Modified pressure (defined on page 72)
R	(Equivalent) spherical radius

R	Principal radius of curvature
r_c	Horizontal cross section radius at a given height ($r_c = r_{c,0}$ at $t = 0$)
r_f	Free droplet radius (assumes the droplet is spherical)
S	Spreading coefficient
$S_{f,i}$	Cell-face area vector
s	Spread length
T_{ij}	Stress tensor
t	Time
Δt	Time step
\hat{t}	Unit tangent vector to an interface (1D) – see Figure 2.2
U	Characteristic velocity
u_i	Velocity vector
u_t	Tangential velocity (1D) – see Figure 2.2
u_{cl}	Contact line velocity
$u_{c,i}$	Compression velocity
$u_{f,i}$	Cell-face velocity
V	Volume (in general)
V_f	Free droplet volume
V_s	Sessile droplet volume
x_i	Position vector

Chapter 1

Introduction

1.1 Internal and external dynamics

Droplet coalescence is a pivotal feature in many natural and applied phenomena, including raindrop formation in clouds, the development of ocean mist, lab-on-a-chip devices, crop spraying and phase-change heat transfer technologies (Cha et al., 2016; Khatir et al., 2016). Within the last half-century, the external dynamics of droplet coalescence have been studied extensively, from the growth of a meniscus bridge between coalescing droplets (Wu et al., 2004) to pinch-off and satellite formation (Zhang et al., 2009), which may repeat numerous times to form a beautiful coalescence cascade (Harbottle et al., 2011; Thoroddsen and Takehara, 2000). Nevertheless, both the conditions required for the coalescence of colliding droplets (Al-Dirawi and Bayly, 2019) and the physical mechanism initiating coalescence (Perumanath et al., 2019) remain active areas of research.

However, the range of external dynamics seen during coalescence belies the wide variety of physical phenomena that occur within coalesced droplets, which has received far less attention. Perhaps the most famous example of internal flow within droplets is the *coffee ring effect*. After a small amount of coffee (or another fluid containing dispersed material) is spilt on a substrate and the fluid has evaporated, a dense ring along the perimeter of the former droplet contact patch is seen, instead of a uniform deposit throughout the contact patch. The cause of the deposit is enhanced evaporation at the contact line, which induces a radial internal flow towards the contact line in order to replace the evaporating fluid. This internal flow carries the suspended particles (which can't evaporate) to, and deposits them at, the contact line. Given that the contact line does not move (recede) during the evaporation, a *coffee ring* is formed (Deegan et al., 1997).

In fact, internal flows initiated by coalescence can be directly seen with the aid of coffee too. Take a cup of coffee without milk and place a small droplet of milk onto the tip of a teaspoon. Slowly lower the teaspoon towards the cup such that the droplet of milk (not the teaspoon itself) comes gently into contact with the free surface of the coffee; the

milk droplet will detach from the teaspoon and be absorbed into the coffee. Whilst the initial coalescence dynamics are far too rapid to see, the milk will form a internal jet/vortex ring under the free surface which should be clearly visible. Now try to detach the droplet from the teaspoon in mid-air above the coffee and observe the differences in internal flow; the implementation of detachment is trivial and left as an exercise to the reader. The dynamics of this surface-tension-driven coalescence process are very intricate, especially considering the droplet and pool have different fluid properties. It is such internal flows, but between two droplets rather than a droplet and pool, that are of interest in this work.

1.2 Mixing within coalescing droplets

The internal flows within a coalesced droplet are responsible for redistributing the fluids from the original droplets. These dynamics effectively define the initial condition from which molecular diffusion must act to homogenise the coalesced droplet and, in cases where a chemical reaction takes place between the constituent fluids, the regions in which a reaction will be initiated. By extending and redistributing the internal fluid interface, herein referred to as *advective mixing*, the area over which diffusion can act is expanded, which improves the efficiency of *diffusive mixing*. Such advective mixing is very beneficial since molecular diffusion (due to the thermal motion of the fluid molecules) is an extremely slow process. For example, for a hemispherical sessile water droplet with an 80 μm spread length and its top half-volume dyed, around half a second is required for diffusion to homogenise the dye distribution. For millimetric droplets, such as those studied in this work, the required time would be much greater (Wilson et al., 2018). Whilst such times may seem insignificant, they are far longer than the time scales on which the internal dynamics generally take place (millisecond for surface-tension-dominant flows of millimetric droplets) and are much too long for applications that comprise multiple successive processes. In general, turbulent eddies can engender effective mixing, but turbulence is difficult to generate and (even harder to) sustain at the millimetric, or shorter, length scales of droplets (Stone et al., 2004). It is therefore clear that achieving good advective mixing is crucial to efficiently realise a homogenous coalesced droplet on a desirably short time scale in many droplet-based applications.

In particular, efficient mixing between coalescing droplets is of great practical importance in, for example, liquid-liquid extraction systems (Eiswirth et al., 2012), the ignition of hypergolic propellants (Law, 2012), and droplet-based microfluidic systems (Teh et al., 2008). Furthermore, effective mixing between droplets of different reagents is required in applications including chemical synthesis, the formation of particles, and *lab-on-a-chip devices* (Cristini and Tan, 2004). Lab-on-a-chip devices, which are droplet-based microfluidic systems that integrate and automate multiple laboratory techniques onto an integrated circuit ('chip'), have received a significant amount of attention over the last decade or so, and have motivated much of the research into droplet mixing. However, an especially interesting group of emerging applications relying on droplet mixing is based on inkjet

technologies, which will be discussed in the next section.

1.3 Inkjet-based technologies

Overview

Inkjet is a technique used to efficiently deposit small droplets at precise locations onto a substrate in a highly controlled way, where the desired product/pattern is formed by coalescence. Perhaps best known for their use in graphical applications, inkjet technologies also underpin a wide range of digital manufacturing methods; examples of products include OLED displays, printed circuit boards, packaging, wearable electronic devices and textiles (Hutchings et al., 2016; Gao et al., 2017). Biofluids can also be deposited using inkjet printers to synthesise DNA (Hood, 2008), fabricate living cells (Li et al., 2018), and print a range of biomaterials (Angelopoulos et al., 2020). The distinctive characteristic of inkjet compared to other printing/manufacturing technologies is the ability to precisely deposit droplets of small volume (typically picolitre), which enable high-resolution products to be fabricated at high speed. Droplets are generated in inkjet printing by one of two techniques: ejection of a liquid jet that breaks up into a stream of droplets due to the Rayleigh-Plateau instability, known as *continuous inkjet printing*, or direct ejection of single droplets through a nozzle due to a pressure pulse, called *drop-on-demand*. The latter technique is the most prominent in modern implementations of inkjet due to improved print resolution and printer reliability (Guo et al., 2017). However, inkjet technologies rely on ink formulations that must be carefully controlled to allow the ink to be jetted (Antonopoulou et al., 2020) – that is, enable the required droplets to be formed – and to ensure that the deposited droplets behave appropriately on the substrate, all while maintaining the properties required for the application.

Issues in graphical applications

Mixing between coalescing droplets is often very important in printing applications. At the most basic level in graphical printing, mixing between adjacent droplets of different colours (known as *colour bleed*) can be detrimental to print quality. Internal flows clearly influence such mixing; for example, it has been demonstrated that if adjacent printed droplets have different surface tension, then colour bleed can be reduced (Oyanagi, 2003). Moreover, key challenges in graphical inkjet printing include maintaining the colourant on the substrate, and avoiding both non-uniform spreading (known as *feathering*) and penetration (into porous substrates), in order to maintain optical density.

In order to fix colourants in place, some (typically wide-format) inkjet printers initiate aggregation/thickening chemical reactions on the substrate, which aim to quickly immobilise the colourant via a drastic increase in fluid viscosity (Frenkel, 2009). Often,

the reaction occurs between a *reaction liquid* that is deposited on the substrate as a film (by means other than inkjet printing, such as curtain coating) and subsequently printed droplets that contain dispersed particles, which destabilise and rapidly aggregate upon mixing with the reaction liquid (Kazuhide and Toshiyuki, 2000; Nito and Hakamada, 2009). For inks containing polymer particles, their aggregation can also increase the robustness of the print by forming a protective layer above the colourant. However, it is challenging to manage the competing demands of maintaining the dispersed state of ink over long periods before use and during jetting, whilst enabling rapid destabilisation on the substrate. Chemical reactions between inks, typically a second black ink and other colours in the ink set, are used to reduce colour bleed in a similar manner (Teraoka et al., 2003). Such reactions between the droplets themselves can also improve print resolution by reducing droplet spread. Somewhat paradoxically though, there must be some mixing between the two fluids for the desired reaction to occur, even though reduced mixing is the purpose of introducing a chemical reaction in such cases.

In graphical printing, chemical reactions are not integral to the application; rather they are introduced to reduce undesirable side-effects of the dynamic processes involved. Moreover, components of the ink connected with the chemical reaction (e.g. a reactive dye) can influence its fluid properties, which as explained above must be carefully controlled in inkjet printing, and therefore the ability to jet the ink and form the required droplets (Tang et al., 2020). An improved understanding of flows within coalesced droplets on substrates, in addition to advances in ink formulation and controlling its interaction with the substrate, could enable reduced colour bleed and improved print robustness without the need for such chemical reactions that add significant complication to inkjet printers. However, a relatively recent application of inkjet has been to harness the potential of chemical reactions between inkjet-printed droplets in order to open up a new and exciting range of applications, as discussed in the next section.

Reactive inkjet printing

Reactive inkjet printing (RIJ) describes techniques that use an inkjet printer to deposit droplets onto a substrate, which subsequently undergo a chemical reaction on mixing to form the desired product in situ. In contrast to graphical applications, the reaction here is integral to forming the product of appropriate chemistry. Smith and Morrin (2012) define two variants of RIJ. In *single RIJ*, an inkjet printer is used to deposit a droplet that reacts with a fluid film covering the substrate. Single RIJ is analogous to the reaction liquid-type of graphical inkjet printing described above. In contrast, two droplets containing different reactants are deposited onto a substrate using different nozzles of an inkjet printer in *full RIJ*; these droplets coalesce on the substrate, usually via direct impact, to initiate the chemical reaction that produces the desired product (Smith and Morrin, 2018). Discussion is limited to the latter variant of RIJ in this work, since it involves the coalescence of two droplets between which efficient mixing is essential.

Whilst inheriting the advantages of conventional inkjet printing noted above (especially print resolution), RIJ addresses what is perhaps its most restrictive limitation: the range of materials that can be printed. Indeed, inkjet printers require the use of carefully formulated inks adhering to a narrow range of rheological properties so that they can be successfully and reliably jetted, which restricts the range of materials that can be directly printed. By forming the desired product in situ via a chemical reaction between two fluids that can be jetted, products consisting of materials that might not be directly jettable, but which have desirable functionality, can be printed. For example, printing of biocompatible ('cell-friendly') scaffolds of gelatin arrays for use in tissue engineering has been successfully achieved with RIJ, where cells are seeded onto the scaffold during printing, and the scaffold's properties tailored as desired (Tse, 2015). Other examples of interesting products that have been printed using RIJ include conductive copper and nickel lines on flexible substrates (Li et al., 2009), fluorescent quantum dots (Bao et al., 2015), and autonomous swimming devices called 'micro-rockets' (Gregory et al., 2016).

RIJ can also be used as an *additive manufacturing* (3D printing) technique to fabricate micron-scale products. In particular, RIJ avoids the need to use photopolymer inks that are required in popular additive manufacturing techniques (e.g. PolyJet), in which polymerisation leading to solidification of deposited droplets is triggered by UV exposure immediately after deposition, with the product built layer-by-layer (Napadensky, 2009). Indeed, RIJ offers the possibility for polymerisation to be initiated by chemical means, so RIJ-based additive manufacturing methods can produce products consisting of a wider range of materials, including polyurethanes (Kröber et al., 2009; Schuster et al., 2019), polyamides (e.g. nylon 6 – Fathi and Dickens, 2013) and polyimides (He et al., 2018). In addition to an additive manufacturing technique, RIJ can be used for similar purposes to lab-on-a-chip microfluidic devices with analogous advantages and additional benefits including increased efficiency, improved reaction yield, reduced material consumption (i.e. smaller droplet volumes), and that the product can be produced in the desired location for the next step in the process (i.e. in situ). Hence, RIJ not only extends the range of products that can be derived from an inkjet printer, but also transforms inkjet technology into a flexible chemical synthesis tool (Smith and Morrin, 2012).

Mixing in reactive inkjet printing

Clearly, efficient mixing between the reactants contained within each coalescing droplet is required to instigate the all-important chemical reaction in RIJ, meaning that droplet mixing is fundamental to its efficacy. Hence, the successful deployment of RIJ in the applications discussed above indicate that efficient mixing occurs in those cases. Moreover, analysis of fluorescent RIJ-printed droplets of polyurethanes show the coalesced droplets are homogeneous, which further suggests that good mixing does arise (Kröber et al., 2009). However, in RIJ of nylon 6, Fathi and Dickens (2013) assessed mixing with fluorescence imaging of larger droplets (formed by jetting multiple droplets), but little mixing was seen

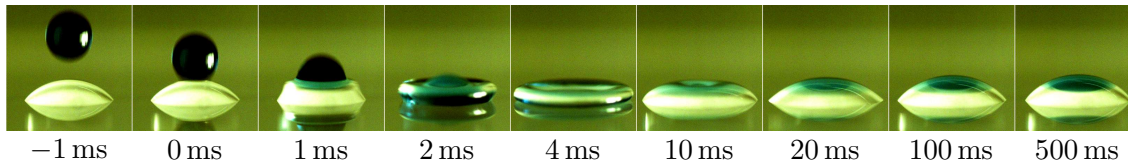


Figure 1.1: Asymmetric impact of a dyed glycerol-water mixture droplet (radius 1.20 mm) onto an undyed sessile droplet (initial radius 1.30 mm) of the same fluid at 1.08 m s^{-1} . The Weber and Ohnesorge numbers were matched to inkjet values, with surprisingly little advective mixing seen. Reprinted figure with permission from Castrejón-Pita et al. (2013). Copyright (2013) by the American Physical Society.

near the contact line and an unclear amount of mixing materialised in the droplet centre.

In an attempt to uncover the dynamics of mixing in inkjet printing, Castrejón-Pita et al. (2013) used high-speed imaging with a front view to visualise internal flows between impacting and sessile coalescing droplets. Whilst inkjet droplets have a typical length scale of $\sim 100 \mu\text{m}$, millimetric droplets were used in this work for visual accessibility, but with the Weber and Ohnesorge numbers (defined in Section 2.5) matched to typical inkjet values. Surprisingly, little advective mixing on a short time scale was observed, as seen in Figure 1.1, an observation that is robust to lateral separation. Of course, the influence of molecular diffusion will be far less for the millimetric droplets studied than for inkjet-printed droplets, which may to some extent explain the lack of observed mixing (Wilson et al., 2018). Furthermore, there is likely to be a complicated two-way coupling between mixing and reaction kinetics. It is nevertheless clear though that the mechanisms of mixing between coalescing droplets, and therefore the success of RIJ, are far from straightforward.

1.4 Contributions of this work

The preceding discussion has demonstrated that internal flows within coalescing droplets are crucial in a multitude of applications, especially those in which good mixing is required. In particular, adequate mixing is an essential requirement for chemical reactions between coalescing droplets, but several previous studies have indicated little to no advective mixing in configurations where successful chemical reactions are known to occur. Besides being a fascinating physics problem to explore, the lack of a fundamental understanding of droplet mixing is a hindrance to potential applications, with a better understanding of mixing and linked reaction kinetics identified as crucial for the development of RIJ towards ultra-miniature high-throughput screening drug discovery methods (Daly et al., 2015). Whilst this work is strongly motivated by inkjet technologies, the small size of picolitre inkjet droplets means that to study their external dynamics is experimentally very challenging, let alone their internal and mixing dynamics. Hence, this work is restricted to millimetric droplets (of microlitre volume, directly relevant to microfluidics), an improved understanding of which will facilitate advances in the understanding of droplets on the inkjet scale. Moreover, the numerical capabilities developed can be scaled down to

study scales directly relevant to those prevalent in inkjet applications, with the inclusion of molecular diffusion.

Mechanisms of mixing between coalescing droplets on a substrate and exposed to air are especially unclear, despite the relevance to many of the interesting applications discussed above. The effect of the presence of a substrate and its wettability on internal flows and mixing during coalescence is largely unknown. The research reported in this work advances our understanding of the fundamental fluid dynamics underpinning the internal and mixing dynamics within coalescing droplets in contact with a substrate. Special attention is given to configurations in which only one of the droplets is sessile at the onset of coalescence, which is the typical case in inkjet printing. In particular:

- High-speed imaging experiments and volume-of-fluid-based numerical simulations are developed in parallel to comprehensively elucidate internal dynamics for configurations in which the droplets are in contact with a substrate. The Kistler dynamic contact angle model (with contact angle hysteresis) allows substrate wettability to be varied in the simulations, which are validated against quantitative image processing of the experimental results. See Chapters 3 and 4 in particular.
- Unlike many previous studies, the droplets considered are surrounded by air (rather than a high-viscosity, immiscible fluid such as an oil), which is relevant to a wide range of the aforementioned applications including inkjet printing, but engenders vigorous free surface movement.
- Careful validation and verification of the simulations is undertaken to ensure their accuracy, both in the droplet configurations of primary interest and others (e.g. free droplet coalescence). See Chapters 4 to 6.
- The influence of substrate wettability is carefully understood and elucidated, with respect to capillary wave dynamics and the formation of both surface and internal jets. See Chapters 6 and 7 in particular.
- The effect of fluid properties on internal flows is systematically determined experimentally and numerically in tandem with substrate wettability, both where they are the equal and different between the coalescing droplets.
- The conditions leading to surface and internal flows during the coalescence of impacting and sessile droplets are considered experimentally, leading to the identification of a *surface jet* in this configuration. See Chapter 7 in particular.
- Mechanisms of mixing with Marangoni flow due to surface tension differences between the coalescing droplets (as is common in RIJ) are identified. Moreover, the efficacy of colour-change reactions for passively assessing fluid mixing is demonstrated, clarifying some ambiguity within the literature. See Chapter 8 in particular.

The structure of this document is as follows. Chapter 2 introduces some key background information and describes experimental and numerical methods that have been used to study internal flows in coalescing droplets. Chapter 3 describes the development of the two experimental setups used to study free-sessile and impacting-sessile droplet coalescence. Chapter 4 describes the development of a customised solver based on the volume-of-fluid method used for numerical simulations in this work. Chapter 5 introduces initially-static free and sessile droplet coalescence, and describes the numerical verification steps undertaken for the customised solver in this configuration. Chapter 6 presents experimental and numerical results – many of which can be found in Sykes et al. (2020b) – investigating the aforementioned free-sessile droplet configuration, focusing on the effect of substrate wettability on internal jet formation. Extensive validation of the numerical simulations is also undertaken in this chapter. Chapter 7 reports the results of high-speed imaging experiments – many of which can be found in Sykes et al. (2020a) – of impacting and coalescing droplets, focusing on surface jet formation and control via Marangoni flow. Chapter 8 considers the same configuration as the previous chapter, but with a focus on assessing mixing between droplets of different surface tension via colour-change reactions. Chapter 9 summarises and discusses the key findings of this work.

Chapter 2

Review of key concepts and previous work

The purpose of this chapter is to introduce the key physical concepts that feature throughout this work, and to elucidate the state of the art regarding research into the internal dynamics of coalescing droplets. There is a special focus on substrate wettability and mixing, both of which are key features of this work. Moreover, experimental and numerical techniques previously used to study the internal flows in droplets are discussed at some length towards the end of the chapter. However, specific reviews of the literature with respect to the dynamics studied in this work are deferred to the first section of each primary results chapter (Chapters 6 to 8).

2.1 Surface tension and its effects

In this section, the concept of surface tension is formally introduced by considering molecular interactions at fluid interfaces, after which the effects of surface tension are discussed.

2.1.1 Molecular origin and definition

At the microscopic scale, each molecule in the bulk of a fluid is surrounded by like molecules, whereas those molecules at a fluid surface are partially surrounded by molecules of another fluid. Due to the relative strengths of adhesion and cohesion, surface molecules occupy a higher energy state than those in the bulk (Berthier, 2013), with the cohesive forces between fluid molecules forming a sessile droplet portrayed in Figure 2.1. As elucidated by Bormashenko (2013b), it is important to note that the surface molecules do not acquire an inward resultant force. Instead, as a result of the discrepancy in energy states, fluids tend to minimise the number of surface molecules to minimise surface energy. Moreover, surface molecules are attracted to each other more strongly than to the molecules

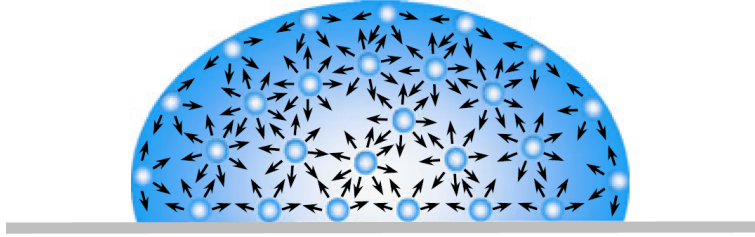


Figure 2.1: Sketch of cohesive forces between fluid molecules within a sessile droplet. Reprinted by permission from Springer Nature Customer Service Centre GmbH: Figure 1.2 from Yuan and Lee (2013). Copyright Springer Nature, 2013.

in the adjoining fluid and so experience asymmetric cohesive forces. At the macroscopic scale, surfaces therefore have an elastic tendency which is known as *surface tension*.

The property of surface tension is defined as the normal force per unit length that the given surface can sustain (Frohn and Roth, 2000). As is common practice, throughout this work the term *surface tension*, σ is used in reference to liquid/gas interfaces, whereas the more general term *interfacial tension*, γ is used when referring to interfaces between two liquids. Interfacial tensions tend to be lower than surface tensions, since the greater number of molecules available for adhesion in the adjoining fluid (being a liquid rather than a gas) reduces the magnitude of the asymmetric cohesive forces experienced by the interface molecules. Surface tension can be approximated as

$$\sigma \approx \frac{E}{2\delta^2},$$

where E is the total cohesive energy of each fluid molecule¹ and δ is its characteristic dimension (Berthier, 2013). As a result, fluids with stronger intermolecular interactions, and smaller molecules, typically have larger surface tensions. Due to the relatively small size of H₂O molecules, and the presence of hydrogen bonding, water has a high surface tension of approximately 72 mN m⁻¹ (at room temperature) compared to most liquids. Hence, certain light objects that are more dense than water can be seen to ‘float’ on the free surface of a water pool, such as steel needles and small insects.

2.1.2 Capillary waves

Waves propagating on a free surface with a short wavelength ($\lesssim 1.7$ cm for water) are dominated by the effects of surface tension rather than gravity; these are referred to as *capillary waves* (Acheson, 1990). Capillary waves can be seen as ripples on a puddle formed by the impact of raindrops and are common in droplet dynamics where perturbations, such as meniscus bridge formation at the onset of coalescence, generate such waves that can have a significant influence on the dynamics.

¹Surface molecules have approximately half the number of like molecules surrounding them compared to molecules in the bulk, so the ‘cohesive energy loss’ is approximately $E/2$.

2.1.3 Chemical modification

As explained in Section 2.1.1, the relative strength of cohesive forces determines the surface tension of a given fluid, though surface tension can be lowered through the addition of a *surfactant* (surface-active agent). Surfactants are generally long organic compounds characterised by having a hydrophilic head and hydrophobic tail (i.e. they are amphiphilic) that diffuse to and adsorb at free surfaces (Berthier, 2013). Hence, surfactants reduce cohesive forces between surface molecules (see Figure 2.1) which leads to a reduction in surface tension. At high concentrations above the *critical micelle concentration*, surfactants self-assemble into aggregates known as *micelles*.

Surfactants are used in a wide variety of sectors like pharmaceuticals, inkjet and agrochemicals as (anti-)foaming agents, wetting agents and dispersants (Mulla et al., 2016). The surfactant concentration at a free surface can change in time as surfactants diffuse towards it, leading to a *dynamic surface tension*. The effect of surfactants on droplet dynamics is therefore non-trivial and depends on a wide variety of properties including adsorption rate and diffusivity. In particular, it has been shown that the internal dynamics and mixing within coalescing droplets in a microchannel depend on the precise chemical nature of the surfactant used (Nash et al., 2018).

2.1.4 Marangoni flow

Gradients in surface tension along a free surface induce a tangential stress that leads to tangential flow toward regions of higher surface tension. The induced surface flow is known as *Marangoni flow* (Marangoni, 1871), with its motion propagating into the bulk by the action of viscosity (Berthier, 2013). Since Marangoni flow acts to effectively replace high surface tension free surfaces with ones of lower surface tension, it acts to reduce surface energy. Mathematically, the viscous stress resulting from the gradient in tangential velocity, u_t balances the surface-tension-induced tangential stress according to

$$\frac{d\sigma}{d\hat{t}} = -\mu \frac{du_t}{d\hat{n}} \quad (2.1)$$

under a lubrication approximation, where μ is the dynamic viscosity, whilst \hat{t} and \hat{n} are the unit tangent and normal vectors to the free surface, respectively, as depicted in Figure 2.2 (Battal et al., 2003).

Surface tension gradients can be caused by temperature variations (surface tension typically reduces with increasing temperature – Eötvös, 1886), non-uniform surfactant distribution, differential evaporation in binary mixtures (induces compositional variations), and even electric fields. In particular, surface tension gradients can be introduced by the coalescence of two droplets consisting of miscible fluids, with Marangoni flow acting to cover fluid from the droplet with higher surface tension (Lohse and Zhang, 2020).

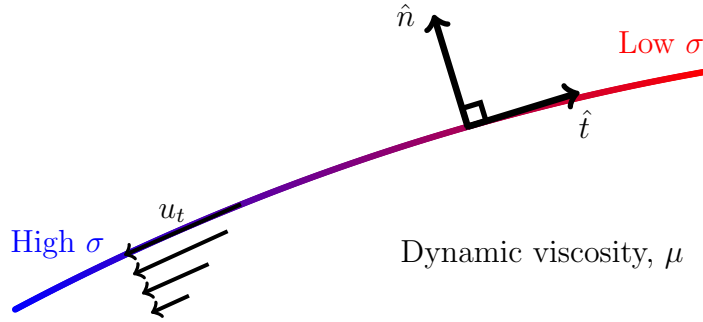


Figure 2.2: Schematic depicting Marangoni flow along a free surface (multicoloured line) of non-constant surface tension, corresponding to Equation (2.1).

For a sessile droplet consisting of a binary fluid mixture, preferential evaporation of the more volatile component together with enhanced evaporation at the contact line (assuming $\theta_{\text{eq}} < 90^\circ$, see Sections 2.2.2 and 2.2.3) results in a higher concentration of the less volatile fluid near the contact line; that is, compositional variation on the free surface. Hence, for alcohol-water mixtures where the alcohol both has a lower surface tension and is more volatile, Marangoni flow along the free surface towards the contact line can be seen (Talbot et al., 2016). Such Marangoni flow in a sessile droplet can interfere with the evaporation-induced internal radial flows that produce a coffee-ring with particle-laden fluids, and can even reverse them to yield a uniform deposit (Hu and Larson, 2006).

Marangoni flow is also involved in another classic transport phenomenon: *tears of wine*. Wine is primarily an alcohol-water mixture, and at the contact line on the wine glass, the greater evaporation rate of the alcohol than the water engenders a higher surface tension there. This evaporation leads to Marangoni flow towards the contact line, and thus causes fluid to be drawn up the side of the glass. At some point, due to gravity the thin film of wine formed on the wine glass breaks up into droplets, which fall into the bulk with the appearance of ‘tears’ (Bain et al., 1994).

2.1.5 Laplace pressure

The action of surface tension to minimise interfacial area engenders an excess pressure within a fluid volume that has a curved interface, which counteracts interface contraction. Hence, there is a pressure difference, Δp across a curved fluid interface known as the *Laplace pressure*. For a free spherical droplet of radius r_f in mechanical equilibrium, the force resulting from surface tension, $2\pi r_f \sigma$ is balanced by the force due to Laplace pressure, $\pi r_f^2 \Delta p$ (Frohn and Roth, 2000). Hence, by equating these two forces, the Laplace pressure for a free droplet in mechanical equilibrium is

$$\Delta p = \frac{2\sigma}{r_f}. \quad (2.2)$$

By convention, positive interface curvature is assumed for convex interfaces. Equation (2.2) only holds for a free spherical droplet, but it is in fact a special (reduced) form of the *Young-Laplace equation*

$$\Delta p = \sigma \left(\frac{1}{R_1} + \frac{1}{R_2} \right), \quad (2.3)$$

where R_1 and R_2 are the principal radii of curvature of an arbitrary interface. Equation (2.3) can be derived by considering the work done in instigating an infinitesimal displacement of a curved fluid interface (see e.g. Bormashenko, 2013b).

Equations (2.2) and (2.3) demonstrate that the Laplace pressure of a droplet depends on both its surface tension and geometry; smaller droplets with a larger surface tension have a greater Laplace pressure. In particular, a Laplace pressure ratio generated by differences in surface tension and/or size between coalescing droplets can drive asymmetric internal flows such as jets within the coalesced droplet. Surface tension differences can therefore induce both Laplace pressure ratios and Marangoni flow, so are particularly significant in the internal dynamics of droplet coalescence. Indeed, the characteristic time scale for mixing of droplets with different surface tensions, driven by Laplace pressure, is

$$\frac{8l\mu_d}{\Delta\sigma},$$

where μ_d is the (constant) dynamic viscosity of the droplets, l is the characteristic length scale, and $\Delta\sigma$ is the difference in surface tension between the droplets (Kovalchuk et al., 2019). In fact, both experimental and numerical studies have demonstrated that surface tension differences have a greater influence than geometric differences on internal flows and advective mixing in free droplet coalescence (Blanchette, 2010; Nowak et al., 2017).

2.2 Wetting

Wettability describes the ability of a liquid to maintain contact with a solid surface (hereinafter exclusively known as a *substrate*) due to intermolecular interactions between the solid and fluid phases. When a fluid is deposited onto a substrate, it can either spread to coat the substrate or ‘bead up’ to form a stationary spherical cap, known as a *sessile droplet* (as already seen in Figure 2.1). In this section, the properties of substrates and sessile droplets are explored.

2.2.1 Spreading coefficient

The ability of a fluid to *wet* (that is, remain in contact with) a substrate depends on a balance between the adhesive forces between the substrate and fluid promoting wetting and the cohesive forces between fluid molecules that lead to surface tension (see Section 2.1.1). This potential can be formalised by considering the interfacial tensions between the three

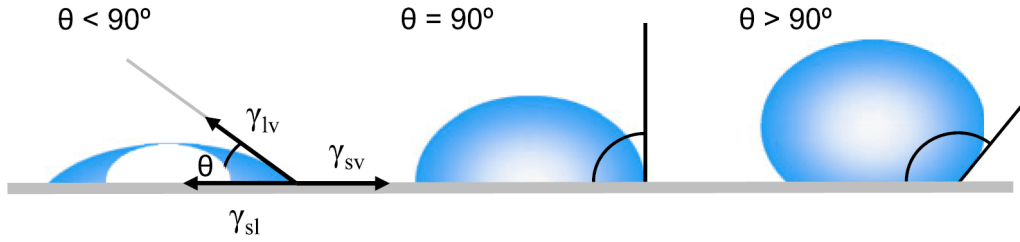


Figure 2.3: Sketch of possible sessile droplet regimes on three different substrate types. Left: a hydrophilic substrate, with the interfacial tensions of the three phases indicated. Centre: the sessile droplet is hemispherical. Right: a hydrophobic substrate. Reprinted by permission from Springer Nature Customer Service Centre GmbH: Figure 1.1 from Yuan and Lee (2013). Copyright Springer Nature, 2013.

phases: γ_{sl} , γ_{sv} and $\gamma_{lv} \equiv \sigma$ which are the solid-liquid (substrate-droplet), solid-vapour (substrate-air) and liquid-vapour (droplet-air, i.e. surface tension) interfacial tensions, as indicated in the left sketch of Figure 2.3. For a liquid to wet a dry substrate, it must be energetically favourable to replace the dry substrate with liquid (Carrier and Bonn, 2015). On this basis, it is useful to define the *spreading coefficient*, S as

$$S = \gamma_{sv} - (\gamma_{sl} + \gamma_{lv}),$$

where $S \geq 0$ implies that wetting is energetically favourable leading to the liquid spreading to completely cover the substrate, referred to as *complete wetting* or *perfect wetting* (de Gennes, 1985). Conversely, it is theoretically possible that there is no adhesion between the substrate and liquid, in which case a macroscopic vapour layer is maintained between the substrate and liquid, referred to as *non-wetting* (Frohn and Roth, 2000; Bonn et al., 2009). The intermediate and most common case between these two extremes occurs when $S < 0$ but there is adhesion between the substrate and liquid, known as *partial wetting*. Note that a macroscopic vapour layer can be maintained between an impacting droplet and a partially-wetting substrate, leading to bouncing (Chubynsky et al., 2020). It is this partial wetting case, in which sessile droplets are formed, that is exclusively of interest in this work.

2.2.2 Young contact angle

Assuming partial wetting, the tangent to the free surface of a sessile droplet at the contact line forms an angle with the substrate known as the *contact angle*, θ as seen in the left sketch of Figure 2.3. On an *ideal substrate* (atomically flat, rigid, impermeable, perfectly smooth, chemically homogeneous, etc.), there exists a unique equilibrium contact angle, θ_{eq} defined by the interfacial tensions and derived via a force balance (Bormashenko, 2013a; Shikhmurzaev, 2008). This equilibrium contact angle is known as the *Young contact angle* and is given by the *Young equation* (Young, 1805), which is

$$\sigma \cos \theta_{eq} = \gamma_{sv} - \gamma_{sl}, \quad (2.4)$$

where γ_{lv} is replaced with σ (surface tension). Equation (2.4) shows that the contact angle is determined solely by the chemical properties of the three phases via the interfacial tensions, not by droplet volume. Hence, the Young contact angle is independent of droplet size given that the ideal substrate assumption holds.

2.2.3 Substrate properties

Substrates are generally somewhat arbitrarily classified according to the equilibrium contact angle of a sessile water droplet (Berthier, 2013):

- If $\theta_{eq} < 90^\circ$, meaning that $\gamma_{sl} < \gamma_{sv}$, then the substrate is said to be *hydrophilic*. For fluids other than water, such substrates are referred to as *wetting*. This situation is depicted in the left sketch of Figure 2.3.
- If $\theta_{eq} = 90^\circ$, meaning that $\gamma_{sl} = \gamma_{sv}$, then a hemispherical droplet is formed to minimise the free surface area, as depicted in the centre sketch of Figure 2.3.
- If $\theta_{eq} > 90^\circ$, meaning that $\gamma_{sl} > \gamma_{sv}$, then the substrate is said to be *hydrophobic*. For fluids other than water, such substrates are referred to as *non-wetting*. This situation is depicted in the right sketch of Figure 2.3.
- Moreover, if $\theta_{eq} \geq 150^\circ$ then the substrate is said to be *superhydrophobic* (Yuan and Lee, 2013). There has recently been significant attention on such substrates due to their self-cleaning and water-repellent properties (Geyer et al., 2020).

Substrates need not have a uniform wettability though. Gradients in wettability can be generated by chemically treating a substrate, which produces an imbalance of the surface tension forces on either side of a sessile droplet and hence self-induced migration (Subramanian et al., 2005). Droplets can even “run uphill” against gravity on inclined substrates with a wettability gradient, if uphill is the direction of decreasing hydrophobicity (Chaudhury and Whitesides, 1992), though impacting droplets do not necessarily move in that direction (Wu et al., 2011). There have been several studies concerning mixing during the coalescence of sessile droplets brought into contact as one migrates along a wettability gradient into the other. In these cases, the wettability gradient itself has been shown to enhance mixing (Castrejón-Pita et al., 2013), as will be discussed in Chapter 6.

2.2.4 Contact angle hysteresis

Almost all real substrates are physically or chemically inhomogeneous; they may be rough on a micrometric scale, possess physical defects from fabrication or subsequent use, and have non-uniform chemical deposits (Dussan V., 1979; Quéré, 2008). As a result of such heterogeneities, the contact line may remain static over a certain range of contact angles,

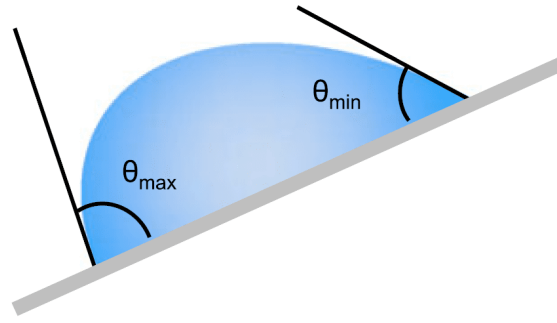


Figure 2.4: Sketch of a droplet sliding down an inclined non-zero-hysteresis substrate, with maximum and minimum contact angles of θ_{\max} and θ_{\min} , respectively. These contact angles are θ_a and θ_r , respectively, at the point the contact lines start to move. Reprinted by permission from Springer Nature Customer Service Centre GmbH: Figure 1.5 from Yuan and Lee (2013). Copyright Springer Nature, 2013.

described as *contact line pinning* (Dettre and Johnson Jr., 1964; de Gennes, 1985). In fact, even ideal substrates can exhibit contact line pinning due to intermolecular interactions between the molecules of the droplet and substrate (Bormashenko, 2013b). Hence, the equilibrium contact angle given by Equation (2.4), based on the assumption of an ideal substrate, is not in general unique, but there exists a range of contact angles for which the contact line pins ($\theta_r < \theta < \theta_a$). The limiting contact angle above which the contact line advances is known as the smallest *advancing contact angle*, θ_a whereas the contact angle below which the contact line recedes is known as the largest *receding contact angle*, θ_r . The difference between θ_a and θ_r is called the *contact angle hysteresis*, $\theta_a - \theta_r$. A very low contact angle hysteresis $\leq 1^\circ$ can be realised by coating a substrate with a lubricating layer of oil to create SLIPS (Slippery Liquid-Infused Porous Surfaces) substrates (Guan et al., 2015).

Contact angle hysteresis has many important consequences, not least that the static contact angle of a sessile droplet observed depends on how it was formed. Given sufficiently slow dynamics, for a sessile droplet formed by dewetting the initial static contact angle (before evaporation) is expected to be θ_r . Conversely, a pendant droplet very slowly placed on a substrate to form a sessile droplet is expected to have an initial static contact angle of θ_a . Observed static contact angles of a sessile droplet therefore depend on its history, which must be taken into account when characterising the wettability of a substrate. It is perhaps more accurate to explicitly highlight this notion by referring to the *as-placed static contact angle* rather than ‘the’ static contact angle (Bormashenko, 2013a).

There are several ways in which to measure θ_a and θ_r . One option is the *tilted substrate method*, where the substrate on which a sessile droplet rests is slowly tilted from the horizontal. The lower contact-line contact angle (when viewed from the side) increases whilst the higher contact-line contact angle decreases, as seen in Figure 2.4 where the two contact angles are denoted θ_{\max} and θ_{\min} , respectively. If $\theta_{\max} < \theta_a$ and $\theta_{\min} > \theta_r$, then the droplet remains stationary with the resulting asymmetry creating a Laplace pressure

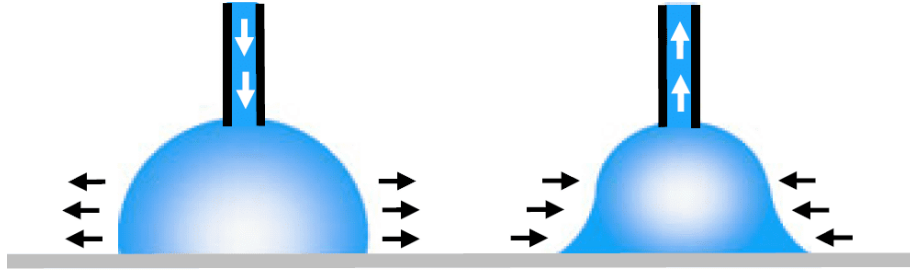


Figure 2.5: Sessile droplets with interested capillaries. Left: fluid is infused through the capillary until the contact line advances, at which point the contact angle is θ_a . Right: fluid is removed through the capillary until the contact line recedes, at which point the contact angle is θ_r . Reprinted by permission from Springer Nature Customer Service Centre GmbH: Figure 1.3 from Yuan and Lee (2013). Copyright Springer Nature, 2013.

difference across the droplet, hence a force which resists gravity. This effect can be seen on the windscreen of a moving vehicle where a rain droplet can ‘stick’ to it for some time, despite gravity and a shear air flow acting to displace it. The θ_{\max} and θ_{\min} contact angles measured at the moment the droplet starts sliding are assumed to be θ_a and θ_r , respectively, in this method. The contact angles measured however may be influenced by the droplet size due to gravity².

An alternative method to measure θ_a and θ_r , which is adopted in this work, involves inserting a capillary into a sessile droplet as seen in Figure 2.5. Additional fluid is infused through the capillary into the droplet until the contact line advances, at which moment the measured contact angle is assumed to be θ_a . Fluid is subsequently removed from the droplet through the capillary to determine θ_r in a similar way.

There are several other methods available to measure θ_a and θ_r , though in practice it is very actually difficult to accurately measure these values via any method. In particular, θ_r is very sensitive to the measurement method used and has been described as “experimentally unmeasurable on the vast majority of solid surfaces” (Bormashenko, 2013a). It is therefore often preferable to measure contact angles directly during the dynamics of interest (e.g. coalescence) to pragmatically characterise substrate wettability.

2.2.5 Capillary length

For a sessile droplet dominated by surface tension, the minimum surface energy configuration is a spherical cap, which is part of a sphere cut off by a plane (i.e. the substrate). Nevertheless, gravity acts to flatten sessile droplets, which can be significant if they are large. Hence, sessile droplets with a characteristic length scale above a certain value deviate from being spherical caps.

²Contact angles on a micrometric scale are not influenced by gravity, but the observable apparent contact angle may well be – see Section 2.6.3 for an explanation of this distinction.

In particular, gravity has a non-negligible influence on the shape of a droplet if the hydrostatic pressure, which is the pressure due to gravity, inside the droplet is not negligible compared to the Laplace pressure (Lautrup, 2011). To derive the ensuing characteristic length scale at which gravity becomes significant, consider a free spherical droplet of radius r_f in mechanical equilibrium. The hydrostatic pressure difference across such a droplet is

$$2\rho g r_f,$$

where g is Earth's gravitational acceleration. The Laplace pressure for such a droplet is given by Equation (2.2). The characteristic length scale at which the hydrostatic and Laplace pressures are similar, known as the *capillary length*, l_c is thus given by

$$l_c = \sqrt{\frac{\sigma}{\rho g}}. \quad (2.5)$$

Hence, for a sessile droplet which has a characteristic length scale smaller than the capillary length, the influence of gravity on its shape is negligible and it takes the form of a spherical cap (Bormashenko, 2013b). Otherwise, the effect of gravity is likely to flatten the sessile droplet. For water, $l_c \approx 2.7$ mm, which is larger than the characteristic length scale of most droplets considered in this work.

The influence of gravity on droplet shape is often characterised by the *Bond number*, Bo (sometimes known as the Eötvös number), which is the ratio of gravitational to surface tension forces. The Bond number is defined as

$$Bo = \frac{g l^2 \Delta \rho}{\sigma}, \quad (2.6)$$

where $\Delta \rho$ is the density difference between the droplet and the surrounding fluid. If $Bo \ll 1$, then the effect of gravity on droplet shape can be neglected. Note that the capillary length can be recovered from Equation (2.6) by setting $Bo = 1$.

It should be noted that whilst it is classically considered that any effect of gravity can be neglected if $Bo \ll 1$, the preceding analysis concerns only the influence of gravity on droplet shape. In fact, it has recently been shown that gravity influences the slow internal flows associated with evaporation in droplets for which $Bo \ll 1$ (Edwards et al., 2018; Li et al., 2019). As such, it is important to consider the potential influence of gravity on factors other than the droplet shape, independent of the Bond number.

2.2.6 Sessile droplet geometry

For image analysis of experiments and defining sessile droplets in numerical simulations, mathematical equations for spherical caps are required. Those used in later sections are given here. Consider a sessile droplet in the form of a spherical cap (i.e. $Bo \ll 1$). Let θ be the contact angle of the spherical cap formed by a sphere of radius R , as seen in

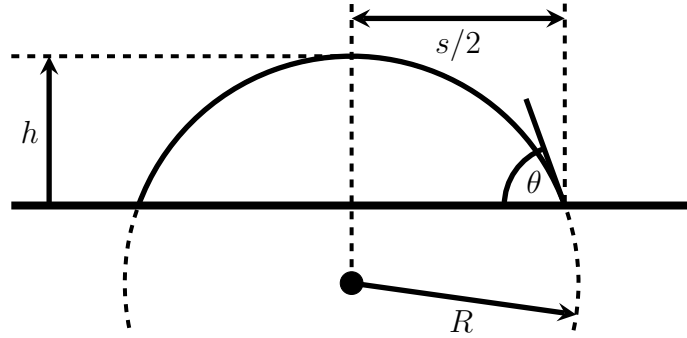


Figure 2.6: The geometry of a sessile droplet in the form of a spherical cap.

Figure 2.6. Then the apex height of the sessile droplet above the substrate, h in terms of R and θ is

$$h = R(1 - \cos \theta) \quad (2.7)$$

by elementary trigonometry. The spread length (diameter of the circular contact patch), s can be related to the same two variables as

$$s = 2R \sin \theta. \quad (2.8)$$

Note that R can not be directly measured experimentally, so it is convenient to eliminate R between Equations (2.7) and (2.8) to express the droplet height in terms of the spread length and contact angle as

$$h = \frac{s}{2} \tan \left(\frac{\theta}{2} \right). \quad (2.9)$$

A full derivation is provided in Appendix A.1.

The volume of a spherical cap, V is given by integrating a circular cross-section between the substrate and the apex. Taking $z = 0$ at the centre of the sphere forming the spherical cap,

$$V = \int_{R-h}^R \pi(R^2 - z^2) dz = \frac{\pi}{3} R^3 (2 - 3 \cos \theta + \cos^3 \theta) \quad (2.10)$$

upon substituting Equation (2.7). A full derivation is provided in Appendix A.2.

It is often useful to know the vertical position of the centre ('centre height') of the sphere forming the spherical cap, c which is given by

$$c = h - R = -R \cos \theta. \quad (2.11)$$

Given V and θ , the equivalent sphere radius, R can be obtained from Equation (2.10), and be substituted into Equation (2.11) to obtain c . Hence, a sessile droplet can be defined in numerical simulations simply by initialising a sphere of centre height c and radius R .

Attempting to measure droplet volume by fitting a circle to an image of a sessile droplet is relatively difficult and can lead to unacceptably elevated error, especially since $V \propto R^3$ so small errors in measuring R are greatly magnified in determining V . However,

the spread length, s and contact angle, θ are typically easier to measure with greater accuracy. R and h can thus be determined directly from Equations (2.7) and (2.8), respectively. This is the approach taken in this work.

As a point of comparison, it can be shown (by e.g. Berthier, 2013) that the height of a large sessile droplet ($Bo \gg 1$) is given by

$$h = 2l_c \sin\left(\frac{\theta}{2}\right) = 2\sqrt{\frac{\sigma}{\rho g}} \sin\left(\frac{\theta}{2}\right).$$

Note that this equation does not depend the droplet size, which confirms that large sessile droplets are flattened by gravity.

2.3 Droplet interactions and coalescence

In this section, a general description of the dynamics of droplet interactions is given, focusing on coalescence. Consider the interaction between two identical *free droplets* (i.e. those not attached to any structure, and typically spherical) in an immiscible outer fluid, moving toward each other. Depending on the relative influences of inertia, surface tension, viscosity and geometry (specifically the lateral offset between their relative velocities), various outcomes of the interaction can arise (see e.g. Qian and Law, 1997; Al-Dirawi and Bayly, 2020), including bouncing, merging (i.e. permanent coalescence) and temporary coalescence (e.g. reflexive separation, stretching separation). It is the permanent coalescence interaction that is of primary interest in this work, though bouncing is also seen under certain conditions in the experiments reported, as discussed in Chapters 6 and 7.

For interacting droplets, the requirement for coalescence is that the gap between them reduces to a distance comparable with that over which molecular interactions act (Nikolopoulos et al., 2009), such that van der Waals forces can cause the film of outer fluid separating the droplets to rupture (Mazutis and Griffiths, 2012). Classical models suggest a singularity at the point of coalescence due to infinite free surface curvature (e.g. Eggers et al., 1999), and the formation of single *meniscus bridge* joining the droplets. However, Perumanath et al. (2019) recently showed using molecular dynamics simulations that multiple meniscus bridges (not necessarily axisymmetric) can form between coalescing nanodroplets due to thermal capillary waves. Moreover, their work suggests that the driving mechanism at the earliest stage of coalescence is thermal fluctuations, suppressed by surface tension, before the classical hydrodynamic stage takes over above the thermal length scale. Hydrodynamic meniscus bridge expansion begins in a viscous regime (when the meniscus bridge is small, so its dynamics are dominated by viscosity), before an inertial regime ensues with meniscus bridge width growth classically considered to be proportional to $t^{1/2}$ (Thoroddsen et al., 2005; Paulsen et al., 2011). In the latter regime, meniscus bridge expansion and internal flow are driven by surface tension (due to negative Laplace pressure) and resisted by inertial and/or viscous forces. However, simulations within the

inertial regime have demonstrated that the $t^{1/2}$ scaling law has a limited region of accuracy, given that it only captures the contribution of longitudinal free surface curvature to the dynamics. An extension including the azimuthal contribution correctly describes meniscus bridge expansion throughout the inertial regime (Sprittles and Shikhmurzaev, 2014b).

The sudden release of surface energy, which accompanies meniscus bridge formation and growth, triggers capillary waves that propagate outward along the free surfaces of both coalescing droplets. These capillary waves lead to significant free surface deformation, especially when they meet having travelled around opposite sides of the droplet. Moreover, the (extra) kinetic energy derived from the released surface energy typically leads to significant droplet oscillations, dissipated by viscosity. Without external influences, the coalesced droplet will acquire a shape of minimum surface energy. Whilst the external dynamics of coalescence just described have been studied extensively and are relatively well understood, this work considers the concurrent internal dynamics (only considering the inertial regime in practice), especially in relation to fluid mixing as introduced in the next section.

2.4 Fluid mixing

Mixing on a molecular level

Throughout this work, it is generally assumed that the coalescing droplets consist of *miscible* fluids, which means that a homogeneous solution on a molecular level can be formed in all proportions within the coalesced droplet. Fluids which can not form such a homogeneous solution in a mixture, at least for some proportions, are known as *immiscible*; a classic example of such fluids is water and oil. In this work, the outer fluid (typically air) is taken to be immiscible with the droplet fluid. Note that the requirement of homogeneity is key in defining miscibility, since immiscible fluids can form mixtures, but the molecules of each fluid remain in discrete volumes. Complete mixing requires molecular diffusion to fully homogenise the fluid, not just advection of the fluid parcels (under the continuum hypothesis) to produce a macroscopically homogeneous mixture.

Molecular diffusion acts to smooth gradients in concentration, c (e.g. of a dye) according to *Fick's first law of diffusion*, which gives the diffusive flux as

$$-D \frac{\partial c}{\partial x_i}, \quad (2.12)$$

where D is the diffusivity. The diffusivity is typically $\mathcal{O}(10^{-9}) \text{ m}^2 \text{ s}^{-1}$ for liquids at room temperature (Cussler, 2009). Note that without gradients in concentration, there is of course still thermal motion of molecules, but no macroscopic changes in concentration.

As discussed above (in Section 1.2), consider again a static hemispherical (that is,

$\theta_{\text{eq}} = 90^\circ$) sessile water droplet (for which $D = 10^{-9} \text{ m}^2 \text{ s}^{-1}$) with its top half-volume dyed. For such a droplet with a 0.08 mm (80 μm) spread length, Wilson et al. (2018) found that the dye distribution becomes homogeneous after approximately half a second due to diffusion, whereas around ten minutes was required for a similar droplet with a 3.80 mm spread length. On the latter time scale, significant evaporation would be expected (perhaps the entire droplet volume for reasonably volatile fluids). Whilst evaporation-induced internal flows would constitute an additional transport mechanism that might improve the mixing rate (Hu and Larson, 2005), such time scales are unacceptably long for most applications, especially those in which a chemical reaction between the droplet fluids takes place. As diffusion acts on short length scales, reducing the length scales of the internal flow features is highly desirable to improve mixing efficiency.

Advection

Advection of fluid parcels, whilst not constituting true mixing, can significantly improve mixing efficiency. In particular, advection should extend the interfacial area over which diffusion can act (i.e. *stretch* the internal fluid interface), and reduce the length scale over which it must act (i.e. *fold* the internal fluid interface to create thin striations), to homogenise the coalesced droplet. Such stretching and folding of an internal fluid interface is herein referred to as *advective mixing*. The extent of advective mixing in a coalesced droplet depends directly on the internal dynamics. Note that simply translating fluid interfaces does not constitute advective mixing as such an action does not reduce length scales or increase interfacial area.

Considering both the diffusive (Equation (2.12)) and advective (cu_i) mass fluxes, an *advection-diffusion equation* for concentration, c , assuming no sources or sinks, is given by

$$\frac{\partial c}{\partial t} + \frac{\partial}{\partial x_j} (cu_j) - \frac{\partial}{\partial x_j} \left(D \frac{\partial c}{\partial x_j} \right) = 0, \quad (2.13)$$

where u_j is the (prescribed – e.g. from the Navier-Stokes equations) fluid velocity and summation over repeated indices is implied. With $D = 0$, Equation (2.13) simply becomes an equation for the advection of c along pathlines.

The *Péclet number*, Pe characterises the relative contributions of the advective and diffusive fluxes in Equation (2.13), and is defined as

$$\text{Pe} = \frac{Ul}{D}, \quad (2.14)$$

where U is the characteristic velocity and l is a characteristic length scale. For mixing in droplets, these values should be representative of the internal flows rather than the external dynamics (i.e. U should not necessarily be the impact velocity, for example). Smaller values of the Péclet number indicate greater importance of diffusion.

Active vs passive mixing

Effective mixing between miscible fluids contained within coalescing droplets (known as the *precursor droplets*) is required in many of the applications discussed in Chapter 1, such as biochemical reagents in lab-on-a-chip microfluidic devices and chemical reactants in reactive inkjet printing. Mixing techniques in droplets (including in microfluidic channels) are generally divided into two categories, depending on whether external energy is supplied. Techniques that rely on external energy input post-coalescence are described as *active mixing*. One means of active mixing for droplets on a substrate is *electrowetting*, which entails modifying wettability with an applied electric field. Electrowetting results in complex flow patterns within the droplet, due to its movement and oscillations of the free surface, which seem to primarily stretch the internal fluid interface to improve mixing efficiency (Paik et al., 2003). Other means of active mixing include acoustic oscillation, microstirrers and ultrasound (Hessel et al., 2005).

However, the provision of external energy is not always practical or desirable, especially in scenarios involving successive coalescence events on a substrate with evolving topology. Therefore, the internal flows initiated by coalescence are often solely responsible for determining the distribution of fluid from each of the coalescing droplets, known as *passive mixing*. There is an inherent difficulty with passive mixing in droplets though: internal flows are generally laminar due to the short length scales (and often small velocities) involved. Hence, turbulent eddies, which can result in good mixing by augmenting molecular diffusion by random movements of fluid parcels, are generally not present in coalesced droplets (Stone et al., 2004; Wilson et al., 2018). Instead, in *laminar flow* the fluid parcels move smoothly in parallel layers, with no interlayer transport except due to molecular diffusion. Hence, for efficient mixing in coalescing droplets (and laminar flows in general), it is essential to have good advective mixing which constitutes stretching and folding of the internal fluid interface. It is therefore advective mixing, via the internal dynamics, that is the primary focus of this work.

Mechanisms of passive advective mixing

At the most basic level, instigating advective mixing between coalescing droplets relies on breaking symmetry, since no advective mixing can occur during the coalescence of identical droplets with no lateral offset (Blanchette, 2010). For example, symmetry can be broken by introducing a Laplace pressure ratio between the droplets, either by difference in surface tension or size according to Equation (2.2), or the presence of a substrate. However, good advective mixing relies on the formation of complex laminar flow structures to stretch and fold the internal fluid interface as much as possible.

Perhaps the most interesting laminar flow structure that can be formed within a coalesced droplet is an *internal jet*, which may or may not constitute a *vortex ring*, but

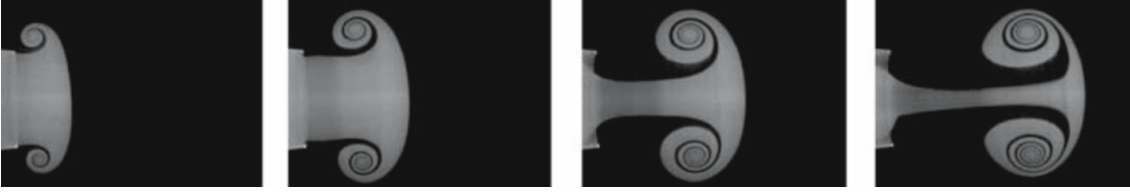


Figure 2.7: Example of the form and propagation of a laminar vortex ring generated by pumping in a deep water pool, visualised by planar laser induced fluorescence (PLIF). Reprinted (with adaptation) by permission from Springer Nature Customer Service Centre GmbH: Springer *Experiments in Fluids* Olcay and Krueger (2008). Copyright 2008.

ordinarily has the same form. Internal jets and vortex rings are relatively common in surface tension dominated flows, such as recoiling liquid filaments where they provide a mechanism to escape pinch-off (Hoepffner and Paré, 2013). Figure 2.7 shows the form of a laminar vortex ring, where only a two-dimensional plane through the axis of the vortex ring is seen. Whilst the vortex ring is formed in a deep pool in Figure 2.7, it has a similar form to an internal jet generated within a droplet. It is clear that the formation of the toroidal ring leads to significant stretching of the internal fluid interface, whilst its poloidal flow leads to considerable folding of the interface as evident from the last frame of Figure 2.7. The formation of an internal jet therefore constitutes good advective mixing, which is generally enhanced within the confines of a droplet.

Jets in coalescing droplets

Jets are often seen during the coalescence of a droplet with a pool of either equal or different fluid properties, as noted in Chapter 1. In particular, vortex rings are formed due to the vorticity generated by the relaxation of surface stresses during the initial stages of coalescence (Cresswell and Morton, 1995), whilst the evolution of such vortex rings has recently been elucidated too (Saha et al., 2019). Surface tension differences influence vortex rings in this configuration due to Marangoni flow, with the detachment of vorticity from the free surface favoured when the pool has a lower surface tension than the droplet, which results in the pool fluid engulfing the droplet fluid (Blanchette et al., 2009).

Internal jets can also be generated in droplet-droplet coalescence, although jets during the aforementioned droplet-pool coalescence have been the subject of a wider range of studies. Note that internal flows during latter are typically easier to study experimentally, since they do not have to be observed via a curved free surface. A sufficient Laplace pressure difference between free droplets can cause the droplet with higher Laplace pressure to be injected into the other in the form of a jet. According to Equation (2.2), Laplace pressure can be modified by varying droplet size or surface tension. Moreover, surface tension differences also initiate Marangoni flow (see Section 2.1.5 for a comparison to geometric differences), which is very beneficial for mixing as it constitutes an additional source of advection for fluid parcels near interfaces, thus augmenting molecular diffusion. The mixing benefits of Marangoni flow will be explored further in Chapter 7.

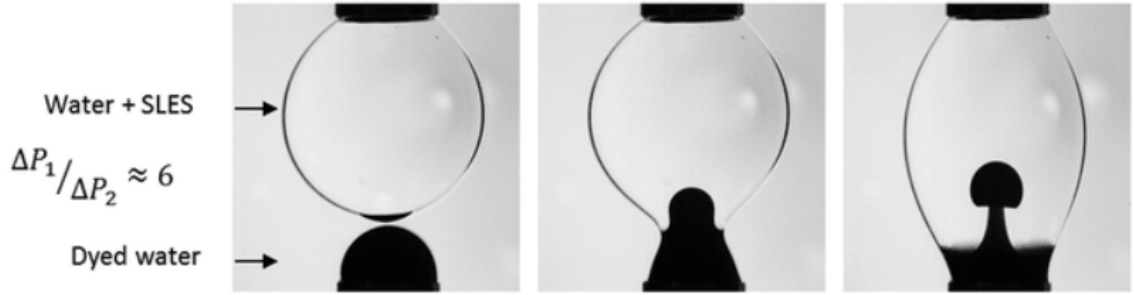


Figure 2.8: An internal jet (visualised with a black dye) formed due to a Laplace pressure ratio (of approximately six) between two initially static free droplets (attached to capillaries), one of which is laden with an anionic surfactant (sodium lauryl ether sulphate), within a high viscosity immiscible outer fluid (96 mPa·s silicone oil) that suppresses free surface movement. The three frames correspond to times of 0 ms, 10 ms and 100 ms, respectively, after coalescence is initiated. Reprinted from Nowak et al. (2017) – published by The Royal Society of Chemistry.

Figure 2.8 (from the work of Nowak et al., 2017) exhibits jet formation in coalescing free droplets with a Laplace pressure ratio of approximately six between them, generated by differences in both droplet size and surface tension. Since these droplets are contained within a high-viscosity outer fluid, the jet is formed almost immediately upon coalescence, before the meniscus bridge connecting the droplets widens significantly. Hence, the jet is almost exclusively due to the initial Laplace pressure difference between the droplets, rather than the ensuing free surface dynamics. Internal jets have also been seen during the coalescence of impacting and sessile droplets, if the latter is much larger (Castrejón-Pita et al., 2013). Internal jet formation in the presence of a substrate will be explored in Chapter 6, focussing on the effect of substrate wettability.

2.5 Dimensionless numbers and time scales

Dimensionless numbers

The *Weber number*, We characterises the importance of inertia compared to surface tension, and is defined as

$$We = \frac{\rho_d U^2 l}{\sigma}, \quad (2.15)$$

where ρ_d is the droplet density, U is the characteristic velocity, and σ is the surface tension. l is a characteristic length scale, typically taken to be the droplet radius.

The *Reynolds number*, Re characterises the importance of inertia compared to viscosity, and is defined as

$$Re = \frac{\rho_d U l}{\mu_d}, \quad (2.16)$$

where μ_d is the droplet dynamic viscosity. Flows in droplet coalescence tend to be laminar

with low Reynolds number. Usually the Weber number takes precedence over the Reynolds number due to considerations regarding surface tension.

A useful combination of the Weber and Reynolds numbers is the *Ohnesorge number*, Oh , which characterises the importance of viscosity compared to (principally) surface tension and inertial forces, and is defined as

$$Oh = \frac{\sqrt{We}}{Re} = \frac{\mu_d}{\sqrt{\rho_d \sigma l}}. \quad (2.17)$$

The Ohnesorge number enjoys wide-scale use in inkjet printing, where $Oh \in [0.1, 1]$ is a commonly accepted requirement for inks to exhibit satisfactory jetting behaviour in drop-on-demand printers (Derby, 2010). It is also typically used to characterise regimes of internal dynamics, where internal jets may form in coalesced droplets of small Ohnesorge number due to the increased prominence of surface energy, coupled with reduced viscous dissipation (e.g. Anilkumar et al., 1991; Xia et al., 2017).

Time scales

The external dynamics of droplet coalescence are in general represented by at least two characteristic time scales. The first is an *inertial time scale*, τ_σ given by

$$\tau_\sigma = \sqrt{\frac{\rho_d l^3}{\sigma}}, \quad (2.18)$$

which describes surface-tension-driven flows. There is also a *viscous time scale*,

$$\tau_\mu = \frac{\mu_d l}{\sigma}. \quad (2.19)$$

Note that the Ohnesorge number describes the balance between these two time scales:

$$Oh \equiv \frac{\tau_\mu}{\tau_\sigma} = \frac{\mu_d}{\sqrt{\rho_d \sigma l}}.$$

Hence, the dynamics of low Ohnesorge number flows generally act on the inertial time scale (McKinley, 2005).

If the coalescing droplets have different surface tensions, then the *Marangoni time scale*, τ_m , which is the characteristic time scale of Marangoni flow (see Section 2.1.4), provides an additional time scale. The Marangoni time scale is given by

$$\tau_m = \frac{(\mu_d + \mu_o)l}{\Delta\sigma}, \quad (2.20)$$

where μ_o is the outer fluid (continuous phase) dynamic viscosity and $\Delta\sigma$ is the difference in surface tension between the droplets (Kovalchuk et al., 2019).

2.6 Moving contact lines

Having considered static sessile droplets in Section 2.2 above, the contact line dynamics of droplets that move on substrates are elucidated in this section.

2.6.1 The moving contact-line problem

The movement of contact lines presents a rather fundamental problem with the classical fluid dynamical description of flow near solid boundaries – that the velocity of fluid flowing along a boundary matches its velocity, known as the *no-slip* boundary condition. As a droplet spreads, the contact line clearly moves with a non-zero velocity relative to the substrate, which appears to violate the no-slip condition. This phenomenon is known as the *moving contact-line problem* and was first pointed out by Huh and Scriven (1971). In fact, classical theory (Navier-Stokes equations plus no-slip) predicts a singularity in the shear stress at a moving contact line, giving rise to non-physical divergence of the energy dissipation rate (Ren and E, 2007). Note that no-slip and contact-line motion are compatible from a kinematic point of view though, given that no-slip and adherence are not equivalent (Dussan V. and Davis, 1974; Dussan V., 1979). The moving contact-line problem has attracted the attention of many researchers who have proposed an eclectic group of theories to resolve it, from those rooted in fluid dynamics (i.e. the continuum hypothesis) to purely molecular interpretations. A selection will be addressed briefly thus.

Perhaps the most commonly applied approach to deal with the moving contact-line problem is to relax the no-slip condition and thus allow fluid to slip (i.e. not match the substrate velocity) at and near the contact line, whilst ensuring that no-slip is respected away from the contact line (maybe asymptotically). Models employing this approach are referred to as *slip models*. There are various formulations of slip models, including the well-used *Navier-slip* model – see Shikhmurzaev (2008), for example. Whilst slip models are applicable to a wide variety of numerical formulations, they do depend on the prescription of a *slip length* (a microscopic length scale) or *slip coefficient*. However, the slip length is not particularly well-defined and must generally be determined via detailed experimental work for all combinations of fluids and substrates of interest, which somewhat degrades the predictive power of numerical simulations. Moreover, Shikhmurzaev points out that slip models do not correctly describe many experimental features seen during contact line motion (e.g. that the interface at a moving contact line appears to ‘roll over’ – see the end of this section), so appear not to reconcile the fundamental issues underlying moving contact lines.

An alternative model proposed by Seppecher (1996) considers the free surface at the contact line to be macroscopically diffuse (the *diffuse-interface model* – not to be confused with the interface-capturing technique discussed in Section 2.8) to effectively remove the singularity. However, for an immiscible fluid interface, the range of intermolecular forces

determines its thickness, which is negligible under the continuum hypothesis. Typically, diffuse-interface models lead to a macroscopic interface and so are inconsistent with experimental observations. Another class of model introduces either macroscopic or microscopic *precursor film* that precedes an advancing contact line, and is left behind by a receding contact line. The moving contact-line problem is resolved by effectively removing the substrate-air interface in the macroscopic case, and modifying the substrate-air interfacial tension in the microscopic case. However, these models do not describe how such precursor films arise in the first place, so only seem to make sense in cases where the substrate has already been wetted.

Perhaps the most promising and consistent explanation of contact-line motion is the *interface formation model* due to Shikhmurzaev (1993). As the name suggests, this model explicitly takes into account that when a contact line advances a new substrate-liquid interface is formed, i.e. the substrate-vapour interface is replaced by a substrate-liquid interface. Hence, molecules undergo a non-instantaneous transition to their new equilibrium states during contact-line motion (Wilson and Kubiak, 2016). A particularly attractive feature of this model is that it explains the existence of maximum contact angle values less than 180° . Moreover, experiments by many researchers, including Yarnold (1938) and Dussan V. and Davis (1974), suggest that free-surfaces ‘roll’ over the substrates, which gives further evidence for the non-equilibrium states of interface molecules not accounted for by many of the other models discussed above.

2.6.2 Dynamic contact angle

The contact angle of a static droplet is given by θ_{eq} , which as already discussed in Section 2.2.4 is not uniquely determined for a substrate with non-zero contact angle hysteresis. On such substrates, the contact line remains pinned for contact angles θ such that $\theta_r < \theta < \theta_a$. Once a contact line starts to move, a larger range of contact angles materialises, where the contact angle of a moving contact line is known as the *dynamic contact angle*, θ_d . Consistent with the representations made above, θ_d is defined here as the angle formed between the free surface and substrate *at the contact line*.

Whilst the dynamic contact angle is selected at the molecular scale, it defines the macroscopic free-surface shape at the contact line (Snoeijer and Andreotti, 2013). The influence of the dynamic contact angle is therefore non-local to the contact line and can have a wide-reaching influence on overall dynamics of droplets (Shikhmurzaev, 2008). In a wide variety of mathematical models (especially ones generally implemented using a finite volume framework – see Section 2.8), θ_d must be specified as a boundary condition. Whilst it is generally considered that θ_d depends on the *contact line velocity*, u_{cl} , some authors assume that $\theta_d = \theta_{\text{eq}}$ for all $u_{\text{cl}} \in \mathbb{R}$ (e.g. Eggers, 2004) as a first approximation, possibly within a slip model, or that θ_d is constant for all $|u_{\text{cl}}|$ in a given direction of contact line motion (Malgarinos et al., 2014).

Some experimental (Blake et al., 1999) and numerical (Wilson et al., 2006) studies on curtain coating suggest that θ_d depends not only on u_{cl} , but also on the flow field and geometry near to the contact line. However, recent numerical work in which air stresses were accounted for (neglected in previous works) demonstrated that the use of a fixed θ_d with the Navier-slip model can correctly describe experimental results regarding wetting failure in curtain coating (Liu et al., 2019).

For *dynamic contact angle models* that depend on u_{cl} (i.e. $\theta_d = f(u_{cl})$), the contact line velocity is often characterised by the *contact line capillary number*,

$$\text{Ca}_{cl} = \frac{\mu_d |u_{cl}|}{\sigma}. \quad (2.21)$$

Indeed, assuming $\text{Ca}_{cl} \lesssim 0.1$ (such that the contact line speed is small compared to the capillary speed, so the free surface is weakly curved), that the dynamics can be approximated by Stokes flow and zero contact angle hysteresis, a balance between viscous and surface tension forces under the lubrication approximation produces a third-order ordinary differential equation for the macroscopic free surface profile (Snoeijs and Andreotti, 2013). An exact solution in an asymptotic limit assuming that the free surface slope changes slowly with height is the *Cox-Voinov law*

$$\theta_d^3 = \theta_{eq}^3 + 9\text{Ca}_{cl} \log(l_c/l_m), \quad (2.22)$$

which is expressed here for advancing contact lines, where l_c and l_m are appropriate macroscopic and microscopic length scales, respectively (Voinov, 1976; Cox, 1986). The former is often taken as the capillary length, as written here. Note that θ_{eq} in Equation (2.22) is generally a ‘local microscopic angle’, which many authors take to be the equilibrium contact angle (as written here); others acknowledge that its value may be dependent on contact line velocity (see Blake, 2006, for details). Equation (2.22) is often simplified to

$$\theta_d^3 \approx \theta_{eq}^3 + c_T \text{Ca}_{cl}, \quad (2.23)$$

where c_T is a coefficient that is typically approximately equal to 72 (Hoffman, 1975; Göhl et al., 2018). Equation (2.23) is known as the *Hoffmann-Voinov-Tanner law* for partial wetting (Tanner, 1979).

Within the interface formation model introduced in the previous section, θ_d does not have to be specified explicitly, which enables the dynamic contact angle to be handled naturally. In particular, the interface formation model assumes that Equation (2.4) holds for moving contact lines (with θ_{eq} replaced by θ_d), whilst γ_{sl} and γ_{sv} have flow-dependent non-equilibrium values at the contact line that yield a corresponding value of θ_d . Hence, the dynamic contact angle emerges as part of the solution, rather than being specified. The influence of the flow field on θ_d is therefore captured directly. The interface formation model has been implemented within a finite element framework to study droplet deposition (Sprittles and Shikhmurzaev, 2012a), for example.

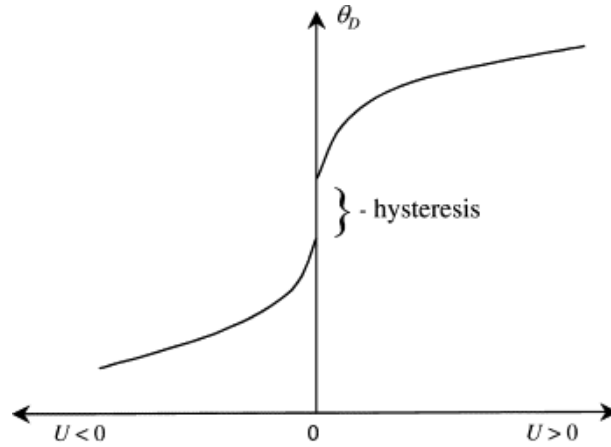


Figure 2.9: Sketch of the measured (i.e. apparent) dynamic contact angle, θ_d against contact line velocity, u_{cl} , for a substrate with non-zero contact angle hysteresis. Reprinted from Blake (2006). Copyright (2006), with permission from Elsevier.

An alternative approach introduced by Blake and Haynes (1969) is *molecular kinetic theory*, which concerns the adsorption and desorption of molecules onto the substrate near the contact line. In this model, the contact line advances when the liquid (droplet) molecules adsorb onto the substrate more than they desorb from it (on average) at the contact line. The velocity-dependence of θ_d is due to disturbances in adsorption equilibria, and so local surface tension changes (Blake, 2006).

2.6.3 Apparent contact angle

Under the continuum hypothesis, the contact line at a given location is a well-defined line at which the free surface meets the substrate. Therefore, there exists a well-defined angle between the two, assumed throughout the previous section, which is here referred to as the *actual contact angle*. Experimentally however, contact angles are typically measured via a tangent to the free surface, necessarily at some non-zero height above the substrate as a result of finite resolution. Therefore, due to free surface bending on the sub-resolution scale, the measured and actual contact angles may not be equal (Wilson and Kubiak, 2016). In particular, viscous forces can play an important role in determining the free surface shape on the sub-resolution scale, even at very low contact line capillary numbers (Dussan V., 1979). To account for this distinction, the term *apparent contact angle* is introduced for the contact angle that can be measured experimentally, i.e. from a tangent to the free surface at some point close to (but not at) the contact line. Whilst the actual contact angle is well-defined for a given scenario, in most cases the corresponding apparent contact angle depends on the measurement resolution, so the spatial resolution becomes an extra unknown. Moreover, whilst actual contact angles are not influenced by gravity, apparent contact angles can be. Note that the concept of apparent contact angles is more nuanced for non-dry (e.g. SLIPS) substrates (Guan, 2017).

The behaviour of apparent contact angles naturally accounts for any effects of the flow

field, since it is a measured (rather than a specified) quantity. The typical dependence of the measured θ_d on contact line velocity, u_{cl} for a substrate with non-zero contact angle hysteresis is sketched in Figure 2.9. In particular, the apparent contact angle increases with increasing $|u_{cl}|$ when the contact line advances, and decreases with increasing $|u_{cl}|$ when the contact line recedes (Blake, 2006).

For numerical simulations in which θ_d is specified directly as a boundary condition, it is ostensibly the actual contact angle that is prescribed, in so far as θ_d is applied *on* the substrate. However, if molecular length scales are not captured in the numerical method (i.e. the mesh resolution is greater than the slip length³), then it is effectively an apparent contact angle that is being imposed. Hence, the dynamic contact angle model used in such simulations should arguably give θ_d as an apparent contact angle. Moreover, in many cases (including in this work – see Section 4.3 and appendix B) the boundary condition is enforced by prescribing the orientation of the free surface shape close to the contact line, necessarily on a macroscopic scale. Hence, in such simulations θ_d is often given by an empirical correlation of the form $\theta_d = f(u_{cl})$, recognising the experimentally observed dependence of θ_d on u_{cl} (see Figure 2.9) – such empirical correlations are given in the next section. Hereafter, θ_d is interpreted as the apparent dynamic contact angle.

2.6.4 Empirical dynamic contact angle models

In carefully controlled experiments, Hoffman (1975) measured the dynamic contact angle of advancing liquid-air free surfaces in glass capillaries over a wide range of contact line capillary numbers to show that θ_d is a function of Ca_{cl} , plus a ‘shift factor’ to account for partial wetting (i.e. that $\theta_{eq} \neq 0^\circ$). In particular, the shift factor was found to be a function of θ_{eq} only. As seen from Figure 2.10, the data collapse onto a single curve.

Whilst Hoffman did not provide an explicit mathematical function for the curve, via a least-square-error fit to Hoffman’s data Jiang et al. (1979) proposed the following correlation for θ_d :

$$\frac{\cos(\theta_{eq}) - \cos(\theta_d)}{1 + \cos(\theta_{eq})} = \tanh(4.96Ca_{cl}^{0.702}). \quad (2.24)$$

Note that this model has no free parameters that need to be prescribed to permit its use.

In the spirit of Hoffman’s original inference, Kistler (1993) provided an empirical correlation for the dynamic contact angle. In particular,

$$\theta_d = f_H [Ca_{cl} + f_H^{-1}(\theta_{eq})], \quad (2.25)$$

where f_H is the *Hoffman function*. Note that $\theta_d = f_H(Ca_{cl})$ in the case of perfect wetting.

³In the finite element simulations of Wilson et al. (2006), the elements are at least an order of magnitude smaller than the slip length, so the perceivable contact angle is effectively the actual contact angle.

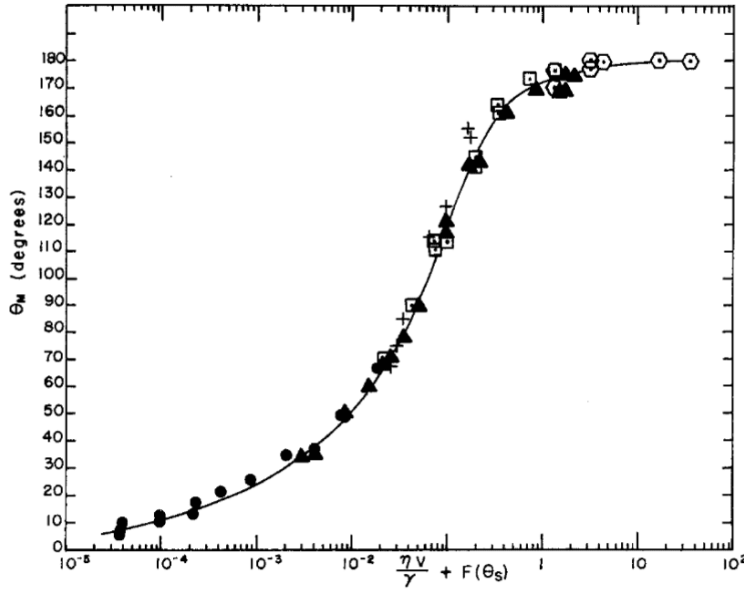


Figure 2.10: Dynamic contact angle, θ_d observed for an advancing liquid-air free surface in a glass capillary for various fluid and flow conditions, plotted against Ca_{cl} plus a shift factor that is a function of θ_{eq} only. All data collapse onto a single curve. Reprinted from Hoffman (1975), Copyright (2015), with permission from Elsevier.

The Hoffman function is given by

$$f_H(s) = \arccos \left\{ 1 - 2 \tanh \left[5.16 \left(\frac{s}{1 + 1.31s^{0.99}} \right)^{0.706} \right] \right\}. \quad (2.26)$$

For low contact line capillary numbers, these empirical models agree well with the theoretical results of Equations (2.22) and (2.23) (Wilson and Kubiak, 2016). Kistler's model, and Hoffman's inference in general, can be adapted to include contact angle hysteresis (see page 76 in Chapter 4) with only θ_a , θ_{eq} (which is in practice inconsequential) and θ_r as required inputs, which are all relatively easy to determine compared to the inputs required in many slip models. Kistler's model has been used to faithfully capture substrate wettability for a wide range of droplet dynamics (e.g. Roisman et al., 2002; Graham et al., 2012; Chu et al., 2020). It does suffer from a theoretical limitation when contact lines are being formed due to droplet impact where $\theta_d = 180^\circ$ initially, which Equation (2.25) does not predict, though this theoretical limitation is not necessarily detrimental to elucidating droplet dynamics in practice (Šikalo et al., 2005; Mukherjee and Abraham, 2007). In particular, for situations in which contact lines only undergo perturbations from an equilibrium state (e.g. of a sessile droplet) on partially-wetting substrates (instead of being formed), consistent with Hoffman's data, the Kistler model often performs very well. In particular, the non-zero contact angle hysteresis version of the Kistler model introduced in Chapter 4 is used to model substrate wettability in this work, with excellent quantitative experimental agreement achieved.

2.7 Experimental studies of internal flows

In this section, various experimental techniques that have been applied to study internal flows within droplets are discussed. Most of these techniques are optical and based on high-speed imaging, due to the short time scales invariably involved in coalescence.

2.7.1 Flow visualisation techniques

Inert dyes

Perhaps the most common means to visualise internal flows in coalescing droplets is by adding an inert dye to one droplet and using a high-speed camera to monitor the ensuing dye movement, as already seen in Figure 2.8. This technique allows for a direct assessment of fluid transport, enabling the extent of advective mixing to be clearly seen, and is especially suitable for identifying jet formation and the structure of internal interfaces more generally. Only an LED light is required to illuminate such flows (rather than a laser), which reduces experimental complication, though implementing adequate lighting is often challenging due to the short time and length scales involved (as will be elucidated in Section 3.3). The lighting requirements also typically limit this technique to the study of millimetric droplets. A similar effect to inert dyes can be had by seeding the droplet with a large number of (colloidal) particles instead, though such particles may themselves have a non-negligible effect on the flow.

Such visualisation generally necessitates viewing the internal dynamics through a curved free surface, which can have a significant distortive effect. Moreover, it is not necessarily possible to perceive all of the internal flows occurring within the droplet using inert dyes, since dye close to the free surface can block the view of the deep interior. These limitations can be somewhat circumvented by acquiring more than one point of view of the dynamics using multiple high-speed cameras though. Whilst advective mixing can be perceived using inert dyes, homogeneous regions (i.e. those mixed on a molecular level – see Section 2.4) can not be directly identified. Perhaps the main limitation of this visualisation technique from the point of view of analysis is that it does not acquire the velocity field, which must be inferred if desired. Hence, it can be challenging to unequivocally determine the underlying physics driving the dynamics seen using only an inert dye.

Examples of research using inert dyes for internal flow visualisation include Castrejón-Pita et al. (2013) for impacting and coalescing droplets, Nowak et al. (2017) for coalescing droplets in oil (see Figure 2.8), and Ersoy and Eslamian (2019) for droplet impact onto liquid films. With silica colloidal particles, Harbottle et al. (2011) were able to visualise internal flows during droplet-pool coalescence.

Fluorescence

Inert dyes can be replaced by ones which fluoresce to display internal flows. To induce adequate fluorescence for high-speed visualisation, it is generally required to use a laser in order to excite the fluorescent dye at a specific wavelength, in which case the technique is known as *laser-induced fluorescence* (LIF). In particular, if the laser light is provided in the form of a sheet, then a single cross section of the droplet can be visualised – in this case, the technique is called *planar laser-induced fluorescence* (PLIF). The use of PLIF can reduce some of the issues noted in the previous section concerning imaging internal flows through curved free surfaces.

Using (P)LIF techniques, aspects of the flow and free surface dynamics occurring where the fluorescent dye is not present, such as contact line dynamics and capillary waves, cannot necessarily be perceived. However, fluorescence can be combined with colour imaging to offset this limitation, such as implemented by Castrejón-Pita et al. (2016) who used PLIF to study droplet impact onto moving liquid free surfaces, where mixing processes and free surface dynamics were both clearly visible. (P)LIF has similar limitations to those of inert dyes regarding the lack of flow field and mixed region information, though it is possible to perform simultaneous optical fluorescence imaging and PIV (see below) in order to obtain velocity fields too. As for inert dyes, fluorescent dyes can have complex chemistry and be surface active, which may alter the dynamics being observed. Hence, such dyes should be used in moderation. It is important to choose dyes (both fluorescent and otherwise) carefully, characterise their influence on the fluids used, and consider the potential implications on the dynamics of interest. To improve optical resolution, fluorescence techniques can be used with a microscope in *fluorescence microscopy*, though the use of such methods is limited by the short time scales involved in droplet dynamics.

Examples of research using P(LIF) include Anilkumar et al. (1991) for droplet-pool coalescence (LIF), Castrejón-Pita et al. (2012) for visualising von Kármán vortex streets during droplet impact onto pools (PLIF), and Fathi and Dickens (2013) for mixing between jetted droplets (fluorescence microscopy using UV LEDs).

Confocal fluorescence microscopy

Confocal fluorescence microscopy is a special type of fluorescence microscopy, which benefits from a higher optical resolution. Unlike standard fluorescence microscopy techniques that illuminate the whole droplet at once, in confocal microscopy the incident light is focussed onto a particular point within the droplet, with out-of-focus emitted light (resulting from fluorescence) blocked. This technique therefore provides a detailed view of a very small volume of the droplet and so avoids averaging depth-wise, but must be repeated over many points via scanning to build-up an optical slice through the droplet. Multiple scans can be completed at different depths to construct a three-dimensional image, which

can yield a wealth of information about the flow structures within the droplet. Moreover, it has the potential to enable the investigation of internal flows in smaller scale droplets, including those prevalent in inkjet printing, than the techniques described above.

Unfortunately, the temporal resolution of planar scanning is generally quite low, so confocal fluorescence microscopy is not currently suitable for studying the fast dynamics immediately following coalescence. Nevertheless, the technique is still useful in the study of mixing. Lai et al. (2010) and Yeh et al. (2013) used confocal microscopes which could scan a plane (with a pixel resolution of 512×512) in 30.5 ms to study the diffusive-mixing stage which ensued several-hundred milliseconds after the initiation of coalescence between two sessile droplets, i.e after the initial short time scale surface tension driven flows subsided. Ingeniously, Kröber et al. (2009) used confocal fluorescence microscopy to study the morphology of a dried deposit in RIJ (see Chapter 1), where one of the coalescing droplets contained a fluorescent dye, to determine the final extent of mixing.

Whilst currently available confocal microscopes execute scanning too slowly to be of use in studying the fast dynamics of surface tension dominated flows, improvements in scanning speed could enable their use. In particular, such an advancement may revolutionise our understanding of internal flows in (inkjet) printed droplets by enabling the internal dynamics of micrometric (rather than millimetric) droplets to be observed. In fact, recent advancements in confocal microscopy have demonstrated much faster planar scanning (of less than 100 μ s in certain circumstances) that could potentially be suitable for studying short time scale internal dynamics at small scales (Mikami et al., 2018).

Colour-change reactions

The visualisation techniques noted above enable the extent of advective mixing within coalescing droplets to be determined, but are not able to directly identify regions that are mixed on a molecular level (see Section 2.4). To expose mixed regions, a colour-change reaction can be employed where the fluids contained within each coalescing droplet change colour when mixed due to differences in pH. In particular, the pH indicator is contained in one droplet that has a particular pH, whereas the other droplet has a different pH such that when the pH indicator comes into contact with the latter (i.e. when there is mixing between the fluids) it changes colour. Hence, there is a clear visual identifier of mixing.

Whilst this technique is apt for identifying mixed regions, it does require the use of colour high-speed imaging which can be challenging (see Section 3.3). Furthermore, this technique does not clearly display internal flow structures or the extent of advective mixing, so is perhaps best used in combination with one of the visualisation techniques noted above. There is also some ambiguity about the effect of the colour-change reaction on the rate of mixing itself; this ambiguity will be discussed and resolved in Chapter 8.

Examples of research using colour-change reactions for studying mixing in droplets

include Davanlou and Kumar (2015) for levitated coalescing droplets on an immiscible liquid layer, Takano et al. (2015) for colliding free droplets, and Khaw et al. (2018) for two sessile droplets, one of which slides into the other to initiate coalescence.

(Micro) particle image velocimetry

Whilst the visualisation techniques described above are excellent for assessing either advective or diffusive mixing, they do not provide specific information on the flow field within droplets. *Particle image velocimetry* (PIV) derives the flow field (velocity vectors) within an illuminated plane by determining the relative motion of tracer particles that passively follow the underlying fluid flow, between two instants a short time apart. A variant of PIV known as *micro-particle image velocimetry* (μ PIV) is typically used to study flows with short length scales and evolving free surfaces, utilising fluorescent tracer particles and a microscope with a small depth of field to observe a single plane without the requirement to only illuminate the plane of interest. A detailed description of μ PIV is provided by Lindken et al. (2009), but both PIV and μ PIV yield velocity vectors (flow fields).

Whilst the flow fields produced by (μ)PIV provide extremely valuable information for determining underlying flow mechanisms, since they yield the internal flow structure, they reveal neither the extent of (advective) mixing nor the topology of internal fluid interfaces. Hence, (μ)PIV generally needs to be used in combination with one of the methods described above in the study of internal flows where mixing is of interest. For example, μ PIV and (wide-field) fluorescence microscopy can be accomplished simultaneously.

Examples of research employing (μ)PIV to study droplet dynamics include Castrejón-Pita et al. (2011) for impacting and coalescing droplets on a substrate, Yeh et al. (2013) for the coalescence of two initially sessile droplets, and Kovalchuk et al. (2019) for coalescing droplets within an immiscible oil outer phase in a microfluidic channel.

2.7.2 Challenges and limitations

As insinuated above, most current means of visualising internal flows in coalescing droplets are only manageable with millimetric droplets. In particular, studies concerning the internal dynamics of inkjet-scale (micrometric) droplets remain elusive, since the short length scales of such droplets demand both increased magnification and shorter exposures, the latter due to their shorter time scales. Both of these requirements exacerbate any difficulty in providing sufficient illumination without causing the droplets to appear as a shadowgraph, hence providing no information on the internal flow. Indeed, only indirect assessments of internal flows and the final extent of mixing have been accomplished for inkjet-scale droplets. Perhaps the most realistic way in which to study internal dynamics at such scales is via numerical simulations including numerical diffusion, which are validated with respect to internal flows at the millimetric scale, as described below.

Internal flows have been studied with respect to a wide variety of droplet configurations, but of special interest are those in which at least one droplet is both free (i.e. spherical and not attached to any structure) and initially static. Such configurations are often favoured numerically (see Table 2.1 on page 39), because the lack of initial inertia enables the flow induced by surface tension to be explicitly studied. However, initially-static free droplets are difficult to generate experimentally. For droplets within a high-viscosity outer fluid, Anilkumar et al. (1991) used a weak acoustic potential well to generate an initial condition of two static free droplets, whilst Eiswirth et al. (2012) used rising droplets with a minimal relative velocity as an approximation to the latter. Due to the difficulty in generating such droplets, some studies approximate free droplets with pendant droplets attached to capillaries (e.g. Nowak et al., 2017) that may self-detach during the coalescence process. This configuration is especially suitable for studies concerning only meniscus bridge growth (Thoroddsen et al., 2005), but capillaries are likely to affect the delicate free surface dynamics after the capillary waves that accompany coalescence reach them. An experimental method, similar to that of Zhang et al. (2009), which yields an effectively-static single free droplet for high surface tension fluids, is introduced by this work and described in Chapter 3.

2.8 Fluid interfaces in numerical simulations

Numerical simulations of multiphase flows are typically more complicated than those concerning only a single fluid due the inclusion of dynamically-evolving fluid interfaces with an interfacial tension, across which there are abrupt changes in fluid properties. In particular, there exists a normal stress jump proportional to the interfacial curvature (Hou et al., 2001). Moreover, in cases with solid boundaries, there is also a need to accurately capture the fluid-structure interaction, potentially including wettability.

Mathematical models expressed in the form of partial differential equations (PDEs), generally based on the Navier-Stokes equations, are used to describe the flow of viscous fluids, with suitable modifications to represent multiphase flows. Such PDEs do not typically have closed-form analytical solutions, so it is required to *discretise* these equations on a *mesh* made up of *cells*, and so into a system of algebraic equations that can be iteratively solved to produce approximate solutions. Various methods for discretising PDEs and describing fluid interfaces in multiphase flows are briefly discussed below, focusing on their application to internal dynamics and mixing of droplets.

There are two main approaches for describing fluid interfaces: *interface-tracking* techniques, in which the mesh is aligned with the interface and is updated to remain aligned with the interface as it moves, and *interface-capturing* techniques, in which the mesh may be fixed and the interface propagates thorough it. In the latter, some additional function ‘marks’ the location of the interface, from which its position can be determined. Whilst interface-tracking techniques are typically characterised by their high accuracy in resolving

the interface, they generally lack robustness with respect to large interface deformation and so are typically only suitable for certain classes of droplet dynamics with relatively modest interface movement (Lupo et al., 2019). Moreover, topological changes in fluid volumes are not generally handled naturally by interface-tracking techniques. *Mesh-free particle methods* such as smooth particle hydrodynamics, moving particle semi-implicit methods and molecular dynamics are also available for simulating multiphase flows, but are not typically applied to study the internal dynamics of coalescing droplets (Sun et al., 2009, being a notable exception), so are not discussed here.

A summary including some of the key numerical works studying internal flows and mixing in coalescing droplets is given in Table 2.1. In the subsections below, the most common discretisation methods and ways of describing fluid interfaces listed in Table 2.1 are discussed. Of course, there are several other ways in which to describe fluid interfaces than are discussed here, such as *boundary integral methods* and *immersed boundary methods* (the latter recently implemented within a volume-of-fluid framework by Göhl et al., 2018), though these methods are not generally applied to study the internal dynamics of coalescing droplets and so are not of interest here.

2.8.1 Finite element method

In the context of coalescing droplets, the most common interface-tracking techniques are based on the *finite element method* (FEM). In FEM, the domain is discretised into elements with linear or curved edges/surfaces, where the mesh is fitted to the interface and evolves with it. As the interface coincides with the boundaries (edges/surfaces) of elements, the position of the fluid interface is known exactly, across which there is a discontinuous change in fluid properties. FEM is therefore described as a *sharp interface method*, which means that the interface remains well-defined. The outer fluid can either be included directly within the model or as an inviscid medium of constant pressure (i.e. dynamically passive), according to its expected influence on the flow.

The preservation of a sharp interface is perhaps the main advantage of FEM, since it allows additional surface stresses, such as induced by surface tension gradients (to capture Marangoni flow), and diffusive fluxes for including evaporation to be modelled (Diddens, 2017). However, such interface-tracking methods are challenging to implement in complex multiphase flows, which are characterised by significant interface movement and topological changes such as break-up and coalescence (Hoang et al., 2013; Raman, 2016). Hence, use of the FEM is not widespread in the study of mixing and internal dynamics, and is typically only used in cases with limited interface movement in highly viscous outer fluids, and where a substrate is not involved. For example, Nowak et al. (2017) used a combined FEM and finite volume method (see below) code – Fluidity – to study the coalescence of droplets with non-equal surface tensions, but with consideration limited to only the early-time dynamics.

Table 2.1: Summary of key numerical works concerning internal flows and mixing in coalescing droplets, with the numerical framework indicated.

Reference	Droplet configuration	Disc. Scheme	Interf Cap.	Int. Dynamics	Validation
Nobari and Tryggvason (1994)	Static in viscous outer fluid	FDM	Front-track.	Scalar field	Validated code ^a
Blanchette et al. (2009)	Droplet-pool	FDM	MAC/Front-track.	Scalar field	Own experiments
Blanchette (2010)	Static in microchannel	FDM	MAC/Front-track.	Scalar field	Prior publication ^b
Eiswirth et al. (2012)	Rising toluene droplets in water	FEM (COMSOL)	Level-set	Velocity vectors	Own experiments
Castrejón-Pita et al. (2013)	Impacting & sessile; dual sessile ^c	LBM	Shan-Chen	Tracer particles	Own experiments
Sun et al. (2014)	Binary collision	LBM	Diffuse interface	Scalar field	Exp. in literature ^d
Sun et al. (2015a)	Static (non-Newtonian)	LBM	Phase-field	Scalar field	Exp. in literature ^e
Sun et al. (2015b)	Binary collision (non-Newtonian)	LBM	Phase-field	Scalar field	Exp. in literature ^f
Raman et al. (2016)	Impacting & sessile	LBM	Phase-field	Tracer particles	Exp. in literature ^g
Tang et al. (2016)	Binary collision	FVM (Gerris)	VOF	Scalar field	Own experiments
Chen et al. (2017)	Impacting water & sessile oil	FVM (Gerris)	VOF	Immisc. fluids	Own experiments
Nowak et al. (2017)	Static in oil	Mixed (Fluidity)	Specialised ^h	Scalar field	Own experiments
Raman et al. (2017)	Impacting & sessile (oblique)	LBM	Phase-field	Tracer particles	Exp. in literature ^g
Xia et al. (2017)	Static in gas	FVM (Gerris)	VOF	Scalar field	Exp. in literature ⁱ
Raman (2018)	Subsequently impacting ^j	LBM	Phase-field	Tracer particles	Exp. in literature ^k
Sun et al. (2018b)	Binary collision	LBM	Phase-field	Scalar field	Exp. in literature ^l
Jia et al. (2020)	Droplet-pool	LBM	Phase-field	Scalar field	Own experiments

^aVarious prior publications for bubbles (Unverdi and Tryggvason, 1992b,a) and other numerical studies. No comparison for the specific study.^bBlanchette and Bigioni (2009); Blanchette et al. (2009) for droplet-pool coalescence of different fluids. No comparison for the specific study.^cSessile droplets were considered on a substrate with a wettability gradient.^dAshgriz and Poo (1990) and Nobari and Tryggvason (1994) for the internal dynamics; Qian and Law (1997) for the external dynamics.^eAnilkumar et al. (1991) and Law (2012) for Newtonian droplets only.^fQian and Law (1997) and Focke and Bothe (2011) for the external dynamics; simulations of Sun et al. (2015a) for mixing of Non-Newtonian droplets.^gDong et al. (2007) for the external dynamics only.^hFluidity is a combined control-volume (FVM) and FEM code. See Pavlidis et al. (2016) for details of the interface-capturing scheme.ⁱAnilkumar et al. (1991) for the internal dynamics; Thoroddsen et al. (2005) for meniscus bridge building.^jBoth droplets impact a substrate with a wettability gradient, and spread into each other to initiate coalescence.^kYang et al. (2013) for the external dynamics only.^lDirect comparison to experiments of Tang et al. (2016). Numerical methodology same as previous work (Sun et al., 2014, 2015b, etc.).

2.8.2 Marker methods

A family of methods used to describe fluid interfaces employ massless particles known as *markers*. In *front-tracking* methods, such markers are placed on the fluid interface and advected according to flow after every time step (like in Figure 4.5 on page 89), in order to keep track of the fluid interface. The interface itself can then be represented via high-order interpolation polynomials to improve the accuracy of both the interface position and surface tension computation (Scardovelli and Zaleski, 1999). The markers are typically redistributed at regular intervals to prevent unwanted accumulation in one region of the interface. Within such methods, the interpretation of topological changes must be prescribed.

Unverdi and Tryggvason (1992b,a) implemented such a front-tracking method within a *finite difference method* (FDM) framework⁴, which Nobari and Tryggvason (1994) applied to study internal flows during the coalescence of initially-static free droplets in a viscous outer fluid. Since both the internal and external interfaces of the droplets can be captured using this technique, the extent of stretching and folding of the interface (i.e. advective mixing) can be easily determined. However, finite-difference-based front-tracking methods are uncommon in recent studies, having been superseded by the finite volume methods described below in terms of flexibility and applicability.

Marker-and-cell (MAC) algorithms also employ markers, but the markers are used to identify one fluid from another and so are spread throughout the computational domain. Indeed, markers are initially placed throughout the (typically) dispersed fluid phase and are advected according to the flow every time step so that they remain within the dispersed phase, thus identifying its location within the whole computational domain. Both Blanchette et al. (2009) and Blanchette (2010) use MAC algorithms combined with front-tracking particles to studying mixing during droplet-pool and free droplet coalescence, respectively, involving surface tension gradients.

2.8.3 Volume-of-fluid method

A commonly-used, modern means of capturing fluid interfaces is the *volume-of-fluid* (VOF) method, originally introduced by Hirt and Nichols (1981). Within VOF, a scalar function known as the *volume fraction* is introduced to enable a multiphase fluid to be treated as a single fluid with combined mixture properties. That is, the fluids share a single set of momentum equations. Similar to MAC algorithms, the volume fraction is initialised as unity throughout the dispersed phase, and zero elsewhere. Cells containing a fluid interface are those in which the volume fraction is between zero and one. An estimate of the interface position can be used to reconstruct the interface either algebraically or geometrically. The

⁴The *finite difference method* is the simplest discretisation technique, based on truncated Taylor expansions. Derivates are given by differences between *nodes* (mesh points) in space and time.

VOF method is generally implemented within a *finite volume method* (FVM) framework⁵, and in this case conserves mass by construction, which is seen as a significant advantage compared to some of the aforementioned ways of describing fluid interfaces (Deshpande et al., 2012; Ludwicki and Steen, 2020). Moreover, topological changes do not require direct intervention in VOF, as in front-tracking methods for example, there is little restriction on domain geometry, and many fluids with different fluid properties can be supported (Scardovelli and Zaleski, 1999). The VOF method is used within a FVM framework in this work, about which further details can be found in Chapter 4.

As seen in Table 2.1, several works concerning internal flows have employed the VOF method. Notably, Xia et al. (2017) used the VOF method within FVM (implemented in Gerris) to elucidate mechanisms of internal jet formation in free droplet coalescence.

2.8.4 Level-set method

The *level-set method* is an interface-capturing technique that relies on a signed distance function with respect to the interface, where the sign of this function distinguishes between each fluid (Sui et al., 2014). That is, the zero level-set represents the interface, the position of which is thus precisely known. Level-set methods are particularly well-suited to problems featuring evolving interface topology and regions of high interface curvature, especially compared to VOF. However, a well-known disadvantage of level-set methods is that they do not generally conserve mass (Keshavarzi et al., 2013). This limitation can be avoided, whilst maintaining the advantages of level-set, by using a *coupled level-set and volume-of-fluid* (CLSVOF) method; partial coalescence is a scenario in which CLSVOF methods are especially advantageous (Deka et al., 2019).

According to Table 2.1, level-set methods have seen limited use in studying internal flows. One exception is the work of Eiswirth et al. (2012), who used the level-set method within a commercial FEM code (COMSOL) to investigate coalescence in liquid-liquid emulsions. However, the numerical setup only allowed internal flows to be represented as velocity vectors (similar to PIV), which is not ideal for assessing advective mixing.

2.8.5 Lattice Boltzmann method

An alternative to the traditional Navier-Stokes equations-based methods used in flow simulations, which generally utilise the interface-tracking/capturing methods and numerical frameworks detailed above, is the *lattice Boltzmann method* (LBM). Derived from kinetic theory, LBM is a mesoscale technique based on the solution of the Boltzmann kinetic equation via collision and streaming of fictitious particles, from which the Navier-Stokes equations and macroscopic fluid properties can be derived (Chen and Doolen, 1998). There are

⁵The *finite volume method* is a discretisation technique in which PDEs are integrated over each cell, with divergence terms evaluated as fluxes through the cell faces. See Chapter 4 for more details.

several multiphase formulations of LBM, including the colour-gradient, Shan-Chen pseudopotential (in which evaporation can be readily included), free-energy and phase-field models (Huang et al., 2015).

Perhaps the main advantage of LBM for droplet dynamics over the traditional simulation methods, being a mesoscopic method, is the relatively natural way in which substrate wettability is captured, including contact angle hysteresis. Other advantages include the ability to handle topological changes naturally, relative ease of numerical implementation, parallel scalability, and the fact that LBM lends itself well to being run on GPUs (Wilson and Kubiak, 2016; Al-Ghaithi et al., 2020). Notable limitations include the relative difficulty in achieving desired fluid properties, especially realistic density ratios, and that the interface can be very diffuse, i.e. the interface thickness large (Zhang and Kwok, 2013).

Table 2.1 shows that several authors have used LBM to study the internal dynamics of droplet coalescence. To assess mixing, massless particles are generally advected with the flow, similar to MAC algorithms (though having no influence on the flow in LBM), from which a scalar field can be derived for visualisation purposes (e.g. Sun et al., 2015a). In particular, several works have used LBM to study the coalescence between impacting and sessile droplets, which involves both a change in topology and substrate interaction (Castrejón-Pita et al., 2013; Raman et al., 2017).

2.8.6 Summary

As seen from the sections above, and Table 2.1 (on page 39) in particular, there is a wide range of numerical methods available to describe the internal dynamics of coalescing droplets. Most past studies of such dynamics have utilised interface-capturing methods due to the large amount of interface movement that typically accompanies coalescence. In particular, most studies used either LBM, which is very adept at capturing substrate wettability, or FVM, coupled with either a VOF or marker-based method for interface-capturing. The latter methods have been shown to describe coalescence in various configurations appropriately. Hence, this work uses a VOF method within a FVM framework, as will be discussed and justified in Chapter 4. First though, the experimental methods utilised in this work are described in the next chapter.

Chapter 3

Experimental design and methodology

This chapter describes the experimental methods developed and applied in this work. All fluids studied were ethanol-water mixtures, or variants thereof, detailed in Section 3.1. Coalescence took place on a silanised substrate, characterised in Section 3.2, and was monitored using high-speed imaging, introduced in Section 3.3. Two distinct setups were utilised to study coalescence: one to study initially-static free-sessile droplet coalescence, described in Section 3.4, and another to study impacting and sessile droplet coalescence, described in Section 3.5. The resulting images underwent image processing, as outlined in Section 3.6.

3.1 Fluids and characterisation

3.1.1 Fluids, dyes and indicators

Base fluids

Since surface tension dominant (low Ohnesorge number) flows are most likely to yield interesting internal flow structures due to reduced viscous dissipation, the fluid was required to have relatively low viscosity. Hence, water was the primary fluid used in this work, which was a very high surface tension too. However, to study the effect of surface tension differences and Marangoni flow, an assortment of fluids with a wide range of surface tension were needed. To isolate the effect of surface tension differences, it was desirable that these fluids had similar densities and viscosities.

One option considered was the use of surfactants. However, as noted in Section 2.1.3, the effect of surfactants on internal flows is not trivial and so it was preferred to avoid their

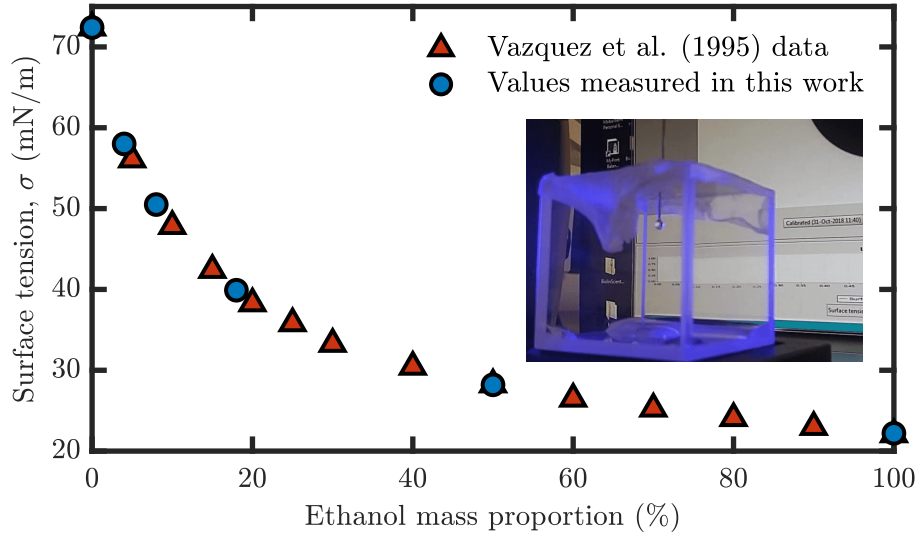


Figure 3.1: Surface tension of ethanol-water mixtures, as measured using a pendant droplet tensiometer in this work (see Section 3.1.3) and by Vazquez et al. (1995). An image of the pendant droplet experimental setup during a measurement is inset.

use, to focus on the fundamental fluid dynamics. In fact, the addition of a relatively small amount of another simple fluid such as an alcohol to water can lead to a large reduction in surface tension, as seen in Figure 3.1 for ethanol. This effect is despite the availability of hydroxyl groups in alcohol molecules for hydrogen bonding, since water molecules are much smaller and can form two hydrogen bonds each (Mizuno et al., 1995). Hence, alcohol-water mixtures enable the desired range of surface tensions with minimal changes in density or viscosity. Ethanol-water mixtures were chosen, as previously used for similar reasons by many other authors (e.g. Kooij et al., 2018). Note however that, as discussed in Section 2.1.4, ethanol is more volatile than water and so preferentially evaporates. Hence, the surface tension of ethanol-water droplets increases with time, which must be taken into account in interpreting the results, as discussed in the next section.

All ethanol-water mixtures used in this work, listed in Table 3.1, were prepared from ethanol absolute ($\geq 99.8\%$ purity, Sigma-Aldrich or VWR) and deionised water. All mixture proportions are specified by mass of ethanol. For the free and sessile droplet coalescence experiments, substrate preparation and the pendant droplet surface tension measurements, Milli-Q water (type 1 ultrapure water, resistivity $18.2 \text{ M}\Omega \text{ cm}$ at 25°C) was used instead of deionised water.

Dyes and indicators

To visualise internal flows post-coalescence, a dye was added to the free/impacting droplet in each experiment. When using monochrome imaging, Nigrosin water soluble (Alfa Aesar), which is a black synthetic dye, was used at a concentration of $0.30 \pm 0.01 \text{ g L}^{-1}$ (300 ppm) to maximise the contrast between the free and sessile droplets. When using colour imaging, Malachite green (Sigma-Aldrich) was used at an approximate concentra-

Table 3.1: Density, ρ , dynamic viscosity, μ , and surface tension, σ , of ethanol-water mixtures at 23 °C. The viscosities reported were derived from González et al. (2007); Khattab et al. (2012), whilst the density and surface tension are measured.

Fluid No.	Ethanol Mass %	Mole Frac.	ρ (kg m ⁻³)	μ (mPas)	σ (mN m ⁻¹)
1	0.0	0.000	997 ± 1	0.93 ± 0.01	72.4 ± 0.2
2	4.0	0.016	990 ± 1	1.07 ± 0.03	58.0 ± 0.5
3	8.0	0.033	984 ± 1	1.20 ± 0.02	50.5 ± 0.4
4	18.0	0.079	968 ± 1	1.56 ± 0.03	39.9 ± 0.3
5	50.0	0.281	911 ± 1	2.28 ± 0.03	28.2 ± 0.3
6	100.0	1.000	785 ± 1	1.10 ± 0.01	22.2 ± 0.2

tion of 0.1 g L⁻¹ (100 ppm) to engender additional colour appearance parameter (e.g. hue, saturation) differences for image processing.

Whilst these inert dyes are effective for visualising internal flows, they do not directly disclose the extent of (diffusive) mixing. By using a colour-change reaction between the fluids, where the colour changes only in mixed regions, the extent of mixing can be observed as explained in Section 2.7.1. To achieve the desired colour change, phenolphthalein (pH) indicator (Sigma-Aldrich, ACS reagent grade) was used with colour imaging; pH is colourless in solution at acidic or near-neutral pH values, but pink in basic (alkaline solution) conditions. When mixing a near-neutral pH fluid containing pH with a strongly basic fluid, both fluids are initially colourless but turn pink when they mix. Hence, mixed regions can be clearly identified.

Since pH is not particularly soluble in water, the fluids containing pH were required to have a relatively high ethanol content. Therefore, the neutral pH solutions used all possessed an ethanol mass percentage of 18.0% or higher in this work, with the pH concentration maximised to ensure that mixed regions developed a vivid pink colour, which could be detected using a high-speed cameras. In particular, pH was added to an 18.0% ethanol mixture at a concentration of 3.0 g L⁻¹; 50.0% and 100% ethanol mixtures at a concentration of 5.0 g L⁻¹. To prepare the 18.0% and 50.0% mixtures, pH was dissolved in pure ethanol before the required amount of water was added. The alkaline solution consisted of aqueous sodium hydroxide (NaOH) solution at a concentration of 0.1 M (0.4 mass percent), which was prepared by adding NaOH (Alfa Aesar, ACS grade), in the form of pellets, to water. NaOH is a strong base; the pH of 0.1 M NaOH was approximately 13.

3.1.2 Density and viscosity

The density of each fluid mixture at 23 °C was measured using a calibrated density bottle of nominal volume 25 mL (Brand Blaubrand, s/n 18.06 47), together with an analytical balance (0.1 mg precision), to determine the mass of an accurately known fluid volume (0.01 mL precision). The volume of the density bottle was calibrated to 25.07 mL with both Milli-Q water and ethanol independently, using the known densities at 23 °C. Three

repeated measurements were made for each fluid studied, with a measurement variability of 0.1 kg m^{-3} – 0.4 kg m^{-3} . Densities are reported to 1 kg m^{-3} precision in Table 3.1 to reflect variation between samples. The viscosity of each fluid mixture, which is known to not vary significantly in ethanol-water mixtures, was derived from either González et al. (2007) or Khattab et al. (2012). The 0.1 M aqueous sodium hydroxide solution used in this work has the same density and viscosity as water.

3.1.3 Surface tension

Tensiometry

A collection of experimental techniques to measure surface tension, where the instrument is known as a *tensiometer*, is shown in Figure 3.2. Drelich et al. (2002) provide a comprehensive description of these methods, whilst a brief overview is given here. The *du Noüy Ring* and *Wilhelmy plate* methods are based on force measurements: the force required to lift a ring from the free surface, and the force exerted during wetting, respectively (Wilhelmy, 1863).

The *maximum bubble pressure* method relies on continuously measuring the internal pressure of an air bubble formed at the end of a submerged capillary in the fluid of interest and was pioneered by Schrödinger (1915). The maximum pressure occurs when the bubble forms a hemispherical cap, with the same radius of the capillary, so the surface tension can be calculated from the reduced Young-Laplace Equation (2.2). By varying the bubble lifetime, dynamic surface tension can be measured using this method. The surface tension of each ethanol-water mixture prepared for the impacting and sessile droplet coalescence experiments was verified using a bubble pressure tensiometer (SITA pro line t15).

The *capillary rise* method is based on meniscus formation and wetting properties, whilst the *spinning droplet* method is based on a balance between interfacial tension and centrifugal force; the latter is useful for measuring very low interfacial tensions. However, the primary surface tension measurements in this work were carried out with a *pendant droplet tensiometer*. In this method, the shape of a *pendant droplet* hanging from a dispensing tip is determined by image processing. The Young-Laplace equation, in the form of a coupled set of ordinary differential equations, is then fitted to the data, yielding the surface tension. The density difference between the two phases is a required input though. The droplet volume can also be determined from the fitted Young-Laplace equation; this feature is taken advantage of in the free and sessile droplet coalescence experiments to determine the free droplet volume. The precision of a pendant droplet tensiometer depends on the droplet volume, where larger volumes (preferably such that the droplet is close to detachment during the measurement) result in greater precision. In fact, Berry et al. (2015) introduced a dimensionless number called the *Worthington number*, $Wo \in [0, 1]$ to

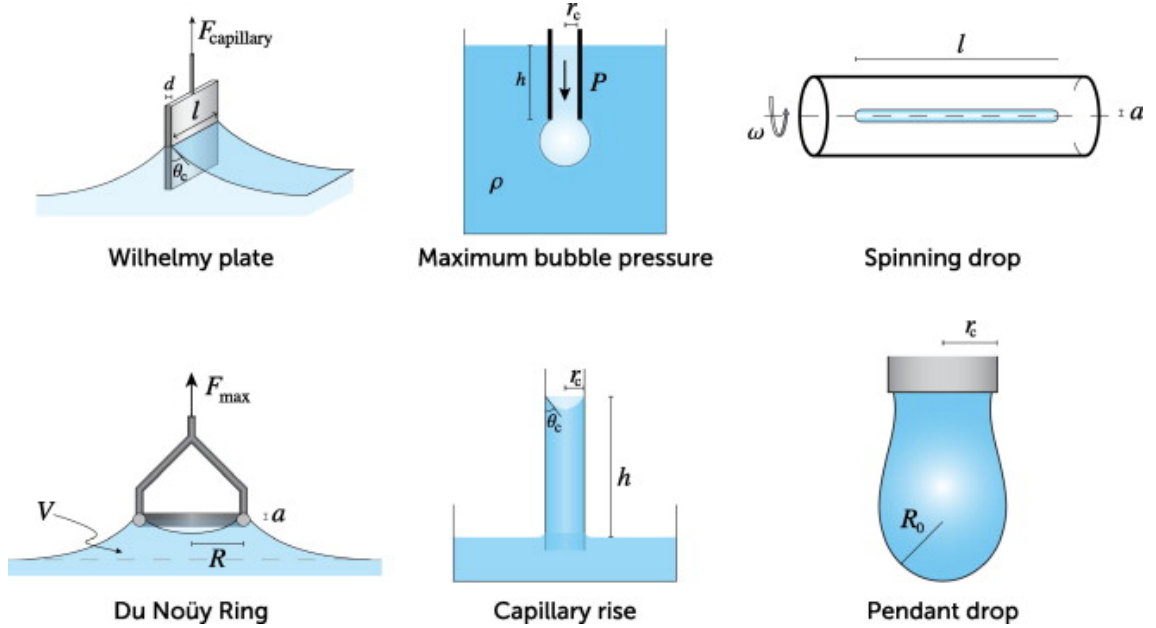


Figure 3.2: Schematics of six tensiometers. Reprinted from Berry et al. (2015), Copyright (2015), with permission from Elsevier.

characterise measurement precision. The Worthington number is defined as

$$Wo = \frac{gV\Delta\rho}{\pi\sigma D_n}, \quad (3.1)$$

where $\Delta\rho$ is the density difference between the droplet and the surrounding fluid (air for surface tension measurements), V is the pendant droplet volume and D_n is the dispensing tip's outer diameter. Larger values of Wo indicate greater precision.

Ethanol-water mixtures

The surface tension of each fluid mixture at 23 °C was measured using a pendant droplet tensiometer (Biolin Scientific Theta T200), equipped with a Navitar body tube lens (Zoom 6000 12 mm Fine Focus, 1-60135), and are given in Table 3.1. For each measurement, the largest sustainable droplet (5 μL –13 μL) was formed at the end of a stainless steel blunt end dispensing tip (Fisnar 22 gauge), within a sealed cuvette (as seen inset in Figure 3.1) to raise the ambient vapour pressure and thus suppress (preferential) evaporation. The pendant droplet was analysed for 60 s in each measurement (repeated at least four times), with its volume being automatically maintained by infusing additional fluid through the dispensing tip. The surface tension measured was always consistent with Vazquez et al. (1995). The error reported combines the random measurement error ($\pm 0.2 \text{ mN m}^{-1}$) and a random error due to variations in each sample prepared.

Note that despite the potential for preferential adsorption of ethanol at the free surface, with its hydrophobic carbon chain (Biscay et al., 2011), and that molecular aggregates are most likely formed at the free surface and in the bulk (Basařová et al., 2016), no evi-

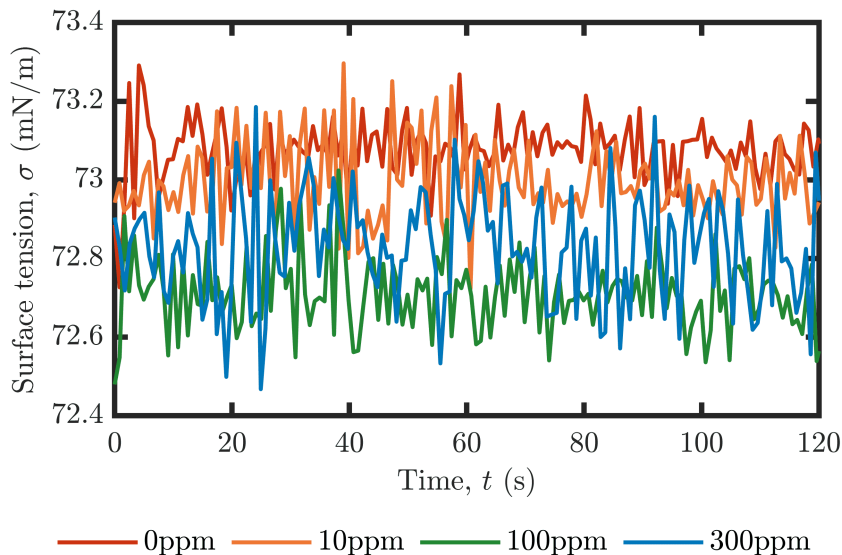


Figure 3.3: Surface tension of water at four Nigrosin dye concentrations, measured by analysing a $13.0\ \mu\text{L}$ pendant droplet in air over 120 s at approximately $21\ ^\circ\text{C}$. Anomalous data over four standard deviations from the mean were filtered out.

dence of non-constant dynamic surface tension was seen with either the bubble or pendant droplet tensiometers. This observation is consistent with those of other researchers (e.g. Basařová et al., 2018), indicating that these mixtures behave as simple fluids here.

Whilst NaOH generally increases the surface tension of fluids, the concentration of the aqueous NaOH solution used in this work ($0.1\ \text{M}$) is not sufficient to significantly change its surface tension from that of water (Lee et al., 2009; Brockmeier et al., 2012).

Dyes

The surface tension of water dyed with Nigrosin at several concentrations (from 0 ppm to 300 ppm) was measured in open air over 120 s using the pendant droplet tensiometer, with the resulting time series plotted in Figure 3.3. The data were filtered to remove points that lie over four standard deviations from the mean; such points would lie outside a 99.99% confidence level, assuming the data were normally distributed. Note that the surface tension was measured at approximately $21\ ^\circ\text{C}$ for Figure 3.3, so the value for the undyed water is slightly higher than reported in Table 3.1, for which the temperature was approximately $23\ ^\circ\text{C}$. Within experimental error, there was no significant difference between the surface tension of the undyed and dyed fluids measured, demonstrating that the presence of Nigrosin dye at the concentration used in this work does not influence surface tension. A similar analysis produced an equivalent result for Malachite green. Hence, within experimental error, the dyed and undyed fluids have identical fluid properties.

Sessile droplet evaporation

For droplets of ethanol-water mixtures, it is important to appreciate that the ethanol will preferentially evaporate and so the surface tension of the droplet will increase in time as the proportion of water rises, which was originally noted in Section 2.1.4. The effect is particularly acute for sessile droplets, where enhanced evaporation at the contact line (assuming $\theta_{\text{eq}} < 90^\circ$) occurs (Hu and Larson, 2002). In some of the experiments reported in this work, a sessile droplet consisting of an ethanol-water mixture is deposited some time before coalescence; the effect of evaporation on such droplets needs to be understood.

Evaporation was quantified by recording the volume loss over time from sessile droplets in open air (equivalent to the coalescence experiments) consisting of four ethanol-water mixtures over 50 s, using the tensiometer described above, as seen in Figure 3.4. The pure water droplet evaporates to some extent over this period, though the three mixtures that contain some ethanol lose more volume mainly due to the higher volatility of ethanol. It can be assumed that most of the differences seen between the pure water droplet and the three other mixtures shown is due to ethanol loss. However, note that volume (rather than mass) loss is measured and reported in Figure 3.4, but ethanol is approximately 20% less dense than water which amplifies the decrease seen; that is, the mass loss of the pure water droplet is the same as its volume loss, but the volume loss from the other three mixtures is greater than its mass loss.

Figure 3.4 indicates greater evaporation for the two mixtures with the larger ethanol contents (8.0% and 18.0%), as expected. Whilst it cannot be stressed enough that the evaporation rate of a sessile droplet is faster than that of an otherwise identical pendant droplet due to the contact line, the change in surface tension of a pendant droplet consisting of these fluid mixtures was measured in time; a surface tension increase of less than 1% was observed (i.e. at most 0.4 mN m^{-1} for the 18.0% ethanol mixture) over the first 24 s (the significance of this time is disclosed in the next paragraph). However, the minimum surface tension difference between fluid mixtures used in this work is 6.0 mN m^{-1} , an order of magnitude larger.

The key to reducing the effects of evaporation is to minimise the time that the sessile droplet remains on the substrate prior to coalescence, thus reducing evaporation and avoiding appreciable changes in surface tension. Note from Figure 3.4 for the smallest non-zero ethanol mass content (4.0%) fluid, the mass loss is almost identical to that of water (within experimental error) up to 24 s, delineated by the right-hand dashed line, indicating that the relative ethanol content of the droplet does not change significantly over that time period. Hence, ethanol-containing droplets are restricted to being formed at most 24 s before coalescence throughout this work; a minimum time for sessile droplets to be on a substrate before coalescence of 16 s was adopted also (for consistency), delineated by the left-hand dashed line in Figure 3.4. Evaporation beyond 24 s is therefore inconsequential in this work, whilst evaporation up to 24 s does not induce sufficient changes in ethanol

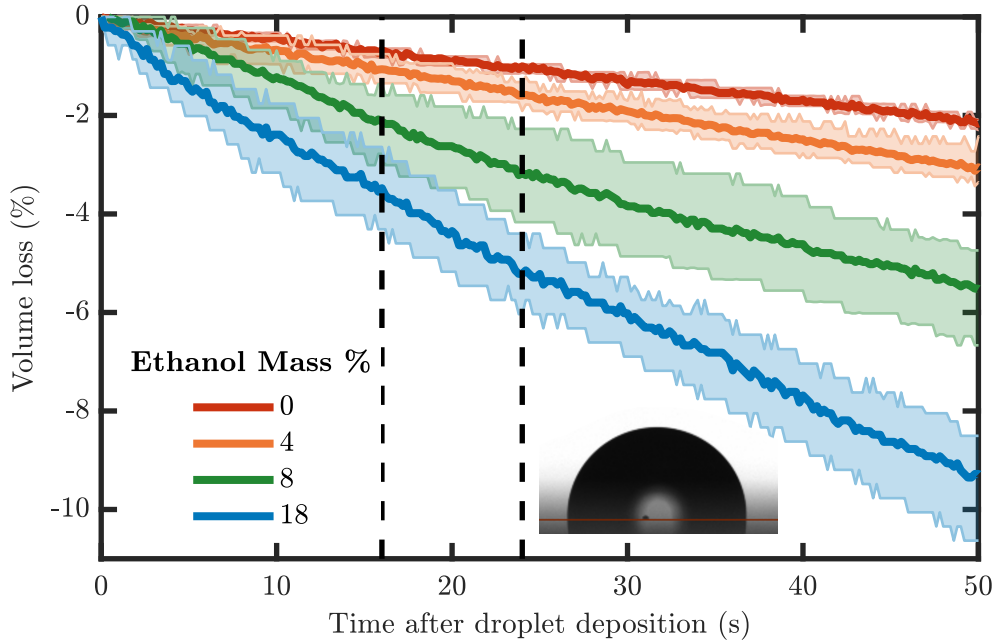


Figure 3.4: Volume loss of a sessile droplet in open air (equivalent to the coalescence experiments) consisting of four ethanol-water mixtures from Table 3.1, measured over 50s. The vertical dashed lines delineate 16s and 24s, which is the range of time that any sessile droplet containing ethanol was allowed to remain on a substrate following generation before coalescence.

concentration to appreciably change the surface tension. As noted in Section 2.1.4, evaporation does induce internal flows in sessile droplets, but these are very slow and act on a long time scale so are insignificant compared to the internal flows induced by the collision and coalescence. Ethanol-water mixtures are not used in the experimental work involving a zero velocity initial condition. Evaporation (preferential or otherwise) therefore does not affect the conclusions and trends identified in later chapters.

Note that the higher ethanol mass percentage mixtures used (50.0% and 100.0%) are not included in Figure 3.4 or the previous discussion since they are only utilised for a qualitative and comparative analysis with each other, so any surface tension variations are unimportant.

3.2 Substrate

3.2.1 Requirements and choice

The influence of the substrate and its wettability on coalescence is of interest in this work, so the choice of substrate is significant. The rationale for the choice made is elucidated here in reference to these requirements and desirable properties:

- Transparency, to enable optical access from below for a bottom view of coalescence

and to improve droplet illumination (see Section 3.3).

- Moderate hydrophobicity, since acquiring a front view of a droplet with a low contact angle using a front-lit arrangement (see Section 3.3) is challenging due to reflections. It was also hypothesised that higher equilibrium contact angles would promote desirable internal jet formation (see Chapter 6).
- High contact angle hysteresis with some pinning, to reduce contact line movement and increase contact angle variation, whilst providing a challenging test of the developed numerical simulations which included hysteresis but not pinning. A large contact angle hysteresis was also helpful for generating the unconventional static initial condition for coalescence (see Chapter 6).

The transparency requirement was an acute limitation. One substrate type evaluated was a synthetic polymer (e.g. polymethylmethacrylate, PMMA), which satisfied both the transparency and hysteresis criteria; it has also been used in related work (e.g. Castrejón-Pita et al., 2011). However, since $\theta_{\text{eq}} \approx 70^\circ$ for water on PMMA (Ma et al., 2007), such substrates were considered too hydrophilic to be used without additional chemical treatment in this work. Hence, to simply satisfy the transparency requirement glass slides were chosen, but since untreated glass is extremely hydrophilic ($\theta_{\text{eq}} \lesssim 10^\circ$) a chemical modification was applied to increase hydrophobicity and hysteresis.

3.2.2 Silanisation

Silanisation is a process of attaching silanes to a substrate via covalent bonds in order to modify chemical properties. Whilst functional (reactive) silanes are used in products such as adhesives and paints as coupling agents, non-functional silanes are used to modify the surface energy and thus wettability of substrates, leading to an increase in its hydrophobicity (Arkles et al., 2009). Depending on the robustness and chemical properties desired, there are many silanisation methods available including immersion (e.g. Xia et al., 2019) and vapour deposition (e.g. Wang et al., 2010). Here, a similar vapour deposition procedure to that of James (2018) was employed.

To prepare each substrate, a new glass slide (Fisherbrand plain glass, thickness 1.0 mm to 1.2 mm) was rinsed with Milli-Q water and dried with a nitrogen gas stream, before being placed in a sealed container with 0.5 mL of a silane solution (dichloromethyl-n-octylsilane, 98%, Alfa Aesar) to allow vapour deposition for 6 min to 8 min. The slide was subsequently rinsed thoroughly with Milli-Q water and air dried prior to use. Other silanisation procedures may produce more robust substrates and ensure that all groups on the silane and glass surface react, but given that droplets were quickly removed by a shear air flow following each coalescence experiment with no discernible change in wettability within a given area, the protocol outlined here is sufficient for this work.

The wettability derived from silanisation depends on the silane structure, orientation

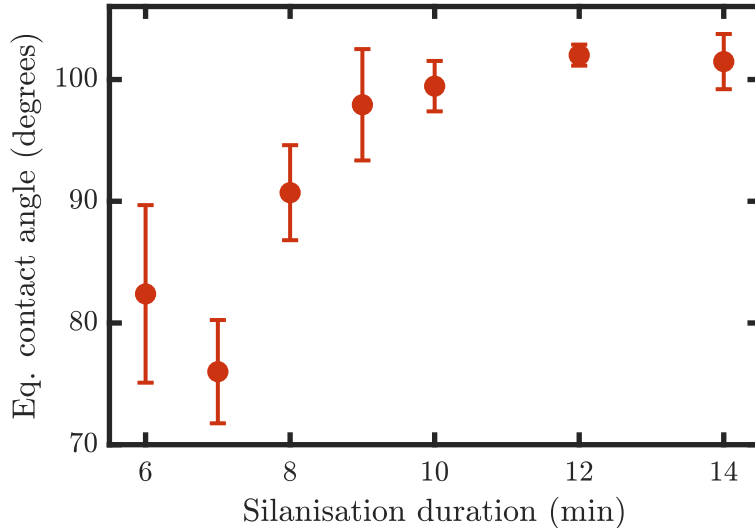


Figure 3.5: The dependence of the as-placed equilibrium contact angle, measured by the Theta tensiometer, on duration of silanisation. The error bars indicate the range of average equilibrium contact angles seen across many substrates produced.

and extent of coverage, i.e. the silanisation duration and the particular silane used. The dependence of equilibrium contact angle on silanisation duration is displayed in Figure 3.5. The contact angle measurements were made on a water droplet deposited from a dispensing tip consistent with the deposition of the sessile droplet in the impacting and sessile droplet coalescence experiments (see Section 3.5); the contact angle was determined by fitting the Young-Laplace equation via the tensiometer already described in Section 3.1.3. As the figure shows, the contact angle generally increases quickly with time for short durations before levelling off for longer durations. The maximum equilibrium contact angle achievable with this protocol and silane combination is approximately 110° . For short durations especially, the method is extremely sensitive to silanisation time, silane volume and relative position; UV pre-treatment of the glass slide did not improve this. As such, Figure 3.5 was only used as a guide and the equilibrium contact angle of a water droplet was measured on every substrate produced; an individual substrate was retained only if it had the desired wettability. Whilst many more substrates than were acceptable for use had to be produced, the procedure provided a valuable method to conveniently produce substrates satisfying all the criteria outlined in Section 3.2.1.

3.2.3 Wettability

For representative substrates, θ_a and θ_r were measured by the tensiometer using the inflation/deflation method outlined in Section 2.2.4. For substrates with $\theta_{eq} \approx 90^\circ$ for water (consistent with the impacting and sessile droplet coalescence experiments), the measured values were typically $\theta_a \approx 110^\circ$ and $\theta_r \approx 70^\circ$, respectively, so the desired high hysteresis was achieved. During the impacting and sessile droplet coalescence experiments though, the contact line generally remained pinned after the initial spreading and receded

only for very small contact angles. Hence, these substrates can be characterised as strongly pinning, with the challenge of measuring θ_r established in Section 2.2.4.

As contact line velocity affects the observed advancing and receding contact angles, for making quantitative comparisons to numerical simulations it was preferred to rely on the image-processed contact angles from the coalescence experiments themselves. Furthermore, the high hysteresis means that a wide range of equilibrium contact angles is seen; those reported in Figure 3.5 result from a particular deposition procedure so are not necessarily the same as seen at $t = 0.0$ ms in the coalescence experiments. Hence, the tensiometer-measured contact angles were only used as a criterion for admitting substrates for use, and the contact angle was measured from the high-speed camera frames at $t = 0.0$ ms for comparison to the numerical simulations in Chapter 6.

3.3 High-speed imaging

Modern high-speed cameras allow fast droplet dynamics to be resolved at incredibly small length scales, enabling the exploration of physics which would be otherwise unachievable. A general review of high-speed imaging, including its fascinating history, is provided in an excellent book edited by Ray (1997). Here, some basic ideas surrounding high-speed imaging of droplet dynamics, focusing on those important in the study of internal flows and mixing, are introduced.

Shadowgraphy

High-speed imaging of droplet dynamics typically utilises a *shadowgraph* setup, where the focal plane (on which the droplets should be located) intersects the straight line between the light source and camera. A diffuser is usually added between the light source and focal plane to produce a uniform background, and sometimes optics are added there to focus the light too. The shadowgraph setup maximises the amount of light reaching the camera's sensor, allowing the use of a short exposure to capture very fast droplet dynamics such as splashing. With shadowgraphy, excellent contrast between the droplets and background can be achieved, so the resulting images are amenable to image processing. However, since the droplets only appear as a shadow, neither variations between nor within droplets can be seen (whether the camera is colour or monochrome), so shadowgraphy is not suitable for studying the internal flows of interest in this work.

Front-lighting

The use of front-lighting, where the light source is placed in front of the focal plane (so pointing roughly in the same direction as the camera lens), is required to study inter-

nal flows. This approach avoids producing a shadowgraph; instead, the light received by the camera’s sensor is reflected off the front of the droplet, with different amounts of absorption/reflection making internal details visible (Kwon et al., 2016). However, with front-lighting significantly less light is incident on the sensor compared to a shadowgraph setup, so such arrangements require greater illumination intensity and/or the use of a higher exposure. The latter limits the potential acquisition frame rate. Careful design of the experimental setup (e.g. use of a white background) can help improve the efficiency of the light source in effectively illuminating the droplets. In particular, concurrent illumination from below and the front was found to be crucial to properly expose internal flows in this work, which necessitated the use of transparent substrates even when not required to support a bottom view. In contrast to shadowgraphy, the images resulting from front-lit setups tend to be noisy and have poorer background contrast, both of which are detrimental to image processing.

Colour vs. monochrome

When used with a front-lit setup, monochrome cameras are capable of capturing variations within droplets and are utilised to do so in this work. However, the acquisition of colour images is desirable for studying droplet mixing since a small change in intensity is more difficult to observe than a corresponding change in other colour appearance parameters (which may not change the intensity), especially hue and saturation (Balch, 1997). Furthermore, the availability of three colour channels provides additional information about the flow and aid in image processing. Unfortunately, a considerable disadvantage of colour cameras is that they are ordinarily much less sensitive than their monochrome counterparts as a consequence of the indirect way in which they detect colour. As such, the requirements for illumination increase substantially with the use of colour high-speed cameras (Kwon et al., 2016). In fact, instigating sufficient illumination whilst avoiding producing a shadowgraph was perhaps the greatest experimental challenge in this work.

Rather than detecting the intensity of the three primary colours in the RGB additive colour model separately, colour cameras typically use a *colour filter array* (CFA) to assemble colour images using a single sensor. To form the CFA, a colour filter is placed onto each pixel of the sensor to filter two out of the three primary colours, arranged as a mosaic. As such, each pixel only detects light of one colour and a *demosaicing algorithm* is used to determine the missing colours in each pixel from the raw data (Balch, 1997). The intensity of light incident on the sensor is therefore vastly reduced, which in turn reduces the sensor’s sensitivity. For example, quoted sensitivities of the monochrome and colour versions of Vision Research’s Phantom v2512 camera (the colour version of which is used in this work) are ISO 32,000D and ISO 6,400D respectively, where D indicates a daylight white balance setting.

The *Bayer CFA* (Bayer, 1976) is the most common CFA and is found in many modern

high-speed cameras, including the colour version of Vision Research’s Phantom v710 that is also used in this work (Tribble, 2014). Since approximately 50% of Bayer CFA pixels detect green light, it is advisable to ensure that the subject is green (e.g. by using a green dye such as the Malachite green used in this work to visualise internal flows) if possible.

Lens choice

Due to the small length scales involved, a zoom lens system (effectively a microscope) is typically used with high-speed cameras to achieve the magnification required to study droplet dynamics. However, the design of such lenses means that they tend to have a small aperture, which is detrimental for maximising the amount of light incident on the camera’s sensor. Whilst a shadowgraph setup generally enables enough light to reach the sensor to support the use of a zoom lens system, the use of zoom lenses with the front-lighting required for studying internal flows typically demands a relatively high exposure, which limits the possible frame rate. Hence, especially when using colour cameras, it can be sensible to compromise on magnification (i.e. image pixel resolution) and use a macro lens instead of a zoom lens, since the aperture of the former is much larger. Some of the lost magnification can be recovered by the use of *extension tubes* though. Extension tubes contain no optics, but act as a spacer between the camera and lens to reduce the minimum focus distance of macro lenses, thereby increasing the effective magnification whilst maintaining a fairly wide aperture. Macro lenses with extension tubes were used with the colour cameras in this work, whilst a zoom lens was used with the monochrome camera.

3.4 Initially-static free and sessile droplets setup

Introduction to the setup

Here, the experimental method used to study internal flows during the coalescence of an initially-static free droplet with a previously deposited sessile droplet is described. The distinguishing features of this setup in relation to previous work are:

- A front view of coalescence on a substrate is acquired at a sufficient frame rate (6,000 FPS) to capture the fast dynamics of the surface tension dominated flow, suitable for image processing. In particular, the use of a zoom lens system yields sufficient image resolution for the contact angles to be accurately determined by image-processing, whilst the internal flows are concurrently captured (cf. Section 3.3).
- The effectively static initial condition enables the substrate properties to be examined without any complicating effect of inertia, providing an excellent basis for the development of numerical simulations in which capturing the substrate wettability

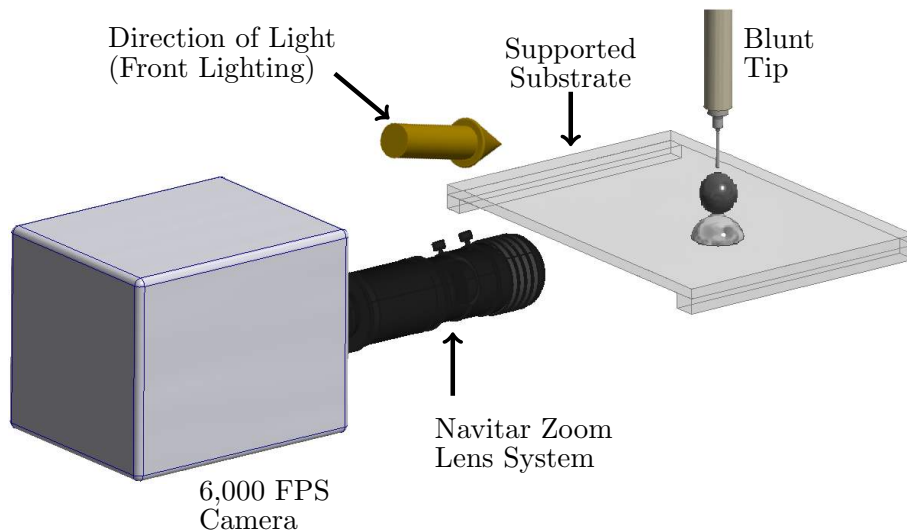


Figure 3.6: Schematic diagram of the experimental setup for studying free-sessile droplet coalescence. Note the 5 mm acrylic blocks below the silanised glass substrate.

is of paramount importance. In particular, the employed initial condition enables the droplets to be initialised in the simulations as two slightly-overlapping spherical fluid regions – see Chapter 4.

- The free droplet at the onset of coalescence is static, yet not attached to any structure that would influence the ensuing intricate free surface dynamics¹, such as the dispensing tip (cf. Nowak et al., 2017). Hence, obtaining quantitative agreement between the experiments and numerical simulations is possible.

For all such experiments, the fluid used was Milli-Q water with Nigrosin dye added to the free droplet to visualise the internal dynamics (see Section 3.1.1). Coalescence occurred on a silanised substrate (see Section 3.2). The results derived from this experimental setup are reported in Chapter 6.

Procedure

A schematic with the main features of the experimental setup is shown in Figure 3.6. The sessile droplet was manually deposited onto the substrate using either a 26 gauge needle syringe (Hamilton GASTIGHT 1701N, 10 μL) or a variable volume pipette (Thermo Scientific Finnpiette F2, 10 μL –100 μL), depending on the desired volume. The substrate was elevated by 5 mm acrylic blocks above an aluminium foil-covered translation stage (providing two-axis horizontal motion) to improve illumination, as seen in Figure 3.7. In particular, this feature enabled concurrent illumination from below, which was found to aid in the visualisation of the internal flows. The free droplet was generated by dripping from a stainless steel blunt end dispensing tip (Fisnar 30 gauge), mounted on a vertical

¹Preliminary experiments indicated that it was not possible to allow the free droplet to self-detach from the dispensing tip at the onset of coalescence without significantly influencing the dynamics.

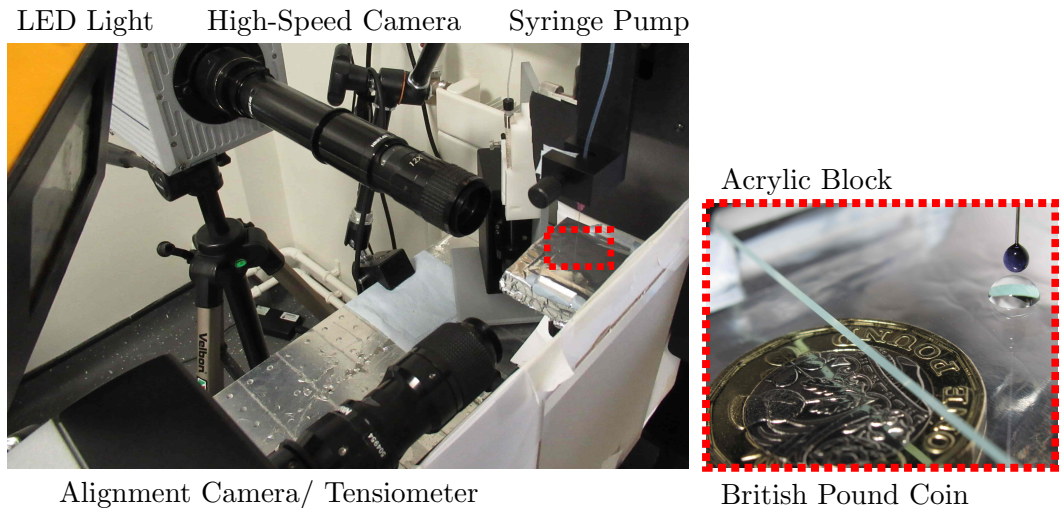


Figure 3.7: Image of the experimental setup for studying free-sessile droplet coalescence (left), with the tensiometer in the foreground. The red dotted box in that image indicates the extent of the right image, which shows the approximate configuration during alignment, taken from the direction in which the LED light is incident.

motorised stage, attached to an automated syringe pump as part of the tensiometer. Since only water was used in this configuration, any evaporation at the meniscus of the dispensing tip was inconsequential.

In each experiment, the sessile droplet was deposited whilst a stable pendant droplet formed. The sessile droplet was conveyed by the translation stage to ensure axisymmetry of the pendant and sessile droplets, monitored by the high-speed camera using a long exposure (low light mode) and an additional alignment camera as part of the tensiometer (described above), positioned perpendicular to each other as shown in Figure 3.7. Once good alignment had been confirmed, further fluid was then injected into the pendant droplet at a rate of $0.1 \mu\text{L s}^{-1}$ until it detached due to gravity and fell vertically towards the sessile droplet. The dispensing tip was carefully positioned such that the droplet free surfaces were $0.17 \pm 0.01 \text{ mm}$ apart at the point of detachment. The volume of the free droplet, V_f was measured by the tensiometer via an edge-detection routine as $6.2 \mu\text{L}$ in all experiments. Having verified the scale provided to the tensiometer's software before beginning the experiments, the error in this value is negligible. On the other hand, the sessile droplet volume, V_s was determined by image processing the high-speed camera images to nullify any effects of evaporation or uncertainty in deposition; the representative error is $\pm 0.1 \mu\text{L}$ due to the resolution of the dispensing devices.

Each experiment was repeated at least five times to establish the typical dynamics that are reported in Chapter 6. All experiments took place at room temperature ($23 \pm 2^\circ\text{C}$) and atmospheric pressure.

Imaging

A single high-speed camera (a monochrome Photron FASTCAM SA5 775K-M3) captured the dynamics from the front. The monochrome camera and modest frame rate enabled a zoom lens system to be used, consisting of body (Navitar 12X Zoom, 1-50486) and adapter (Navitar 2X F-mount, 1-62922) tubes, with no lens attachment, yielding a working distance of 86 mm. The pixel resolution was 1024×768 , giving an effective resolution of $134.5 \pm 1.5 \text{ px mm}^{-1}$ that was sufficient to accurately measure the apparent contact angles. The camera was inclined downwards approximately 2° relative to the substrate to reduce glare around the free surface. Images were recorded at 6,000 frames per second (FPS), with an exposure of approximately 143 μs .

A black reference calibration (shading correction) was carried out before each experiment to ensure uniformity of each pixel's black level and so good image quality, since the sensitivity of individual sensor pixels can be influenced by temperature variations during otherwise consistent operation. The camera was focused on the sessile droplet contact line and manually triggered upon visual identification of coalescence. The droplets were front-lit (see Section 3.3) by a single cold white 84 W LED (MultiLED LT) light, positioned above and to the right of the zoom lens (seen in Figure 3.7) to maximise brightness and minimise reflections. A white background, in addition to the previously discussed substrate position, was crucial for enabling the use of a sufficiently short exposure. The light was only switched on for a short and consistent time (approximately 10 s) during each experiment.

3.5 Impacting and sessile droplets setup

Introduction to the setup

Here, the experimental method used to study internal flows during the coalescence of an impacting droplet with a previously deposited sessile droplet is described. The distinguishing features of the setup in relation to previous work are:

- The use of dual synchronised colour high-speed cameras to provide simultaneous front and bottom views of internal flows during coalescence on a substrate (cf. Section 3.3). Previously, Castrejón-Pita et al. (2013) used one colour and one monochrome high-speed camera to image internal flows in impacting and coalescing droplets from the front and bottom simultaneously. Zhang et al. (2015) used an ingenious setup with a beam splitter to obtain simultaneous front and top views (the latter in one dimension, at a given instant) of gravity currents in coalescing sessile droplets.
- The camera, lens and lighting configuration enables a high acquisition frame rate

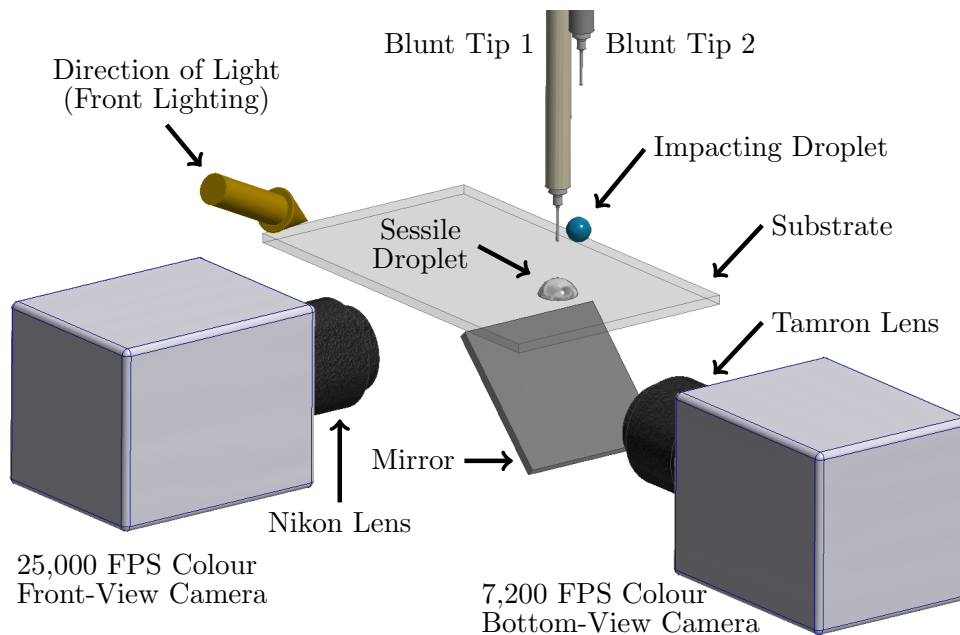


Figure 3.8: Schematic diagram of the experimental setup for studying impacting-sessile droplet coalescence. The undyed, sessile droplet was deposited from blunt tip 1; the dyed, impacting droplet was deposited from blunt tip 2.

and resolution for both the front (25,000 FPS) and bottom (7,200 FPS) views, more than sufficient to study the fast coalescence dynamics without any motion blur. Castrejón-Pita et al. (2013) captured front and bottom views at 1,000 FPS and 300 FPS, respectively, whilst the density-driven flows studied by Zhang et al. (2015) occurred on a much longer time scale, so 30 FPS was sufficient.

- The experimental design allows the lateral separation between the droplets to be easily varied such that the impacting droplet could coalesce with the sessile droplet either before or after hitting the substrate, whilst maintaining an optical path to support bottom view imaging in all cases.

These experiments make use of the full range of ethanol-water mixtures identified in Table 3.1, with Malachite green dye added to the free droplet to visualise internal flows and a phph indicator used to establish the extent of fluid mixing (see Section 3.1.1). In all cases, coalescence occurred on a silanised substrate (see Section 3.2). The results derived from this experimental setup can be found in Chapters 7 and 8.

Procedure

A schematic with the main features of the experimental setup is shown in Figure 3.8. Each precursor (impacting or sessile) droplet was generated by dripping from a stainless steel blunt end dispensing tip (Fisnar 30 gauge) using a manually-controlled syringe pump (World Precision Instruments Aladdin), set at a flow rate of $0.5 \mu\text{L s}^{-1}$ until the pendant

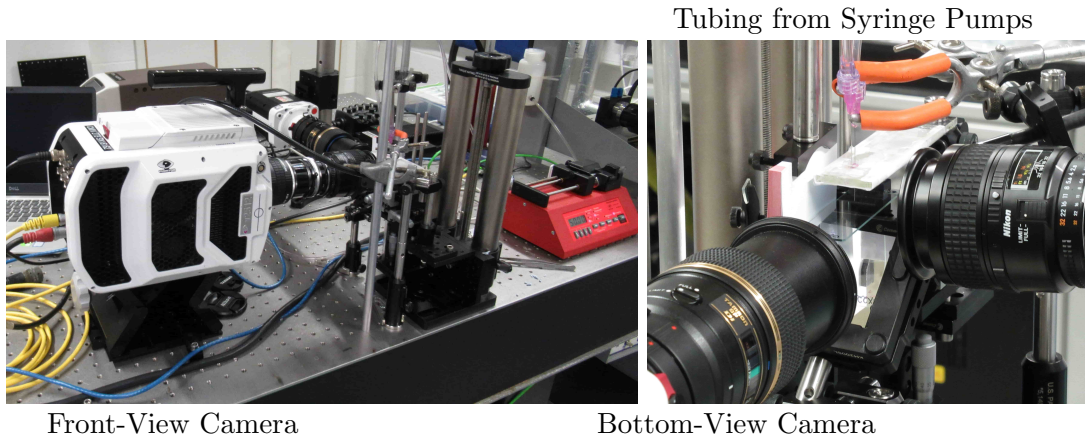


Figure 3.9: Images of the experimental setup for studying impacting-sessile droplet coalescence. Left: a wide view of the setup, with the front-view high-speed camera in the foreground. Right: a view of the cantilevered substrate, with the bottom view camera lens in the foreground.

droplet detached due to gravity and fell vertically towards the substrate. Independent, identical dispensing systems (syringe pumps and dispensing tips) were used to generate the undyed sessile and dyed impacting droplets, with the dispensing tips located 4 mm apart. The dispensing tip used to generate the sessile droplet was mounted with the blunt end 5.5 ± 0.5 mm above the substrate so the droplet was deposited gently and acquired an approximately circular footprint. The dispensing tip used to generate the impacting droplet was mounted higher to achieve a greater impact velocity, with the blunt end 16.5 ± 0.5 mm above the substrate. The impacting droplet was always in the deposition regime, where it simply spread radially outwards after striking the substrate without any breakup or splashing which would occur for higher impact velocities (Rioboo et al., 2001), as studied by others (e.g. Wang and Bourouiba, 2018). Since ethanol-water mixtures are used in this configuration, evaporation at the meniscus of the dispensing tips is a concern given that preferential evaporation of ethanol could affect the relative fluid content there, and thus in the deposited droplet. Hence, an extra droplet was generated (and caught before hitting the substrate) immediately before each precursor droplet was deposited to remove any effect of evaporation.

The silanised substrate was mounted as a rigid cantilever on a translation stage providing 2-axis horizontal motion (Comar Optics), with $10 \mu\text{m}$ precision in each direction, as shown in Figure 3.9. The combined structure was mounted on an elevation stage (Comar Optics), thereby providing the substrate with 3-axis motion. The substrate, supporting the sessile droplet after deposition, was conveyed by the translation stage to achieve the desired lateral separation with respect to the subsequently deposited impacting droplet. Droplet positions were determined by two cameras using a long exposure (low light mode) and fiducial markers; a front view gave the lateral separation and a bottom view ensured centreline alignment.

Preferential evaporation of ethanol from the sessile droplet occurred whilst it sat on

the substrate as the alignment procedure was executed. Hence, the time between successive droplet depositions (i.e. the sessile and impacting droplets) was kept deliberately short and approximately constant (20 ± 4 s). Supported by the evidence presented in Section 3.1.3, the volume loss over the period of interest (up to 24 s) is not sufficient to appreciably change the surface tension and therefore does not affect the trends identified in this work. Furthermore, each fluid mixture was produced on the day of use and the surface tension of a sample was verified using the bubble pressure tensiometer described in Section 3.1.3.

Each experiment was repeated at least three times to establish the typical dynamics that are reported in Chapters 7 and 8. All experiments took place in air at room temperature (23 ± 1 °C) and atmospheric pressure.

Imaging

Previous work imaging internal flows during droplet coalescence on a substrate has generally been limited to a single perspective, usually with a top or bottom view (e.g. Yeh et al., 2015), but occasionally complemented by a front view (e.g. Castrejón-Pita et al., 2013) or two views for slower dynamics (e.g. Zhang et al., 2015). However, simultaneous imaging has already been shown to be essential for accurately evaluating the extent of mixing within coalesced droplets, for which relatively low frame rates are sufficient (Paik et al., 2003). In many published works, the lack of a front view means that the full detail of the flow through the depth of the droplet cannot be determined, so surface and internal phenomena cannot be distinguished. Using two high-speed cameras to capture both front and bottom views simultaneously, a more complete understanding of the internal dynamics is derived. Moreover, surface and internal dynamics can be distinguished. Colour cameras are used to provide greater image detail from which to study mixing (see Section 3.3).

A high-speed camera (a colour Phantom v2512) captured the dynamics from the front, using a Nikon AF Micro 60 mm lens with aperture set to f/4. The effective magnification of the lens was increased using extension tubes (Kenko 32 mm and a Nikon K extension ring set) to give a working distance of 37 mm. The pixel resolution was 1024×768 , yielding an effective resolution of 91.5 ± 0.5 px mm⁻¹. Images were recorded at 25,000 FPS, with an exposure of 12 μs. It is important to appreciate that the sensitivity of the v2512's sensor is extremely high, which enabled the use of a significantly higher frame rate (an order of magnitude) than similar experiments reported previously. To reduce glare around the free surface in this view, the camera was inclined slightly relative to the substrate (approximately 3°). Note that the use of a Navitar lens was attempted with this camera configuration, but the minimum usable exposure was approximately 500 μs (with poor light contrast). The resulting maximum 2,000 FPS frame rate was deemed unacceptably low, which is why the macro lens assembly was chosen (cf. Section 3.3).

For some experiments, the front view camera described above was replaced by an alternative high-speed camera (a colour Phantom v710), using the same physical and lens

configuration. With this camera, the pixel resolution was 1024×512 , yielding a typical² effective resolution of $122.5 \pm 0.5 \text{ px mm}^{-1}$. The limitations of this camera compared to the v2512 necessitated a higher primary exposure of $65 \mu\text{s}$, so the frame rate was limited to 14,000 FPS. Whilst the internal flow features were adequately represented with this higher exposure, many other areas were saturated due to overexposure. Hence, an extreme dynamic range (EDR/ secondary exposure) of $20 \mu\text{s}$ was used. This feature of Phantom cameras enables the brightest parts of the image to be only exposed for the shorter EDR time by resetting pixels above a preset threshold to zero for the final part of the exposure; in this case, the pixels are reset $45 \mu\text{s}$ into the primary exposure. The result is an image with more detailed darker features (due to the higher primary exposure), but where the brighter areas are not overexposed (due to the shorter secondary exposure). When using this feature, colour casting can arise but was almost completely eliminated in this work by adjusting the white balance.

A second high-speed camera (a colour Phantom Miro LAB 310) captured the dynamics from below, through the substrate via an optical mirror (Thorlabs ME2S-G01) mounted 45° to the substrate (visible in the right-hand image of Figure 3.9). This configuration is preferable to a top view, since it clearly captures the droplet footprint on the substrate and avoids distortion from the curved free surface. A fixed aperture macro lens (Tamron SP AF 90 mm f/2.8) was used with two extension tubes (Kenko 20 mm and 12 mm). The pixel resolution was 768×576 , yielding an effective resolution of $65.0 \pm 0.5 \text{ px mm}^{-1}$. Images were recorded at 7,200 FPS, with an exposure of $120 \mu\text{s}$.

The camera arrangement is shown in Figures 3.8 and 3.9. A black reference calibration (current session reference) was carried out before each experiment. The cameras were manually triggered by a single $500 \mu\text{s}$ pulse provided directly to each camera by a pulse generator (TTi TGP110). Both cameras were focused on the droplet impact point on the substrate and positioned to fully capture the droplets for all lateral separations studied. The droplets were front-lit (see Section 3.3) by a single constant light source (200W Metal Halide lamp, 89 North PhotoFluor II), positioned approximately 50 mm from the impact point, to the right of the front view camera's lens and oblique to the horizontal (seen behind the front view camera's lens in the right-hand image of Figure 3.9). As in Section 3.4, a white background in each camera view was found to be essential for maximising the amount of light reaching the cameras' sensors. The light source shutter was only opened for a short and consistent time encompassing coalescence (usually less than 5 s) to maintain a constant temperature environment.

3.6 Image processing

Image processing utilising custom MATLAB codes was used extensively in this work to extract quantitative data from the high-speed imaging experiments, both to aid in elu-

²For one experiment reported that uses this camera, the effective resolution was 115.5 px mm^{-1} .

validating the physical mechanisms underpinning the flows, as well as for comparison to numerical simulation results. In particular, it was desired to extract geometric quantities such as edge profiles, total droplet height, internal interface location/height and spread length, in addition to apparent contact angles and impacting droplet velocities/radii.

Edge detection

To determine all such quantities, the positions of the internal/external droplet edges are required. For shadowgraph images, it is typically sufficient to ‘threshold’ the image in order to separate the foreground (droplets) from the background, based on pixel contrast values, to identify the external edges. However, with front-lit droplets the contrast difference between the bulk droplet and background pixels is greatly reduced. Therefore, an edge detection routine was used to identify discontinuities in pixel contrast (which characterise edges), rather than thresholding, in this work. To improve droplet contrast for edge detection, an approximation to the background was subtracted from each image, before the contrast was changed to saturate 1% of pixels using the `imadjust` function in MATLAB.

Another effect of front-lighting is that the resulting images are relatively noisy, with random imperfections that makes edge detection challenging due to detection of erroneous edge pixels. To reduce the influence of such random imperfections, each image was smoothed before edge detection was undertaken. In particular, a Gaussian low-pass filter (standard deviation 2) was applied via the frequency domain, using a process described in detail by Gonzalez et al. (2004). Briefly, the image was converted to become square (by adding zeros as necessary) and additionally zero-padded to reduce wrap-around error, producing the image f . A Gaussian filter of the same size, h was created before it was convolved with f to yield

$$f * h = \mathcal{F}^{-1}\{\mathcal{F}\{f\} \cdot \mathcal{F}\{h\}\},$$

where \mathcal{F} is the Fourier Transform operator and \cdot denotes element-wise multiplication. The padding was then removed from $f * h$ to yield the blurred version of f , on which edge detection was undertaken.

There are a wide range of edge detection routines available (e.g. Canny, Prewitt, Sobel), but in this work the subpixel edge detection routine suggested by Trujillo-Pino et al. (2013) was used, the code implementing which is freely available from the MATLAB Central File Exchange. This edge detection routine is apt for imperfect (realistic/noisy) images that typically have close contours, and has been shown to accurately detect edges in droplets previously (e.g. Andersen and Taboryski, 2017; Jadidbonab et al., 2018). Moreover, it also computes the normal vector (pointing towards regions of lower intensity) with respect to each edge pixel detected, which is utilised to filter edges and identify the edge type (i.e. external, internal, superfluous). For example, since the dyed fluid is generally located above the undyed fluid (the latter of higher pixel intensity), all internal edges have normals that point approximately upwards. Edge pixels are also filtered based upon

proximity and associated with each other to define edges. Examples of both filtered and unfiltered detected edges overlaid onto the underlying image can be found in Figure 6.4 on page 119, where it is clear that the left external edge is not accurately detected in the upper reaches of the droplet. However, the important quantity in that case (contact points for the spread length) is accurately and robustly identified – the philosophy of image processing in this work was to achieve an accurate and robust assessment of the required quantities, rather than perfectly and uniquely detect all external and internal edges.

For the colour images, exploitation of the constituent RGB colour channels was possible, with the red channel used to distinguish between dyed and undyed fluid (for internal edges), whilst the blue channel enabled each droplet to be identified from the background (for external edges). For experiments benefiting from multiple high-speed cameras (with front and bottom views), the internal fluid interface between the dyed and undyed fluids was tracked using the bottom view, which yields a time series of horizontal position in the plane of the front view. For each horizontal position detected, the height of the free surface above the substrate at that location was extracted from the corresponding front-view frame. This analysis yielded the two-dimensional position of surface phenomena in the plane of the front view. Horizontal positions were matched between the front and bottom views based on the right contact point of the undisturbed sessile droplet. The matched position was confirmed with a fiducial marker on the substrate, from which distances were derived accounting for the different effective resolution of each view. Summarising, the horizontal position of the internal leading edges were tracked from the bottom view, whilst the corresponding free surface height was acquired from the front view. The timing was based on the front view (highest frame rate) with each bottom view frame matched to front-view times. Due to the high frame rates of both views compared to the time scales of the phenomena studied, the error resulting from the temporal discrepancy is negligible. Timing was synchronised by identifying $t = 0.0$ ms independently in each view.

Measurement of contact angles

From the filtered detected external edges of the droplets, it is desired to obtain a time series for the apparent dynamic contact angle via image processing, for both analysis and validation purposes. The equilibrium contact angle of a static sessile droplet can be measured by fitting the Young-Laplace equation or an ellipse. To obtain the dynamic contact angle of a droplet out of equilibrium, polynomial or linear fitting of the detected edge at the contact line is commonly used (Atefi et al., 2013; Quetzeri-Santiago et al., 2020). In this work however, the method suggested by Mirzaei (2017) is used instead, which does not require fitting of analytical curves. This method was implemented in MATLAB during this course of this work, strongly motivated by the code³ of Andersen and Taboryski (2017) that is freely available from the MATLAB Central File Exchange.

³The original code of Andersen and Taboryski supports both the elliptical and polynomial fitting methods. The contact angle code used in this work was developed from their code, with the general algorithm maintained, though significant alterations were made to account for the visible internal flow.

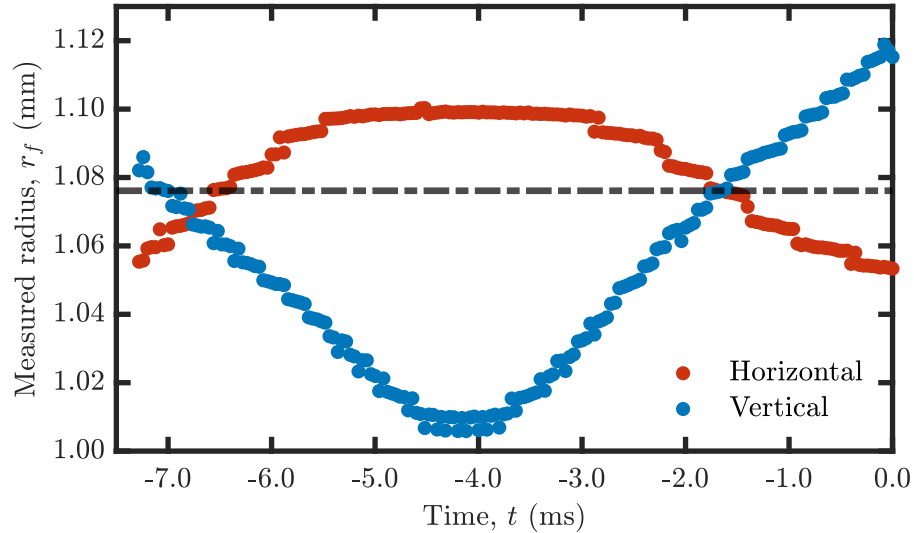


Figure 3.10: Image-processed radius of a 4.0% ethanol-water mixture falling droplet, generated by dripping, computed as half the distance between the horizontal and vertical extremities separately. The reported radius (always given to 0.01 mm resolution) in this case is 1.08 mm (dashed line). $t = 0.0$ ms at the moment the droplet strikes the substrate.

Briefly, the side-view external edges near the contact line were detected and filtered, as described above. Reflections in the substrate meant that the detected edges often continued below the substrate, with the contact-line height and position determined by identifying the discontinuous change in the edge normal vector evident for contact lines with $\theta_d \neq 90^\circ$. The contact angle measurement method of Mirzaei involves the computation of n contact angles, where n is typically taken to be approximately 10% of the droplet height in terms of pixels. To determine each contact angle, a linear fit to the detected edge was made within a mask of height $n/2$ and width n , with the southern point of the mask located on each of the first n pixels in the detected edge above the contact line. The reported dynamic contact angle was calculated as a Gaussian weighted average of the set of n contact angles measured. Mirzaei suggested that an error of $< 1^\circ$ can be achieved using this method, but as explained in Chapter 6 an error of $\pm 2^\circ$ is assumed in this work. An example of the detected contact angle tangents at the contact points in a typical free-sessile droplet coalescence experiment can be seen in Figure 6.4 on page 119.

Impacting droplet properties

As explained in Section 3.5, droplets are often generated in this work by dripping from a capillary, in which case the droplet radius, r_f and velocity on striking the substrate need to be determined for all fluid mixtures listed in Table 3.1. Unfortunately, the falling droplets generated by dripping are rarely truly spherical due to capillary waves engendered by detachment, given the low Ohnesorge number. In particular, falling droplets oscillate about a spherical shape as they fall, and so it is difficult to determine the droplet radius from a single frame.

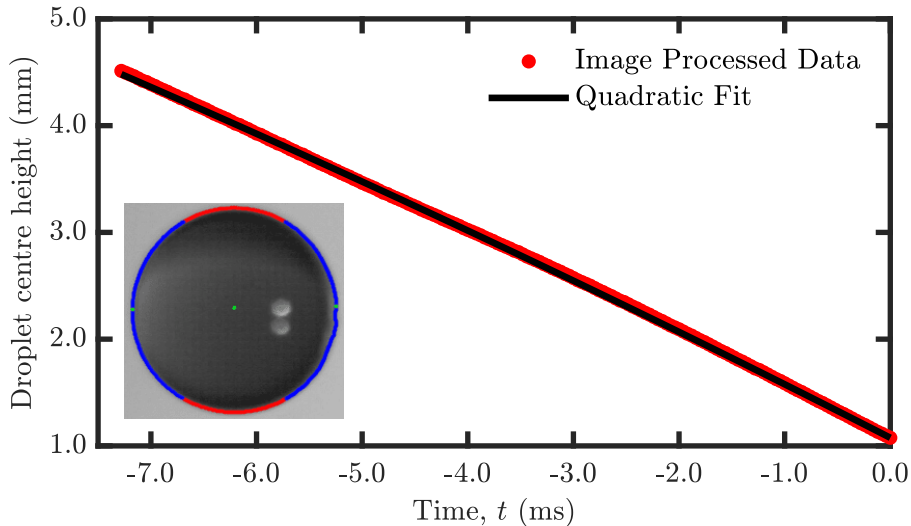


Figure 3.11: Image-processed centre height of a 4.0% ethanol-water mixture falling droplet, generated by dripping, computed as the mean of the values determined from the horizontal (inset) and vertical extremities. $t = 0.0$ ms when the droplet strikes the substrate.

Therefore, in this work a sequence of frames capturing the impacting droplet as it fell towards the substrate is analysed, with the horizontal and vertical radii computed as half the distance between the north/south and east/west (as shown inset in Figure 3.11) points of the droplet on each frame, respectively. Time series of such values for a typical droplet (consisting of a 4.0% ethanol-water mixture) generated by dripping are shown in Figure 3.10 (where $t = 0.0$ ms at the time the droplet hits the substrate), with an approximate 10% variation in the measured radius seen due to the capillary waves. Enabled by the asymmetry of the capillary wave dynamics, it can be assumed that the ‘true’ value of r_f (corresponding to a spherical droplet) occurs when the horizontal and measured values are approximately equal. This assumption is supported by the observation that the opposite local extrema in Figure 3.10 occur at similar times, i.e. when one direction is maximally stretched by the capillary waves, the droplet assumes its most compressed state in the other direction. Note that in Figure 3.10 there exist two times at which the measured radii in each direction coincide, but their values are slightly (< 0.01 mm) different. The value of r_f is chosen as the one with the minimum deviation between measurement directions at a given time, indicated by the dashed horizontal line in Figure 3.10, with an error less than the reported resolution of 0.01 mm.

The impact velocity upon striking the substrate also needs to be computed under similar conditions. To do so, the same underlying data (droplet extremity positions) as for determining the radius is used, from which the position of the droplet centre is computed as it falls towards the substrate. In particular, the centre height above the substrate is calculated twice, from the horizontal and vertical directions independently, with the mean taken and plotted in Figure 3.11. As for Figure 3.10, $t = 0.0$ ms at the moment the droplet strikes the substrate. The gradient of the line in Figure 3.11 gives the falling droplet velocity, whilst the data should be well fitted by a quadratic polynomial given that

the droplet detaches from the capillary and falls towards the substrate due to gravity. The suitability of a quadratic fit is confirmed in Figure 3.11, given the overlap seen. To reduce error, ten quadratic fits to the data are taken, sequentially and cumulatively excluding the last ten measured by points before $t = 0.0$ ms. The median impact velocity (at $t = 0.0$ ms, given by the coefficient of the linear term of the fitted polynomials) is reported, which is always given to a resolution of 0.01 m s^{-1} .

For both the impact velocity and radius, the reported values for each fluid mixture are based upon between four and ten repeated experiments and analyses, with the mean value taken (excluding outliers, if applicable). The reported error is the maximum of the largest underlying experiment value deviation from the mean or 0.02 (mm for r_f ; m s^{-1} for the impact velocity), the latter being a pessimistic estimate of the base error in the analysis procedure/logic. The impact velocity and droplet radius for each fluid mixture used in this work are reported with the experimental results in Chapters 7 and 8.

Chapter 4

Numerical methodology and development

This chapter introduces the numerical simulations developed and applied to study internal flows during droplet coalescence in this work. In particular, the choice of a VOF model implemented within OpenFOAM is elucidated and justified in Section 4.1. The mathematical model and boundary conditions applied are considered in Sections 4.2 and 4.3, respectively, whilst the numerical implementation within OpenFOAM is discussed in Section 4.4. The initial conditions are described and assessed in Section 4.5, before the customised solver developed is applied to free droplet coalescence scenarios from the literature in Section 4.6.

4.1 Preliminary aspects

Choice of mathematical model

The requirements on which basis the mathematical model and interface-capturing scheme utilised in this work were chosen are listed here:

- Ability to simulate the internal and external dynamics of droplet coalescence, from the initial stages of post-coalescence to the longer time scale diffusive mixing phase, in both axisymmetric and non-axisymmetric configurations.
- Accurate treatment of substrate wettability and its influence on the dynamics.
- Ability to explicitly assess advective mixing via a passive scalar; not tracer particles.
- Flexibility and adaptability to build upon the initial work on internal jets presented in this thesis. In particular, the potential to enhance the model by including fluid miscibility, with and without surface tension differences, and molecular diffusion.

A detailed exposition of the various mathematical models available to describe fluid interfaces and discretise the governing equations is provided in Section 2.8 of Chapter 2. With respect to the characteristics of the various numerical methods discussed in that section, for flexibility with respect to initial condition, range of dynamics captured and potential for including miscibility, the use of a sharp-interface model, and FEM more generally, was ruled out. For solver adaptability and means of tracking advective mixing, LBM was avoided despite its appealing treatment of wetting. Hence, a diffuse-interface model within a FVM framework was chosen. With a view to incorporating fluid miscibility and molecular diffusion, the level-set interface capturing technique (even CLSVOF) was not appropriate. Therefore, the mathematical model utilised in this work was based on the VOF interface-capturing technique implemented within a FVM numerical framework.

Choice of numerical framework

A common choice for the implementation of a VOF model to investigate surface tension driven flows is Gerris/Basilisk, as noted in Chapter 2. However, as the surface tension is derived from an analytical reconstruction of the interface in these codes, they are not ideal for modelling molecular diffusion between different fluids, though they do support molecular diffusion limited to one phase (López-Herrera et al., 2015). Instead, an alternate numerical framework to implement the VOF model (OpenFOAM) is used in this work in which the surface tension force is determined algebraically directly from the volume fraction.

It should be noted that the rationale behind to the choice of numerical framework was not limited to the precise physics explored in this work. Rather, to some extent the intention instead was to develop numerical capability ripe for future development and deployment to other scenarios. Therefore, whilst Gerris/Basilisk possess many of the features required to produce the results presented here, the numerical framework developed in OpenFOAM has many other advantages (discussed below) and can be easily adapted to include additional physics and support other droplet configurations as will be described in relation to future work.

OpenFOAM

OpenFOAM (an abbreviation of ‘Open-source Field Operation And Manipulation’) is an open-source toolbox for solving PDEs discretised using the FVM, particularly relating to fluid dynamics. Developed originally as FOAM primarily by Henry Weller and Hrvoje Jasak (though credit for the vanilla solver that was customised in this work is mainly due to Henrik Rusche) as PhD students at Imperial College in the ’90s, the code was first released under an open-source licence (and the name ‘OpenFOAM’ introduced) in 2004 (Chen et al., 2014). OpenFOAM has suffered a somewhat convoluted and contentious history, splintering into three flavours, but all have a very similar codebase with some

alterations/enhancements. In particular, the OpenFOAM Foundation flavour (version 4.1), maintained by Weller and others, was used in this work.

High-level advantages of OpenFOAM include solver efficiency (the code is written in C++, a modern programming language), code quality, its open-source but well-supported nature, stable MPI parallelisation, and relative ease of adaptation (Deshpande et al., 2012). Hence, OpenFOAM allows users to focus on the physics and dynamics, rather than problems with the code and its use. Moreover, the VOF implementation within OpenFOAM has been successfully applied in many droplet dynamics studies of impact/splashing (Feng, 2017; Boelens et al., 2018), collisions (Li and Fritsching, 2011), droplet-droplet coalescence (Farhangi et al., 2012; Ghaffari et al., 2015), droplet-pool coalescence (Berberović et al., 2009), coalescence-induced jumping (Khatir et al., 2016; Wasserfall et al., 2017; Chu et al., 2020), and boiling (Kunkelmann, 2011). However, OpenFOAM does not appear to have been applied to study internal flows and mixing in coalescing droplets previously.

4.2 Mathematical model

Mixture properties

The VOF method introduced in Chapter 2 allows a multiphase fluid system (e.g. droplets and vapour) to be modelled as a single fluid with combined fluid properties, known as *mixture fluid properties*. To do so, a conserved scalar known as the *volume fraction*, $\alpha \in [0, 1]$ is defined. The volume fraction identifies the dispersed phase (the droplets, where $\alpha = 1$) within the continuous phase (the air, where $\alpha = 0$) – see Figure 4.1 on page 75. Through the definition of the volume fraction, the mixture fluid properties can be calculated as weighted averages of the physical properties of each single fluid phase. In particular, the *mixture density*, ρ_m is given by

$$\rho_m = \alpha\rho_d + (1 - \alpha)\rho_o, \quad (4.1)$$

where ρ_d and ρ_o are the droplet and air densities, respectively. Similarly, the *mixture dynamic viscosity* is given by

$$\mu_m = \alpha\mu_d + (1 - \alpha)\mu_o, \quad (4.2)$$

where μ_d and μ_o are the droplet and air dynamic viscosities, respectively. In OpenFOAM, the viscosity is specified as the kinematic viscosity, ν , defined as

$$\nu = \frac{\mu}{\rho}, \quad (4.3)$$

where μ and ρ are the appropriate dynamic viscosity and density, respectively. Note that whilst the properties of the droplets and air may be constant, the mixture properties

defined by equations (4.1) and (4.2) are not constant over the domain.

Navier-Stokes equations

A single set of Navier-Stokes equations is solved for the combined fluid. Whilst the individual fluids are incompressible, the density of the combined fluid varies in space and time. Hence, the continuity equation is

$$\frac{\partial \rho_m}{\partial t} + \frac{\partial}{\partial x_j} (\rho_m u_j) = 0, \quad (4.4)$$

where u_j is the fluid velocity and summation over repeated indices is implied. The Cauchy momentum equation reads

$$\frac{\partial}{\partial t} (\rho_m u_i) + \frac{\partial}{\partial x_j} (\rho_m u_i u_j) = \frac{\partial T_{ij}}{\partial x_j} + F_i, \quad (4.5)$$

where T_{ij} is the stress tensor and F_i represents the body forces. A derivation of these equations can be found in many standard textbooks (see Acheson, 1990, for example).

As the fluids here are Newtonian and incompressible, the stress tensor is given by

$$T_{ij} = -p\delta_{ij} + \tau_{ij} = -p\delta_{ij} + \mu_m \left(\frac{\partial u_i}{\partial x_j} + \frac{\partial u_j}{\partial x_i} \right), \quad (4.6)$$

where p is the pressure and δ_{ij} is the Kronecker delta. To improve numerical efficiency within OpenFOAM, the divergence of the viscous stress tensor is reformulated as

$$\frac{\partial \tau_{ij}}{\partial x_j} = \frac{\partial}{\partial x_j} \left(\mu_m \frac{\partial u_i}{\partial x_j} \right) + \frac{\partial \mu_m}{\partial x_j} \frac{\partial u_j}{\partial x_i},$$

assuming that the divergence of velocity is zero, i.e. incompressibility (Rusche, 2002).

For several reasons, including simplifying the specification of pressure boundary conditions, in OpenFOAM the pressure, p is generally replaced by a *modified pressure*,

$$p' = p - \rho_m g_j x_j \quad (4.7)$$

in which the hydrostatic contribution is subtracted, where g_j is the acceleration vector due to Earth's gravitational force. Note that in terms of p' , atmospheric pressure is zero assuming incompressibility and a quiescent flow (Rusche, 2002). The pressure gradient term, which is implicit in Equation (4.5), is therefore rewritten as

$$\frac{\partial p}{\partial x_i} = \frac{\partial p'}{\partial x_i} + g_j x_j \frac{\partial \rho_m}{\partial x_i} + \rho_m g_i. \quad (4.8)$$

However, gravity is neglected in the simulations of this work (see below), so $g_i = 0 \text{ m s}^{-1}$ and the last two terms in Equation (4.8) are zero. Hence, $p = p'$ in this work.

Body force

Note that a surface force due to surface tension is not included in Equation (4.5). The reason for this is that surface tension is included within this model through approximation as a body force. Indeed, the contribution of momentum due to surface tension can be determined by integrating the force per unit free surface area due to surface tension over the free surface as

$$\int_{S(t)} \sigma \kappa \hat{n}_i \, dS,$$

where $S(t)$ represents the free surface, κ is the free surface curvature, σ is the surface tension and \hat{n}_i is the unit normal to the free surface pointing out of the dispersed phase. This integral can be converted to a volume integral by the introduction of the Dirac delta function, δ as

$$\int_V \sigma \kappa \hat{n}_i \delta(x_j - x'_j) \, dV, \quad (4.9)$$

where V represents the volume of the domain and prime denotes values on the free surface. Thus the integrand is formally zero everywhere except on the free surface. In particular, the integral in Equation (4.9) can be used to determine the momentum contribution due to surface tension with a diffuse-interface as in the VOF method, but the position of the free surface must be known explicitly.

It is however possible to infer the position of the free surface from the volume fraction, where the gradient of volume fraction is only non-zero in the region of the free surface. Indeed, Equation (4.9) is replaced by a body force in Equation (4.5) through the *Brackbill continuum surface force model* (Brackbill et al., 1992) by approximation as

$$F_i = \sigma \kappa \frac{\partial \alpha}{\partial x_i}. \quad (4.10)$$

The free surface curvature, κ is given by

$$\kappa = -\frac{\partial}{\partial x_j} \left[\frac{\partial \alpha}{\partial x_j} / \left(\frac{\partial \alpha}{\partial x_k} \frac{\partial \alpha}{\partial x_k} \right)^{\frac{1}{2}} \right], \quad (4.11)$$

where the quantity in square brackets represents the unit normal to the free surface. The normal is therefore computed algebraically from the volume fraction, rather than a geometric reconstruction of the free surface.

Equation (4.10) is the final form of F_i used in Equation (4.5), since simulations are restricted to cases where gravity is negligible (classically $\text{Bo} \ll 1$). In fact, the inclusion of the gravitational body force in Equation (4.10) would cancel the hydrostatic component that would arise in the modified pressure – see Equation (4.8). Despite this observation, it was noticed during the course of this work that the inclusion of gravity had an unexpected deleterious effect on the ability to accurately capture surface tension effects in the numerical simulations, most likely due to the density gradient term in Equation (4.8), since ρ_m is

inhomogeneous within the VOF model. Whilst not an issue in this work, this observation would warrant further investigation if the inclusion of gravity was desired.

Final form of the momentum equation

Taking into account the modified pressure, the reformulated gradient of the viscous stress tensor, the inclusions to the body force term, and setting gravity to zero (all discussed above), the final form of the momentum equation used in this work is

$$\frac{\partial}{\partial t}(\rho_m u_i) + \frac{\partial}{\partial x_j}(\rho_m u_i u_j) = -\frac{\partial p'}{\partial x_i} + \frac{\partial}{\partial x_j} \left(\mu_m \frac{\partial u_i}{\partial x_j} \right) + \frac{\partial \mu_m}{\partial x_j} \frac{\partial u_j}{\partial x_i} + \sigma \kappa \frac{\partial \alpha}{\partial x_i}. \quad (4.12)$$

Volume fraction advection

The volume fraction, α is advected according to an advection-diffusion equation (see Section 2.4) of the form

$$\frac{\partial \alpha}{\partial t} + \frac{\partial}{\partial x_j}(\alpha u_j) + \frac{\partial}{\partial x_j}(u_{c,j} \alpha (1 - \alpha)) = 0, \quad (4.13)$$

where $u_{c,j}$ is a *compression velocity*. The third term on the LHS of Equation (4.13) is present solely to yield a sharp free surface by limiting numerical diffusion associated with advection of an (analytical) step function. It is only non-zero in the region of the free surface, as $\alpha(1 - \alpha)$ vanishes away from the free surface. The coefficient of the compression term is taken to be unity. Further discussion regarding the compression term and the numerical implementation of this equation are deferred to Section 4.4.6.

Passive scalar

For coalescing droplets of identical miscible fluids, there is no physical internal interface between the fluids from each droplet within the coalesced droplet, in which $\alpha = 1$ everywhere. From the volume fraction alone, only velocity vectors and contours (pressure, velocity, etc.) are available to visualise internal flows. Thus, in order to assess advective mixing an additional passive scalar, β is included in the model. This scalar is transported according to an equivalent advection-diffusion equation to that for α , which is

$$\frac{\partial \beta}{\partial t} + \frac{\partial}{\partial x_j}(\beta u_j) + \frac{\partial}{\partial x_j}(u_{c,j} \beta (1 - \beta)) = 0. \quad (4.14)$$

Recall that advective mixing is of interest in the current work, consistent with the size of the droplets (millimetric) and short time scales (millisecond) considered, so there is no molecular diffusion term in Equation (4.14). It is important to note that, unlike α (i.e. Equation (4.13)), there is a one-way coupling between β (i.e. Equation (4.14)) and the

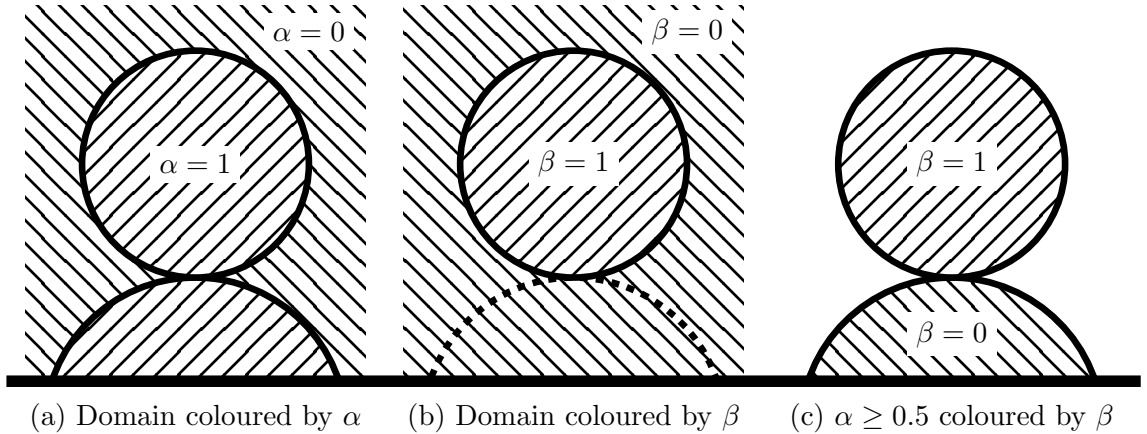


Figure 4.1: A passive scalar, β is used to assess advective mixing, initialised as unity within one droplet (the free droplet here) and zero elsewhere, as shown in panel (b). $\alpha = 1$ is initialised in both droplets, as depicted in panel (a). Hiding the vapour phase (thresholding such that $\alpha \geq 0.5$), the fluid from each droplet can be distinguished via β , as in panel (c). Note that the sessile droplet free surface, delineated by a dashed line, is not perceivable in panel (b).

flow (i.e. Equations (4.4) and (4.12)). Hence, β is truly passive and has no influence on the dynamics.

Whilst α is initialised as unity within both droplets, β is initialised as unity within exactly one of the droplets, and zero elsewhere. Hence, hiding the vapour phase by thresholding $\alpha \geq 0.5$ and colouring the droplets by β , each droplet appears a different colour (with a visible internal interface), as demonstrated in Figure 4.1. Hence, advective mixing can be assessed.

The provision and transport of a non-diffusive passive scalar is not a standard part of OpenFOAM and so had to be implemented within the solver customised in this work in a similar way to that of α . Moreover, the same discretisation schemes and solver settings were used for Equation (4.14) as for Equation (4.13). Details about the numerical implementation of β and verification are given in Section 4.4.6.

4.3 Boundary conditions

Generally in this work, droplets in contact with a substrate within an immiscible vapour phase are considered. Hence, there are two physical boundaries for which boundary conditions on u_i , p' , α and β need to be specified: the substrate and an (arbitrary) atmospheric boundary. Additionally, simulations were performed in a quarter domain with *symmetry planes* on the inner boundaries to reduce computational cost – see Section 4.4.3, and Figure 4.2 on page 81 in particular. On the symmetry planes, a zero Dirichlet boundary condition is applied to the normal velocity, with zero normal Neumann boundary conditions on the volume fraction, passive scalar and modified pressure.

Substrate

As explained in Chapter 2, the dynamic contact angle implies a boundary condition on the free surface shape near the contact line. Within the VOF framework, θ_d is therefore specified as a boundary condition on the volume fraction, α in addition to the passive scalar, β for consistency. Hence, a dynamic contact angle model is required to prescribe θ_d , with Kistler's model selected for use in this work. Moreover, in order to capture contact angle hysteresis, a modified form of Kistler's model to that given in Chapter 2 was used, which has previously been applied by several other authors to study various aspects of droplet dynamics (e.g. Farhangi et al., 2012; Moghtadernejad et al., 2015; Ludwicki and Steen, 2020). In particular, the dynamic contact angle is given by

$$\theta_d = f_H [\text{Ca}_{\text{cl}} + f_H^{-1}(\Theta)], \quad (4.15)$$

where Ca_{cl} is the contact line capillary number (Equation (2.21)) and f_H is the Hoffman function,

$$f_H(s) = \arccos \left\{ 1 - 2 \tanh \left[5.16 \left(\frac{s}{1 + 1.31s^{0.99}} \right)^{0.706} \right] \right\}. \quad (4.16)$$

Unlike in Chapter 2, θ_{eq} does not appear in Equation (4.15), but is replaced with a dummy variable, Θ to allow contact angle hysteresis to be captured. The value of Θ in Equation (4.15) depends on the direction of contact line motion via

$$\Theta = \begin{cases} \theta_a & \text{for } u_{\text{cl}} > 0, \\ \theta_{\text{eq}} & \text{for } u_{\text{cl}} = 0, \\ \theta_r & \text{for } u_{\text{cl}} < 0, \end{cases} \quad (4.17)$$

in which θ_a , θ_{eq} (which is inconsequential in practice as u_{cl} is seldom identically zero) and θ_r are prescribed. Between Equations (4.15) to (4.17), only these three parameters need to be prescribed. Hence, this dynamic contact angle model can be used without a wealth of experimental data to fix various free parameters. Note however that the model does not include pinning; the prescribed dynamic contact angle is discontinuous at $u_{\text{cl}} = 0$ and there is no explicit boundary condition on the position of the contact line. Fortunately, the lack of pinning turns out to be inconsequential, as elucidated in Chapter 6.

The dynamic contact angle model specifies θ_d for a given contact line velocity, which is applied on each and every time step in the numerical simulations. By definition, contact angles determine the orientation of the free surface, characterised by its normal, at the contact line. Hence, the boundary conditions on α and β are actually applied to the free surface normal at the contact line (located by the volume fraction), which feeds into the advection of the volume fraction (equivalently passive scalar) to ensure that the prescribed dynamic contact angle is adhered to.

However, the free surface normal emerging on each time step need not be the same as

that prescribed by the dynamic contact angle model. Hence, the boundary condition on α and β is actually applied as an update to the free surface unit normal that emerges at the contact line, $\hat{n}_{0,i}$. In particular, the updated free surface unit normal at the contact line, $\hat{n}_{c,i}$ is given by

$$\hat{n}_{c,i} = a \hat{n}_{s,i} + b \hat{n}_{0,i}, \quad (4.18)$$

where $\hat{n}_{s,i}$ is the unit normal to the substrate, whilst $a, b \in \mathbb{R}$ are scalars into which the dynamic contact angle specified by the dynamic contact angle model is fed – the expressions for, and derivation of, these scalars are given in Appendix B.

This free surface normal update procedure is implemented within vanilla OpenFOAM and is used to apply static and dynamic contact angle boundary conditions alike. Whilst there is a dynamic contact angle model implemented within vanilla OpenFOAM¹, Kistler’s model is not. Hence, the solver customised in this work was adapted to support the use of Kistler’s model based upon code available on GitHub (Rattner and Garimella, 2014; Nabil and Rattner, 2016). Validation of this code by means of quantitative comparison to experiments is undertaken in Chapter 6.

Coupled with Kistler’s model, no-slip is enforced on the substrate, while the boundary condition on the modified pressure, p' is chosen to be determined by the velocity (`fixedFluxPressure` in OpenFOAM). In particular, the no-slip boundary condition is applied to the cell faces on the substrate within the finite volume representation, but since OpenFOAM uses a collocated methodology the cell-centre values closest to the substrate are non-zero. Moreover, the mass flux of the cell at the contact line is determined by integrating over the whole cell, whilst no-slip is only applied to the one face coinciding with the substrate. Hence, an *effective slip* is introduced via the numerical method that removes the shear stress singularity, which is the crux of the moving contact-line problem (Afkhani et al., 2009). Note that molecular slip ($\mathcal{O}(10 \text{ nm})$) according to Geng et al., 2019) would be on a much smaller scale than the cell size, which is typically $\sim 14 \mu\text{m}$ in the simulations quantitatively compared to experiments in Chapter 6, to which contact-line motion is not very sensitive (Saha and Mitra, 2009). The contact line velocity determined from the centre of the cell closest to the substrate at the contact line (characterised by α) with this effective slip is fed into the dynamic contact angle model via $\text{Ca}_{c,l}$ and Equation (4.17).

Atmospheric boundary

Atmospheric boundaries are artificial in the sense that they must be specified at an arbitrary position, where no such physical boundary exists, to restrict the domain size. There are some theoretical issues regarding choices for boundary conditions on atmospheric boundaries (see e.g. Kirkpatrick and Armfield, 2009), but the domain size was always chosen in this work such that the atmospheric boundaries remain sufficiently far

¹The existing dynamic contact angle model in OpenFOAM is $\theta_d = \theta_{eq} + (\theta_1 - \theta_2) \tanh(u_{cl}/u_l)$, where θ_1, θ_2 define the limits of θ_d and u_l is some velocity scaling (see e.g. Feng, 2017). It does not support contact angle hysteresis and does not appear to have a firm physical basis so its use is avoided in this work.

from the droplets that their precise properties had a negligible effect on the dynamics – see Chapter 5. Zero normal Neumann and Dirichlet boundary conditions were applied for velocity and modified pressure respectively:

$$\frac{\partial u_i}{\partial n} = 0, p' = 0 \quad \forall x_i \in \partial\Omega, \quad (4.19)$$

where $\partial/\partial n$ denotes the (boundary) normal gradient and $\partial\Omega$ denotes the boundary itself (Wasserfall et al., 2017; Deka et al., 2019).

The volume fraction, α and passive scalar, β obey zero Neumann and Dirichlet boundary conditions for outflow and inflow, respectively (Boelens et al., 2018). Mathematically,

$$\begin{cases} \partial\alpha/\partial n = 0 & \text{for } u_j n_j > 0 \text{ and } x_i \in \partial\Omega, \\ \alpha = 0 & \text{for } u_j n_j < 0 \text{ and } x_i \in \partial\Omega, \end{cases} \quad (4.20)$$

where n_j is the outward pointing normal to the boundary. Hence, droplet fluid can leave the domain, but only vapour can enter to ensure that the solution remains theoretically consistent. However, as the droplets remain far from the atmospheric boundaries at all times, the boundary condition there is somewhat inconsequential as there is only ever vapour near such boundaries.

4.4 Numerical framework

In this section, the numerical framework used to solve the mathematical model, subject to boundary conditions specified above, is described. Briefly, the equations are discretised onto an adaptively-refined hexahedral mesh using the finite volume method and solved using the PISO algorithm. The solver details and the numerical implementation of the crucial bounded scalars α and β are described in some detail.

4.4.1 Finite volume method

As noted before, this work makes use of the *finite volume method* (FVM), which is briefly outlined here – for a more detailed exposition, see textbooks such as Patankar (1980) and Versteeg and Malalasekera (1995). In FVM, the domain is discretised into *cells* (also known as *control volumes*), which are all hexahedral in this work. The precise structure of the mesh used will be discussed in Section 4.4.3. Typically, fluid properties are calculated and stored at cell-centres with interpolation used to derive cell-face data from cell-centre data as necessary, which is the case in OpenFOAM.

The equations to be solved are integrated over each cell (control volume), which implies integral conservation of the physical quantities over any group of cells (Patankar, 1980). In particular, the divergence terms are transformed to surface integrals via the

divergence theorem and are thus evaluated as fluxes through each of the cell faces. For example, the advective term in the momentum equation is integrated as²

$$\int_V \frac{\partial}{\partial x_j} (\rho_m u_i u_j) \, dV \approx \sum_f u_{f,i}^n (\rho_m^{n+1} u_j^{n+1})_f S_{f,j}^n,$$

where f denotes a cell face, $S_{f,j}$ is the cell-face area vector and V is the volume of the cell over which the term is integrated (Albadawi et al., 2013). Thus, $(\rho_m u_j)_f S_{f,j}$ is the mass flux through the cell face f . For neighbouring cells, the mass flux through the shared face out of one is equal to that into the other, ensuring mass conservation.

The remaining volume integrals are approximated by finite-difference-like formulations (Versteeg and Malalasekera, 1995). For example, the volume integral of transient terms are replaced with an implicit Euler formulation in this work, so

$$\frac{d}{dt} \int_V \rho \psi \, dV \approx \rho V \frac{\psi^{n+1} - \psi^n}{t^{n+1} - t^n}, \quad (4.21)$$

where ψ^n is the value of ψ on time step n , t^n .

Once each integral has been appropriately approximated, the integral equations over each cell are reduced to a system of algebraic equations of the form

$$a_{i,j} x_j = b_i, \quad (4.22)$$

where x_j represents the unknown variables and $a_{i,j}, b_i$ are arrays of known values, which needs to be iteratively solved at each time step based on either the initial condition or the solution on the previous time step. The pressure-velocity calculation procedure used by the solver in this work (PISO algorithm) is discussed in Section 4.4.5.

4.4.2 Discretisation

The section above describes the principles of discretisation, but there is a requirement to choose specific discretisation schemes in practice; schemes are required to integrate transient terms (as demonstrated for an implicit Euler formulation in Equation (4.21)) and for spatial gradients to be used in combination with the divergence theorem. Spatial schemes rely on interpolation from the cell-centres to cell-faces for fluxes to be computed, where inaccurate fluxes can lead to unphysical numerical solutions with spurious oscillations and other numerical issues (Versteeg and Malalasekera, 1995). To help ensure accurate computation of fluxes, codes such as OpenFOAM generally employ flux-limited high-resolution schemes which are *total variation diminishing* (TVD)³, a property from which preservation of monotonicity follows. Hence, spurious oscillations are prevented to yield a physical

²Note that the advection term is treated semi-implicitly in the numerics – see Section 4.4.5.

³Such schemes ensure that the total variation (the sum of absolute difference in the field over each cell in the discretised domain) does not increase on each and every time step.

Table 4.1: OpenFOAM discretisation schemes used in this work.

Term	OpenFOAM Scheme	Reference
Time derivatives	<code>Euler</code>	Kunkelmann (2011)
Gradients	<code>Gauss linear</code>	Wasserfall et al. (2017)
Tensor advection	<code>Gauss limitedLinearV 1</code>	Larsen et al. (2019)
Viscous stress	<code>Gauss linear</code>	Wasserfall et al. (2017)
Scalar advection	<code>Gauss vanLeer01</code>	Larsen et al. (2019)
Scalar compression	<code>Gauss interfaceCompression</code>	Deshpande et al. (2012)
Laplacian	<code>Gauss linear corrected</code>	Kunkelmann (2011)

solution (Tu et al., 2013).

The OpenFOAM discretisation schemes used in this work are listed in Table 4.1. The limited linear scheme used was a variant which takes the direction of steepest gradients into account within the calculation – Albadawi et al. (2013) give a detailed description of this second-order TVD scheme. A special version of the van Leer scheme (van Leer, 1979) was used for the advection of α and β to bound the blending factor between 0 and 1. In particular, the underlying scheme is van Leer, but becomes upwind if the blending factor goes out of bounds to stabilise the solution. The Gauss interface compression scheme is specifically designed for the compression term described above (Rusche, 2002). See Moukalled et al. (2016) and the OpenFOAM documentation for further discussion. Note that the scheme selection reported in Table 4.1 does not necessarily represent an optimum choice, but was found to be appropriate in practice.

4.4.3 Computational domain and mesh

Geometry

The computational domain used in this work was three-dimensional. However, the simulations reported are axisymmetric so, to reduce computational cost, a quarter domain was used with symmetry planes on the inner boundaries. An image of the mesh within the quarter domain used is shown in Figure 4.2, with the initial condition for a typical free-sessile droplet coalescence simulation set. The size of the domain was set based upon the free droplet radius, r_f so to allow changes in scale to be made whilst maintaining effective domain size. A domain size of $4r_f \times 5r_f \times 4r_f$ was generally used (where $5r_f$ corresponds to the direction in line with the droplet axis of symmetry), with the dynamics found to be very insensitive to the domain size, as demonstrated in Chapter 5.

For the droplet configuration shown in Figure 4.2, 2D-axisymmetric simulations would of course be sufficient. However, 2D-planar simulations, in which the droplets would be approximated by infinite cylinders, are not appropriate, as explained in the next section.

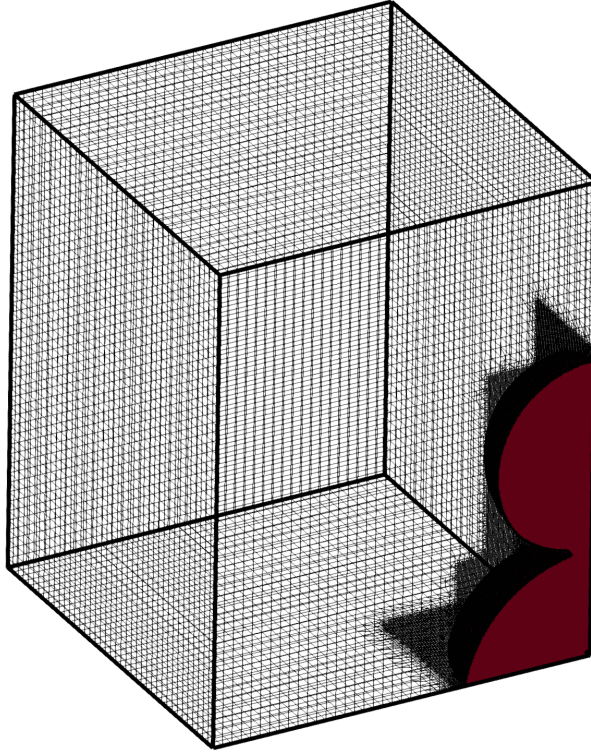


Figure 4.2: A depiction of the quarter domain and hexahedral adaptive mesh used in this work, with the initial condition for free and sessile droplet coalescence. Note that only the mesh on the boundary of the domain (i.e. not the inner mesh) is shown to make the mesh structure visible. From this viewpoint, the bottom boundary is the substrate; forward and right (inner) boundaries are symmetry planes; the other three are atmospheric boundaries.

Vorticity considerations

The behaviour of vorticity is different in 2D-planar flows compared to 2D-axisymmetric/3D flows. The *vorticity*, ω_i of a flow is defined as the curl of the flow velocity u_i ,

$$\omega_i = \varepsilon_{ijk} \frac{\partial u_k}{\partial x_j}, \quad (4.23)$$

where ε_{ijk} is the Levi-Civita symbol. Vorticity is a measure of the local rate of rotation of fluid elements (Acheson, 1990). Assuming that the fluid is Newtonian, incompressible and isotropic, taking the curl of the momentum equation (assuming constant density) yields the *vorticity equation*, which reads

$$\frac{D\omega_i}{Dt} = \frac{\partial \omega_i}{\partial t} + \underbrace{u_j \frac{\partial \omega_i}{\partial x_j}}_{\text{Vortex advection}} = \underbrace{\omega_j \frac{\partial u_i}{\partial x_j}}_{\text{Vortex stretching \& tilting}} + \underbrace{\nu \frac{\partial^2 \omega_i}{\partial x_j \partial x_j}}_{\text{Vortex diffusion}}, \quad (4.24)$$

where the physical interpretation of each term is indicated below it. Equation (4.24) assumes that F_i is a conservative force, which is equivalent to its curl being identically zero, i.e.

$$\varepsilon_{ijk} \frac{\partial F_k}{\partial x_j} = 0. \quad (4.25)$$

Whilst gravity is a conservative force, it is not true that the force due to surface tension (Equation (4.10)) is conservative. However, in this exposition it is the behaviour of vorticity within a bulk single phase that is of interest, so this inconsistency with the momentum equation used in this work (Equation (4.5)) is not a concern here.

The specific contribution of the individual terms on the RHS of Equation (4.24) can be made clear by expansion of an individual component. In particular, the second component is

$$\frac{D\omega_2}{Dt} = \underbrace{\omega_1 \frac{\partial u_2}{\partial x_1}}_{\text{Vortex tilting}} + \underbrace{\omega_2 \frac{\partial u_2}{\partial x_2}}_{\text{Vortex stretching}} + \underbrace{\omega_3 \frac{\partial u_2}{\partial x_3}}_{\text{Vortex tilting}} + \underbrace{\nu \frac{\partial^2 \omega_2}{\partial x_j \partial x_j}}_{\text{Vortex diffusion}}.$$

It is thus clear that the components of the $\omega_j \frac{\partial u_i}{\partial x_j}$ term act to stretch and tilt/turn the vortex tubes separately, allowing vorticity to be transferred across scales. Crucially, it is the only term in Equation (4.24) that describes the *influence of the flow* on the structure of vorticity – the others describe the transport and diffusion of vorticity due to viscosity only. The stretching and tilting mechanisms are particularly important in vortex rings, where vorticity is transferred to smaller scales within the toroidal ring (see Figure 2.7). In contrast to vortex stretching and tilting, vorticity diffusion described by the last term on the RHS of Equation (4.24) only scales the intensity of vorticity.

Having elucidated the behaviour of vorticity in 3D (equivalently 2D-axisymmetric) flows, the differences that arise with 2D-planar flows, defined as

$$u_1 = u_1(x, y, t); u_2 = u_2(x, y, t); u_3 = 0,$$

are now considered for comparison. For 2D-planar flow, there is only one non-zero component of the vorticity vector, which is

$$\omega_3 = \frac{\partial u_2}{\partial x_1} - \frac{\partial u_1}{\partial x_2},$$

so the vorticity vector, w_i is parallel to the nil third axis. Moreover, the vortex tilting and stretching term is identically zero since $\omega_1 = \omega_2 = 0$ and $u_3 = 0$. Hence, Equation (4.24) reduces to

$$\frac{D\omega_i}{Dt} = \frac{\partial \omega_i}{\partial t} + u_j \frac{\partial \omega_i}{\partial x_j} = \nu \frac{\partial^2 \omega_i}{\partial x_j \partial x_j} \quad (4.26)$$

for 2D-planar flow. Comparing Equation (4.26) to Equation (2.13), it can be determined that, for 2D-planar flow, the vorticity equation is simply an advection-diffusion equation, with the consequence that vorticity acts only as a diffusive transported scalar. In other words, in 2D-planar flow vorticity is simply advected from where it is generated at fluid interfaces (or initialised elsewhere) into the bulk and diffuses due to viscosity, without being influenced – only transported – by the flow itself. No vortex enhancement or transfer of vorticity to smaller scales is possible.

Hence, the action of vorticity between 2D-planar and 3D (equivalently 2D-axisymmetric)

flows is qualitatively different. Given the relationship between vorticity and internal jet formation elucidated by Xia et al. (2017) for free droplet coalescence, it is therefore not appropriate to study internal flows during droplet coalescence with 2D-planar simulations, especially those in which jet formation is expected. Nevertheless, 2D-planar simulations of such dynamics can be found in the literature (e.g. Eiswirth et al., 2012), though significant qualitative differences between those simulations and experiments (especially a lack of recirculation within jets) are evident. Therefore, 3D simulations (with a quarter domain to reduce computational cost) were exclusively deployed in this work.

Mesh

The domain was discretised into regular hexahedral cells, producing a highly-orthogonal good-quality mesh with minimal skewness. As for domain size, the mesh density is defined by the number of cells per (smallest) free droplet radius, r_f . Since the vapour has little effect on the droplet dynamics of interest, the use of adaptive mesh refinement was desirable to ensure that the mesh was more dense within the droplet than the vapour phase, reducing computational cost both in terms of time and memory. The whole droplet region is of interest for the internal dynamics, rather than just the droplet interface as in most studies. Therefore, the entire droplet region, defined by $\alpha > 0.01$, was refined. Each cell such that $\alpha > 0.01$ (defining the refinement criterion) was divided into eight equally-sized new hexahedral cells – the data was interpolated and fluxes recalculated to populate the new cells. Moreover, the new cells could themselves be refined at the next opportunity if they met the refinement criterion; cells were unrefined if they ceased to meet the refinement criterion (i.e. if droplet cells became vapour cells). Each cell was assessed for (un)refinement every two time steps. Mesh adaption is computationally expensive in itself; whilst the (un)refinement interval could have been increased without a significant influence on the results, it was preferred to keep it small, favouring accuracy over speed.

In this work, a base mesh density of 10 cells per r_f was used, which is the minimum mesh resolution in the vapour phase. Three levels of adaptive mesh refinement (i.e. a multiple of 2^3) were deployed such that the mesh resolution throughout the droplet was 80 cells per r_f . Despite the diffuse interface, further refinement had a negligible effect on the results – a mesh sensitivity analysis is presented in Chapter 5. For a typical free-sessile droplet coalescence simulation, the mesh structure at $t = 0.0$ ms and $t = 0.2$ ms is shown in Figure 4.3. The high mesh density within the droplet region mentioned above is clearly evident. Figure 4.3 also indicates that the maximum number of cells is at $t = 0.0$ ms, which is due to practical considerations in ensuring that the region where the droplets were initialised was refined⁴. Indeed, for $t > 0.0$ ms the adaptive mesh refinement algorithm ensures that few cells in the vapour phase are refined.

⁴The rectangular refined volume seen in Figure 4.3a was manually set to encapsulate the volume in which droplets were defined – see Section 4.5 for details.

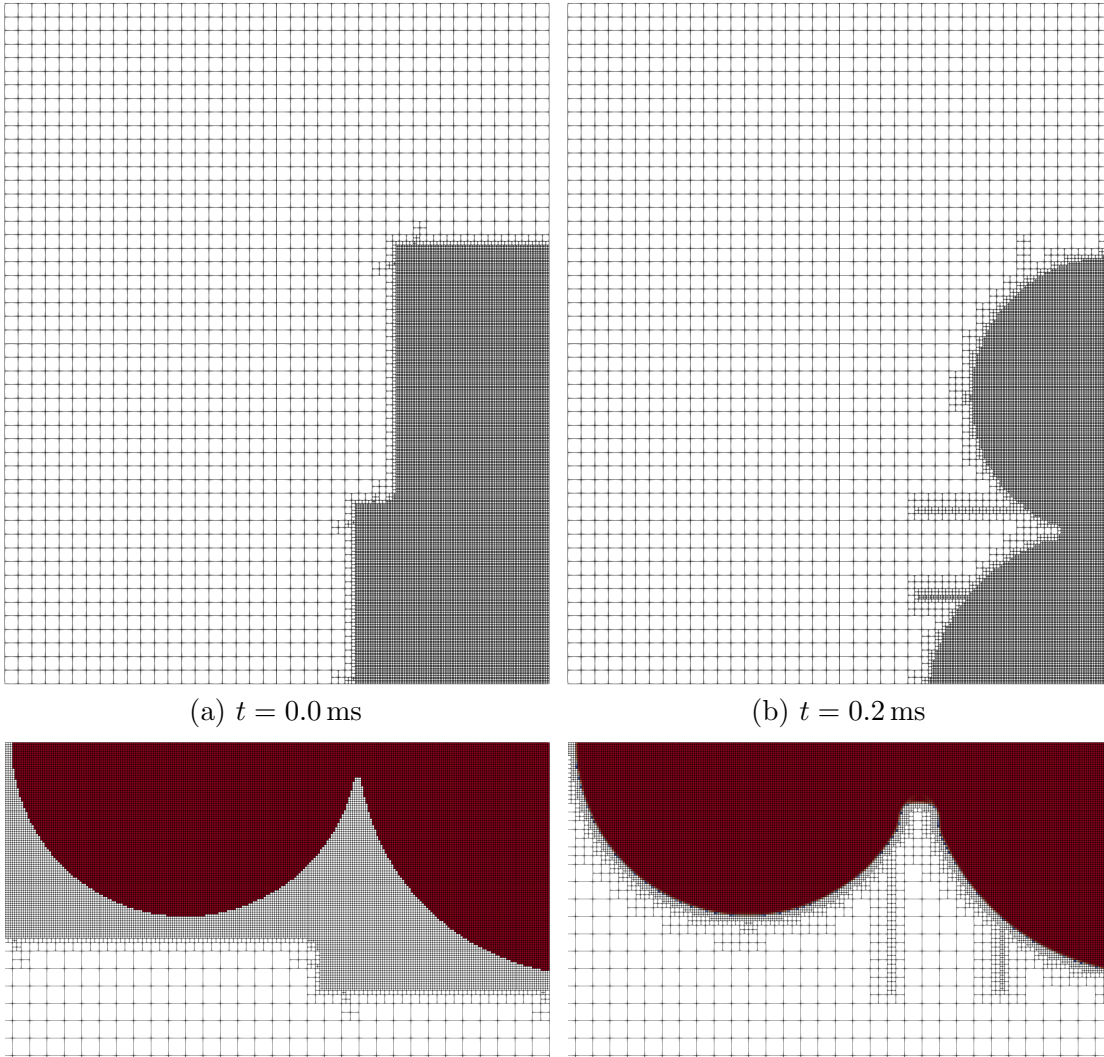


Figure 4.3: Mesh structure for a typical free-sessile droplet coalescence simulation at (a) $t = 0.0$ ms and (b) $t = 0.2$ ms. Top row: the mesh on a complete inner boundary (symmetry plane). Bottom row (rotated): the region near to the droplets. All cells are hexahedral, with a 10 cells per r_f base mesh density, and 3 levels of adaptive mesh refinement everywhere $\alpha > 0.01$ (i.e. 80 cells per r_f within the whole droplet region).

4.4.4 Customised solver

The VOF model described above is implemented within the `interFoam` solver of OpenFOAM 4.1, which has been extensively validated (see e.g. Deshpande et al., 2012) and is a transient isothermal multiphase solver that supports the modelling of two immiscible phases. The source code of the `interFoam` solver was customised during the course of this work, with the following modifications implemented:

- Merging of the codes for static and adaptive mesh (`interDyMFoam`) versions of `interFoam` to create the base of the new solver (a single `interFoam` solver is provided as standard in OpenFOAM 6 and later versions);
- Inclusion of the Kistler dynamic contact angle model (see Section 4.3);

- Addition of a bounded passive scalar, β which enabled internal flows and advective mixing to be monitored (see Sections 4.2 and 4.4.6);
- Alteration of the time step control such that the initial time step could be explicitly specified at run-time and enforced (see Section 4.4.8).

4.4.5 Pressure-velocity calculation procedure

The pressure-velocity calculation procedure for the Navier-Stokes equations employed by the customised solver is briefly described in this section. The PISO (Pressure-Implicit with Splitting of Operators) algorithm, originally proposed by Issa (1986), is used⁵. Note that α and β are advected at the beginning of every time step, whereas the dynamic contact angle model is applied during the PISO algorithm when the surface tension force is computed. For each time step, the PISO algorithm consists of three primary steps:

1. **Momentum predictor step.** The velocity is updated by solving the momentum equation (Equation (4.12)) with the modified pressure, p' treated explicitly. Moreover, the nonlinear advection term $\frac{\partial}{\partial x_j}(\rho u_i u_j)$ is handled by treating it in flux form $\frac{\partial}{\partial x_j}(\rho \phi u_j)$, where ϕ is the explicit flux – this treatment is permissible as the pressure-velocity coupling is much stronger than the nonlinear velocity coupling.
2. **Pressure corrector step.** An equation for the modified pressure, p' (derived from the momentum equation) is solved, using the velocity from the previous momentum predictor step⁶. The mass flux is first computed with the pressure treated explicitly; then the pressure equation is solved `nNonOrthogonalCorrectors` times to obtain p' .
3. **Momentum corrector step.** The velocity is updated using the value for pressure obtained in the previous pressure corrector step.

The pressure and momentum corrector steps (2 and 3 in the list above) are repeated `nCorrectors` times on each time step. The ‘PIMPLE controls’ (those controlling the PISO algorithm) chosen are displayed in Table 4.2. More details about the general PISO algorithm are given by Versteeg and Malalasekera (1995), whilst Moukalled et al. (2016) describe the PISO implementation in OpenFOAM.

4.4.6 Bounded scalars

The advection of physically bounded scalars poses a particular challenge for diffuse-interface FVM methods. Indeed, both the volume fraction, $\alpha \in [0, 1]$ and passive scalar,

⁵Within OpenFOAM, the PIMPLE algorithm (which combines the PISO and SIMPLE – typically used for steady-state simulations – algorithms) is used. However, as `nOuterCorrectors` is set equal to one it effectively reduces to the standard PISO algorithm described here.

⁶If the momentum predictor step were not performed (i.e. `momentumPredictor` were set to no), then the velocity would be treated explicitly in the pressure corrector step.

Table 4.2: PISO algorithm controls which are specified in the PIMPLE subdictionary of `system/fvSolution` in each OpenFOAM case. No under-relaxation was applied.

Option	Value	Notes
Momentum predictor	yes	Update velocity before solving for p' .
No. outer correctors	1	Reduces PIMPLE to PISO.
No. correctors	3	No. pressure and momentum corrector steps.
No. non-orthogonal correctors	1	Repeated solution of pressure equation.
Mesh dynamic	yes	Correct pressure for moving mesh.

$\beta \in [0, 1]$ change rapidly between zero and one across their respective interfaces and so accurate computation of their flux through cell faces is required in order to avoid excessive numerical diffusion. Such numerical diffusion may lead to inaccurate computation of the surface tension force and cause the scalars not to respect their physical bounds. The next couple of subsections discuss the computation of α , whilst β is considered in the last.

Interface compression

The third term – that is, the compression term – on the LHS of Equation (4.13),

$$\frac{\partial}{\partial x_j}(u_{c,j}\alpha(1-\alpha))$$

is present to reduce numerical diffusion on the α interface by effectively compressing it through the introduction of a small compression velocity, $u_{c,j}$ perpendicular to the interface. Note that the compression term has a user-modifiable coefficient, c_α . Many values of c_α can be found in the literature, where unity is usually the lowest and a common choice for generic free surface problems (Theobald et al., 2020). An optimum choice of c_α does not necessarily exist, and the appropriate value depends on many factors including the underlying flow physics and other solver settings – see Appendix C. The value of c_α therefore should not be treated independently. The approach taken in this work was to specify $c_\alpha = 1$, a low value to avoid over compression that might have an undue influence on the delicate free surface dynamics, and then adjust the solver settings and mesh density as required to remove any undue numerical diffusion.

The compression velocity, $u_{c,j}$ acts perpendicularly to the interface and is based on the cell-face volumetric flux, ϕ in the discretised version of Equation (4.13). Formally, $\phi = S_{f,j}u_{f,j}$ where $S_{f,j}$ is the cell-face area vector and $u_{f,j}$ is the velocity projected onto the cell face (not the cell-centre value). In practice, ϕ emerges from the solution of the momentum equation (see Section 4.4.5). In OpenFOAM 4.1, the compression velocity is given by

$$u_{c,i} = c_\alpha \left| \frac{\phi}{(S_{f,j}S_{f,j})^{\frac{1}{2}}} \right| \hat{n}_i, \quad (4.27)$$

where \hat{n}_i is the unit normal to the interface. Note however that Equation (4.27) is actually

an equation for the flux-flux compression velocity; that is, the velocity on the cell-face rather than at the cell-centre. Indeed, the fluxes of Equation (4.13) are computed across cell-faces in the discretised form as explained in Section 4.4.1. Equation (4.27) can be found in the `alphaEqn.H` file of the vanilla `interFoam` solver.

As insinuated in Equation (4.11), \hat{n}_i is mathematically defined as

$$\hat{n}_i = \frac{\partial \alpha}{\partial x_i} \bigg/ \left(\frac{\partial \alpha}{\partial x_k} \frac{\partial \alpha}{\partial x_k} \right)^{\frac{1}{2}}. \quad (4.28)$$

As was the case for velocity though, the cell-face values are required in Equation (4.27). Hence, the volume fraction gradients are actually interpolated from the cell centres to the cell faces in the numerical framework before being substituted into Equation (4.28). Note that away from the free surface, the volume fraction gradients vanish so Equation (4.27) becomes zero (i.e. there is no compression). To stabilise the computation, an additional small term, δ_N is added to the denominator of Equation (4.28), which is given by

$$\delta_N = \varepsilon \left(\frac{\sum_{k=1}^N V_{\text{cell},k}}{N} \right)^{-\frac{1}{3}},$$

where N is the number of cells, ε is a scaling constant (typically taken as 1×10^{-8}) and $V_{\text{cell},k}$ is the volume of the k th cell. The formulation in brackets represents the average cell volume, so it is clear that δ_N is typically a very small number. The same approach is used to compute the normal for the free surface curvature, κ in Equation (4.11) and is implemented in the `interfaceProperties.C` file within the OpenFOAM source code.

Flux-corrected transport algorithms

The inclusion of the compression term in the advection-diffusion equation for α successfully limits numerical diffusion in pseudo-static configurations. However, standard numerical schemes are far too diffusive to support the advection of bounded scalars, even with interface compression. Hence, OpenFOAM uses a *flux-corrected transport* (FCT) algorithm to guarantee boundedness in the solution of hyperbolic problems with bounded variables; in particular, the advection of α via Equation (4.13).

Originally introduced by Boris and Book (1973), the essence of FCT algorithms is to introduce an anti-diffusive stage into the computation of the cell-face flux such that neither new extrema are generated in the solution, nor are existing extrema accentuated. In particular, Zalesak (1979) introduced the multidimensional version of the algorithm which is suitable for use in fluid dynamics, ensuring transported properties are maintained within physical limits (e.g. $\alpha \in [0, 1]$). To elucidate the concept, the FCT algorithm in one dimension computes the corrected cell-face flux, F^C as

$$F^C = F^L + \lambda(F^H - F^L),$$

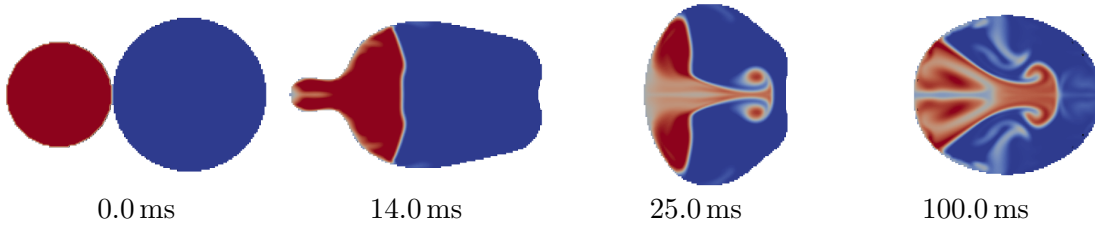


Figure 4.4: An example of a free droplet coalescence simulation using a variant of the customised solver in which the passive scalar, β is implemented with a standard numerical scheme (not the MULES FCT scheme). Excessive numerical diffusion is clear.

where F^L is the cell-face flux computed using a low-order, bounded scheme and F^H is the cell-face flux computed using a higher-order, but potentially unbounded, scheme. $F^H - F^L$ can be considered to be an anti-diffusive flux, whilst $\lambda \in [0, 1]$ is a blending factor chosen such that no new local extrema are generated in the solution. As a result, the higher-order method is used away from regions of rapid change in the solution, and is replaced by a lower-order monotonicity-preserving method in the region of rapid change, where the use of higher-order methods would violate physical bounds on the solution (Zalesak, 2005). A multidimensional extension can be applied within FVM.

MULES (Multidimensional Universal Limiter for Explicit Solution) is the OpenFOAM iterative implementation of the multidimensional FCT algorithm. In MULES, λ is determined iteratively and global extrema can be set (e.g. $\min(\alpha) = 0$ and $\max(\alpha) = 1$), the latter ensuring that it is not only local extrema that are respected (Márquez Damián, 2013). The combination of the compressive term in Equation (4.13) and the use of MULES enables the advection of α with limited numerical diffusion, whilst ensuring $\alpha \in [0, 1]$.

Passive scalar

Whilst MULES and Equation (4.13) are implemented for the volume fraction, α within vanilla OpenFOAM, there is no default support for the transport of a bounded passive scalar, β that is necessary for assessing advective mixing. Hence, a separate implementation of Equation (4.14) was required within the customised solver under the framework described above to enable the advection of β without excessive numerical diffusion. Indeed, the requirement for MULES is obvious considering Figure 4.4 in which Equation (4.14) was solved for β using a standard numerical scheme instead of MULES for demonstration purposes. Excessive numerical diffusion (especially at $t = 100.0$ ms) is clear in Figure 4.4, whilst the interface remains appropriately compressed when Equation (4.14) was solved using MULES (see e.g. Figure 4.5).

The MULES implementation of Equation (4.14), for β , within the customised solver was verified using massless particle tracing⁷ on the velocity field as seen in Figure 4.5 for

⁷The particle tracing seen in Figure 4.5 was implemented within ParaView, with particles are advected along pathlines using simulation data written 0.5 ms apart, rather than every simulation time step.

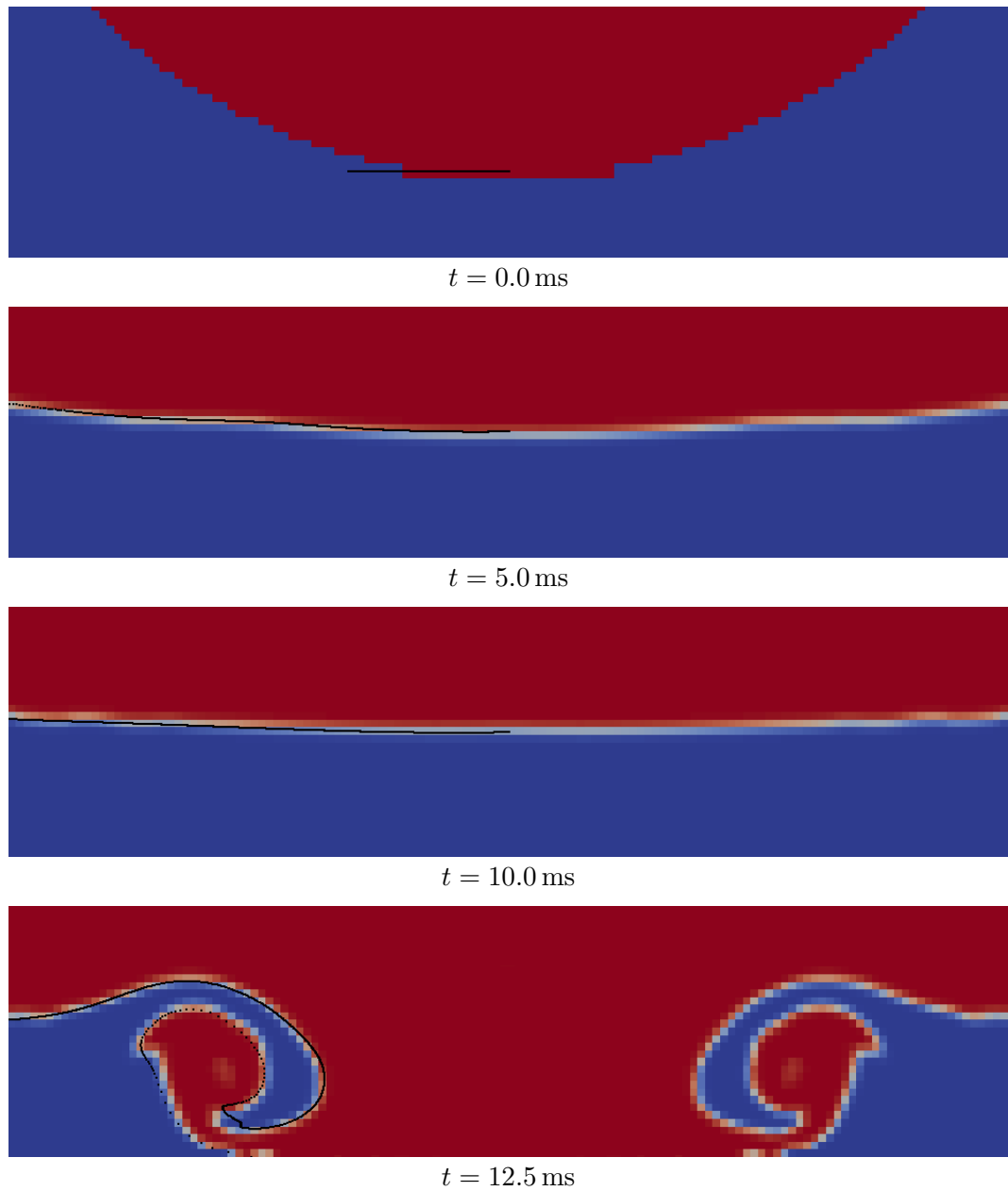


Figure 4.5: Frames showing both the droplet and air phases coloured by the passive scalar, β for a typical free and sessile droplet coalescence simulation from Chapter 6. Only part of the computational domain is shown. Blue regions indicate where $\beta = 0$, whilst red indicates where $\beta = 1$. At $t = 0.0$ ms, massless particles are initialised toward the left of the internal interface (seen as a horizontal black line) and are advected along pathlines by the velocity field (independent of β) with 0.5 ms time resolution to verify the passive scalar implementation within the customised solver.

a typical free and sessile droplet coalescence simulation from Chapter 6. This means of testing the passive scalar implementation is appropriate since there is a one-way coupling between β and the velocity field. In particular, the particles in Figure 4.5 are initialised coinciding with the internal interface of β at $t = 0.0$ ms and, as seen from the figure, remain on the interface for all $t > 0.0$ ms which verifies the implementation of β , i.e. β captures the internal interface as desired. Moreover, qualitative and quantitative experimental validation of the coalescence results is provided in Chapter 6.

4.4.7 Iterative algorithms

Once the PDEs describing the flow are reduced to a system of algebraic equations (Equation (4.22)), an iterative algorithm is required to solve the linear system on each time step. Full details of the iterative solution algorithms and controls used are given in Appendix C so only an overview is given here.

The linear systems for the bounded scalars (α and β) are solved using a preconditioned conjugate gradient (PCG) method, using a diagonal-based incomplete Cholesky (DIC) preconditioner, as solving these linear systems is not particularly computationally intensive. In contrast, solving linear system for pressure is the most computationally expensive step of the solution algorithm, so a multigrid solver (GAMG – geometric-algebraic multigrid) was deployed, using a few iterations of the Gauss-Seidel method as a smoother to reduce high-frequency errors. GAMG was found to be far more efficient (by at least a factor of two) than the PCG method for pressure in this work, which is consistent with the findings of Márquez Damián (2013). Finally, the velocity was updated using a conjugate gradient method for asymmetric matrices (PBiCG – preconditioned bi-conjugate gradient), with a diagonal-based incomplete lower–upper decomposition (DILU) preconditioner, which is the asymmetric equivalent of DIC, due to the relatively low computational cost of this step in the PISO algorithm.

4.4.8 Time marching

A *Courant number*, Co is computed over each cell in order to determine an appropriate time step, Δt . Within FVM/OpenFOAM, the Courant number is a measure of the rate at which information is transported under the influence of the cell-face flux, ϕ and is defined as

$$Co = \frac{\Delta t \sum_f |\phi|}{2V}, \quad (4.29)$$

where \sum_f denotes a sum over each cell face and V is the cell volume. It was found during the course of this work that a very small Courant number was required to maintain interface stability. Hence, a maximum Courant number (of any individual cell) condition

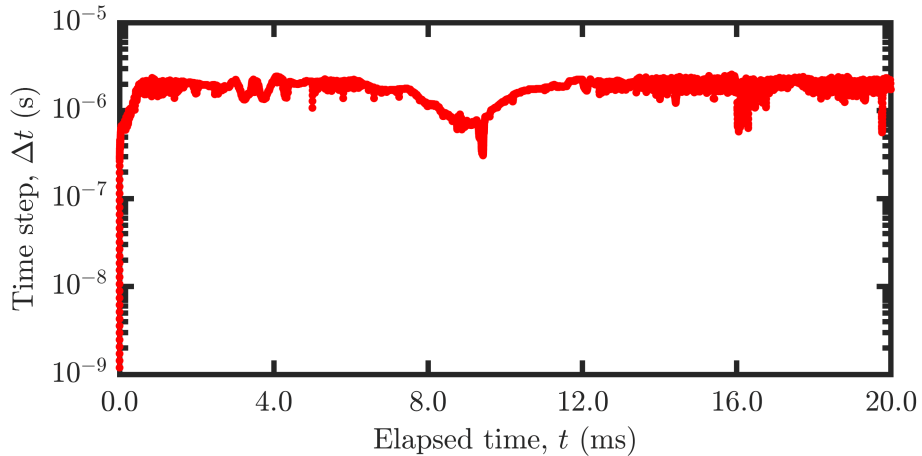


Figure 4.6: Evolution of the adjustable time step over a typical free-sessile droplet coalescence simulation from $t = 0.0$ ms to $t = 20.0$ ms, with $\max(\text{Co}) = 0.15$ enforced.

of 0.15 was imposed on all simulations reported⁸.

To reduce computational cost, the time step was adjusted throughout the simulation to ensure that Δt was as large as possible, whilst respecting $\max(\text{Co}) \leq 0.15$. The evolution of the time step throughout a typical free-sessile droplet coalescence simulation from Chapter 6 is shown in Figure 4.6, which indicates a typical time step of $\Delta t \approx 10^{-6}$ s.

Whilst $\max(\text{Co}) \leq 0.15$ was found to be a sufficient condition for maintaining interface stability throughout the majority of the simulation, a much smaller initial time step was required. The initial time step determined by OpenFOAM was found to be invariably too high, so the customised solver was modified to enable a user-selected initial time step to be specified. The initial time step was set as 1×10^{-9} s throughout this work. As can be seen in Figure 4.6, Δt rapidly rises from its enforced initial value to be generally three orders of magnitude higher, but the initial period of small time steps was enough to ensure that the interface remained stable as the meniscus bridge expanded between the droplets.

4.5 Initial condition

4.5.1 Volume fraction and passive scalar

Since the volume fraction, α describes the position of the droplets, its initial condition defines the initial droplet configuration. Recall from Section 4.4.3 that the base mesh of 10 cells per r_f was refined where $\alpha > 0.01$ to achieve a suitable resolution for representing droplets. However, setting the α distribution directly on the base mesh would yield very poorly defined droplets. Hence, before the initial α (and passive scalar, β) distribution was

⁸In OpenFOAM, there is also the possibility to set the maximum Courant number on the interface (`maxAlphaCo`) separately to the whole domain. This value is chosen to be 0.15 here, which is less restrictive than $\max(\text{Co}) \leq 0.15$ so that it had no practical influence on the simulations.

set, the mesh underwent a refinement process in a manually-selected volume encompassing the whole region in which the droplets were to be initialised. The initial mesh for a typical free-sessile droplet coalescence simulation can be seen in Figure 4.3a, whereas the mesh after adaptive mesh refinement had taken over is shown in Figure 4.3b.

Free droplets are assumed to be spherical with volume V_f , so were initialised as spheres with the requisite radius, r_f . The volumes of free droplets were precisely known in the experiments described in Chapter 3, so V_f (rather than r_f) was used to match free droplet sizes when comparing simulations to experiments.

Sessile droplets, defined by their volume, V_s and equilibrium contact angle, θ_{eq} , are assumed to be spherical caps (see Section 2.2.6), which is consistent with the Bond number of all droplets simulated in this work. Sessile droplets were also initialised as spheres, but with their centre outside of the domain for droplets with $\theta_{\text{eq}} < 90^\circ$, according to Equation (2.11). The radius, R of the sphere can be calculated using Equation (2.10) from V_s and θ_{eq} . Unlike free droplets though, the volume of the sessile droplets in the experiments was not necessarily precisely known, so the spread length, s and equilibrium contact angle, θ_{eq} – both of which are relatively easy to accurately determine via image processing – were used to match sessile droplet sizes when comparing simulations to experiments, instead of V_f . R was then calculated from Equation (2.8) rather than Equation (2.10).

4.5.2 Meniscus bridge

Coalescing droplets were initialised as just-touching spheres such that they would meet at a single point with an interface-fitted mesh. However, due to the discrete nature of the free surface caused by the hexahedral mesh and interface-capturing scheme used in this work, the initialisation of α inevitably yields a meniscus bridge of finite width between the droplets. Due to the diffuse interface and discrete nature of the mesh, such initialisation can lead to vapour being trapped within the droplet (due to $\alpha = 1$ droplet cells being separated by only one or two $\alpha = 0$ vapour cells) and forming a high-pressure vapour bubble shortly after the meniscus bridge begins to expand, as seen in Figure 4.7a at $t \approx 5.0$ ms. The process of vapour trapping seen (‘bleeding’ of $\alpha = 1$ cells) would not be expected physically and is a well-known numerical artefact of VOF-based simulations that can be noticed in many published works (e.g. Deka et al., 2017; Viswanathan, 2019), though it is generally inconsequential in studies considering only the external dynamics of coalescence.

It is important to distinguish the unphysical vapour trapping discussed here from toroidal bubbles caused by capillary waves (that is, free surface disturbances due to either meniscus bridge formation or building) that arises in some simulations of low-viscosity fluids that do not model the viscous vapour phase⁹ (e.g. Duchemin et al., 2003; Sprittles

⁹Such toroidal bubbles have themselves been shown to not arise experimentally in gases, with their formation suppressed by viscous vapour (Sprittles and Shikhmurzaev, 2014a).

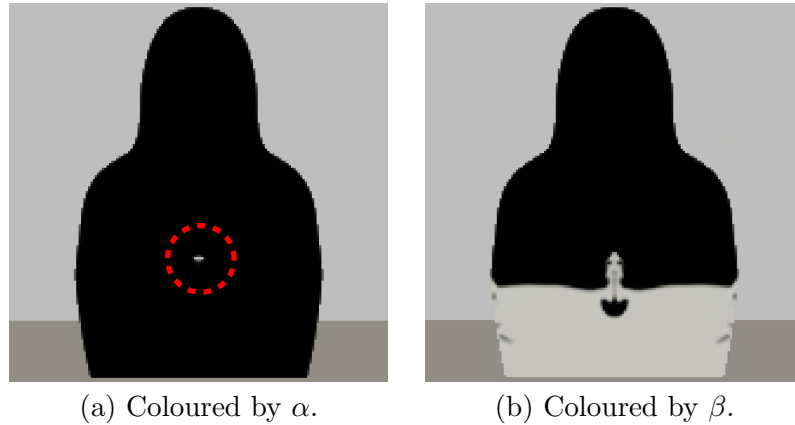


Figure 4.7: A typical free-sessile droplet coalescence simulation at $t \approx 5.0$ ms with droplets simply initialised as spheres. (a) Vapour is trapped within the coalesced droplet during the initial meniscus bridge building processes, highlighted by the dashed red circle. (b) The trapped vapour bubble destabilises the internal interface to produce a non-physical ‘jet’ due to its high pressure. The initial condition is modified as indicated in Figure 4.8 to prevent such vapour trapping and interface destabilisation in the results presented in following chapters.

and Shikhmurzaev, 2012b). In such cases, capillary waves propagate ahead of the expanding meniscus bridge, which brings the coalescing droplets’ free surfaces into close-enough proximity that at least one additional meniscus bridge is formed, thus causing a toroidal bubble to be trapped. In contrast, the vapour trapping seen in this work occurs before there is any significant free surface movement, caused by α ‘bleeding’ into neighbouring vapour cells – that is, numerical diffusion. Moreover, only the post-coalescence dynamics (from a finite meniscus bridge width) are considered in this work.

Such unphysical vapour trapping as seen in the uncorrected simulations in this work is detrimental to studies of internal flows as it may lead to the destabilisation of passive scalar interfaces, as seen in Figure 4.7b. The condition leading to vapour trapping was determined in this work to be droplet ($\alpha = 1$) cells separated by a one-cell vapour ($\alpha = 0$) layer at $t = 0.0$ ms, as seen in Figure 4.8a that shows the meniscus bridge region of just-touching droplets¹⁰ in which $\alpha = 1$ (red cells) regions were simply defined by spheres, as discussed above. The yellow cells indicated in this figure are initialised with $\alpha = 0$, but these cells prematurely ‘fill’ to have $\alpha > 0$, causing the vapour (where $\alpha = 0$) in the inner cell (indicated white in Figure 4.8a) to be trapped. The trapped vapour gathers on the axis of symmetry as seen in Figure 4.7a. Note that approximating a curved free surface by a piecewise linear function is the cause of the one-cell-thick vapour layer, not mesh resolution (or lack thereof). There was no evidence of vapour trapping or an unstable interface (as in Figure 4.7) in the experiments, giving confidence that such vapour trapping was a numerical artefact rather than a physical effect.

To eliminate vapour trapping in this work, the initial condition on α was modified

¹⁰The refined mesh resolution in Figure 4.8 is 50 cells per r_f (instead of 80 cells per r_f as typically used in this work) to ensure that all of the features being discussed in this section are seen.

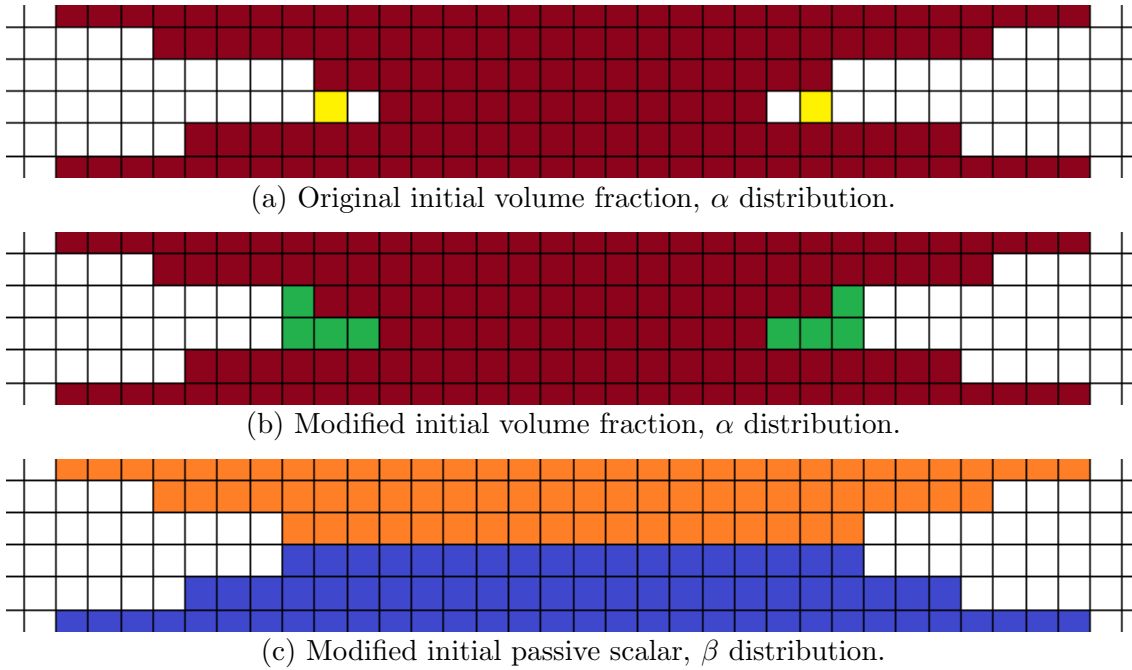


Figure 4.8: Initial volume fraction, α and passive scalar, β distribution in the region of the meniscus bridge between droplets, with $\alpha > 0.5$ displayed and the hexahedral mesh shown (50 cells per r_f – less than usual in the refined region). Red cells: $\alpha = 1$ set by defining droplets as spheres. White cells: $\alpha = 0$. Yellow cells: $\alpha = 0$ but which ‘fill’ to trap vapour. Green cells: $\alpha = 1$ set manually to prevent vapour being trapped. Orange cells: $\beta = 1$. Blue cells: $\beta = 0$. All orange and blue cells are initialised with $\alpha = 1$.

in all simulations reported by extending the meniscus bridge resulting from the definition of droplets as spheres to remove one-cell-thick vapour layers in the initial condition. The extension is indicated by green cells in Figure 4.8b, which are initialised with $\alpha = 1$ in addition to the red cells. In particular, the meniscus bridge is expanded to such a radial extent that all one-cell-thick vapour layers are removed, and vapour layers of greater cell thickness are less than a multiple of two cells wide than they are thick. For example, in Figure 4.8b one radial cell is removed from the four-cell-wide, two-cell-thick vapour layer in addition to the entire one-cell-thick vapour layer. Such a modification¹¹ was applied to the α (and thus β) initial condition for all simulation results reported this work; no trapped vapour was observed during meniscus bridge expansion in any simulation to which this modification of the initial condition was applied.

Importantly, the volume of ‘additional’ fluid introduced by expanding the meniscus bridge in the initial condition is extremely small and so has no appreciable side-effect on the dynamics of interest in this work. Moreover, it does not affect the propagation of capillary waves resulting from meniscus bridge expansion, as verified in Section 5.2.3. The modification is however successful at preventing non-physical destabilisation of the internal interface during meniscus bridge expansion, enabling quantitative agreement of

¹¹To initialise α , the droplets were defined as spheres as described above and then the meniscus bridge expanded by setting $\alpha = 1$ within the appropriate cylindrical region.

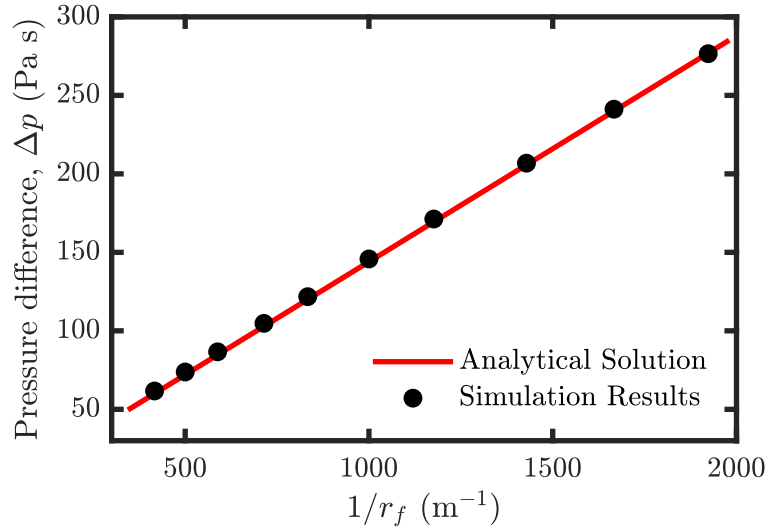


Figure 4.9: Analytical pressure difference droplet across the free surface, compared to simulated results, for a free water droplet of radius r_f after 5×10^{-3} capillary time units.

the internal dynamics between the simulations and experiments. The passive scalar, β is initialised as unity in every cell where $\alpha = 1$ above the horizontal level nominally separating the droplets, as shown in Figure 4.8c.

4.5.3 Velocity and modified pressure

In the numerical results presented, all droplets are initially static so the domain was initialised with zero velocity ($u_i = 0$) everywhere. The modified pressure, p' , which recall from Equation (4.7) is the total pressure with the hydrostatic contribution subtracted, must also be specified. Clearly the modified pressure is initially non-zero within the droplets due to Laplace pressure (see Section 2.1.5), the value of which is well-known within the bulk of each precursor droplet. However, as described in the previous section, the initial meniscus bridge between the droplets inevitably has a finite width near which the modified pressure distribution is not clear a priori. Hence, the modified pressure was initialised as zero ($p' = 0$) everywhere to allow the simulation to freely recover the modified pressure distribution.

It is clearly important to verify that the known analytical value of the modified pressure within the droplet bulk is correctly recovered in a sufficiently short time, so as not to have an undue influence on the dynamics. In any case, confirming that Equation (2.3) for the Laplace pressure is correctly recovered is an important benchmark for validation of surface-tension-driven flow simulations, whatever initial condition is specified (Ahmad et al., 2018; Raman et al., 2016).

In order to verify the correct recovery of Laplace pressure, a single free spherical water droplet was initialised in the standard numerical setup used for the coalescence results reported, for which the analytical value of Laplace pressure is given by Equation (2.2).

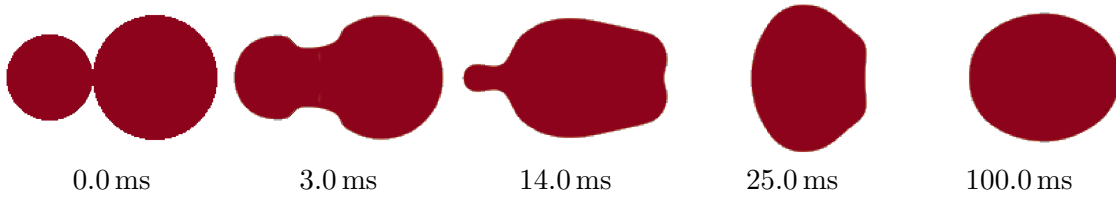


Figure 4.10: External dynamics during the coalescence of two initially-static free toluene droplets in water, initialised as two just-touching spheres with size ratio 0.69. This simulation is consistent with an experiment of Eiswirth et al. (2012).

Multiple droplet radii, from 0.5×10^{-3} m to 2.4×10^{-3} m, were considered. Recall that $g_i = 0$ so such a droplet is temporally stable. However, to be consistent across the droplet sizes considered, the Laplace pressure was measured after 5×10^{-3} simulated units on the applicable capillary time scale (i.e. at $t = 0.005\tau_\sigma$). For a droplet with $r_f = 1$ mm, $t = 0.005\tau_\sigma \approx 19 \mu\text{s}$, before which time meniscus bridge growth is expected to be negligible. The analytical and simulated mean Laplace pressure within the droplet (defined as cells where $\alpha > 0.9999$ here) are plotted against the reciprocal of droplet radius in Figure 4.9. Excellent agreement between the simulated and analytical results is seen, confirming the correct rapid recovery of Laplace pressure and validating both the surface tension formulation within the numerical framework and the employed initial condition for pressure.

4.6 Free droplet coalescence examples

In this section, examples of free droplet coalescence simulations using the customised solver described in previous sections are presented.

Toluene droplets in water

Figure 4.10 shows the external dynamics during the coalescence of two initially-static free droplets, consistent with the experiments of Eiswirth et al. (2012). In particular, the droplets consist of toluene and are immersed in water as the outer fluid phase – the fluid properties given by Eiswirth et al. are used. As seen, the dynamics are characterised by rapid growth of the meniscus bridge between the precursor droplets of size ratio 0.69, with the initially-smaller droplet forming a tail that is injected into the larger droplet. After injection, the droplet shape is highly deformed from equilibrium ($t = 25.0$ ms frame), but relaxes towards a spherical shape ($t = 100.0$ ms frame), aided by the relatively high outer fluid viscosity (compared to if the outer phase was a gas).

The results in Figure 4.10 compare favourably to the experimental results of Eiswirth et al., though with an approximate 2.0 ms timing discrepancy, which may be due to the initial condition, since in the experiments the droplets were rising at the point of coa-

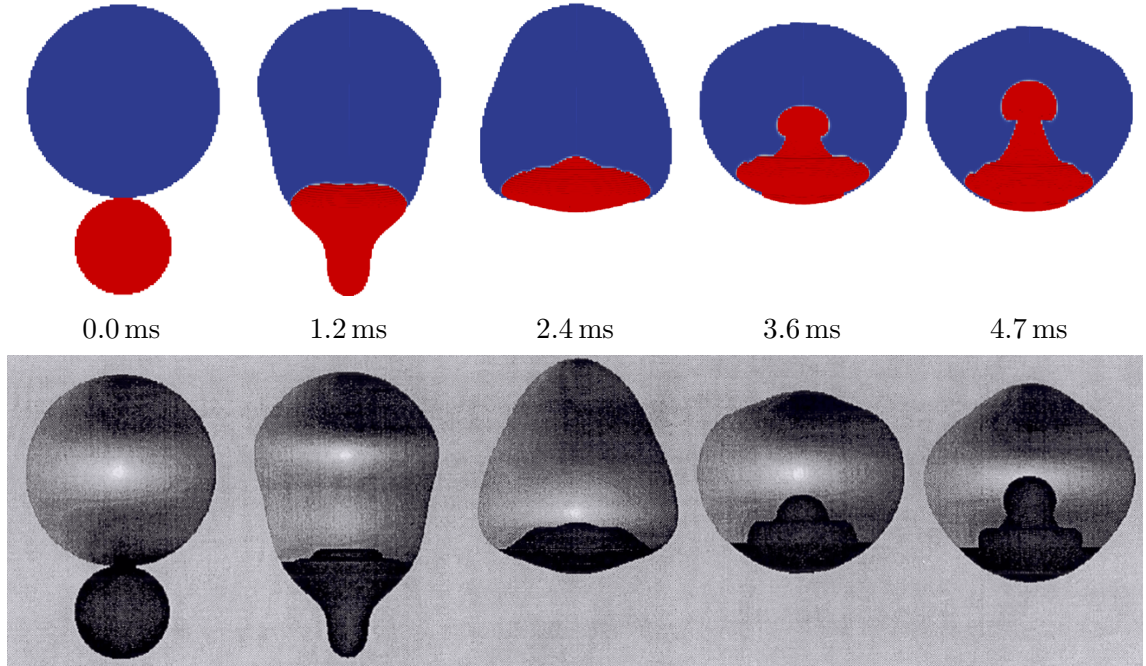


Figure 4.11: Internal and external dynamics during the coalescence of two initially-static low-viscosity free droplets, initialised as two just-touching spheres with size ratio 0.481. Top row: simulations using the customised solver developed in this work. Bottom row: finite-difference-method front-tracking simulations of Nobari and Tryggvason (1994). Here, $Oh = 2.4 \times 10^{-3}$; $\rho_d/\rho_o = 20.0$; $\mu_d/\mu_o = 0.1$.

lescence and so were not completely static as they were in the simulations. Note that a corresponding simulation to that shown in Figure 4.10 was conducted using a 2.5D domain (planar), though vastly different results that were inconsistent with the experimental data were obtained, as expected from Section 4.4.3 due to vorticity.

Low Ohnesorge number droplets

Figure 4.11 shows the internal and external dynamics during the coalescence of two initially-static free droplets, as simulated with the customised solver (top row), alongside the finite-difference-method front-tracking simulations of Nobari and Tryggvason (1994) with equivalent parameters (bottom row). In particular, the droplets have $Oh = 2.4 \times 10^{-3}$ (using the smaller droplet diameter as the length scale) and size ratio 0.481, with $\rho_d/\rho_o = 20.0$ and $\mu_d/\mu_o = 0.1$. The smaller precursor droplet is injected into the larger one in the form of a jet, aided by the low droplet viscosity. The results derived from the customised solver (top row) compare well with those seen in the simulations of Nobari and Tryggvason (bottom row), though the former progresses slightly faster. Note that Nobari and Tryggvason did not make a direct comparison of their numerical results to experiments and so a clear-cut comparison concluding the accuracy of the simulations can not be justly made. However, it is clear that the customised solver is able to capture both the internal and external dynamics of the free droplet coalescence appropriately, whilst

qualitative and quantitative experimental validation of the customised solver for free and sessile droplet coalescence is presented in Chapter 6.

4.7 Summary

In this chapter, the framework for the OpenFOAM numerical simulations utilised in later chapters was introduced. The simulations use a customised version of the `interFoam` solver, which is based on the VOF method. Several modifications were made to vanilla `interFoam` in order to create a customised solver suitable for studying the internal dynamics of coalescing droplets. These modifications included the addition of the Kistler dynamic contact angle model (enforced as a boundary condition on the substrate) and a bounded passive scalar to enable advective mixing to be assessed. The implementation of the VOF model in OpenFOAM using the FVM was discussed, including the treatment of the bounded scalars (α and β) that are especially important in this work. The boundary and initial conditions were also explained and verified to be appropriate wherever necessary, before the customised solver was deployed to simulate the coalescence of free droplets, which demonstrated its efficacy for studying such coalescence dynamics.

Additional validation and verification of the customised solver introduced in this chapter is undertaken in the following chapter in the context of free and sessile droplet coalescence, before it is deployed to elucidate the physics of such coalescence events.

Chapter 5

Numerical verification for free and sessile droplet coalescence

In this chapter, the favoured numerical configuration of axisymmetric initially-static free and sessile droplet coalescence is introduced. This configuration is of particular interest in this work since it accentuates the effect of both capillary waves and substrate wettability on the dynamics of coalescence, which will be explored in Chapter 6, without any interference from initial droplet inertia. An equivalent experimental configuration was described in Section 3.4, which is used to quantitatively validate the simulations in Chapter 6. The focus of this short chapter is numerical verification of the customised solver described in the previous chapter, whilst the effect of fluid properties on the dynamics of coalescence in this configuration is also discussed.

5.1 Free and sessile droplet coalescence

5.1.1 Numerical setup

Droplets were initialised as just-touching spheres, with the joining meniscus bridge modified as described in Section 4.5. The centre of the sphere of which the sessile droplet (assumed to be a spherical cap) is part was placed such that some of its volume lies outside the domain (below the substrate) to define the spherical cap of the desired volume, V_s . Full geometric information regarding spherical caps can be found in Section 2.2.6, but a sessile droplet form can be uniquely defined by any two of θ , s , c , R and h , which are the contact angle, spread length, centre of the defining sphere, radius of the defining sphere and cap height, respectively.

Recall from Section 4.4.3 that an adaptively refined mesh with 10 base cells per free droplet radius, r_f and 3 levels of refinement was used for typical simulations in this work,

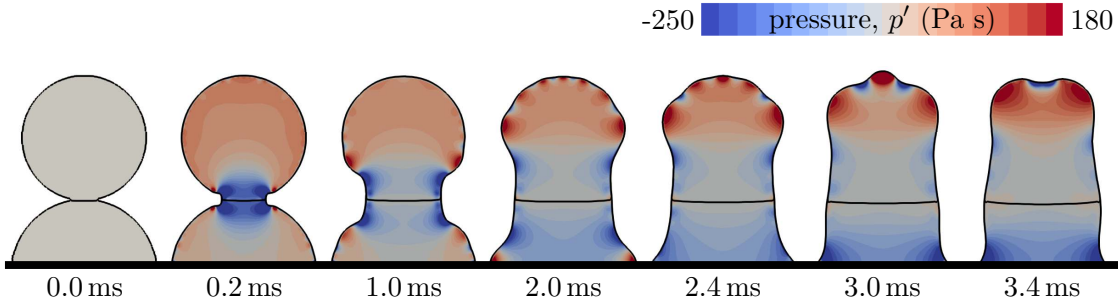


Figure 5.1: Free surface and internal interface profiles of free and sessile water droplet coalescence, with a contour plot coloured by modified pressure, p' . In this simulation, $\theta_a = 100^\circ$, $\theta_{eq} = 82^\circ$, $\theta_r = 50^\circ$, $V_s = 3.9 \mu\text{L}$ and $V_f = 6.2 \mu\text{L}$.

within a (quarter) domain of size $4r_f \times 5r_f \times 4r_f$. An initial time step of 1×10^{-9} s was enforced, but thereafter was adjusted whilst respecting a maximum Courant number of 0.15 – see Section 4.4.8. Under these conditions, a typical simulation of free and sessile water droplet coalescence from $t = 0.0$ ms to $t = 20.0$ ms required approximately 300 core hours, with a wall clock time around 23 hours, using 16 cores on a single node (of the ARC4 CentOS 7 cluster at the University of Leeds) containing Intel Xeon Gold 6138 (‘Skylake’) processors.

Throughout the numerical work, it can be assumed that the droplets consist of water in air at 23°C , unless otherwise stated. In particular, the droplets have a density of $\rho_d = 997 \text{ kg m}^{-3}$ and a kinematic viscosity of $\nu_d = 9.3 \times 10^{-7} \text{ m}^2 \text{ s}^{-1}$ (as specified in OpenFOAM), corresponding to a dynamic viscosity of $\mu_d = 9.3 \times 10^{-4} \text{ Pa s}$. The air has a density of $\rho_o = 1.2 \text{ kg m}^{-3}$ and a kinematic viscosity of $\nu_o = 1.5 \times 10^{-5} \text{ m}^2 \text{ s}^{-1}$, corresponding to a dynamic viscosity of $\mu_o = 1.8 \times 10^{-5} \text{ Pa s}$.

5.1.2 Initial coalescence dynamics

The initial dynamics during free and sessile droplet coalescence ($V_s = 3.9 \mu\text{L}$; $V_f = 6.2 \mu\text{L}$; $\theta_a = 100^\circ$; $\theta_{eq} = 82^\circ$; $\theta_r = 50^\circ$) are shown in Figure 5.1, with a contour plot of modified pressure¹ (effectively Laplace pressure) allowing capillary waves to be seen.

The large region of negative modified pressure in the meniscus bridge leads to its rapid expansion that triggers capillary waves. These capillary waves propagate outward along, and significantly disturb, the free surface of the coalesced droplet during the meniscus bridge building stage of the dynamics. After approximately 2.0 ms, the leading downward travelling capillary waves reach the substrate and cause the contact line to recede. These capillary waves are effectively reflected away from the substrate and back up the free surface of the droplet in tandem with the ongoing meniscus bridge building dynamics. Moreover, the initially upward travelling capillary waves act to stretch the droplet upwards.

¹The $t = 0.0$ ms frame in Figure 5.1 is not coloured due to prescription of the zero modified pressure initial condition – see Section 4.5.

As seen, the capillary waves and their interaction with the substrate play a significant role in the coalescence dynamics shown in Figure 5.1, pronounced by the lack of initial inertia. Indeed, all of the coalesced droplet's kinetic energy hails from excess surface energy due to the non-equilibrium initial condition in the droplet configuration studied. Hence, this configuration is a very challenging test of numerical simulations for studying surface-tension-driven flows involving non-trivial substrate interaction. The study of the mechanisms of internal flow and mixing, in addition to the effect of substrate wettability and experimental validation of the numerical simulations, is deferred to Chapter 6.

5.2 Sensitivity analyses

5.2.1 Mesh

It is important to determine the sensitivity of the simulation results to the resolution of the mesh. As an adaptively refined mesh is used, with refinement throughout the whole droplet volume, it is important to consider both the refined and unrefined parts of the mesh within this mesh sensitivity analysis. To do so, six meshes with three different numbers of cells per free droplet radius, r_f within the droplet were considered as detailed in Table 5.1. Two different levels of refinement were considered. For example, a mesh with 10 cells per r_f and 3 levels of refinement (as used in this work) has $10 \times 2^3 = 80$ cells per r_f within the whole droplet volume. With each of these six meshes, a typical simulation from Chapter 6 was conducted involving the coalescence of a free and sessile droplet with $V_s = 3.6 \mu\text{L}$, $V_f = 6.2 \mu\text{L}$, $\theta_a = 100^\circ$, $\theta_{\text{eq}} = 82^\circ$ and $\theta_r = 75^\circ$. The evolution of spread length, internal interface height and total droplet height are presented in Figures 5.2 to 5.4, respectively.

All of the meshes considered are relatively fine within the droplet region (especially compared with mesh resolutions generally used in the literature) so it is not surprising that there is no large quantitative difference between any of them in any of the three metrics considered. Even in regions of rapid change, where differences are likely to be accentuated as only the cell-centre values are used to derive the plotted data across a diffuse interface (the interface is defined as either $\alpha = 0.5$ or $\beta = 0.5$, as appropriate), the differences due to the number of cells in the droplet region are small and, in particular, negligible for the conclusions of this study. Moreover, the dynamics were found to be remarkably insensitive to the mesh resolution within the air, characterised by the number of base cells per r_f . Higher numbers of base cells with a constant refined region resolution (achieved by fixing the number of cells within the droplet region and reducing the number of refinement levels) have been considered than are shown here with almost no quantitative difference in any of the three metrics.

In this work, 80 refined cells per r_f were deployed, with a base mesh resolution of 10 cells per r_f , indicated by the green markers in Figures 5.2 to 5.4. The mesh sensitivity analysis detailed here confirms that all free surface and internal features are sufficiently

Table 5.1: Meshes employed in the mesh sensitivity analysis. ‘Refined cells’ refers to those cells within the refined region of the domain (the entire droplet volume and near its free surface), while ‘base cells’ specifies the minimum resolution in the air (the unrefined regions). Droplet resolutions are computed with $r_f = 1.14$ mm, consistent with the (numerical and laboratory) experiments predominant in Chapter 6.

No. Refined Cells per r_f	No. Base Cells per r_f	Refinement Levels	Total No. Cells at $t = 0.2$ ms	Refined Mesh Resolution (μm)
64	4	4	0.58×10^6	17.81
64	8	3	0.58×10^6	17.81
80	5	4	1.06×10^6	14.25
80	10	3	1.06×10^6	14.25
96	6	4	1.76×10^6	11.88
96	12	3	1.78×10^6	11.88

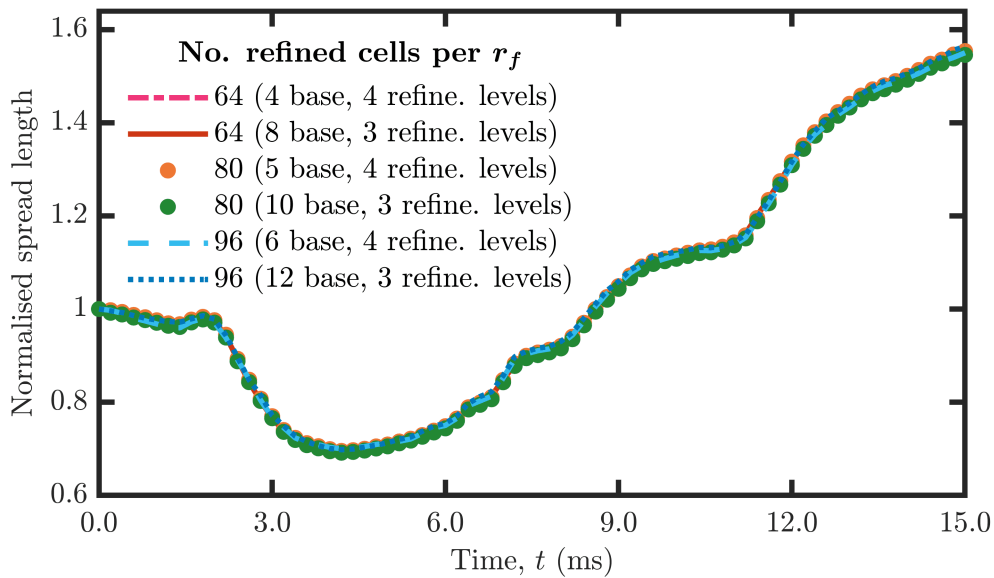


Figure 5.2: Spread length evolution, normalised by its initial value, for the six meshes detailed in Table 5.1. $V_s = 3.6$ μL , $V_f = 6.2$ μL , $\theta_a = 100^\circ$, $\theta_{\text{eq}} = 82^\circ$ and $\theta_r = 75^\circ$. The green filled marker represents the mesh resolution typically used in this work.

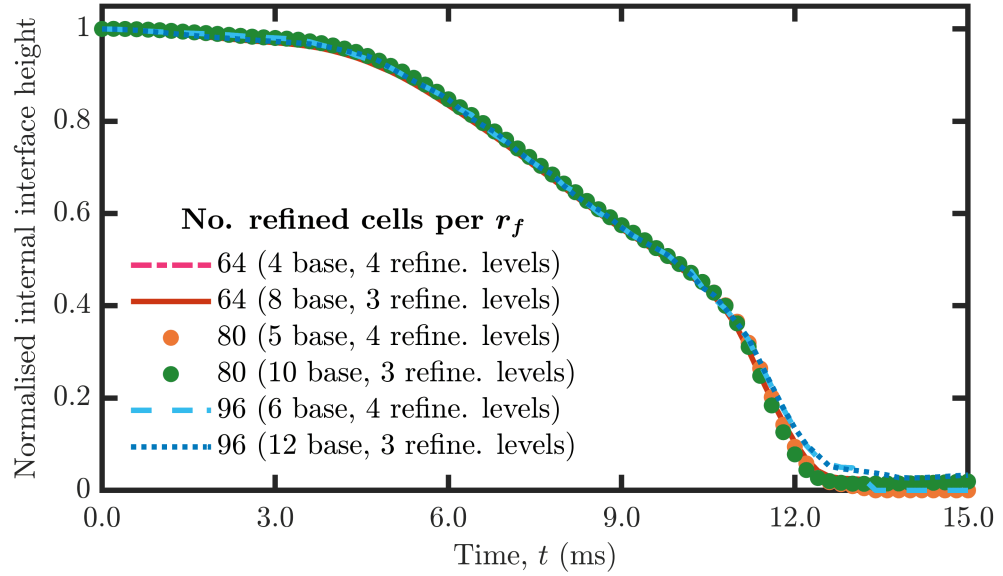


Figure 5.3: Internal interface height evolution, normalised by its initial value, for the six meshes detailed in Table 5.1. $V_s = 3.6 \mu\text{L}$, $V_f = 6.2 \mu\text{L}$, $\theta_a = 100^\circ$, $\theta_{\text{eq}} = 82^\circ$ and $\theta_r = 75^\circ$. The green filled marker represents the mesh resolution typically used in this work.

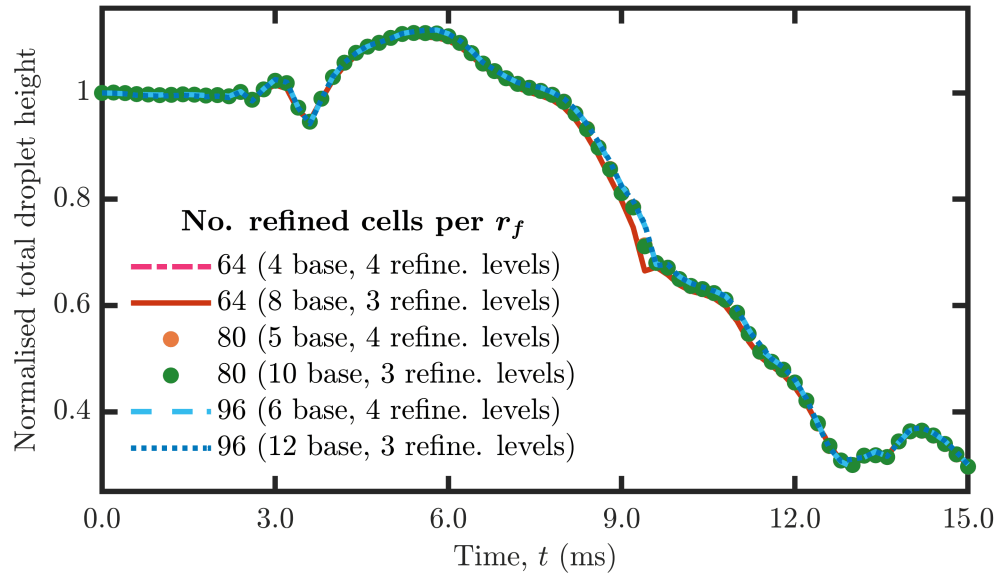


Figure 5.4: Total droplet height evolution, normalised by its initial value, for the six meshes detailed in Table 5.1. $V_s = 3.6 \mu\text{L}$, $V_f = 6.2 \mu\text{L}$, $\theta_a = 100^\circ$, $\theta_{\text{eq}} = 82^\circ$ and $\theta_r = 75^\circ$. The green filled marker represents the mesh resolution typically used in this work.

Table 5.2: Error over time of three key quantities (droplet height; interface height; spread length) for a typical free-sessile droplet simulation assuming various (quarter) domain sizes, compared to the typical domain size of $4r_f \times 5r_f \times 4r_f$. Absolute differences are scaled by the *minimum* value at each time step. Bold font identifies values $\geq 1\%$.

Domain Size	Droplet Height Error		Interface Height Error		Spread Length Error	
	Mean	Max.	Mean	Max.	Mean	Max.
$2r_f \times 4r_f \times 2r_f$	0.1%	0.9%	0.6%	4.5%	0.2%	1.1%
$2r_f \times 5r_f \times 2r_f$	0.1%	0.5%	0.2%	0.9%	0.1%	0.4%
$3r_f \times 4r_f \times 3r_f$	0.1%	0.6%	0.3%	1.7%	0.1%	0.5%
$3r_f \times 5r_f \times 3r_f$	0.1%	0.8%	0.2%	1.1%	0.1%	0.5%
$4r_f \times 4r_f \times 4r_f$	0.1%	0.9%	0.3%	1.7%	0.1%	0.4%
$4r_f \times 6r_f \times 4r_f$	0.1%	1.4%	0.1%	0.6%	0.1%	0.3%
$5r_f \times 5r_f \times 5r_f$	0.1%	0.7%	0.4%	2.6%	0.1%	0.4%
$5r_f \times 6r_f \times 5r_f$	0.2%	0.9%	0.1%	0.8%	0.1%	0.4%

resolved with such a mesh resolution, whilst further refinement would have had a negligible effect on the results presented in this work.

5.2.2 Domain size

As noted in Section 4.4.3, a domain size of $4r_f \times 5r_f \times 4r_f$ was chosen for the quarter domain used in the simulations reported in this work. Since the substrate and symmetry boundaries are always in contact with the droplets, the domain size only determines the distance of the droplets to the atmospheric (open) boundaries. Whilst it is desired to keep the domain as small as possible for computational efficiency, the domain must be large enough that the artificial, arbitrarily placed atmospheric boundaries have no appreciable effect on the dynamics of interest.

To determine the sensitivity of the simulation results to domain size, eight simulations assuming different domain sizes (both smaller and larger than the one typically used in this work) were conducted, with the error in three metrics of interest computed relative to a simulation using the typical domain size of $4r_f \times 5r_f \times 4r_f$. The simulation was a typical free-sessile droplet coalescence simulation seen in Chapter 6 ($V_s = 3.9 \mu\text{L}$; $V_f = 6.2 \mu\text{L}$; $\theta_a = 100^\circ$; $\theta_{\text{eq}} = 82^\circ$; $\theta_r = 50^\circ$), from $t = 0.0 \text{ ms}$ to $t = 20.0 \text{ ms}$. The three metrics were the total droplet height, internal interface height and spread length (thus covering the internal dynamics, external dynamics and substrate interaction). For each metric, the absolute difference between its value for the domain size in question and $4r_f \times 5r_f \times 4r_f$ was computed at each write time (every 0.25 ms), then scaled by the minimum (Table 5.2) or mean (Table 5.3) value *on each time step*. The mean and maximum values of this quantity over all (write) times considered are displayed in Tables 5.2 and 5.3. Mathematically, the maximum spread length error, for example, in Table 5.2 is calculated as

$$\max_t \frac{|s_{m,t} - s_{o,t}|}{\min(s_{m,t}, s_{o,t})},$$

Table 5.3: Error over time of three key quantities (droplet height; interface height; spread length) for a typical free-sessile droplet simulation assuming various (quarter) domain sizes, compared to the typical domain size of $4r_f \times 5r_f \times 4r_f$. Absolute differences are scaled by the *mean* value at each time step. Bold font identifies values $\geq 1\%$.

Domain Size	Droplet Height Error		Interface Height Error		Spread Length Error	
	Mean	Max.	Mean	Max.	Mean	Max.
$2r_f \times 4r_f \times 2r_f$	0.1%	0.5%	0.6%	4.5%	0.2%	1.3%
$2r_f \times 5r_f \times 2r_f$	0.1%	0.4%	0.2%	0.9%	0.1%	0.5%
$3r_f \times 4r_f \times 3r_f$	0.1%	0.4%	0.3%	1.7%	0.1%	0.5%
$3r_f \times 5r_f \times 3r_f$	0.1%	0.4%	0.2%	1.1%	0.1%	0.6%
$4r_f \times 4r_f \times 4r_f$	0.1%	0.6%	0.3%	1.7%	0.1%	0.5%
$4r_f \times 6r_f \times 4r_f$	0.1%	0.7%	0.1%	0.6%	0.1%	0.4%
$5r_f \times 5r_f \times 5r_f$	0.1%	0.4%	0.4%	2.6%	0.1%	0.5%
$5r_f \times 6r_f \times 5r_f$	0.1%	0.5%	0.1%	0.8%	0.1%	0.4%

where $s_{m,t}$ and $s_{o,t}$ are the spread length at time t computed on the domain size in question and the typical domain size of $4r_f \times 5r_f \times 4r_f$, respectively.

As seen in Tables 5.2 and 5.3, both the maximum and mean errors on all three metrics are generally very small and, importantly, show no clear trend with respect to the typical domain size. The largest errors arise in the *maximum* internal interface height – the reason being that this height becomes almost zero when the interface reaches the substrate, so small differences appear as much larger scaled errors. Hence, the mean error yields a better reflection of the genuine error for this metric. Given the small errors, it can be concluded that the dynamics are very insensitive to the precise domain size chosen. Indeed, the flow within the coalesced droplet itself dominates the dynamics in practice, rather than those within the (low-viscosity) air. In fact, many simulations of such droplet dynamics do not include air within the model (e.g. Duchemin et al., 2003; Sprittles and Shikhmurzaev, 2012b), though the inclusion of air is an inescapable feature of the VOF simulations used in this work. From the analysis in this section though, it is clear that the use of a $4r_f \times 5r_f \times 4r_f$ domain size is appropriate to study dynamics of interest in this work.

5.2.3 Initial meniscus bridge width

As discussed in Section 4.5.2, the initial meniscus bridge joining the coalescing droplets is not only finite in the interface-capturing numerical simulations used in this work, but its width is also modified from the shape defined by the spheres used to initialise the droplets (enacted on a hexahedral mesh) in order to prevent non-physical air entrainment at the onset of coalescence. The effect of the initial meniscus bridge width on the capillary waves emitted during its expansion is determined in this section. In particular, it is important to know whether the meniscus bridge modification (described in the aforementioned section) is detrimental to accurately capturing the dynamics of interest, i.e. whether the dynamics

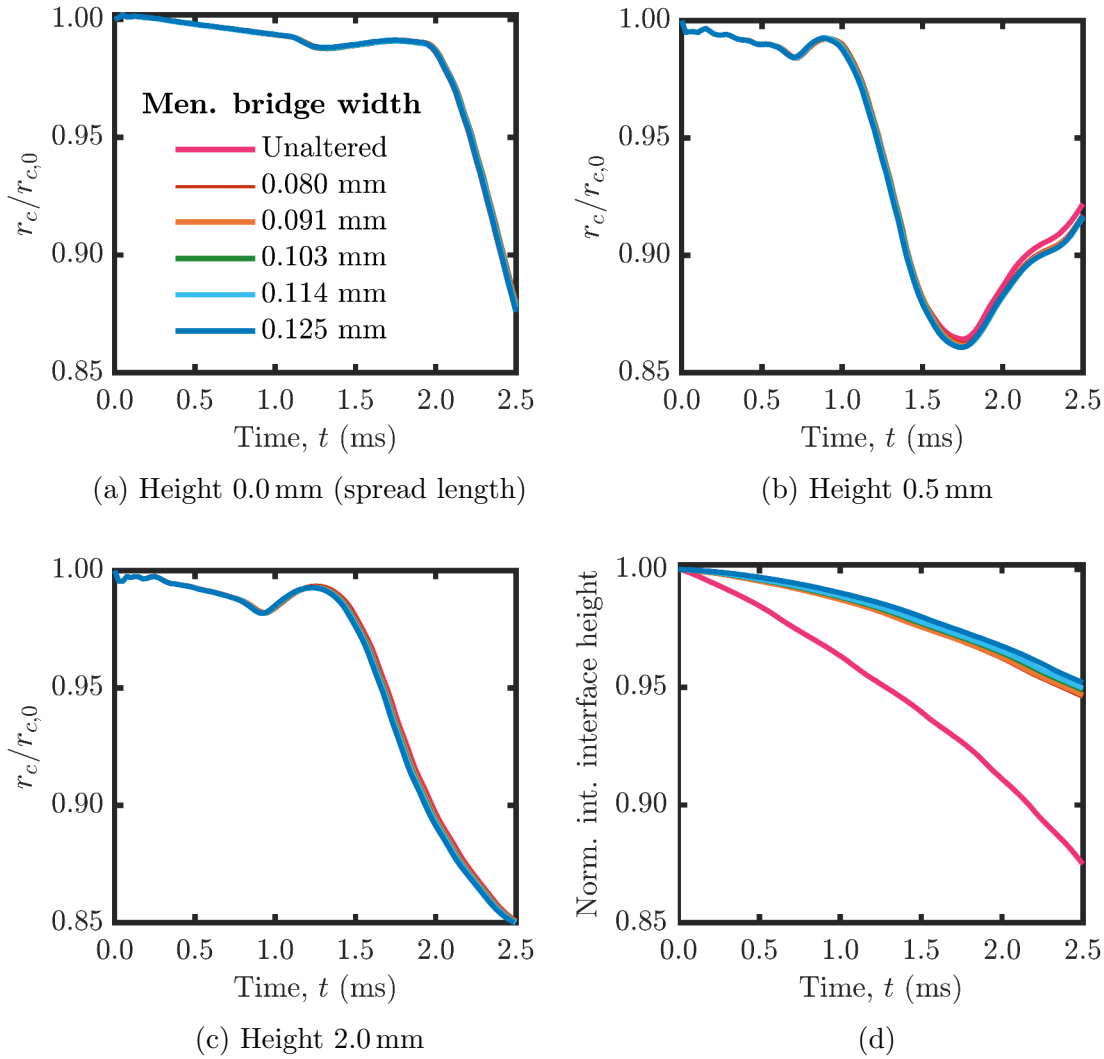


Figure 5.5: Simulations of free and sessile droplet coalescence, varying the initial meniscus bridge width. ‘Unaltered’ refers to the initial volume fraction condition defining the droplets without the modification described in Section 4.5.2. r_c is the radius of a horizontal cross-section of the coalesced droplet at a given height ($r_c = r_{c,0}$ at $t = 0.0$ ms). For all simulations, $\theta_a = 100^\circ$, $\theta_{eq} = 82^\circ$, $\theta_r = 75^\circ$, $V_s = 3.6 \mu\text{L}$ and $V_f = 6.2 \mu\text{L}$.

are strongly dependent on the precise initial meniscus bridge width. To make this determination, a typical free-sessile droplet coalescence case was simulated ($\theta_a = 100^\circ$; $\theta_{eq} = 82^\circ$; $\theta_r = 75^\circ$; $V_s = 3.6 \mu\text{L}$; $V_f = 6.2 \mu\text{L}$). Several simulations were conducted with varying initial meniscus bridge forms, including that derived from simply defining the droplets as spheres (‘unaltered’) which results in air being trapped, with the modification described in Section 4.5.2 applied (leading to an initial bridge width of 0.091 mm within the domain), and four other wider or narrower meniscus bridges.

Figure 5.5 presents the results of these simulations. To assess the effect on emitted capillary waves, the horizontal extent of the droplet was measured at various heights, over a period from $t = 0.0$ ms to $t = 2.5$ ms – that is, the radius of the horizontal cross-section, r_c at a given height, where $r_c = r_{c,0}$ at $t = 0.0$ ms. The three heights considered are

0.0 mm (i.e. the spread length), 0.5 mm and 2.0 mm, where the meniscus bridge is located approximately 1.1 mm above the substrate. Hence, this analysis captures both upward and downward propagating capillary waves, and the all-important substrate interaction. The evolution of r_c for each meniscus bridge width is plotted in Figure 5.5, at each height considered, alongside the normalised interface height.

All lines seen in Figures 5.5a to 5.5c are almost indistinguishable from each other, even for the simulation with an unaltered meniscus bridge that results in air being trapped. This observation confirms that the precise initial meniscus bridge width and form does not greatly influence emitted capillary waves in the simulations within this work. Moreover, the meniscus bridge modification described in Section 4.5.2 is certainly not detrimental to accurately capturing the dynamics of interest.

However, considering Figure 5.5d it is clear that modification of the meniscus bridge is crucial to avoid trapping air at the onset of coalescence, and thus faithfully capture internal flows². Indeed, Figure 4.7 on page 93 shows frames which are similar to those of the unaltered simulation in Figure 5.5 – the internal interface height of the simulation with the unaltered meniscus bridge plotted in Figure 5.5d is influenced by the air bubble, which is unphysical. However, it can be seen that the internal dynamics are only very weakly dependent on the precise meniscus bridge width for all other simulations (in which air trapping does not occur). Moreover, it has been checked that the long-term dynamics (both external and internal) are not significantly influenced by the precise meniscus bridge width either, verifying that the initial condition used (including the modification) in this work is appropriate.

5.3 Effect of fluid properties

5.3.1 Matched Ohnesorge number

At least after the earliest stages, the coalescence dynamics of the low Ohnesorge number droplets considered in this work are expected to occur on the inertial time scale, τ_σ , which is defined by Equation (2.18) in Section 2.5. Within the customised solver, dimensional variables are specified so it is worth checking that consistent dynamics with respect to the inertial time scale are seen for simulations with fixed Ohnesorge number ($\text{Oh} = 3.57 \times 10^{-3}$, with r_f constituting the length scale, in this case), but different underlying dimensional values of parameters that feed into it. Such a test not only constitutes numerical verification for the customised solver, but will also confirm that the dynamics proceed on the expected time scale.

Simulations assuming five value combinations of the parameters r_f , μ_d and σ were

²Quantitative experimental validation of the internal interface height, matching the profiles in Figure 5.5d with the initial bridge modification, are presented in Figures 6.6 and 6.7 of Chapter 6.

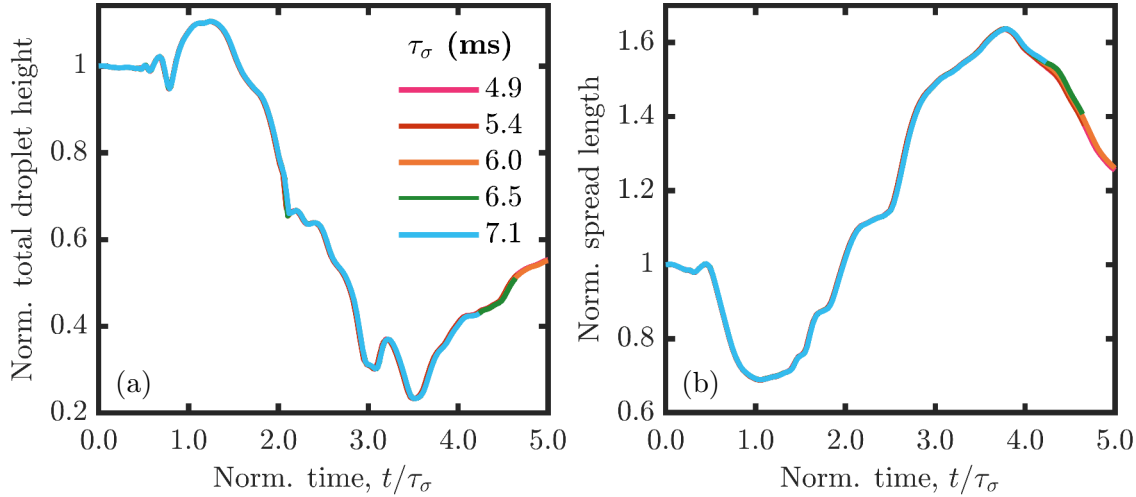


Figure 5.6: Total droplet height and spread length evolution in time, each normalised by their value at $t = 0.0$ ms. $\text{Oh} = 3.57 \times 10^{-3}$ is fixed, though μ_d , r_f and σ are varied. Time is normalised by the inertial time scale, τ_σ . The fluid and geometric properties corresponding to each simulation (identified by τ_σ in the legend) are given in Table 5.4. For all simulations, $\theta_a = 100^\circ$, $\theta_{\text{eq}} = 90^\circ$, $\theta_r = 80^\circ$ and $V_s/V_f = 0.667$.

carried out, with R set dependent on the value of r_f in order to maintain a constant droplet volume ratio of $V_s/V_f = 0.667$. The parameter value combinations used are listed in Table 5.4. All other parameters (ρ_d , ρ_o , μ_o , etc.) are fixed. Note that both values of r_f used are large enough that the Péclet number is negligible (i.e. molecular diffusion is equally insignificant for all simulations). Whilst the Ohnesorge number is fixed, $\tau_\sigma \in [4.9, 7.1]$ ms for each combination.

The evolution of two important metrics characterising droplet coalescence on a substrate (the total droplet height and spread length, both normalised by their values at $t = 0.0$ ms) are plotted in Figure 5.6 for each of the five simulations. All data collapse onto a single curve as expected, given that time is non-dimensionalised by the inertial time scale. Only very minor deviations are seen in regions of most rapid change. Hence, the dynamics proceed on an inertial time scale and it is confirmed that the customised solver correctly rationalises the dimensional parameters to produce non-dimensional results as would be expected for a fixed Ohnesorge number.

Table 5.4: Fluid and droplet properties for the five simulations seen in Figure 5.6, all of which have $\text{Oh} = 3.57 \times 10^{-3}$. R is the equivalent spherical radius of the sessile droplet ($\theta_{\text{eq}} = 90^\circ$). For all simulations, $\rho_d = 997 \text{ kg m}^{-3}$, $\rho_o = 1.2 \text{ kg m}^{-3}$ and $\mu_o = 1.5 \times 10^{-5} \text{ Pa s}$ (the properties of water – see Section 5.1.1).

τ_σ (ms)	r_f (mm)	R (mm)	μ_d (mN m^{-1})	σ (mPa s)
4.9	1.127	1.241	0.93	60.3
5.4	1.127	1.241	0.85	50.0
6.0	1.360	1.498	1.10	70.0
6.5	1.360	1.498	1.02	60.0
7.1	1.360	1.498	0.93	50.0

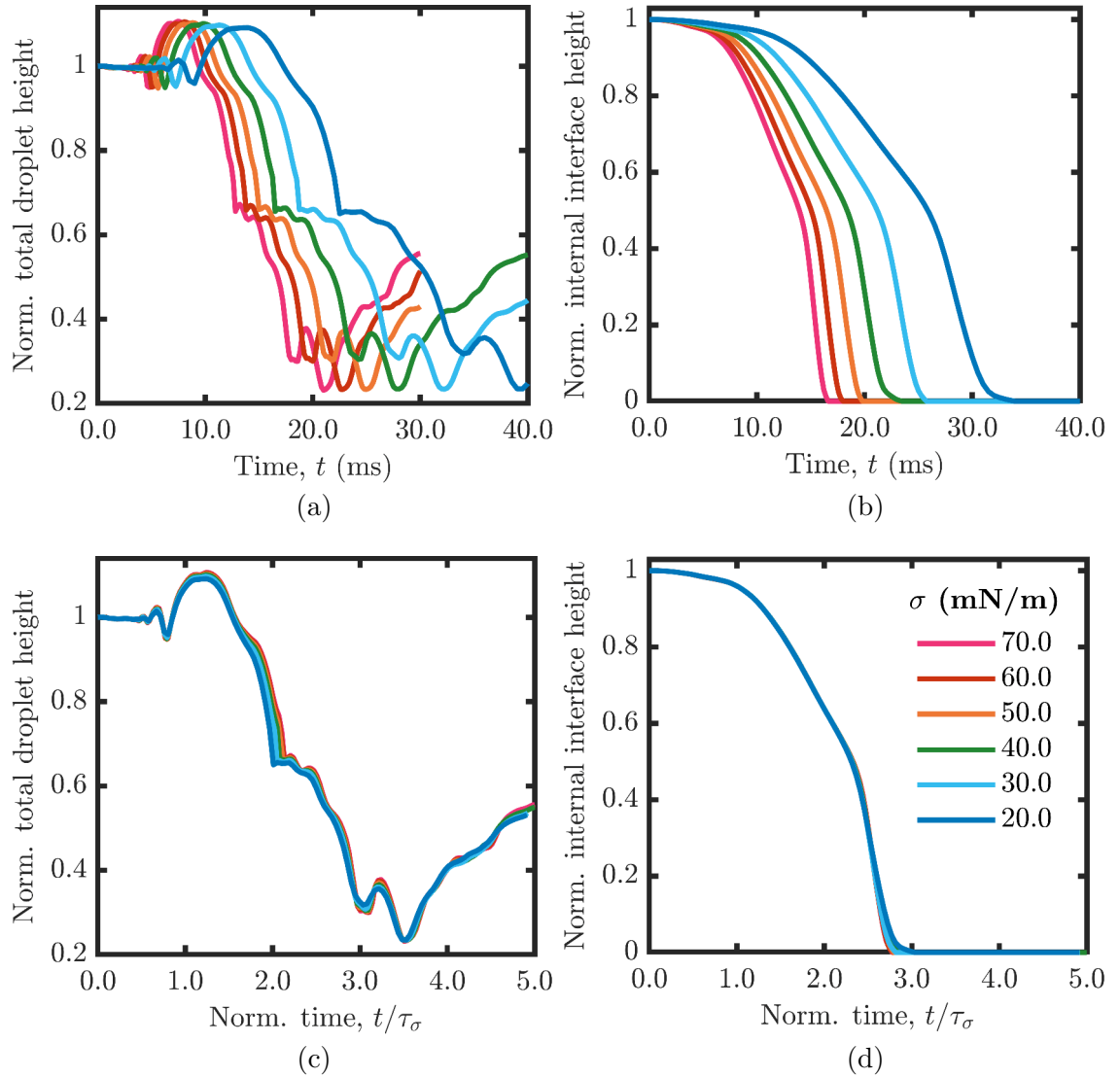


Figure 5.7: Simulations of free and sessile droplet coalescence, with surface tension, σ varied. For $\sigma \in [20.0, 70.0]$ mN m^{-1} , $\text{Oh} \in [0.003, 0.006]$ and $\tau_\sigma \in [6.0, 11.2]$ ms. For all simulations, $\theta_a = 100^\circ$, $\theta_{\text{eq}} = 90^\circ$, $\theta_r = 80^\circ$, $V_s = 7.0 \mu\text{L}$ and $V_f = 10.5 \mu\text{L}$.

5.3.2 Surface tension

In this section, the effect of varying surface tension on the internal and external dynamics of free-sessile droplet coalescence is investigated. All fluid properties except surface tension are fixed, assuming values consistent with those of water (see Section 5.1.1), whilst the other parameters are $\theta_a = 100^\circ$, $\theta_{\text{eq}} = 90^\circ$, $\theta_r = 80^\circ$, $V_s = 7.0 \mu\text{L}$ and $V_f = 10.5 \mu\text{L}$. Surface tension is varied such that $\sigma \in [20.0, 70.0]$ mN m^{-1} , leading to $\text{Oh} \in [0.003, 0.006]$, with r_f being the length scale underpinning the latter.

The total droplet and internal interface heights, both normalised by their values at $t = 0.0$ ms, are plotted in Figure 5.7 – against dimensional time in Figures 5.7a and 5.7b, and time non-dimensionalised by the inertial time scale in Figures 5.7c and 5.7d. Decreasing surface tension leads to slower dynamics, but all data collapse almost exactly onto a single

curve when both axes are non-dimensionalised (Figures 5.7c and 5.7d), which confirms that the dynamics proceed on an inertial time scale for all surface tensions considered. Note however that there is not precise overlap between the curves (most noticeable in regions of most rapid change), which is expected due to the variation of Ohnesorge number, though it is clear that the dynamics do not materially change with respect to τ_σ for the range of surface tensions considered. However, in Chapter 6 it is shown for similar simulations with varying droplet viscosity ($\mu_d \in [1.2, 2.2]$ mPa s) that substantial changes in the internal dynamics can arise. Equivalent absolute changes in μ_d thus tend to be more significant than those in σ , since $\text{Oh} \propto \mu_d$ whilst $\text{Oh} \propto \sigma^{-1/2}$, τ_σ is a function of σ but not μ_d , and changing μ_d not only affects the Ohnesorge number but also the droplet/outer fluid viscosity ratio (see the next section).

As seen in Figures 5.7a and 5.7b, varying the surface tension greatly varies the time scale of the dynamics. Hence, for droplets on a scale at which molecular diffusion – which acts on a time scale $\sim l^2/D$, where l is the characteristic length scale and recall from Equation (2.12) that D is the diffusivity – is significant, the increased time over which diffusion has to act may alter the mixing dynamics, though changing the droplet viscosity (assuming that the flow is surface-tension-dominated) has no such effect. Hence, absolute changes in σ may be more significant than those in μ_d for small droplets due to the action of molecular diffusion, assuming that the shorter length scale does not push the dynamics out of the range over which the inertial time scale is prevalent.

5.3.3 Outer fluid

For microfluidic channels, it is known that the outer fluid properties (notably the viscosity, μ_o) can influence the internal dynamics of coalescing droplets, and hence that μ_d/μ_o is an important parameter in determining the flow (Nowak et al., 2016). Here, the effect of the outer fluid is characterised for free-sessile droplet coalescence in Figure 5.8 by varying μ_o through two orders of magnitude from the typical value of 1.8×10^{-5} Pa s (i.e. that of air). An increase of one order of magnitude has almost no influence on both the external and internal dynamics, whilst an increase to 1.8×10^{-3} Pa s results in significant changes, with a lack of a rapid decrease in the internal interface height seen – using the terminology of Chapter 6, the internal dynamics are ‘transitional’, whilst a jet forms in the two other cases. It is therefore important to consider the outer fluid properties here as in microfluidic channels, though it is clear that smaller changes in such values do not necessarily lead to large changes in the dynamics. In particular, similar dynamics are likely to be seen for most gases, with the outer fluid therefore playing a minimal role on the flow. This observation rationalises the lack of sensitivity to both mesh resolution outside the droplet (Section 5.2.1) and domain size (Section 5.2.2) seen. Whilst it may be tempting to conclude that gases have no influence on coalescence dynamics, as noted in Section 4.5.2 numerical artefacts (such as toroidal bubbles) can arise if the outer fluid is treated as inviscid and dynamically passive in simulations.

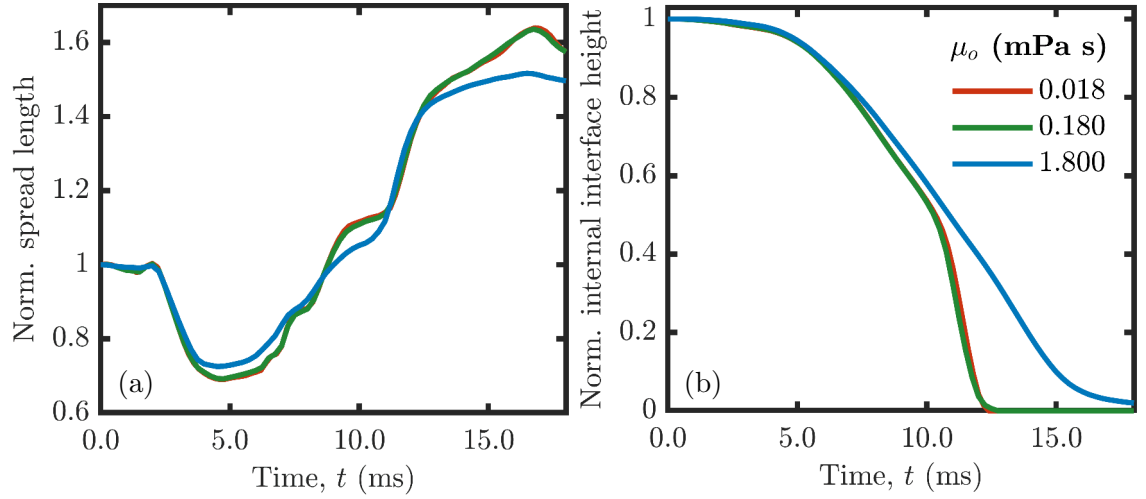


Figure 5.8: Simulations of free and sessile droplet coalescence with the outer fluid viscosity, $\mu_o \in [0.018, 1.800]$ mPa s varied. For all simulations, $\theta_a = 100^\circ$, $\theta_{eq} = 90^\circ$, $\theta_r = 80^\circ$, $V_s = 4.0 \mu\text{L}$ and $V_f = 6.0 \mu\text{L}$.

5.4 Summary

This chapter has briefly described and elucidated the dynamics of free and sessile droplet coalescence, including the effects of capillary waves, time and surface tension. More importantly though, the results presented comprise numerical verification of the customised solver and simulation setup for the specific droplet configuration of interest in this work. Hence, there is significant confidence in the numerical simulations such that they can be deployed for predictive and analytical purposes in the next chapter, where quantitative and qualitative comparisons to the experiments described in Chapter 3 are also be made.

Chapter 6

Internal jets

This chapter considers the effect of substrate wettability on internal jet formation during the coalescence of initially-static free and sessile droplets. Indeed, substrate wettability has been the subject of surprisingly few studies concerning droplet mixing despite its importance in a wide range of applications, especially in additive manufacturing-based technologies which often rely on printing onto materials of varying wettability. Droplet volume ratio and fluid properties are also considered to yield a more detailed exposition of the dynamics. Most of the content in this chapter has been published in Sykes et al. (2020b), though significantly more detail, and many additional results, are given here.

6.1 Introduction

As described in Section 2.4, a desirable way to improve advective mixing is through the formation of an internal jet that stretches and folds the internal fluid interface. Internal jets in coalescing droplets not in contact with a substrate (free droplets) have been studied extensively, with their properties and dynamics primarily determined by Laplace pressure differences as explained in Section 2.1.5 (Anilkumar et al., 1991; Eiswirth et al., 2012). As the kinetic energy of internal jets is inherited from excess free surface energy, jet formation relies on the flow being dominated by surface tension (Liu et al., 2013b). Given a sufficient increase in Ohnesorge number, enough surface energy can be eliminated by viscous dissipation that the smaller droplet is simply lodged into the larger droplet with little advective mixing (Nobari and Tryggvason, 1994). Recently, jet formation in free droplets has been associated with the formation of a vortex ring, where growth and eventual detachment are both required, after which the vortex ring must have sufficient momentum to overcome viscous dissipation for a jet to form (Xia et al., 2017).

Internal jets can be seen in other cases too, such as colliding droplets where jet emergence has a non-trivial relationship with velocity (Tang et al., 2016). Another example is droplet-pool coalescence (the limit of large size ratio) for both slowly coalescing and

impacting droplets (Saha et al., 2019). In these cases, jets may be enhanced by surface tension gradients due to Marangoni flow and the influence of surface tension on Laplace pressure (Nowak et al., 2017; Luo et al., 2019). Hence, a size difference between coalescing droplets of different fluids is not necessarily required for jet formation.

There is limited study of internal jet formation in the presence of a substrate, though as mentioned in Section 2.4 a jet can be formed during the coalescence of an impacting and a sessile droplet if the latter is much larger. When a substrate is involved, there is the added aspect of a three-phase contact line which can affect the flow (Narhe et al., 2004). Several studies have considered internal flows within coalescing sessile droplets on a substrate with a wettability gradient, which can enhance mixing (Castrejón-Pita et al., 2013). Motion of the contact line during coalescence has been shown to be beneficial for mixing by inducing jet-like horizontal recirculatory flow for both identical and distinct fluids (Lai et al., 2010; Yeh et al., 2013). However, a recent numerical study has indicated mixing is not enhanced by a wettability gradient for simultaneously deposited droplets with non-zero lateral separation (Raman, 2018), emphasising the dependence of mixing on the initial droplet configuration.

Dynamic contact angles also play a role in mixing on substrates with uniform wettability. Internal flows have been considered between impacting droplets with varying lateral separation and (fixed) non-zero hysteresis, but little mixing was observed (Raman et al., 2016). For initially sessile, sliding droplets on superhydrophobic substrates, low contact angle hysteresis enhances the rate and extent of mixing due to increased droplet oscillation and deformation compared to high hysteresis substrates (Nilsson and Rothstein, 2011). However, Nilsson and Rothstein compared only two substrates (of 3° and 50° hysteresis) and measured the extent of mixing rather than determining the internal dynamics. In particular, though dynamic contact angles have recently been shown to be important in determining droplet dynamics during splashing (Quetzeri-Santiago et al., 2019), there is a lack of a systematic study of their effect on mixing during coalescence. Moreover, recall from Table 2.1 (on page 39) that no numerical studies have considered the effect of substrate wettability on mixing, except for substrates with a wettability gradient.

In this chapter, the influence of substrate wettability on internal jet formation during the coalescence of an initially-static free droplet with a sessile droplet of the same fluid is systematically studied for the first time, using both high-speed imaging and numerical simulations. The customised solver introduced in Chapter 4 is used for this study, whilst numerical verification of this solver for the droplet configuration of interest was undertaken in Chapter 5. The experimental procedure (described in Section 3.4) ensures that the droplets are dominated by surface tension and have negligible velocity at the onset of coalescence. Hence, the influence of capillary waves reflected from the contact line on the internal flow and jet formation are determined in tandem with the effect of volume ratio and droplet fluid properties. Throughout, careful comparison to the more widely studied free droplet coalescence is made to elucidate the differences caused by the substrate.

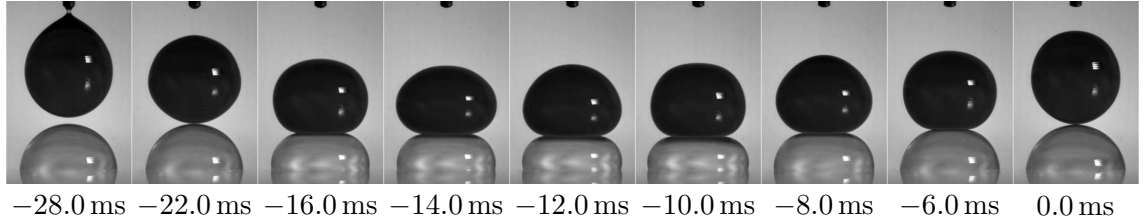


Figure 6.1: Image montage illustrating the bouncing dynamics that generate the effectively static initial condition for free-sessile droplet coalescence.

6.2 Experimental observations

6.2.1 Initial condition

The experimental results in this chapter are derived from the free and sessile droplet experimental setup described in Section 3.4. Recall that only water was used as a fluid in these experiments, with the free droplet formed by gravity-induced detachment from a dispensing tip directly above an already-deposited sessile droplet. As seen in Figure 6.1, coalescence did not occur immediately after the free droplet landed. Instead, the free droplet slowly bounced on a trapped air layer that was sufficiently thick to prevent intermolecular (van der Waals) forces from causing it to instantly rupture, delaying coalescence (Al-Dirawi and Bayly, 2019). Viscous dissipation reduced the minimal initial kinetic energy during this time. After one bounce, the high surface tension recovered the original spherical droplet shape and coalescence was initiated at the point of separation, which defines the initial condition for coalescence (Berry and Dagastine, 2017). The relative droplet velocity was estimated to be $\ll 5 \times 10^{-2} \text{ mm ms}^{-1}$ at this time, which is sufficiently small that any remaining kinetic energy was dominated by meniscus bridge growth post-coalescence (Zhang et al., 2009). Hence, the initial condition is effectively two static droplets, where the free droplet was not attached to any structure which would influence the ensuing intricate free surface dynamics. Time zero ($t = 0.0 \text{ ms}$) is taken as the frame immediately before the air layer visibly ruptured.

To achieve bouncing as seen in Figure 6.1, the flow was required to be surface tension dominated (thus only water was used), whilst the substrate needed to have a high contact angle hysteresis so as to ensure that the contact line of the sessile droplet remained pinned and the sessile droplet regained its initial spherical cap shape at the onset of coalescence. Bouncing (rather than immediate coalescence) was desirable since it minimised the initial kinetic energy of the free droplet to match the static initial condition used in the simulations – the importance of minimisation of initial kinetic energy is discussed in relation to the forthcoming Figure 6.3 on page 118.

6.2.2 Fluid properties

The Ohnesorge number, with the length scale chosen as the free droplet radius ($r_f \approx 1.14\text{ mm}$), is $\text{Oh} \approx 3.2 \times 10^{-3}$. This value indicates that the flow was dominated by surface tension. The corresponding Bond number is $\text{Bo} = 0.18$. Furthermore, it was observed that the sessile droplet forms a spherical cap for moderate volumes ($\leq 10\ \mu\text{L}$), confirming that surface tension dominates gravitational forces and the dynamics can be appropriately modelled without including gravity.

6.2.3 Droplet volume ratio

Figure 6.2 shows a montage of experiments for four different sessile droplet volumes, with a fixed free droplet volume of $V_f = 6.2\ \mu\text{L}$. As elucidated for the simulations described in Section 5.1.2, in each case rapid widening of the meniscus bridge between the coalescing droplets generates capillary waves that propagate outwards along the free surface, both towards the top of the coalesced droplet and towards the substrate. The upward travelling capillary waves converge at the top of the droplet (visible at $t = 3.0\ \text{ms}$), where they stretch the free surface upwards to form a tall cylindrical column (visible at $t = 6.0\ \text{ms}$). Due to the excess surface energy and higher internal pressure acquired, the column subsequently collapses towards the substrate to form a sessile droplet of lower surface energy (Xia et al., 2017). Free surface oscillations are initially large due to the substantial conversion of surface energy to kinetic energy, but subsequently reduce due to viscous dissipation.

The dye added to the free droplet allows the internal dynamics to be visualised. In Figure 6.2a, where $V_s = 3.9\ \mu\text{L}$, the coalesced droplet flattens after column collapse to a pancake shape (visible at $t = 12.0\ \text{ms}$) at its maximum spread length, but subsequently recoils to reveal a flat internal interface at $t = 25.0\ \text{ms}$. Any advective mixing is insignificant, so the subsequent diffusive mixing stage required to homogenise the coalesced droplet could be on the order of minutes (see Section 1.2). However, on increasing the sessile droplet volume to $V_s = 5.5\ \mu\text{L}$ in Figure 6.2b, a vertical flow of dyed fluid into the undyed fluid below is visible at $t = 15.0\ \text{ms}$, which quickly develops into an internal jet. The jet appears to be slightly offset in Figure 6.2b due to slight asymmetry in the initial condition, but its presence is a consistent feature of multiple repeated experiments. Moreover, the jet is maintained on increasing the sessile droplet volume to $V_s = 11.0\ \mu\text{L}$ and $V_s = 17.0\ \mu\text{L}$ in Figures 6.2c and 6.2d, respectively. In the latter two cases, the jet encompasses a greater volume of the undyed fluid, yielding a disproportionately larger internal interface with respect to the increase in sessile droplet volume, which can be considered to be improved advective mixing.

Figure 6.2 demonstrates a significant difference between internal flows in configurations involving sessile droplets and those with only free droplets. Indeed, in Figure 6.2b the larger volume droplet is injected into the other to form a jet, which is opposite to the

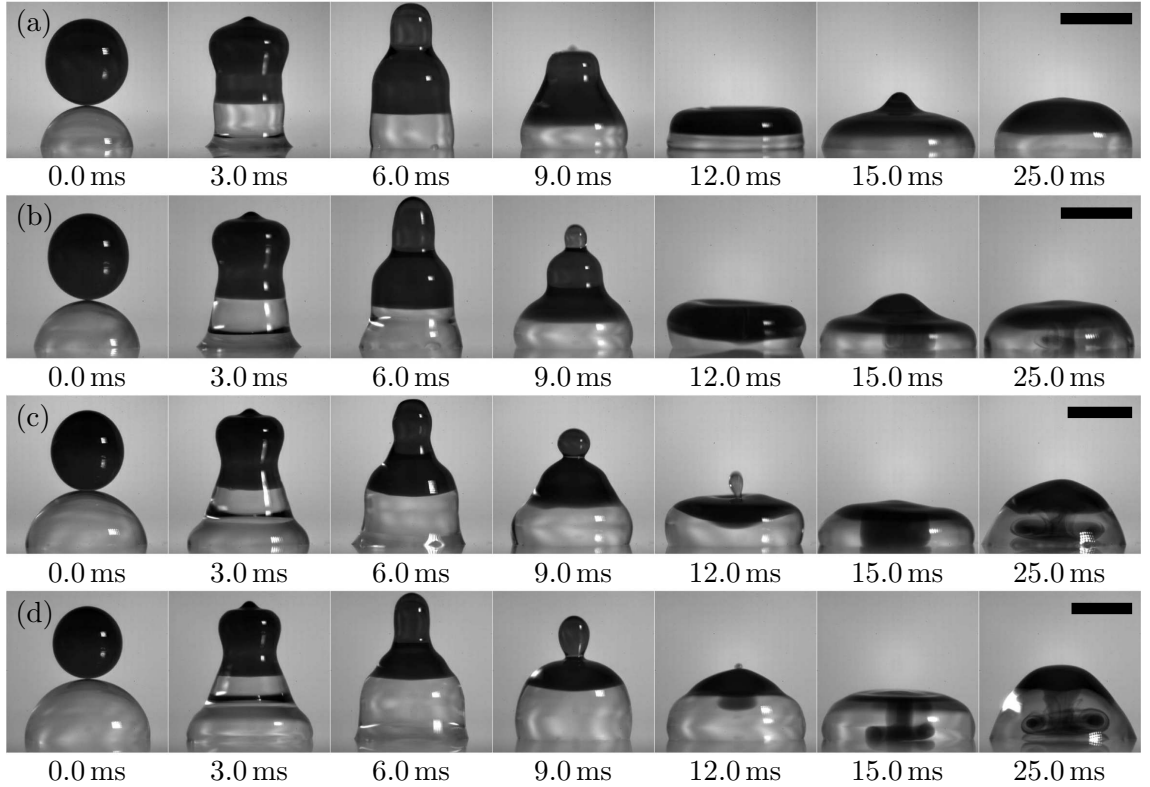


Figure 6.2: Front views of coalescence between a dyed free droplet and an undyed sessile droplet of the same fluid. The free droplet volume is fixed ($V_f = 6.2 \mu\text{L}$) whilst the sessile droplet volume is varied between panels: (a) $V_s = 3.9 \mu\text{L}$; (b) $V_s = 5.5 \mu\text{L}$; (c) $V_s = 11.0 \mu\text{L}$; (d) $V_s = 17.0 \mu\text{L}$. An internal jet is seen only in the latter three panels. All scale bars are 2.0 mm.

typical situation in free droplet coalescence (see Section 4.6). Indeed, the sessile droplet has a lower curvature (and smaller Laplace pressure) at the onset of coalescence than if the substrate were not present, for the fixed volume. Furthermore, the jets seen in Figure 6.2 do not appear to be of the vortex-ring kind seen in free droplets (see e.g. Xia et al., 2017), but are instead reminiscent of an impinging jet, with the substrate redirecting the downward flow to drive recirculation. The presence of the substrate may therefore enhance internal jet formation, potentially enabling good advective mixing for smaller droplet volumes than would otherwise be expected.

There are clearly several contributory factors to jet formation in Figure 6.2. With an increase in sessile droplet volume, the curvature between the droplets at the onset of coalescence is greater, which leads to stronger capillary waves (Deka et al., 2019). Hence, greater stretching of the coalesced droplet is observed with increasing sessile droplet volume, leading to a larger excess surface energy that can be translated into kinetic energy to form a jet. Sufficient vertical space is also required in the undyed fluid for a jet to form; this space is of course expanded by increasing the sessile droplet volume. Importantly, the high substrate hysteresis also delays outward spreading of the droplet during column collapse, which increases the height of the internal interface within the coalesced droplet. Separately, wettability also affects the interaction between the substrate and the downward

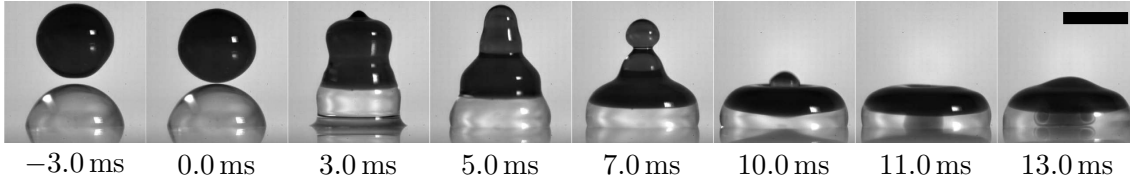


Figure 6.3: Front views of coalescence between a dyed free droplet and an undyed sessile droplet of the same fluid, where coalescence occurs as soon as the droplets collide, i.e. the initial condition is *not formed by bouncing* (only in this figure). $V_f = 6.2 \mu\text{L}$ and $V_s = 5.5 \mu\text{L}$. The scale bar is 2.0 mm.

propagating capillary waves, which may influence jet formation too. The effect of substrate wettability is particularly interesting, but consistently varying the limiting advancing and receding contact angles (θ_a and θ_r) whilst maintaining the initial static contact angle would be experimentally challenging. Moreover, high contact angle hysteresis is required for the bouncing initial condition as identified above. Hence, substrate wettability is varied in the numerical simulations starting in Section 6.4 instead.

6.2.4 Revisiting the initial condition

Before discussing the simulations, the initial condition for the experiments (preceded by bouncing and indicated in Figure 6.1) is first briefly reconsidered. As is clear from Figure 6.1, the height from which the free droplet is released is very small, so it is perhaps tempting to think that the free droplet could be considered initially static even if coalescence occurred immediately on collision, without bouncing. By slightly raising the height of the capillary from which the free droplet detaches, increasing the free surface separation by less than 20% at detachment compared to Figure 6.2b, coalescence can be achieved without bouncing whilst maintaining the droplet volumes, as seen in Figure 6.3.

The undissipated inertia of the free droplet in Figure 6.3 leads to faster expansion of the meniscus bridge compared to the equivalent experiment in Figure 6.2b, as is clear from the $t = 3.0$ ms frame. Moreover, the capillary waves triggered by detachment from the capillary in Figure 6.3 (clearly visible in the $t = -3.0$ ms frame) disturbs the propagation of capillary waves emanating from meniscus bridge growth post-coalescence. Hence, without bouncing, the increased vertical stretching and faster onset of column instability (see the $t = 7.0$ ms frame) lead to faster dynamics, but consistent with the equivalent bouncing case an internal jet is seen. Indeed, the bouncing dynamics used to generate the initial condition allow the inertia and capillary waves (due to detachment) of the free droplet to be almost completely dissipated before the onset of coalescence, yielding an effectively static initial condition. Comparing Figures 6.2b and 6.3, it is clear that bouncing is necessary to consider the droplets effectively static at the onset of coalescence and therefore justify the use of a zero velocity initial condition in the numerical simulations. A seemingly small free droplet velocity at the onset of coalescence, coupled with strong undissipated capillary waves, can have a significant influence on the surface-tension-driven dynamics.

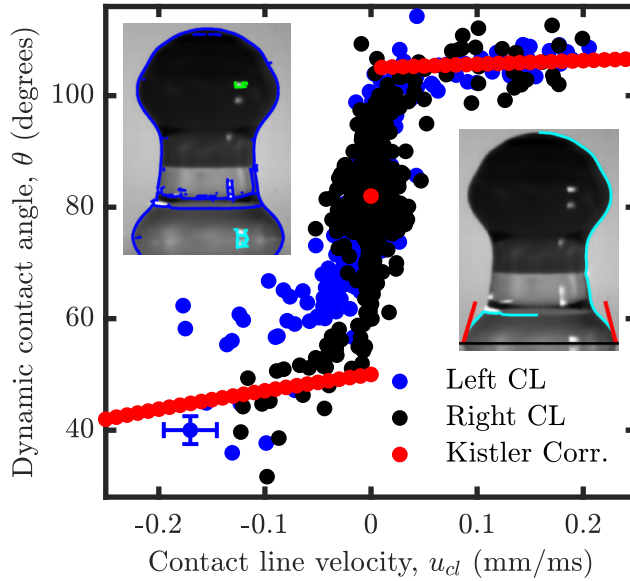


Figure 6.4: Image-processed contact angles against contact line velocity, the latter approximated from the evolution of spread length. Inset images show detected edges and tangents to contact lines on the $t = 2.0$ ms frames. Experimental error bars are omitted from all but one point (bottom left).

6.3 Comparisons to numerical simulations

The purpose of this section is to validate the numerical simulations against the previously seen experiments, and further explore their dynamics, before the substrate wettability is modified. First though, the substrate properties in the experiments will be compared to the dynamic contact angle model used in the simulations.

6.3.1 Substrate wettability

To assess the substrate wettability, contact angles were extracted from a typical free-sessile droplet coalescence experiment by image processing as detailed in Chapter 3. The contact angles are plotted in Figure 6.4 against contact line velocity, the latter approximated by forward-differencing the spread length at the temporal resolution of the camera (6000 FPS). An example of a processed frame (at $t = 2.0$ ms, where the left and right measured contact angles are $73.5^\circ \pm 2.0^\circ$ and $75.5^\circ \pm 2.0^\circ$, respectively) is inset in Figure 6.4. The left inset image shows the initial detected edges; the right image, filtered edges. The estimated error in the measurement of the dynamic contact angle is $\pm 2.0^\circ$ (combining systematic and random errors of $\pm 1.0^\circ$ each), whilst that of u_{cl} is $\pm 0.03 \text{ mm ms}^{-1}$ based on the spread length and time resolution. The dispersion of the points is otherwise a reflection of variability. The red lines represent the detected tangents at the left and right contact points, from which the contact angles are determined.

Figure 6.4 shows that the substrate has a hysteresis of $\theta_a - \theta_r \approx 50^\circ$, with $\theta_a \approx 105^\circ$. With regard to the receding contact angle, the substrate is best described as being prone to

pinning. Hence, a wider range of receding contact angles are seen in Figure 6.4. It should also be noted that the right contact angle is more amenable to image processing, due to the requisite light position, which accounts for the discrepancy between the left and right contact lines; both the contact angle measurement and perceived contact line position are affected by this. The discrepancy may also be a consequence of slight asymmetry in the initial condition (i.e. a small lateral offset between the free and sessile droplets).

The Kistler model used in the numerical simulations is also shown in Figure 6.4 with $\theta_a = 105^\circ$, $\theta_{eq} = 82^\circ$ and $\theta_r = 50^\circ$ prescribed. Excellent agreement with the experimental data is evident, confirming the applicability of Kistler’s model and the underlying limiting contact angles prescribed. Indeed, the indicated error in the experiments means that the majority of the plotted points are consistent with Kistler’s model. The only appreciable limitation of the Kistler model in the droplet configuration studied is that it does not include pinning, as the contact line velocity determines the contact angle; the lack of pinning turns out to be inconsequential as elucidated when making a quantitative comparison between the experiments and simulations below. Hence, it is confirmed that Kistler’s model properly captures substrate wettability in the numerical simulations reported.

6.3.2 Qualitative assessment

Having validated the dynamic contact angle model, a qualitative comparison is made in Figure 6.5 between the simulations and the two experiments from Figure 6.2 (those for which gravity is certainly negligible). The prescribed advancing and receding contact angles ($\theta_a = 105^\circ$, $\theta_r = 50^\circ$) are consistent with Figure 6.4. To match the pertinent experiments, $\theta_{eq} = 82^\circ$ in Figure 6.5a and $\theta_{eq} = 80^\circ$ in Figure 6.5b. The simulation results display both the free surface (defined by $\alpha = 0.2$) and internal interface (defined by $\beta = 0.2$) profiles and are represented by a cut-plane through the axis of symmetry, whereas the experiments adopt an external front view which causes depressions in the free surface to be somewhat inconspicuous (e.g. at $t = 13.0$ ms in Figure 6.5b).

From Figure 6.5, it is clear that the simulations are in excellent qualitative agreement with the experiments. All the main features are captured accordingly, including the column stretching and subsequent collapse. Some small deviations in the precise free surface profiles are seen, but it should be noted that the simulations are compared to a ‘typical’ experiment, whilst minute variations in the initial condition can lead to small (but otherwise insignificant) discrepancies between each experiment. Nevertheless, the VOF model with an algebraic representation of the interface properties captures complicated dynamics seen in the experiments with remarkable (and perhaps surprising) accuracy. Importantly, the simulations correctly predict the formation of a jet only where one is seen experimentally (i.e. Figure 6.5b). Of special note are the free surface shapes near the contact lines, where excellent agreement between the experiments and simulations is evident – this observation reaffirms the applicability of the dynamic contact angle model utilised.

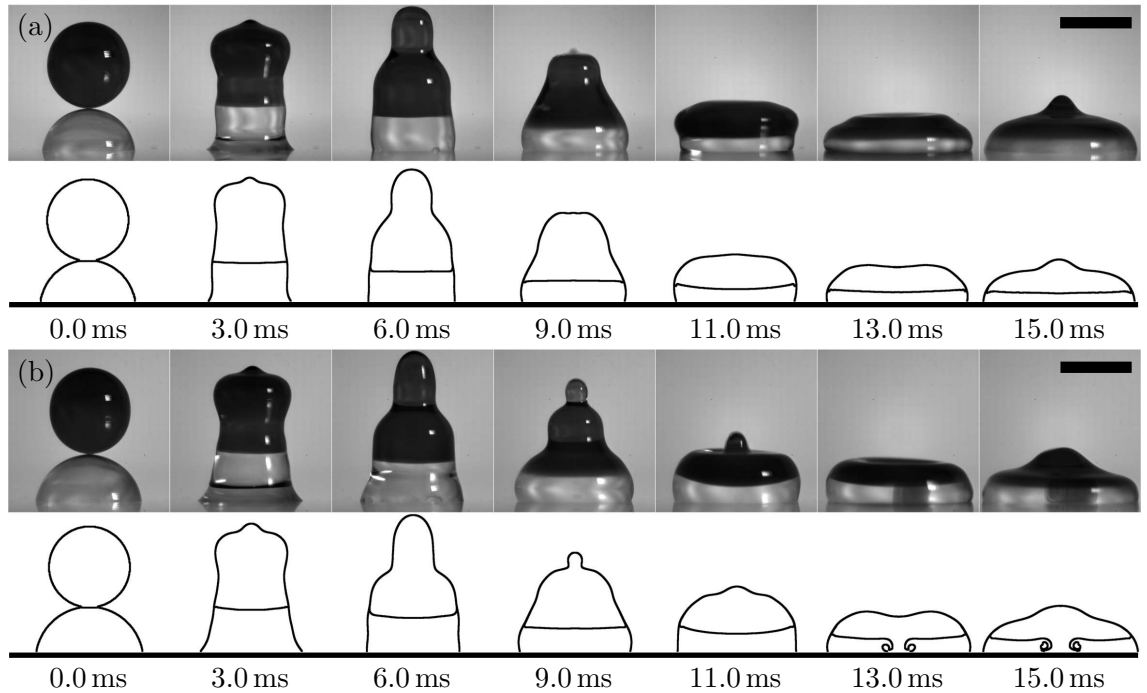


Figure 6.5: Front views of coalescence between a dyed free droplet and an undyed sessile droplet of the same fluid. Free surface and internal interface profiles are shown for the simulations. The free droplet volume is fixed ($V_f = 6.2 \mu\text{L}$) whilst the sessile droplet volume is varied between panels: (a) $V_s = 3.9 \mu\text{L}$, with little advective mixing ($\theta_{\text{eq}} \approx 82^\circ$); (b) $V_s = 5.5 \mu\text{L}$, with an internal jet ($\theta_{\text{eq}} \approx 80^\circ$). For the simulations, $\theta_a = 105^\circ$ and $\theta_r = 50^\circ$ are prescribed. All scale bars are 2.0 mm.

6.3.3 Quantitative analysis

Having confirmed qualitative agreement between the simulations and experiments, further image processing was undertaken on the experiments shown in Figure 6.5 to extract the spread length, s , total droplet height and internal interface height, enabling a quantitative comparison between the experiments and simulations. The results for the experiment shown in Figure 6.5b ($V_s = 5.5 \mu\text{L}$; $V_f = 6.2 \mu\text{L}$), in which a jet materialises, are given in Figure 6.6 together with four simulations assuming a small range of prescribed advancing and receding contact angles ($\theta_{\text{eq}} = 80^\circ$ is fixed) consistent with Figure 6.4. Inset simulation frames are from the series shown in Figure 6.5b ($\theta_a = 105^\circ$; $\theta_r = 50^\circ$). As expected, the greatest differences between the prescribed contact angles arise in the spread length, though very similar features are observed for the four combinations considered which approximately cover the range of experimental values.

The contact line remains approximately pinned, hence the spread length is almost constant, between $t = 3.0 \text{ ms}$ and $t = 8.0 \text{ ms}$ in the experiment, demarcated by the vertical dashed lines in Figure 6.6a. However, once the downward travelling capillary waves reach the contact line at $t \approx 2.0 \text{ ms}$, a reduction in spread length is initiated in the simulations. A decrease in spread length is perhaps counter-intuitive, but emphasises reflection of capillary waves from the contact line and the concurrent upward stretching of the droplet.

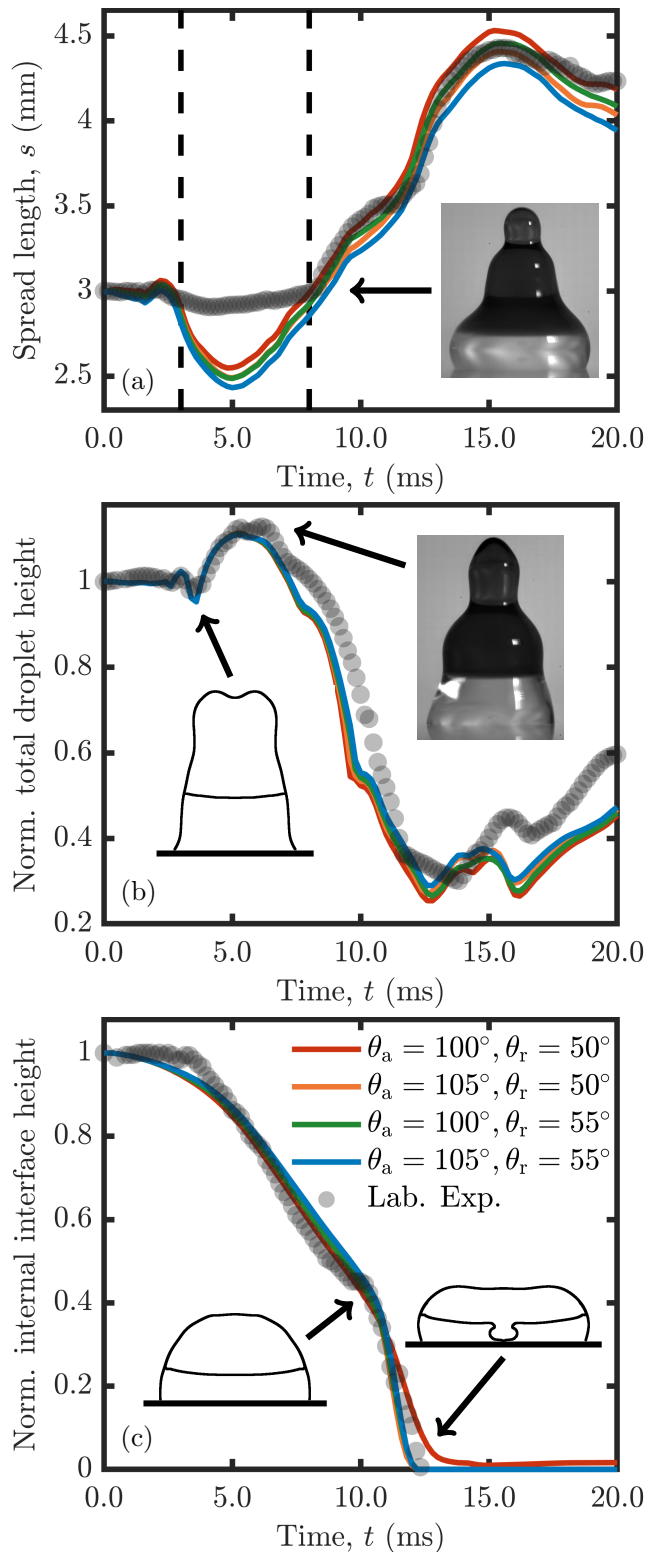


Figure 6.6: Image-processed experiments with $V_s = 5.5 \mu\text{L}$ (corresponding to Figure 6.5b) and simulation results (solid lines). Vertical dashed lines delimit the extent of contact line pinning in the experiments. $\theta_{\text{eq}} = 80^\circ$ in all simulations. Heights are normalised by their value at $t = 0.0$ ms.

As noted in the qualitative comparison above, the free surface shapes near the substrate remain comparable between the experiment and simulations throughout, indicating that the apparent contact angles are similar. However, since pinning is not captured in the Kistler dynamic contact angle model, the contact line recedes in the simulations. The contact line only pins in the experiment at low contact angles, so there is only a small volume of fluid near the contact line. Hence, the spread length in the simulations recovers to yield excellent agreement with the experiment for $t \geq 8.0$ ms, where the spread length quickly increases to its maximum shortly after column collapse has concluded. This agreement indicates that modelling wettability without pinning it is not detrimental to understanding the observed dynamics here.

The total droplet height remains approximately constant in Figure 6.6b until the capillary waves arrive at the top of the droplet (at $t = 3.0$ ms), initiating oscillation before stretching the droplet upwards to form the column. Due to stretching, the maximum height attained is significantly greater than at $t = 0.0$ ms; the droplet subsequently collapses towards the substrate. The rapid decrease in height is slightly delayed in the experiment compared to the simulations due to the aforementioned differences in spreading. There may also be a very small influence here from the slight upward velocity in the experimental initial condition. The rate of collapse temporarily reduces at $t \approx 9.5$ ms in both the experiment and simulations, which coincides with the disappearance of the column, appearing as a shoulder in Figure 6.6b. This shoulder is a consequence of contact angle hysteresis delaying outward spreading and has been seen before for similar droplet configurations but higher Ohnesorge number and lower hydrophobicity (Wang and Sun, 2018). Note that the central depression between $t \approx 11.0$ ms and $t \approx 14.0$ ms cannot be perceived from the external front view for image processing and so appears as a straight line, whereas a dip is correctly seen in the (cut-plane) simulation results. Slightly quicker droplet recoil is seen in the experiment, again due to the differences in spreading. Note that recoil occurs after, and so does not affect, jet formation. In any case, the same features are evident in both the experiment and simulations, demonstrating that the simulations accurately capture the relevant physics.

The internal interface height¹ is shown in Figure 6.6c. Initially, its value decreases due to the elevated Laplace pressure in the free droplet, and continues to decrease at an approximately constant rate as the droplet spreads outwards for $t \geq 5.0$ ms. At $t \approx 10.0$ ms, the rate of decrease increases sharply as the internal jet is formed. Since the minimum internal interface height is generally plotted, once the jet reaches the substrate its value remains zero. Importantly for this study, between the qualitative assessment described above and Figure 6.6c, it is clear that the internal dynamics are captured in the simulations very well. The rate and extent of internal interface height decrease is in quantitative agreement with the experiment considered in Figure 6.6c; internal jet formation is correctly predicted. These observations confirm the applicability of the simulations to study internal jet formation in this configuration.

¹The internal interface height is measured on the axis of symmetry, which is generally where it is lowest.

6.4 Modifying substrate wettability

Having analysed the dynamics of free and sessile droplet coalescence in detail above, and moreover confirmed the applicability of the numerical simulations to study them, the influence of substrate wettability on internal jet formation is now considered.

6.4.1 Changing receding contact angle

To assess the effect of substrate wettability on internal jet formation, Figure 6.7 demonstrates the consequence of increasing the receding contact angle for the experiment shown in Figure 6.5a, for which no jet materialises ($V_s = 3.9 \mu\text{L}$; $V_f = 6.2 \mu\text{L}$). $\theta_a = 100^\circ$ and $\theta_{\text{eq}} = 82^\circ$ are fixed. The image-processed experimental data shows good agreement with the $\theta_r = 50^\circ$ simulation in all three metrics presented.

As the receding contact angle increases, the contact line recedes more freely leading to a greater initial decrease in spread length, as seen in Figure 6.7a. With the associated decrease in contact angle hysteresis, the maximum spread length after column collapse also reduces. The shoulder (temporary reduction in spreading rate) at $t \approx 10.0 \text{ ms}$ also becomes more prominent. These factors combine to hold the droplet up during the vertical stretching phase of the dynamics, before column collapse, which is evident in the total droplet height (Figure 6.7c). Indeed, Figure 6.7c confirms that column collapse is slightly delayed for the largest receding contact angle considered ($\theta_r = 70^\circ$), due to the lower minimum spread length acting to hold the droplet up. Moreover, due to the higher contact angle hysteresis, the shoulder (temporary reduction in the rate of height decrease) during column collapse is more prominent for lower receding contact angles.

The resulting transformation in the internal dynamics seen Figure 6.7b is more dramatic. Whilst no internal jet is formed with $\theta_r = 50^\circ$, increasing the receding contact angle (to $\theta_r = 70^\circ$) destabilises the internal interface to generate a jet, thus dramatically improving advective mixing. The differences in outcome are clear from the inset frames in Figure 6.7, which show the internal interface and free surface profiles at $t = 13.0 \text{ ms}$. Note that the evolution from no jet to jet is not abrupt but occurs over a small range of receding contact angles for which a slow decrease in internal interface height is seen (e.g. for $\theta_r = 60^\circ$); the internal dynamics are considered to be *transitional* over this range of θ_r . A jet is said to have formed only for cases in which an abrupt change in the internal interface height is evident (e.g. for $\theta_r = 70^\circ$).

Having determined that substrate wettability influences internal jet formation, the root cause of this effect is now explored. Clearly, enhanced vertical stretching on increasing θ_r yields a greater excess of surface energy to contribute to jet formation. Figure 6.7b also shows that increasing θ_r holds the internal interface higher during the stretching and initial collapse phases ($t \approx 3.0 \text{ ms}$ to $t \approx 10.0 \text{ ms}$), which has already been identified above

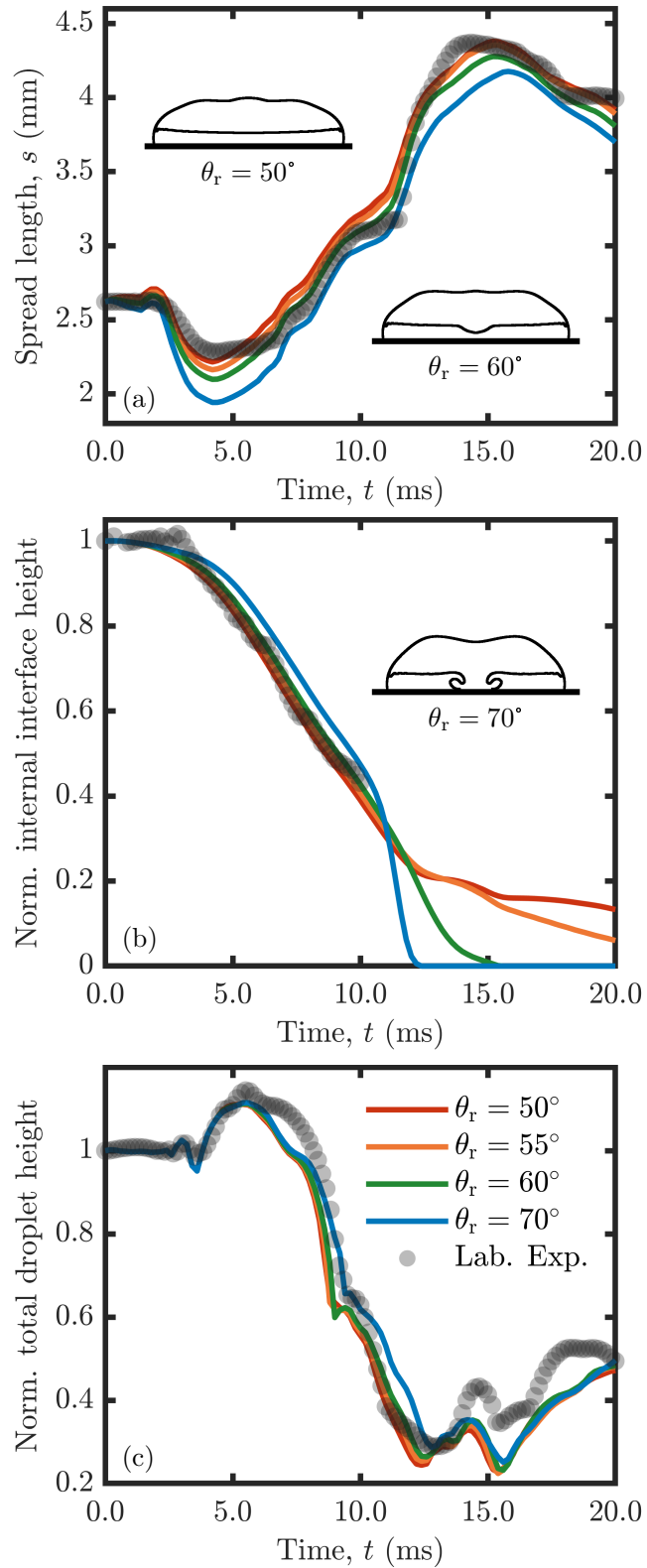


Figure 6.7: Image-processed experiments with $V_s = 3.9 \mu\text{L}$ (corresponding to Figure 6.5a) and simulation results (solid lines). $\theta_a = 100^\circ$ and $\theta_{\text{eq}} = 82^\circ$ in all simulations. Heights are normalised by their value at $t = 0.0$ ms. Inset frames correspond to $t = 13.0$ ms.

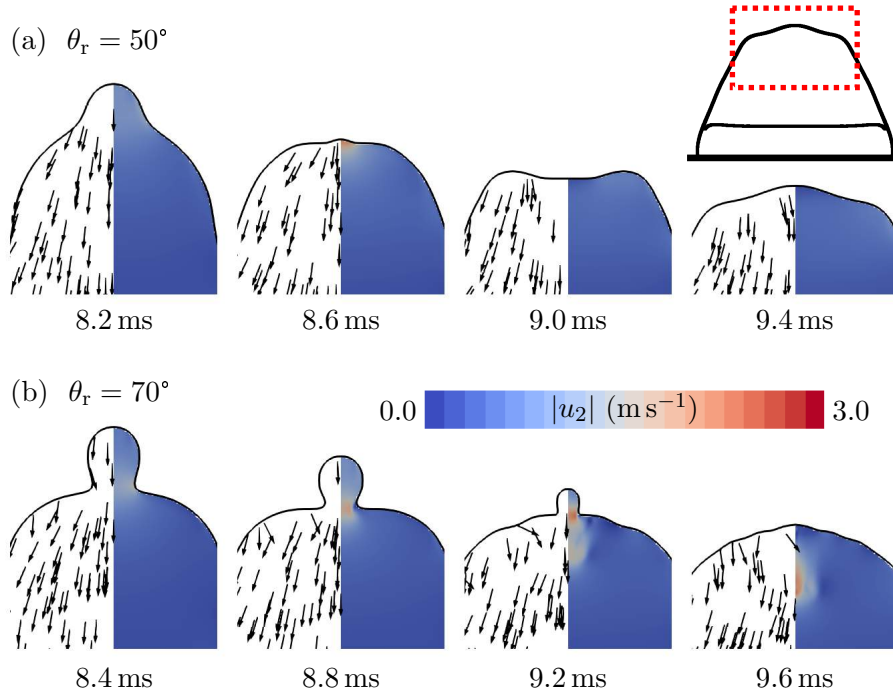


Figure 6.8: Free surface profiles and velocity fields, with $\theta_a = 100^\circ$, $\theta_{eq} = 82^\circ$, $V_s = 3.9 \mu\text{L}$ and $V_f = 6.2 \mu\text{L}$. The dotted red box on the 9.4 ms panel (a) frame (with free and internal interfaces shown) indicates the extent shown in the other frames. Unscaled velocity vectors (left); contour plot coloured by the magnitude of vertical velocity (right). (a) $\theta_r = 50^\circ$, with no jet. (b) $\theta_r = 70^\circ$, with a jet.

as being beneficial for jet formation. However, the change in substrate wettability also influences the propagation of capillary waves which is the key factor, as will be demonstrated in the next section.

6.4.2 Mechanism of jet formation

Tip-generated internal flow

Figure 6.8 shows the free surface profiles and velocity fields at the top of the coalesced droplet, encompassing the end of column collapse, for two of the simulations from Figure 6.7 ($V_s = 3.9 \mu\text{L}$, $V_f = 6.2 \mu\text{L}$, $\theta_a = 100^\circ$ and $\theta_{eq} = 82^\circ$). Unscaled velocity vectors are shown on the left, whilst the contour plot on the right is coloured by the magnitude of vertical velocity, $|u_2|$. No jet is seen in Figure 6.8a, where $\theta_r = 50^\circ$, whilst a jet emerges in Figure 6.8b, where $\theta_r = 70^\circ$.

Only in the case with a jet (Figure 6.8b) does the stretched column thin at its base enough to form a small ‘tip’ on top of the coalesced droplet. The pressure within this tip is elevated due to its high curvature. Together with the constriction at its base, a rapid downward vertical flow is thus generated as the tip drains into the bulk, seen in the 8.8 ms and 9.2 ms frames of Figure 6.8b. This high vertical velocity is maintained in the bulk after

the tip has been absorbed and goes on to generate a jet by impingement on the substrate. In contrast, for the case with $\theta_r = 50^\circ$ (Figure 6.8a), such a tip is not formed. Hence, there is no means to accelerate the downward vertical flow and a jet does not form. The velocity fields near the substrate (in the undyed fluid region) are similar for both cases and quiescent compared to the tip-generated vertical flow, confirming that differences in spreading behaviour on the momentum in this region do not have a significant role in the large-scale internal dynamics. Jet formation here is therefore associated with thinning of the column at its base to form a neck (thus a tip), which wettability evidently influences.

Capillary waves

Similar free surface dynamics to those identified in the previous section have been studied in the context of partial coalescence, where the potential for the tip to pinch-off and form a satellite droplet is of interest. A competition between vertical and horizontal collapse owing to surface tension via capillary waves (rather than the Rayleigh-Plateau instability) determines the extent of neck thinning and potential for pinch-off in droplet-pool coalescence (Blanchette and Bigioni, 2006). In free droplet coalescence, it has recently been shown that capillary waves propagating along the larger droplet, in addition to the smaller droplet where column collapse occurs, affects thinning and pinch-off (Deka et al., 2019). Without a substrate, the capillary waves don't typically reach the apex of the larger droplet before pinch-off occurs (Zhang et al., 2009), but capillary waves can be reflected away from a substrate and thus influence the dynamics. Note that the numerical work here is restricted to cases in which the neck eventually expands to prevent pinch-off; partial coalescence was not seen in the experiments presented above (but satellite droplet formation was seen for much larger sessile droplets – see the forthcoming Figure 6.13 on page 133). Nevertheless, the influence of capillary waves on neck thinning can be determined from the pressure field in a similar way to partial coalescence studies.

Figure 6.9 shows contour plots on the right of the droplets, coloured by pressure, together with unscaled velocity vectors on the left, for the two cases in Figure 6.8. Recall that a jet materialises only when $\theta_r = 70^\circ$ here. The upward travelling capillary waves from meniscus bridge expansion generate the column as previously discussed, whilst the downward travelling capillary waves are reflected from the substrate at $t \approx 2.0$ ms. By $t = 4.0$ ms, the leading reflected capillary wave is already propagating back up the free surface, seen as a region of positive free surface curvature near the intersection between the internal interface and free surface in both Figures 6.9a and 6.9b. The leading reflected capillary wave is more prominent in Figure 6.9b due to the lower contact angle reduction required for contact line movement (i.e. less energy is dissipated) and the resulting greater reduction in spread length compared to Figure 6.9a. In each case, the leading reflected capillary wave subsequently interacts with the region of negative curvature at the base of column; the interaction is delineated by black dotted boxes at $t = 5.0$ ms. The reflected capillary waves prevent the negative curvature from propagating further down the free

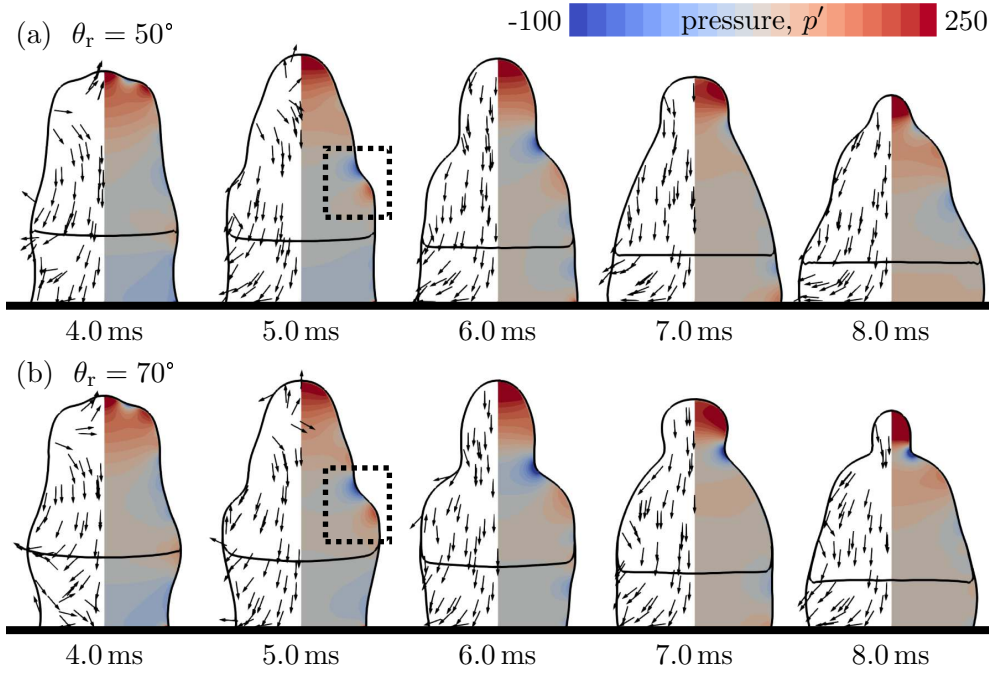


Figure 6.9: Free surface and internal interface profiles where $\theta_a = 100^\circ$, $\theta_{eq} = 82^\circ$, $V_s = 3.9 \mu\text{L}$ and $V_f = 6.2 \mu\text{L}$. Unscaled velocity vectors (left); contour plot coloured by the modified pressure, p' (right). The black dotted boxes highlight capillary wave interactions. (a) $\theta_r = 50^\circ$, with no jet. (b) $\theta_r = 70^\circ$, with a jet.

surface and dissipating. Instead, the interaction enhances the negative curvature at the base of the column and thus intensifies horizontal collapse. However, the intensity of the low pressure region behind the negative curvature, and thus the rate of horizontal collapse, depends on the strength of the reflected capillary waves. For the lower receding contact angle (Figure 6.9a), vertical collapse overcomes the concurrent horizontal collapse before the neck thins enough for a tip to form. For the higher receding contact angle (Figure 6.9b), an intense low pressure region is maintained which leads to sufficient horizontal collapse for a tip to form, though the rate of horizontal collapse is not enough to cause pinch-off. The substrate wettability therefore directly influences the ability to form a tip at the top of the droplet via capillary waves, and thus the ability for a jet to form.

Confirming the influence of reflected capillary waves

In the context of partial coalescence, several numerical studies have confirmed the influence of capillary waves within a particular region by zeroing the velocity field there after a given time and restarting the simulation (Blanchette and Bigioni, 2006; Deka et al., 2019). The effect of this process is to nullify the capillary waves in that region. Notably, Blanchette and Bigioni were able to confirm the mechanism underpinning satellite formation and partial coalescence using this method. Here, the zeroing method is utilised in order to confirm the influence of reflected capillary waves suggested above.

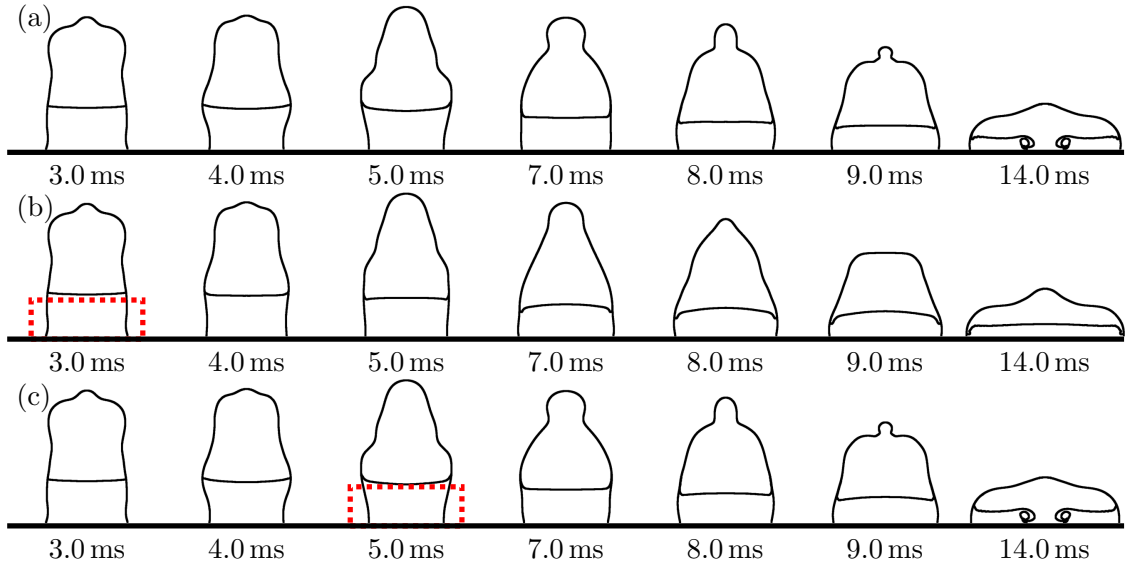


Figure 6.10: Free surface and internal interface profiles where $\theta_a = 100^\circ$, $\theta_{eq} = 82^\circ$, $\theta_r = 70^\circ$, $V_s = 3.9 \mu\text{L}$ and $V_f = 6.2 \mu\text{L}$. Panels (b) and (c) show the same simulation as panel (a), but have their velocities zeroed within 1 mm of the substrate (delineated by the red dotted boxes) at (b) $t = 3.0$ ms; (c) $t = 5.0$ ms.

The simulation considered in Figure 6.9b, in which a jet usually emerges, is taken as the baseline. Free surface and internal interface profiles from this case are displayed in Figure 6.10a. With the results shown in Figure 6.10b, this simulation was repeated and stopped at $t = 3.0$ ms, just after the leading capillary wave had been reflected from the contact line. The velocity field was zeroed within 1 mm of the substrate (which is below the original sessile droplet height), delineated by the red dotted box in Figure 6.10b, and the simulation restarted. As is seen in Figure 6.10b, no jet was seen in the restarted simulation, with free surface dynamics similar to Figure 6.9a materialising. Consistent with the inference above, a tip was not formed. This result provides further evidence both to the requirement for capillary wave reflection to form the aforementioned small tip, and the tip's influence on jet formation.

The zeroing exercise was repeated for various different times; no jet was observed for interruption times of $t = 2.0$ ms and $t = 4.0$ ms either. However, for interruption times of $t = 5.0$ ms (shown in Figure 6.10c) and greater, a jet forms as in the undisturbed simulation. From the free surface profile and pressure distribution of the undisturbed simulation (Figure 6.9b), the leading reflected capillary wave passes the 1 mm mark between $t = 4.0$ ms and $t = 5.0$ ms, which explains the concurrent transition in jet existence. These tests corroborate the correlation between capillary wave reflection, tip generation and jet formation, thus giving further support to the conclusions made above.

Further information can be derived from quantitative measures as shown in Figure 6.11. For the earlier interruption times, a smaller initial spread length reduction is seen in Figure 6.11a due to the contact line being paralysed when the velocity near the substrate is zeroed. However, the zeroing time is typically sufficiently long after the leading

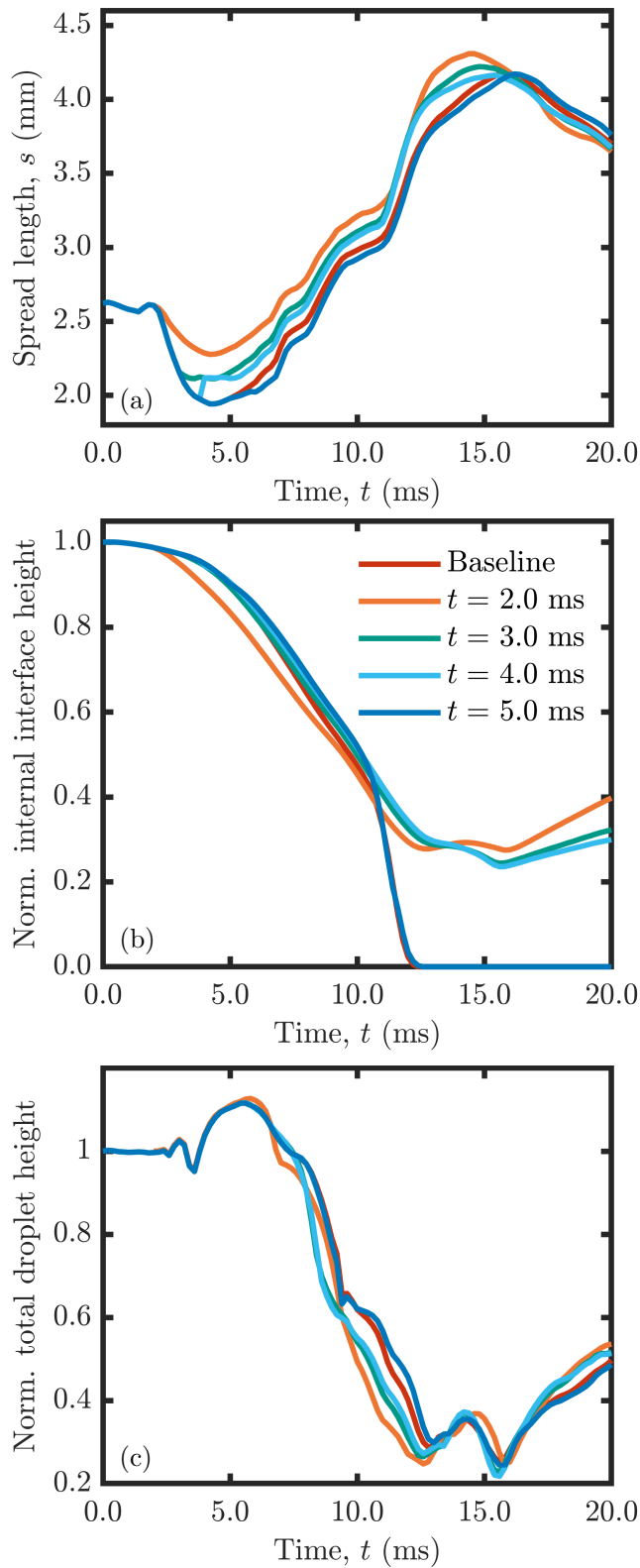


Figure 6.11: Simulations results, where the velocity is zeroed within 1 mm of the substrate at the specified times (baseline simulation was uninterrupted) to determine the influence of reflected capillary waves – see Figure 6.10 for selected frames. The legend indicates the zeroing times. Here, $\theta_a = 100^\circ$, $\theta_{eq} = 82^\circ$, $\theta_r = 70^\circ$, $V_s = 3.9 \mu\text{L}$ and $V_f = 6.2 \mu\text{L}$.

capillary wave has been reflected (at least for $t \geq 3.0$ ms zeroing times) that the subsequent contact line dynamics are not generally a concern for the free surface profile on top of the coalesced droplet. The internal flows are represented in Figure 6.11b, showing that during the stretching and initial collapse phases (from $t \approx 3.0$ ms to $t \approx 10.0$ ms) the internal interface heights are similar, except for the simulation zeroed at $t = 2.0$ ms. However, no jet is formed with any of the 2.0 ms, 3.0 ms and 4.0 ms zeroing times, which confirms that internal jet formation is not solely/mainly due to the space available in the lower fluid. Finally, Figure 6.11c demonstrates that with reduced initial contact line retraction (i.e. earlier interruption times), the aforementioned shoulder during the collapse phase of the dynamics becomes less prominent, since outward spreading is initiated sooner. Indeed, the zeroing process has a similar effect to reducing θ_a (in accelerating outward spreading), and so reducing contact angle hysteresis, which was identified above as being associated the formation of the shoulder (see Section 6.3.3).

Momentum concentration

Another factor which could plausibly contribute to jet formation is concentration of momentum due to the reduction in spread length seen when increasing θ_r ; similarly, outward spreading (enhanced for low θ_a) may suppress momentum. From Figure 6.8b, it is clear that significant momentum is imparted from the top of the coalesced droplet rather than the bottom, where quiescent flow exists. Hence, it is expected that momentum modification by spreading does not have an appreciable role in determining jet formation compared to reflected capillary waves.

To thoroughly test this inference, simulations were conducted with combinations of both zeroing velocity (nullifying reflected capillary waves) and modifying the prescribed limiting advancing contact angle to separate the effects of capillary wave reflection and spreading on momentum concentration/suppression. Recall from Figure 6.11 that switching reflected capillary waves off at $t = 4.0$ ms for simulations that usually yield an internal jet (i.e. that shown in Figure 6.10a) means that a jet does not form, even though the spreading behaviour is similar to the undisturbed simulation – see the red and orange lines in Figure 6.12. Now, rather than switching reflected capillary waves off at $t = 4.0$ ms, θ_a is set to 160° (from $\theta_a = 100^\circ$) at $t = 4.0$ ms instead², in order to reduce outward spreading (i.e. momentum suppression) without affecting the leading reflected capillary waves. Such a simulation is represented by the green line in Figure 6.12 – an internal jet is seen, which is to be expected since the reflected capillary waves are unhindered. Finally, both the reflected capillary waves are switched off (i.e. zeroing the velocity within 1 mm of the substrate) and θ_a is set to 160° at $t = 4.0$ ms together – see the blue line in Figure 6.12. As expected due to the lack of reflected capillary waves, no internal jet is formed, despite the lack of spreading. The results in Figure 6.12, especially the lack

²Setting $\theta_a = 160^\circ$ from $t = 0.0$ ms would have some unwanted affect on the reflection of the leading capillary waves – see the upcoming Figure 6.15 on page 135.

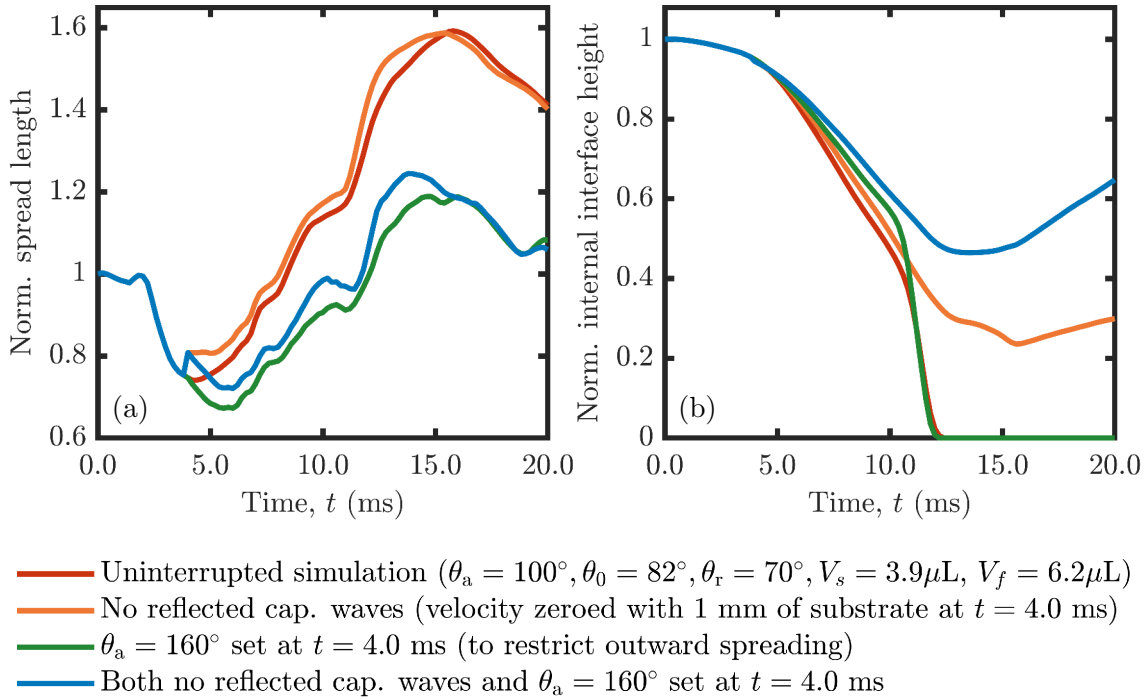


Figure 6.12: Simulation results to confirm the distinct contributions of spreading and reflected capillary waves on jet formation. Zeroing the velocity nullifies reflected capillary waves, whereas increasing θ_a restricts outward spreading (reducing momentum suppression). A jet only arises when reflected capillary waves are present (red and green lines), showing no correlation with spreading (i.e. momentum concentration/suppression).

of correlation between spreading behaviour and internal flows, confirm that momentum concentration or suppression due to spreading are not controlling factors in jet formation here, though it may have a secondary effect as discussed below.

Experimental evidence

Increasing the sessile droplet volume provides additional experimental evidence for the influence of the small tip on jet formation. Indeed, Figure 6.13 shows an experiment with a much larger sessile droplet volume³ of $V_s = 25.0\mu\text{L}$ to what has been considered up to this point. Moreover, the experiment represented in Figure 6.13 was repeated until random variations in the initial condition resulted in satellite droplet formation at $t \approx 8.0$ ms. The lack of tip draining into the bulk due to satellite droplet formation means that the momentum required to form an internal jet (see Figure 6.8) is not imparted on the dyed fluid that remains within the sessile droplet after pinch-off. Hence, a flat internal interface is seen for several milliseconds after pinch-off, for $t \leq 14.0$ ms – that is, an internal jet does not form. It is therefore clear that draining of the tip into the bulk is a requirement for jet formation under the mechanism elucidated above, not simply the

³The assumption that gravity is negligible may not be true for such droplet volumes ($31.2\mu\text{L}$ for the coalesced droplet). As no direct comparison to the simulations is made, and the length scales of the features of interest (i.e. the tip) remain small, any effects of gravity are inconsequential to the discussion here.

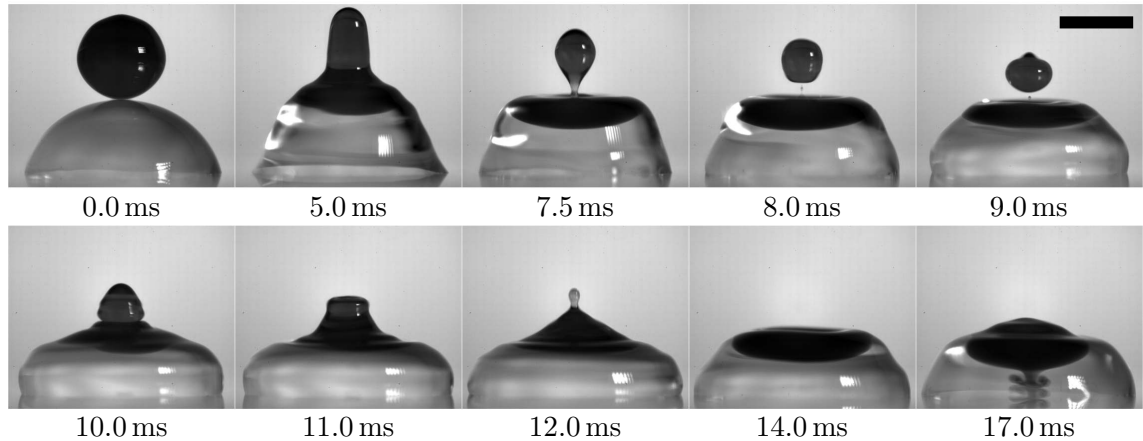


Figure 6.13: Front view of coalescence between a dyed free droplet and an undyed sessile droplet of the same fluid. $V_f = 6.2 \mu\text{L}$ and $V_s = 25.0 \mu\text{L}$. The initial condition is modified such that the dyed fluid pinches off to form a satellite droplet, which subsequently coalesces with the larger sessile droplet. The scale bar is 2.0 mm.

presence of a tip itself.

The satellite droplet subsequently coalesces with the sessile droplet approximately 10.0 ms after the original onset of coalescence. As expected, the satellite droplet is much smaller than the original free droplet so the coalescence dynamics are much faster than seen above (e.g. in Figure 6.5), with considerable column stretching and a very small, elongated tip formed within 2.0 ms (at $t = 12.0$ ms). This tip is subsequently absorbed into the bulk without pinch-off and, due to the mechanism of jet formation elucidated above, an internal jet forms as seen at $t = 17.0$ ms. The jet itself is very thin due to the narrow nature of the tip and so the concentrated momentum it imparts on the bulk.

Figure 6.13 therefore supports the inferences made above regarding the influence of small tips on jet formation, though not the formation of such tips – the size of the sessile droplet means that substrate wettability does not have a large influence here. Moreover, Figure 6.13 suggests that jet formation in cases with pinch-off (including partial coalescence) is not likely due to the lack of fluid draining into the bulk, unless the satellite droplet subsequently coalesces and the tip formed effectively drains into the bulk, as is the case here. However, one could perhaps imagine a scenario in which pinch-off is slow enough (perhaps due to a higher vapour viscosity) that sufficient tip draining into the sessile droplet could occur before the satellite droplet separates, for an internal jet to form without subsequent coalescence. Identifying conditions in which internal jets can form within partially-coalescing droplets would represent an interesting topic for future study.

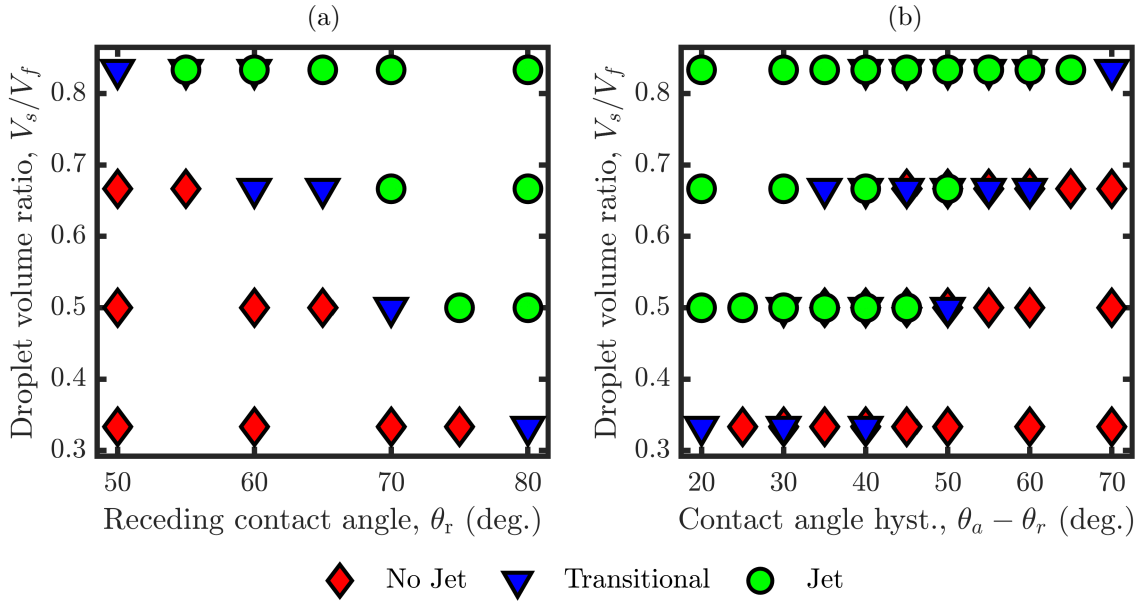


Figure 6.14: Numerically-generated regime maps for jet dependence on droplet volume ratio and substrate wettability. For each $\{V_s/V_f, \theta_r\}$ combination, three simulations were conducted with $\theta_a \in \{100^\circ, 110^\circ, 120^\circ\}$. $\theta_{eq} = 90^\circ$ and $V_f = 6.0 \mu\text{L}$ are fixed.

6.4.3 Droplet volume

Receding contact angle

To systematically explore the parameter space, $\theta_{eq} = 90^\circ$ and $V_f = 6.0 \mu\text{L}$ are now fixed in the simulations. This choice of parameters ensures that the sessile droplet is exactly half of the free droplet, with identical initial curvature and hence Laplace pressure, when $V_s = 3.0 \mu\text{L}$. The receding contact angle, θ_r and sessile droplet, V_s are varied to produce a regime map for internal jet formation in Figure 6.14a. Examples of the classifications ('No Jet', 'Transitional' and 'Jet') are inset in Figure 6.7. Approximately 2.3×10^4 core hours and 69 simulations were required to produce Figure 6.14a. The same data is replotted against contact angle hysteresis in Figure 6.14b.

Figure 6.14a shows that jet formation is promoted by increasing either the receding contact angle or the (sessile-to-free) droplet volume ratio. For larger volume ratios, the reflected capillary waves must travel further along the originally sessile droplet, which reduces their strength due to viscous dissipation. In fact, there likely exists a critical droplet volume ratio beyond which the substrate does not affect jet formation, since the distance that the capillary waves must travel before having any effect is too far (e.g. in Figure 6.13). In this case, the internal dynamics are likely to be akin to those of free droplets, especially in regard to the mechanisms underpinning jet formation. However, the effect of the substrate will be felt for droplets of small and similar volume ratios, which are of greatest practical (e.g. lab-on-a-chip and inkjet) and fundamental interest. For a given sessile droplet volume, decreasing the equilibrium contact angle, θ_{eq} yields

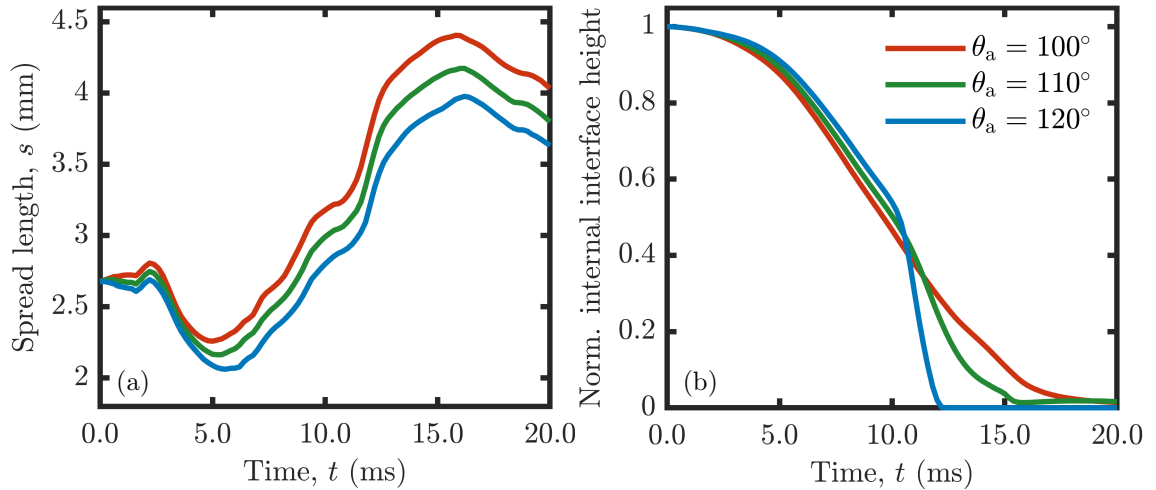


Figure 6.15: Simulations results with $\theta_{\text{eq}} = 90^\circ$, $\theta_r = 60^\circ$, $V_s = 5.0 \mu\text{L}$ and $V_f = 6.0 \mu\text{L}$, whilst θ_a is varied. The internal interface height is normalised by its value at $t = 0.0$ ms.

greater curvature within the meniscus bridge and stronger capillary waves (Deka et al., 2019). Conversely, increasing free surface area escalates viscous dissipation.

Advancing contact angle

The effect of the advancing contact angle, θ_a should also be considered. In fact, for each $\{V_s/V_f, \theta_r\}$ combination in Figure 6.14a, three simulations with different advancing contact angles, $\theta_a \in \{100^\circ, 110^\circ, 120^\circ\}$ were conducted and are plotted. No differences in classification transpired, except for the largest sessile droplet volume studied ($V_s = 5.0 \mu\text{L}$) when $\theta_r = 55^\circ$ or $\theta_r = 60^\circ$, for which an advancing contact angle of $\theta_a = 120^\circ$ incited jet formation (as opposed to the transitional situation for $\theta_a \in \{100^\circ, 110^\circ\}$). An increase in θ_a restricts outward spreading, which may be somewhat beneficial for jet formation by increasing the internal interface height and concentrating the momentum generated by the tip. However, the influence of the advancing contact angle is subordinated to that of the receding contact angle due to the latter's influence on reflection of the leading capillary wave. Hence, jet formation in this configuration is only weakly dependent on the advancing contact angle.

The spread length and internal interface height for a case from Figure 6.14a that exhibits inconsistent jet appearance with varying θ_a (fixed parameters $\theta_{\text{eq}} = 90^\circ$, $\theta_r = 60^\circ$, $V_s = 5.0 \mu\text{L}$ and $V_f = 6.0 \mu\text{L}$) are shown in Figure 6.15. As seen in Figure 6.15a, θ_a does not greatly influence the contact line dynamics until after leading capillary wave reflection, which suggests why the effect of θ_r is dominant (cf. Figure 6.7). The maximum spread length is of course quite different for the three values of θ_a considered though. Moreover, for the case considered the internal interface height already shows transitional behaviour with $\theta_a = 100^\circ$, for which the interface height (Figure 6.15b) consistently decreases to approximately zero at $t = 20.0$ ms. Thus, the increase in θ_a to 120° is able to reduce the

minimum spread length enough to enhance the leading reflected capillary wave sufficiently that the internal interface destabilises to produce a jet.

Contact angle hysteresis

For a fixed advancing contact angle, modifying the receding contact angle also adjusts the contact angle hysteresis. Previous work has indicated that low hysteresis is beneficial for mixing (Nilsson and Rothstein, 2011). Whilst this inference is generally supported by the current work, each point in Figure 6.14a contains a 20° degree hysteresis range which indicates that hysteresis is not the decisive factor in jet formation. Moreover, the data in Figure 6.14a are replotted against the contact angle hysteresis, $\theta_a - \theta_r$ in Figure 6.14b. An acute lack of clear regime boundaries is seen in Figure 6.14b, indicating that contact angle hysteresis itself is not an accurate predictor of jet formation. This observation is not surprising given that the importance of the advancing contact angle to jet formation is subordinated to that of the receding contact angle.

Laplace pressure relation to applications

For $V_s = 3.0 \mu\text{L}$ and $\theta_{\text{eq}} = 90^\circ$, the sessile droplet is exactly half of the free droplet ($V_f = 6.0 \mu\text{L}$). Hence, the initial droplet curvatures and Laplace pressures are identical, yet an internal jet can still form if $\theta_r \geq 75^\circ$. Moreover, the Laplace pressure of a $2.0 \mu\text{L}$ sessile droplet (with $\theta_{\text{eq}} = 90^\circ$) is greater than that of a $6.0 \mu\text{L}$ free droplet, whilst the latter is injected into the former, opposing the initial Laplace pressure difference. Coalescence in this configuration therefore provides the ability to mix droplets in unconventional ways, without relying on a particular Laplace pressure difference. Indeed, Figure 6.14a indicates that internal jet formation can be expected for a wide range of substrate wettabilities when the initial droplet Laplace pressures are equal, unlike in free droplet coalescence, which may be desirable in microfluidic applications.

6.4.4 Droplet viscosity

Effect of droplet viscosity on jet formation

It is well known that increasing droplet viscosity increases viscous dissipation, which dampens capillary waves and suppresses internal flows. However, increasing viscosity also reduces the rate of change of curvature during meniscus bridge expansion and so reduces the strength of emitted capillary waves (Thoroddsen et al., 2005). Column formation and the strength of reflected capillary waves, both of which have been shown to be beneficial for jet formation already in this work, are therefore diminished with increasing droplet viscosity. Hence, it is expected that increasing droplet viscosity should be unfavourable for

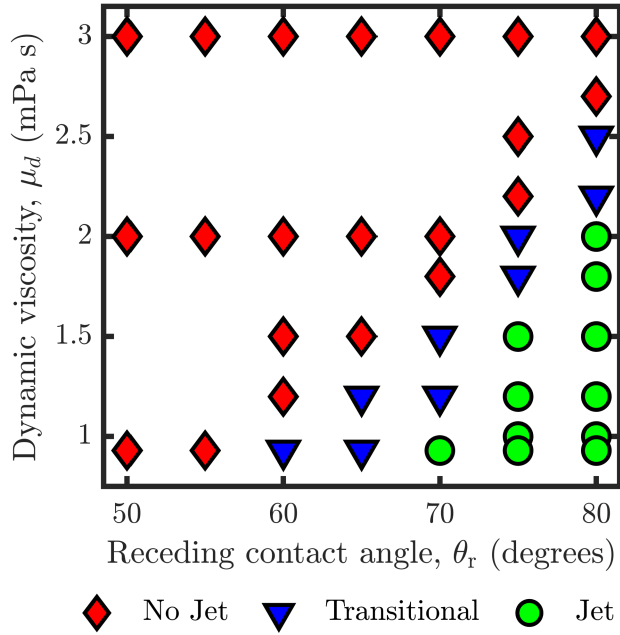


Figure 6.16: Numerically-generated regime map for jet dependence on droplet viscosity and substrate wettability. $\theta_a = 100^\circ$, $\theta_{eq} = 90^\circ$, $V_s = 4.0 \mu\text{L}$ and $V_f = 6.0 \mu\text{L}$ in all simulations.

jet formation. This prediction is confirmed in Figure 6.16 for which $\theta_a = 100^\circ$, $\theta_{eq} = 90^\circ$, $V_s = 4.0 \mu\text{L}$ and $V_f = 6.0 \mu\text{L}$ (corresponding to the second highest row in Figure 6.14); the droplet viscosity, μ_d and receding contact angle, θ_r are varied. The same trend in jet formation with respect to the receding contact angle identified above is seen across different droplet viscosities. The key result derived above is thus confirmed across a range of droplet viscosities. Interestingly, the extent of the transitional viscosity range is similar across those receding contact angles exhibiting all three regimes.

The droplet viscosity affects the dynamics both via the Ohnesorge number, determining the degree of surface tension dominance, and the droplet/outer phase viscosity ratio, as discussed in Section 5.3.3. Changes in either viscosity affect capillary wave propagation (Deka et al., 2019), whilst only the droplet viscosity feeds into the Ohnesorge number as defined above. Consideration is limited to exploring droplet viscosity changes here with respect to likely applications. It is important to appreciate though that direct extrapolation to changes in Ohnesorge number or viscosity ratio is not appropriate. Hence, the data in Figure 6.16 are plotted against droplet viscosity, μ_d rather than the viscosity ratio or Ohnesorge number.

Example frames from the 6th column of data ($\theta_r = 75^\circ$) in Figure 6.16 are shown in Figure 6.17. All parameters are fixed ($\theta_a = 100^\circ$; $\theta_{eq} = 90^\circ$; $\theta_r = 75^\circ$; $V_s = 4.0 \mu\text{L}$; $V_f = 6.0 \mu\text{L}$) except for the droplet viscosity, μ_d , which is varied through all three internal dynamic regimes (no jet, transitional, jet). The free surface dynamics until column collapse are similar for all three droplet viscosities, but the droplet viscosity clearly affects the formation of the small tip, which is not present at all for the largest droplet viscos-

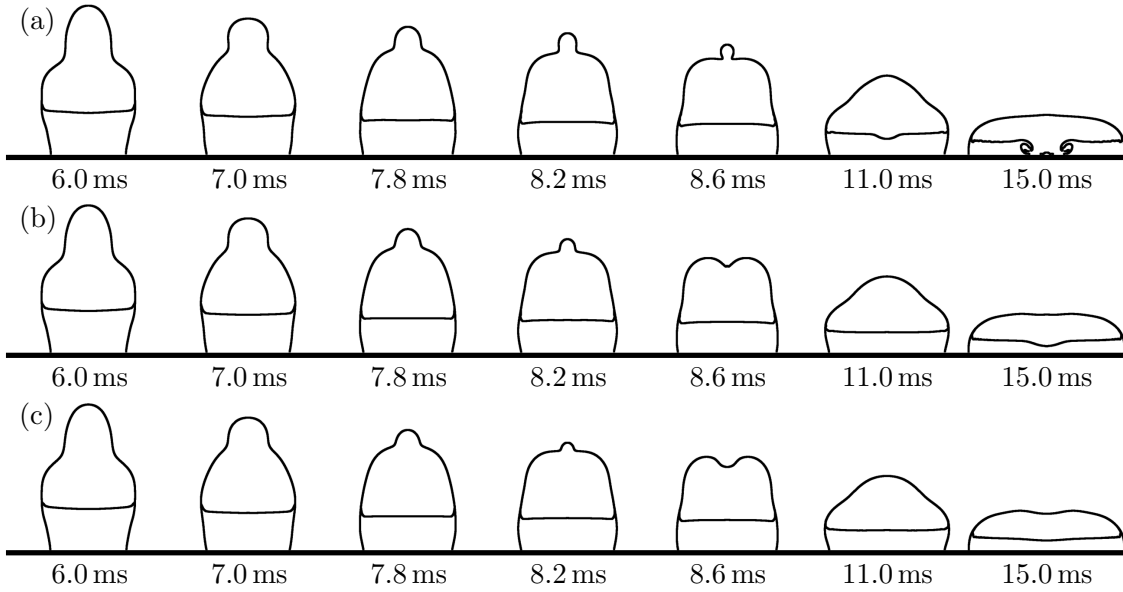


Figure 6.17: Free surface and internal interface profiles for droplets with $\theta_a = 100^\circ$, $\theta_{eq} = 90^\circ$, $\theta_r = 75^\circ$, $V_s = 4.0 \mu\text{L}$ and $V_f = 6.0 \mu\text{L}$. The droplet viscosity, μ_d is varied between panels: (a) $\mu_d = 1.2 \text{ mPa s}$; (b) $\mu_d = 1.8 \text{ mPa s}$; (c) $\mu_d = 2.2 \text{ mPa s}$.

ity (Figure 6.17c). Moreover, comparing Figures 6.17a and 6.17b indicates that the key requirement for a jet to form (rather than transitional internal flows) is neck thinning at the base of the small tip (as in the $t = 8.6 \text{ ms}$ frame in Figure 6.17a). A thin neck allows fluid draining from the small tip to be accelerated sufficiently that enough momentum is imparted onto the bulk fluid for a jet to form before the momentum is dissipated by viscosity. Indeed, the existence of an internal jet in Figure 6.16 exactly coincides with the presence of a tip of high curvature (with a thin neck) identified as being crucial for internal jet formation in previous sections for a fixed droplet viscosity.

Comparison to free droplets

According to Figure 6.16, an internal jet can be formed when $\theta_r = 80^\circ$ and $\text{Oh} = 7.0 \times 10^{-3}$ (based on $\mu_d = 2.0 \text{ mPa s}$), given a volume ratio of $V_s/V_f = 0.667$. This volume ratio is remarkably small compared to what would be required in free droplets. According to Xia et al. (2017), the requirement for internal jet formation in free droplets within air is that the (large-to-small) droplet *size* ratio is greater than

$$3.4228 \times 10^6 \text{Oh}^4 - 1.6309 \times 10^5 \text{Oh}^3 + 3.2054 \times 10^3 \text{Oh}^2 + 17.7020 \text{Oh} + 1, \quad (6.1)$$

with the Ohnesorge number length scale being the small droplet radius⁴. As explained above, the free droplet is injected into the sessile droplet in the configuration studied in this work, and so the free droplet assumes the same role as the smaller droplet in

⁴Xia et al. used the small droplet *diameter* as their length scale, so the coefficients in their work are different (but equivalent) to those found in Equation (6.1).

free droplet coalescence, regardless of the relative droplet volumes. Indeed, substituting $\text{Oh} = 7.0 \times 10^{-3}$ (i.e. taking $r_f = 1.127$ mm as the length scale) into Equation (6.1) suggests that a (linear) size ratio of 1.23 would be required to form a jet with the equivalent Ohnesorge number in free droplet coalescence. This size ratio corresponds to a volume ratio of 1.88, almost a three-fold increase on the value of 0.667 identified above for free and sessile droplets.

Considering the effective radius, R of the sessile droplet (i.e. the radius of the sphere of which the spherical cap is part) at the onset of coalescence, the effective size ratio between the droplets is 1.10 when the volume ratio is 0.667. Nevertheless, it is clear that the substrate enhances jet formation here and there is a potential to enable jet formation with larger droplet viscosities compared to free droplet coalescence.

6.5 Discussion and summary

In this chapter, internal jet formation during the coalescence of an initially-static free droplet with a sessile droplet of the same fluid was studied, focusing on the influence of substrate wettability. The dynamics were successfully simulated using a VOF model, showing good quantitative agreement with the laboratory experiments that were discussed too. The use of the Kistler dynamic contact angle model allowed the influence of substrate wettability to be captured very accurately despite the model not including pinning.

Compared to free droplet coalescence, where a jet may be formed when the smaller droplet is drawn directly into the larger one, on a substrate an internal jet can arise via a different mechanism. Here, jet formation was shown to depend on a thinning neck that led to a tip with high curvature and pressure on top of the coalesced droplet, which incited a rapid downward flow towards the substrate. The importance of such a tip to jet formation was also demonstrated experimentally for a case exhibiting pinch-off. The generation of this tip depends on the contact line dynamics via reflected capillary waves. Substrate wettability therefore directly influences jet formation and mixing efficiency. Strong reflection of capillary waves is required to generate sufficient neck thinning, so higher receding contact angles are beneficial for producing a jet.

The ability to assemble a regime map of droplet volume ratio (sessile to free) against receding contact angle, with clear regime boundaries, demonstrates the influence of substrate wettability and confirms that increasing the volume ratio encourages jet formation, as expected. However, the reflected capillary wave mechanism identified in this work can lead to jet formation at very different volume ratios from those that produce jets during free droplet coalescence. Whilst it is generally true that low contact angle hysteresis is beneficial for mixing, hysteresis itself is not an accurate predictor of jet formation; the effect of the advancing contact angle is subordinated to that of the receding contact angle. Jet formation is inhibited by increasing droplet viscosity, though jets can appear at droplet

viscosities higher than expected for free droplets for a given volume ratio.

The results indicate the potential of engineering substrate wettability to improve mixing via the formation of internal jets in microfluidic systems. To achieve good advective mixing, capillary waves reflected from the contact line should be enhanced where possible, which is achieved by increasing the receding contact angle in the configuration studied. The influence of contact line movement in a certain direction may be dominant, so contact angle hysteresis alone is not necessarily the decisive factor. It is therefore imperative to consider substrate wettability for applications involving coalescing droplets for which the internal dynamics, and associated fluid mixing, may be influential.

Chapter 7

Surface jets

In this chapter the initial condition is no longer two static droplets. Instead, coalescence between an impacting and a pre-deposited sessile droplet is considered, where some interesting and surprising effects of inertia will become evident. Towards the end of the chapter, coalescence between droplets of different fluids and mixing driven by Marangoni flow will be analysed. Most of the content in this chapter has been published in Sykes et al. (2020a), though significantly more detail, and some additional results, are given here.

7.1 Introduction

Coalescence may be initiated during the impact of a falling droplet with a sessile droplet on a substrate, which is the typical configuration in inkjet printing. For millimetric droplets with identical fluid properties, similar volumes and inertial dimensionless numbers matched to typical inkjet values, experiments have demonstrated no discernible mixing within the coalesced droplet, as seen in Figure 1.1. This conclusion is robust to lateral separation between the precursor droplets and has been corroborated by numerical simulations for substrates of various wettabilities (Raman et al., 2016; Raman, 2018). Improved advective mixing can be achieved by the formation of a vortex ring if the sessile droplet is much larger than the impacting droplet, or potentially via alterations to substrate wettability as elucidated in Chapter 6. Vortex rings can be formed in a similar manner during the impact of a droplet onto a deep pool (Saha et al., 2019), whereas capillary wave dynamics influence mixing considerably for shallow pools (Ersoy and Eslamian, 2019). However, droplet-pool coalescence is critically different from the coalescence of droplets on a substrate due to the absence of a contact line. Indeed, Chapter 6 has shown that substrate wettability has a significant effect on internal flows.

The results until this point have considered coalescing droplets with equal fluid properties, but an intrinsic feature of many applications is that the precursor droplets consist of different fluids (e.g. in RIJ, as discussed in Chapter 1), where differences in the relative

fluid properties can influence the internal dynamics. For precursor droplets of different densities, a stratified coalesced droplet may be formed by an internal gravity current on a longer time scale than the surface tension induced flow (Zhang et al., 2015). Alternatively, the use of non-Newtonian fluids can lead to intricate internal flow structures and good advective mixing (Sun et al., 2015a). Differences in the rheological properties of Newtonian droplets can be used to control the final internal structure of coalesced droplets, with the viscosity ratio between an oil droplet and an (immiscible) sessile water droplet defining the maximum penetration depth of the former (Chen et al., 2017). In the context of RIJ, some studies have considered mixing between impacting and coalescing micrometric droplets of different reactive fluids, but did not resolve the internal dynamics which would be difficult at this length scale, as discussed in Chapter 2 (e.g. Fathi and Dickens, 2013).

Surface tension differences between coalescing droplets are particularly significant for the internal dynamics, since surface tension influences the Laplace pressure and surface tension gradients drive Marangoni flow, as elucidated in Section 2.1.5. Due to the induced tangential flow, a droplet of lower surface tension will tend to envelop a droplet of higher surface tension after coalescence, which can generate an internal jet (Luo et al., 2019). The tangential flow velocity increases linearly for moderate surface tension differences, becoming sublinear for larger differences. The velocity reduces with increasing Ohnesorge number as viscous forces retard the motion (Liu et al., 2013a). Hence, relatively small surface tension differences may lead to significant changes in the dynamics. Such surface tension differences are usually established using different simple fluids, but they can also be due to surfactants. For surfactants, the solutal Marangoni flow induced may depend on the precise chemical nature of the surfactant which can influence the internal dynamics (Nash et al., 2018). Surface tension differences due to surfactants have been shown to reduce colour bleed in inkjet-printed droplets, as explained in Chapter 1.

Many studies involving surface tension differences, including those discussed in the previous paragraph, concern droplets within an immiscible, high viscosity outer fluid (typically an oil). In particular, these include droplets confined within a microfluidic channel where the high viscosity of the outer fluid suppresses free surface oscillations through viscous dissipation, reduces the rate of meniscus bridge growth and impedes interfacial flow. In these scenarios, the curvature of the precursor droplets and individual Laplace pressures persist for longer, which promotes internal jet formation, whilst surface flows are diminished. Moreover, the jet morphology and dynamics have been shown to depend on the viscosity ratio between the droplets and outer fluid (Nowak et al., 2016), as seen for free and sessile coalescing droplets in Chapter 5. In cases where the outer fluid flows within the microchannel, the precursor droplet order can affect the internal and interfacial flow (Kovalchuk et al., 2019).

In contrast to confined microfluidics, other microfluidic devices rely on manipulating droplets on a solid substrate, known as *open-surface microfluidics* (Jiao et al., 2019). For these systems, coalescence in a low viscosity gaseous outer fluid (typically air) is of inter-

est. For droplets on a substrate, the contact line dynamics also affect the internal and external dynamics (Lai et al., 2010), where improved advective mixing due to Marangoni flow (Ng et al., 2017) and delayed coalescence (Bruning et al., 2018) may arise. The initial droplet configuration can influence the dynamics in this case and jet-like internal flows can be generated by recirculation for precursor droplets of either identical or different surface tension (Yeh et al., 2013). With the presence of a free surface open to air, purely interfacial phenomena can arise, such as Marangoni-induced spreading of a droplet impacting a deep pool (Taherian et al., 2016). Both experimental and numerical studies have shown that these impacts can lead to Marangoni-induced droplet ejection (Blanchette et al., 2009; Shim and Stone, 2017; Sun et al., 2018a). For precursor droplets of fluids which undergo a precipitating chemical reaction upon mixing, the magnitude of the surface tension difference can determine the extent of spreading and mixing and hence the precipitate pattern (Jehannin et al., 2015). Complex interfacial flow structures and instabilities may also be generated, such as by evaporation-augmented Marangoni flow during the impact of an alcohol droplet with an (immiscible) oil pool (Keiser et al., 2017). These observations indicate the possible rich internal and interfacial dynamics which could be expected during the coalescence of impacting and sessile droplets of different surface tension.

In this chapter, the internal and interfacial dynamics (at the free surface) during the coalescence of an impacting droplet with a miscible sessile droplet on a solid, flat substrate is studied by means of colour high-speed imaging, as discussed in Chapter 3. Ethanol-water mixtures, with a low proportion of ethanol, were used to ensure the flow was dominated by surface tension and that the surface tension of each precursor droplet could be independently modified, enabling the unexplored influence of surface tension differences to be studied in this experimental configuration. Surfactants were avoided due to the unclear influence of their chemical composition on the dynamics. The influence of lateral separation and surface tension differences is considered to elucidate both the initial internal and interfacial dynamics, in addition to the longer-term mixing efficiency.

7.2 Experimental details

The results contained within this chapter are derived from the impacting and coalescing droplets experimental setup described in Section 3.5. The velocity and radius of the impacting droplet were determined by image processing (see Section 3.6) and are recorded in Table 7.1. These values correspond to the equivalent spherical radius of the precursor sessile droplet (i.e. immediately before it was deposited on the substrate). It is important to note that due to contact angle hysteresis a wide range of equilibrium contact angles are possible; those reported in Table 7.1 are consistent with the deposition of the sessile droplet in the coalescence experiments – the as-placed contact angle (see Section 2.2.4).

The deposition of the impacting droplet is dynamically characterised by the Weber and Ohnesorge numbers, with the length scale chosen as the impacting droplet radius,

Table 7.1: Impacting droplet radius, r_f and velocity, u of the ethanol-water mixtures used in the study of surface jets. The equilibrium contact angles reported were made on a droplet consistent with the deposition of the sessile droplet in the coalescence experiments.

Fluid No.	Ethanol Mass %	θ_{eq} (degrees)	r_f (mm)	u (m s^{-1})
1	0.0	91 ± 2	1.16 ± 0.02	0.50 ± 0.04
2	4.0	82 ± 2	1.07 ± 0.02	0.51 ± 0.06
3	8.0	74 ± 2	1.02 ± 0.02	0.50 ± 0.04
4	18.0	66 ± 2	0.96 ± 0.02	0.51 ± 0.04

r_f . The velocity is that of the impacting droplet immediately before landing. Here, $We \approx 5$ and $Oh \approx 5 \times 10^{-3}$ for a *typical droplet* (i.e. $\rho_d = 10^3 \text{ kg m}^{-3}$; $\mu_d = 10^{-3} \text{ Pa s}$; $\sigma = 50 \times 10^{-3} \text{ N m}^{-1}$; $r_f = 10^{-3} \text{ m}$; $u = 0.5 \text{ m s}^{-1}$), which indicates that the flow is dominated by surface tension as opposed to viscosity. The equivalent Reynolds number is $Re = \sqrt{We}/Oh \approx 500$. It is important to note that the impacting droplet velocity quickly reduces after deposition, so the resulting internal flow is much slower; hence, this Reynolds number does not well characterise the internal flow dynamics. The Bond number is $Bo \approx 0.2$, where $\Delta\rho \approx 10^3 \text{ kg m}^{-3}$ is the density difference between the droplet and surrounding air. The dimensionless numbers indicate that surface tension dominates over gravitational forces despite the relatively large droplet size.

7.3 Droplets with equal fluid properties

7.3.1 Modest lateral separation

Onset of coalescence

For small lateral separations, the impacting droplet collides with the sessile droplet before hitting the substrate. The requirement for coalescence during this interaction is that the air layer between the droplets drains enough that intermolecular (van der Waals) forces can cause the remaining film of air to rupture, as discussed in Chapter 2. The axisymmetric (zero lateral separation) impact of a dyed droplet of fluid 2 (4.0% ethanol) onto an undyed droplet of the same fluid is shown in Figure 7.1 with both front and bottom views. Note that time zero ($t = 0.0 \text{ ms}$) is taken as the frame immediately before the first visible contact between droplets, rather than the time at which coalescence occurs due to the impacting droplet inertia.¹ Due to the Weber number, coalescence is not immediate but there is an approximate 5.0 ms delay whilst the trapped air layer drains. During this period, there is significant droplet deformation and a resultant large increase in free surface energy. In fact, the excess of surface energy at the onset of coalescence almost leads to pinch-off (partial coalescence) at $t \approx 9.0 \text{ ms}$. Unfortunately, the time that coalescence occurred in

¹Cf. Chapter 6 where the initial condition is by design of static droplets and the pre-collision droplet shapes are recovered at the onset of coalescence, which is taken to be $t = 0.0 \text{ ms}$.

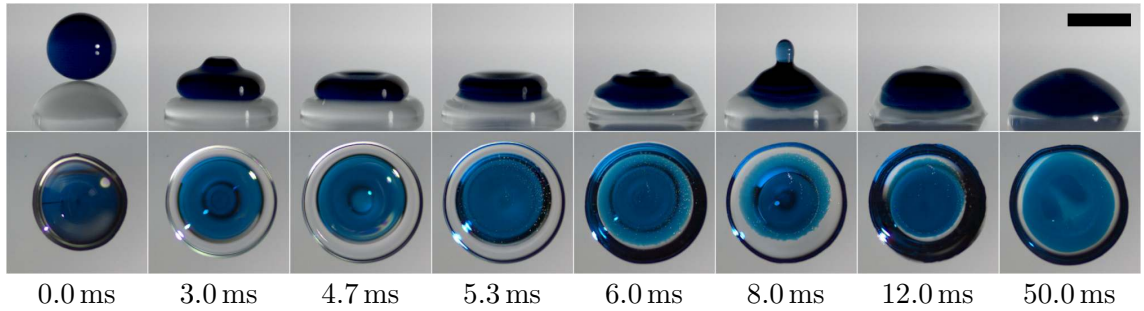


Figure 7.1: Front and bottom views of a dyed impacting droplet coalescing with an undyed sessile droplet of the same fluid (fluid 2; 4.0% ethanol), in an axisymmetric configuration. Coalescence occurs approximately 5.0 ms after the droplets collide. The scale bar is 2.0 mm.

this configuration depended critically on the precise initial conditions (i.e. small variations in the initial condition led to large changes in the dynamics), precluding the methodical study of the axisymmetric configuration when the surface tension of both the impacting and sessile droplets were large (58.0 mN m^{-1} in Figure 7.1).

Figure 7.2 exhibits two larger lateral separations compared to Figure 7.1, but with the same fluid properties (fluid 2; 4.0% ethanol). Again, due to the Weber number there is a delay (approximately 2.0 ms) between collision and coalescence at both of these lateral separations. In contrast to the axisymmetric case, free surface deformation is not significant during the non-coalescence period here and, importantly, the precise time of coalescence and dynamics remain the same with small changes in the initial condition, i.e. the results are repeatable. Hence, such lateral separations can be safely studied whilst neglecting the delay in coalescence. Once coalescence occurs, a small amount of air is entrained around the internal interface, which is visible as small bubbles at $t = 4.0 \text{ ms}$ in Figure 7.2 for both lateral separations. This phenomenon does not influence the long-term internal dynamics and mixing behaviour studied here. Note that delayed coalescence and air entertainment does not occur when the impacting droplet strikes the substrate first and coalescence is initiated as the impacting droplet spreads across the substrate (see Section 7.3.2).

Post-coalescence dynamics

For both lateral separations seen in Figure 7.2, the inertia of the dyed droplet significantly disturbs the sessile droplet on impact, generating capillary waves that travel in both directions along the free surface. These capillary waves, combined with the spreading of the impacting droplet, cause the left contact line to move outwards, which dissipates some energy introduced by the impact (Kapur and Gaskell, 2007). In contrast, the right contact line remains pinned, with the capillary waves insufficient to displace it on the high hysteresis substrate used in this work. Right contact-line motion may also be inhibited by the outward movement of the left contact line, which commences before the leading capillary wave reaches the right contact line and draws undyed fluid towards it by mass conser-

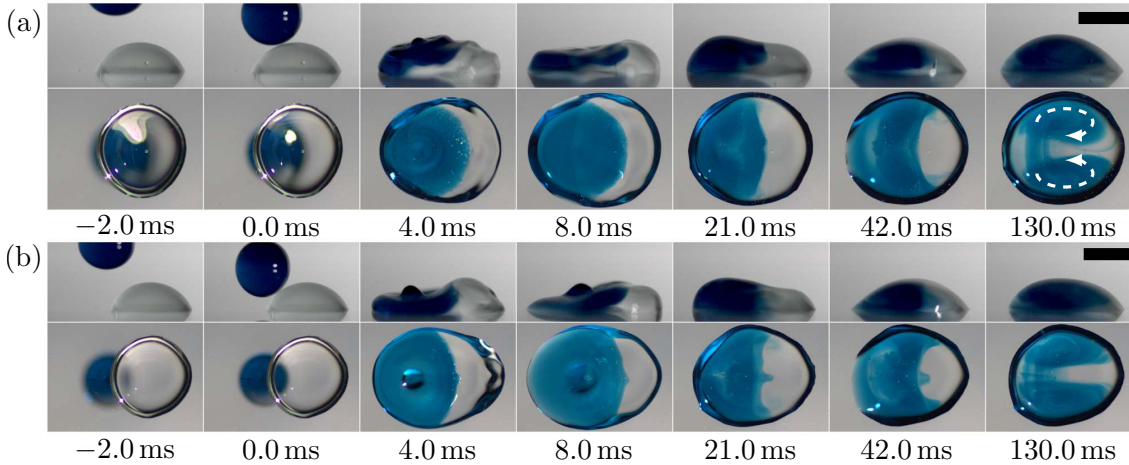


Figure 7.2: Front and bottom views of a dyed impacting droplet coalescing with an undyed sessile droplet of the same fluid (fluid 2; 4.0% ethanol), for two lateral separations in which the impacting droplet collides with the sessile droplet before the substrate: (a) 0.8 mm; (b) 1.6 mm. Both scale bars are 2.0 mm.

vation. After the initial spreading, the left contact line also becomes pinned. Combined with the excess of dyed fluid on the LHS of the coalesced droplet, the pinned contact lines induce a recirculatory internal flow as indicated on the 130.0 ms bottom view frame of Figure 7.2a. Due to this internal flow structure, the dyed fluid is primarily located on the outside of the droplet, whereas the undyed fluid is trapped within the centre. Note that such internal flow is not observed in the ostensibly similar experiments of Castrejón-Pita et al. (2013), primarily due to higher Ohnesorge number utilised ($Oh \approx 0.25$) in that work, which yields a reduced influence of surface tension and much greater viscous dissipation.

While recirculatory internal flow alters the distribution of dyed and undyed fluid, it simply advects rather than stretching and folding the internal fluid interface; there is little advective mixing. Nevertheless, utilising both views there does appear to be some mixing on the LHS of the coalesced droplet (especially visible at $t = 42.0$ ms in Figure 7.2a) due to undyed fluid being propelled into a region where dyed fluid originally resided. Since the precursor droplets consist of the same fluid, the only mechanisms of advective mixing on a short time scale result from the inertia of the impacting droplet and the initial Laplace pressure difference between the coalescing droplets. The inertia derived from these effects is largely dissipated (primarily by viscosity) within a few hundred milliseconds of coalescence, leaving a relatively small internal interface over which molecular diffusion must act to homogenise the coalesced droplet. As detailed in Chapter 2, molecular diffusion acts very slowly so it is clear that achieving good advective mixing is crucial for efficiently realizing a homogeneous coalesced droplet on desirably short time scales here.

Despite the difference in lateral separation, the internal flows for both cases shown in Figure 7.2 are remarkably similar. There is a small difference at early times, when penetration of dyed fluid develops along the droplet centreline for the larger lateral separation (Figure 7.2b), visible at $t = 21.0$ ms. This flow structure is located close to the substrate

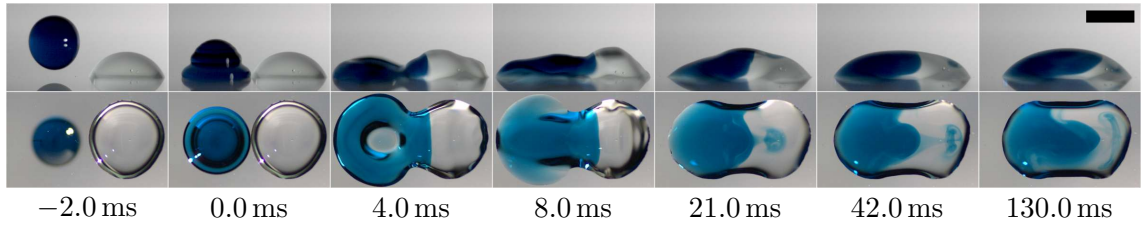


Figure 7.3: Front and bottom views of a dyed impacting droplet coalescing with an undyed sessile droplet of the same fluid (fluid 2; 4.0% ethanol); coalescence occurs as the impacting droplet spreads across the substrate into the sessile droplet. The scale bar is 2.0 mm.

as is clear from the 42.0 ms front-view frame, but does not persist at later times when the internal flow becomes dominated by recirculation. In fact, the only enduring difference between these cases is the droplet footprint on the substrate, with the final droplet shape being closer to a spherical cap in the former case, whereas the footprint is more elliptical in the latter. As seen, the difference in droplet footprint does not greatly influence the internal dynamics however.

7.3.2 Large lateral separation

If the lateral separation between the precursor droplets is large enough, then the impacting droplet can land on the substrate before spreading into the sessile droplet to induce coalescence, a situation which may arise when depositing lines or otherwise patterning a substrate (Hsiao and Betton, 2016). Figure 7.3 presents an experiment with such a lateral separation. Compared to the two cases in Figure 7.2, the only experimental difference is in the lateral separation. Note that coalescence occurs immediately on collision of the droplets, i.e. there is no delay in coalescence.

With this large lateral separation, the internal flow becomes significantly different with a jet emanating from the dyed fluid region into the undyed fluid of the precursor sessile droplet, visible at $t = 21.0$ ms. From the bottom view, there may appear to be good advective mixing within the coalesced droplet, with significant stretching and some folding of the internal fluid interface. However, the front view shows that the jet is confined to the free surface of the sessile droplet, so there is actually little advective mixing. Similarly, the undyed fluid in the centre of the coalesced droplets cannot be perceived from the front view for both cases in Figure 7.2. Therefore, Figures 7.2 and 7.3 emphasise a need for caution when investigating internal dynamics using only a single view, as previously indicated for mixing (Paik et al., 2003).

Jets during coalescence have already been seen in Chapter 6, but note that the jets progressed into the bulk coalesced droplet there; they were *internal jets*. In contrast, the jet seen in Figure 7.3 is confined to the free surface, so a sharp fluid interface is maintained in the bulk. Such surface flows could be utilised to encapsulate a sessile droplet by a second droplet, possibly with different fluid properties (Koldewej et al., 2019), or to modify its

interfacial properties. Alternatively, for droplets deposited to form a continuous line, a sharp transition in line properties may be desired, where the presence of such a surface flow could be detrimental. It is therefore of interest to understand the formation of the *surface jet* in Figure 7.3, and later whether it can be enhanced or suppressed by modifying the fluid properties of the original droplets.

7.3.3 Surface jet formation

The dynamics leading to the formation of the surface jet identified in the previous section (specifically Figure 7.3) are systematically uncovered and elucidated in this section.

Initial post-coalescence dynamics

In Figure 7.3, the impacting droplet spreads into the sessile droplet approximately 1.5 ms after landing on the substrate to induce coalescence. At this moment, the impacting droplet still has considerable inertia, though some energy has already been dissipated by the displacement of the left contact line. It also has excess surface energy, having not formed a spherical cap, and bears an advancing contact angle which is larger than the range of equilibrium contact angles. However, on collision (at $t = 0.0$ ms), the height of the impacting droplet near the point of coalescence is much less than that of the sessile droplet due to its deformed shape. Rapid expansion of the meniscus bridge between the droplets following coalescence generates capillary waves which travel outwards along the free surface of the coalesced droplet, as discussed extensively in Chapter 6. These capillary waves disturb the free surface of the undyed fluid (visible in the 4.0 ms front-view frame), but are dominated by the ongoing spreading dynamics in the dyed fluid region.

While these initial post-coalescence dynamics take place near the meniscus bridge, the dyed fluid continues to spread radially outwards in all other directions until the maximum spread length is reached, which is typically 3.0 ms after coalescence. The spreading dynamics are essentially unaffected by coalescence, except in the immediate region of the point of coalescence. There, the spreading dynamics combine with meniscus bridge growth to push dyed fluid into the region originally occupied by undyed fluid, past the point of coalescence. The impacting droplet otherwise experiences typical deposition dynamics. A large free surface depression develops around its centre with a diameter comparable to that of the droplet immediately before impact, while fluid migrates radially outwards to the advancing contact line (cf. Rioboo et al., 2001). The resulting free surface topology at the maximum spread length is illustrated in Figure 7.4 as a cut-plane through the centres of the precursor droplets. As in Chapter 6, the central depression across the dyed fluid is not conspicuous from an external front view due to the axisymmetry of typical deposition dynamics (i.e. it is hidden by the higher outer free surface), but it can be perceived by the relative pixel intensity within the dyed fluid region in the 4.0 ms bottom

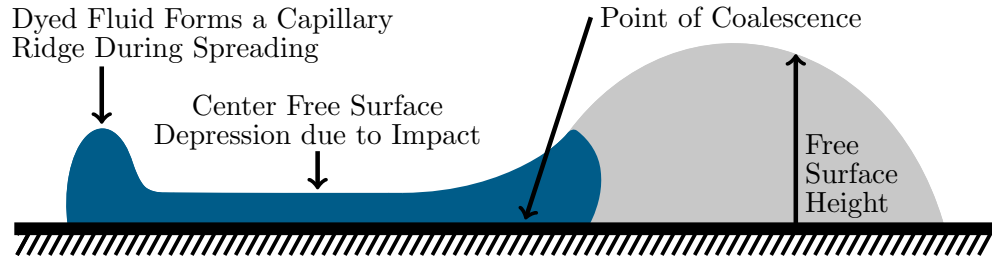


Figure 7.4: A sketch depicting the coalescence of two droplets of the same fluid at the instance the maximum spread length is reached (typically 3.0 ms after coalescence), represented as a cut-plane through the precursor droplet centres. The dyed (blue) impacting droplet lands on the substrate before spreading into the undyed (clear/grey) sessile droplet to initiate coalescence (as in Figure 7.3).

view frame of Figure 7.3. A capillary ridge forms near the contact line (away from the meniscus bridge) since the relatively high minimum advancing contact angle of the substrate prevents further spreading, whilst the radial flow continues to transport dyed fluid outwards to accumulate behind the contact line (Bonn et al., 2009). The generation of such a capillary ridge is dependent on the substrate wettability, as on a perfectly wetting substrate the droplet would spread to coat the substrate with a uniform thickness.

Travelling wave

The free surface at the maximum spread length depicted in Figure 7.4 is severely deformed, whilst the flow is dominated by surface tension. The contact line cannot advance further as dyed fluid continues to accumulate in the capillary ridge due to the contact angle remaining in the equilibrium range. Therefore, fluid is quickly reflected away from the left contact line (that is, capillary ridge) to reduce the free surface area. During the reflection, the left contact angle decreases but the contact line does not recede. Meanwhile, energy is viscously dissipated near the fluid interface due to meniscus bridge growth, as dyed fluid is pushed into the undyed fluid region. The latter effect is indicated in Figure 7.4 by the position of the fluid interface relative to the point of coalescence. Furthermore, the right contact line (that of the undyed fluid) remains pinned at this time. The asymmetry in the dynamics resulting from these factors ensures the fluid reflected from the contact line is primarily transported in a single direction towards the undyed fluid along the axis of symmetry between the precursor droplets (Ristenpart et al., 2006). Due to the left contact line being pinned, the reflected fluid forms a *travelling wave* rather than simply displacing the contact line to form a spherical cap.

The travelling wave precipitates a progressive increase in free surface height across the depressed free surface as visible in Figure 7.5, with free surface edges shown at five time instants, overlaid onto the front view at $t = 5.8$ ms (the first of the five times). A large and rapid increase in free surface height precedes the wave, with the free surface height becoming approximately uniform away from the contact lines at $t = 9.9$ ms. Note that the

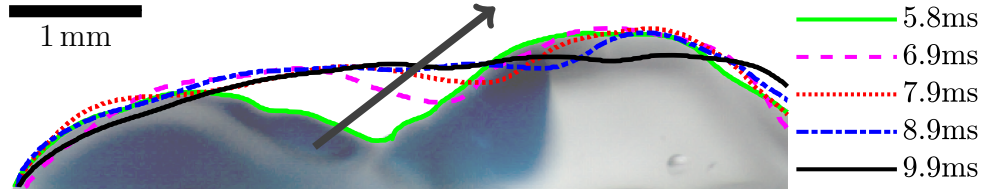


Figure 7.5: Free surface evolution illustrated by image-processed edges at five early times during the coalescence of two droplets of the same fluid (fluid 2, 4.0% ethanol), overlaid onto the 5.8 ms front view (faded by 25%). The grey arrow indicates increasing time. The data correspond to Figure 7.3.

increase in free surface height occurs wholly within the dyed fluid region of the coalesced droplet. The free surface movement therefore acts to raise dyed fluid within the droplet, which is primarily drawn from the capillary ridge. The upward motion of dyed fluid also draws undyed fluid towards the left contact line near the substrate by mass conservation, thus generating an overturning internal flow, with dyed fluid moving towards the right in the upper part of the droplet. After the travelling wave has passed, the free surface height does not vary significantly, as seen in Figure 7.5 where the edges almost overlap close to the left contact line, especially for $t \geq 6.9$ ms. The wave itself continues across the free surface of the undyed fluid (see the 8.9 ms edge in Figure 7.5). However, dyed fluid is not immediately drawn forward with the wave; instead the surface jet emanates from the dyed fluid approximately 3.0 ms after the reflected wave has passed over the fluid interface due to a surface flow induced by the preceding dynamics.

Bulk interface and jet heights

To elucidate the dynamics of surface jet formation, the leading edges of both the bulk fluid interface and surface jet at the free surface were tracked via image processing as described in Section 3.6. Figure 7.6 displays the free surface height corresponding to the horizontal position of these leading edges (see inset frames), normalised by the initial sessile droplet height. The data correspond to Figure 7.3 as a typical example for the prevailing experimental conditions. From the bottom view, only the maximum penetration of dyed fluid is visible, though it is not necessarily uniform across the droplet depth. In particular, the convex nature of the fluid interface depicted in Figure 7.4 cannot be directly perceived from a bottom view. However, since the leading edge of the bulk (at the time the surface jet breaks away) and the surface jet are located close to the free surface they can be accurately tracked.

Figure 7.6 shows the variation of surface height in time and thus confirms that the free surface at the bulk fluid interface rapidly rises at early times, when the meniscus bridge growth dominates the dynamics there. The concurrent spreading dynamics are subordinated to the meniscus bridge growth, though the former acts to push the bulk fluid interface into the originally undyed fluid region, which contributes to the rise in the bulk

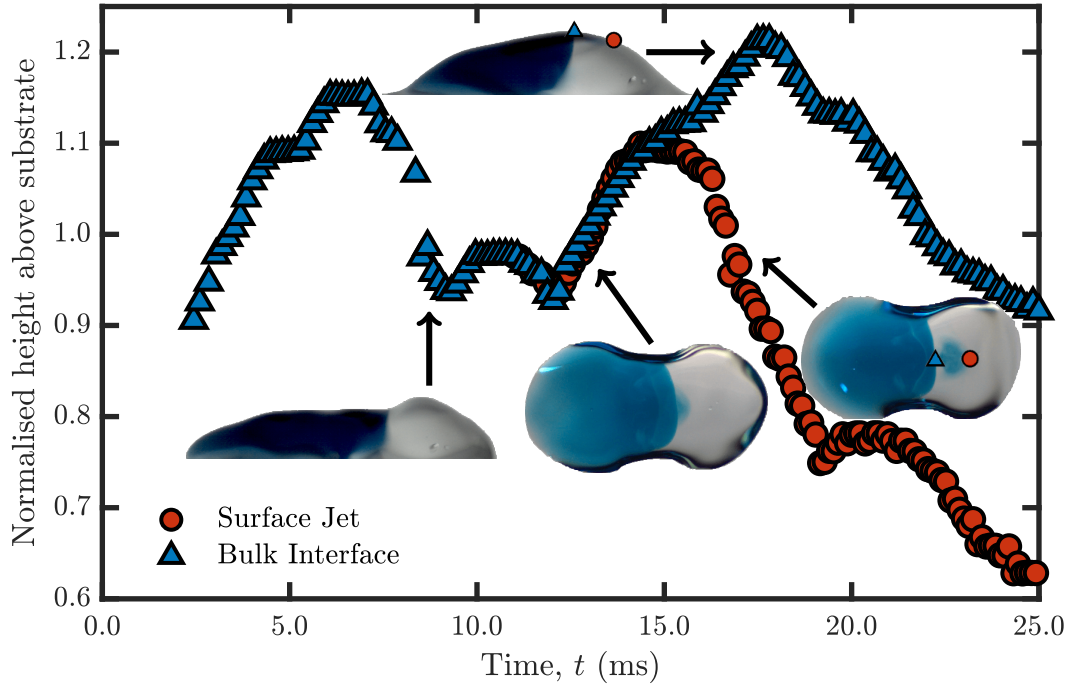


Figure 7.6: Normalised (by the initial sessile droplet height) free surface height for the bulk and jet leading edges, as indicated on the inset frames. The free surface height is extracted by image processing from each front view frame, matched to the horizontal position determined from the corresponding bottom view frame (see Section 3.6). Both droplets consist of fluid 2 (4.0% ethanol). The data correspond to Figure 7.3.

fluid interface free surface height, as the free surface of the undyed fluid is higher than that of the dyed fluid. For the coalescence of symmetric, identical precursor sessile droplets, the free surface height at the fluid interface (directly above the point of coalescence) would be expected to level off and fluctuate around the equilibrium height of the coalesced droplet. However, in Figure 7.6 the aforementioned travelling wave induces a reduction in free surface height at the bulk fluid interface when it approaches approximately 7.0 ms after coalescence. Hence, the travelling wave is characterised by a local depression in the free surface near the bulk fluid interface (also visible in Figure 7.5) as the free surface is higher ahead, similar to a breaking wave. Figure 7.6 therefore shows that the travelling wave passes the bulk fluid interface approximately 9.0 ms after coalescence, beyond which the free surface at the bulk fluid interface rises and the surface jet forms.

The tracking algorithm used in the image processing routine automatically identifies the formation of surface structures emanating from the bulk fluid interface (a surface jet here) in the bottom view, then proceeds to track both the bulk and newly formed leading edges simultaneously. As seen in Figure 7.6, the surface jet does not form immediately as the travelling wave passes the bulk fluid interface, nor advances as fast as the travelling wave. These observations indicate that the surface jet forms due to a surface flow induced by the dynamics accompanying the travelling wave. However, the travelling wave not only generates a surface flow, but also an overturning internal flow as noted above. This inference is supported by the convex nature of the bulk fluid interface shortly after the

formation of the surface jet, as seen at $t = 21.0$ ms in Figure 7.3. Indeed, the interface is further right in the upper reaches of the droplet (not just at the free surface), indicating an internal flow in the same direction as the surface jet. The internal flow is quickly damped by viscosity, so the bulk fluid interface becomes stagnant, but the surface flow faces less resistance and endures to generate and transport the surface jet. After the surface jet has formed, the height of its leading edge is initially similar to the bulk fluid interface, but soon decreases (beginning at $t = 15.0$ ms) due to the remaining free surface oscillations and conventional capillary waves. The corresponding response of the bulk fluid interface in Figure 7.6 is delayed relative to the surface jet due to their horizontal separation at this time, with the delay increasing as the surface jet moves further away, but the same trends are observed in both as expected. After 18.0 ms, the height of both tracked leading edges decreases as they progress at different rates towards the right contact line.

Evaluation of other potential causes of the observed surface jet

In the previous sections, a new phenomenon during coalescence of impacting and sessile droplets has been elucidated, namely the formation of a surface jet. The free surface and internal dynamics were carefully analysed with the aid of image processing to develop the inference that the observed surface jet is the result of a surface flow precipitated by a travelling wave reflected from the left contact line. At this point, it is important to consider other potential causes of surface jet formation (especially relative fluid properties), within the limits of experimental uncertainty.

Surface flows are often caused by differences in fluid properties between coalescing droplets. However, the fluid properties of each precursor droplet in Figure 7.3 where the surface jet is seen are the same, within experimental error. Hence the surface jet does not arise due to density differences, which would typically occur on longer time scales and for a larger Bond number anyway (Zhang et al., 2015). There is also no evidence of density-driven stratification even at later times (up to 1 s after coalescence). As the flow here is surface tension driven ($Oh \approx 5 \times 10^{-3}$), any small difference in viscosity between the coalescing droplets certainly could not generate such flow structures.

The surface tensions of the precursor droplets are nominally the same, and hence Marangoni flow is not expected to occur. However, even if the surface tensions were slightly different (i.e. within the experimental error), Marangoni effects do not explain the jet formation. A distinct and well-defined surface jet is observed, which travels exclusively in one direction, rather than spreading to cover the higher surface tension free surface of the undyed fluid which would occur in a Marangoni flow (see Section 7.4.1 where a surface tension difference is deliberately introduced). Furthermore, if Marangoni flow were responsible, it would only produce local recirculation in the bulk close to the free surface on the short time scale of surface jet formation, rather than the overturning internal flow observed throughout the depth of the droplet here. Therefore, Marangoni flow can not be

the cause of the surface jet seen in Figure 7.3 – though it can modify or even inhibit the jet, as discussed in Section 7.4.1.

Having considered other potential causes of the surface jet, the observations and deductions made in this section substantiate the conclusions drawn in previous sections. That is, the surface jet observed in Figure 7.3 is the result of a surface flow precipitated by a travelling wave reflected from a capillary ridge at the left contact line.

Requirements for surface jet formation

The primary mechanism which generates the observed surface jet is the rapid ascent of the depressed free surface (seen in Figure 7.4) associated with the impacting droplet dynamics, enabled by the surface tension dominated flow (i.e. low Ohnesorge number). Within the deposition regime, the rate of spreading and the maximum spread length increase with impact velocity. The impact velocity must therefore be sufficient for the droplet to spread far and fast enough that the central free surface depression and capillary ridge can form. A large impact velocity may be detrimental to capillary ridge formation due to the associated increase in the maximum spread length, indicating that an intermediate velocity within the deposition regime is required for surface jet formation. The maximum spread length also depends on the advancing contact angle, which was relatively high (approximately 105°) in this work. The substrate wettability is also important after the maximum spread length is reached, as the contact line must remain pinned during fluid reflection to avoid dampening the free surface dynamics and to enable the formation of the travelling wave. In conclusion, the formation of a surface jet depends on the surface tension ratio (a low Ohnesorge number), the impacting droplet velocity (an intermediate Weber number in the deposition regime) and the substrate wettability ($\theta_a \approx 105^\circ$ and pinning here).

7.3.4 Surface jet properties

Propagation

Having understood the formation of the observed surface jet in the previous section, its properties are now considered. Figure 7.7 shows the horizontal position of the bulk and jet leading edges in time, for two experiments with slightly different lateral separation but identical fluid properties – the data correspond to Figures 7.3 and 7.8d. As seen in Figure 7.7, the leading edge of the bulk fluid interface initially migrates quickly into the undyed fluid region due to the ongoing spreading dynamics. The interface continues to advance whilst the meniscus bridge grows, but stalls as the travelling wave approaches due to the latter's effect on the free surface. After the travelling wave passes, the leading edge of the bulk fluid interface retracts due to the internal flow identified above. Note that the bulk leading edge is not necessarily on the free surface at this stage, which explains

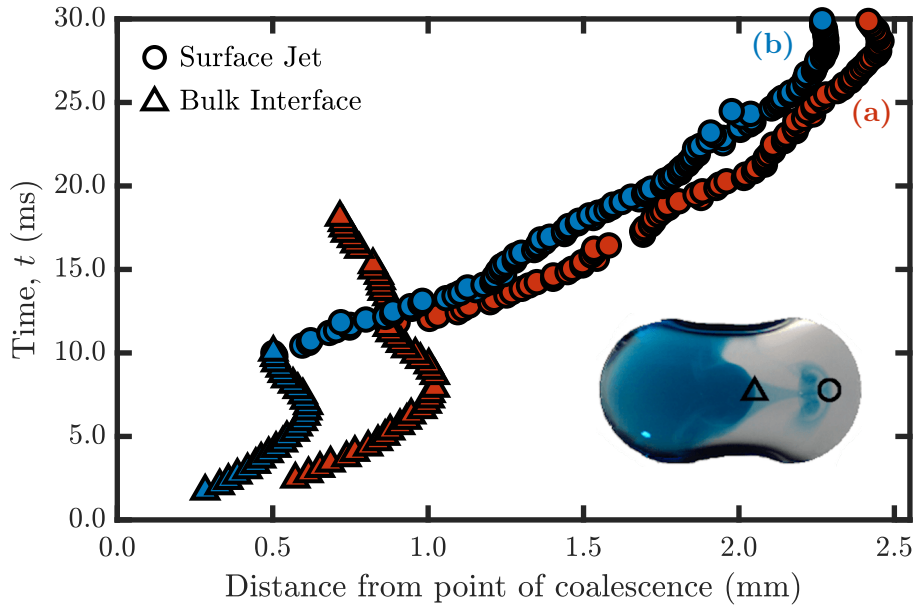


Figure 7.7: Horizontal position of the bulk and jet leading edges, as indicated on the inset frame from case (a), determined from the bottom view frames. In both cases, a fluid 2 (4.0% ethanol) impacting droplet spreads into a sessile droplet of the same fluid. Panel (a) has a lateral separation of 2.91 mm, corresponding to Figure 7.3/7.8a. Panel (b) has a lateral separation of 3.23 mm, corresponding to Figure 7.8d.

why this retraction can occur despite the generally advancing internal and surface flow of the dyed fluid. Figure 7.7 also shows that the jet travels at an almost constant speed across the free surface until it approaches the contact line, and is not greatly influenced by fluctuations in free surface height. The bulk fluid interface continues to slowly retract after the surface jet is emitted, with the surface flow continuing to carry dyed fluid in the opposite direction, despite the internal flow in the upper region of the droplet.

Robustness to lateral separation

The robustness of the surface jet to lateral separation is examined by varying the lateral separation between the precursor droplets (compared to Figure 7.3, with otherwise identical experimental conditions) in Figure 7.8, though the impacting droplet always strikes the substrate before colliding with the sessile droplet. In particular, four different lateral separations from 3.07 mm to 3.25 mm are considered, an increase of 5% to 12% compared to the 2.91 mm lateral separation in Figure 7.3, which is the same experiment as shown in Figure 7.8a. Increasing the lateral separation increases the spread length of the impacting droplet at the point of coalescence. However, the spreading dynamics of the impacting droplet are essentially unaffected by coalescence except in the immediate vicinity of the sessile droplet, so the formation of the capillary ridge and the subsequent fluid reflection are not influenced by small changes in lateral separation. Therefore, as the substrate is strongly pinning, any change in the spread length of the coalesced droplet corresponds to a change in lateral separation. Hence, the central depression (see the sketch in Figure 7.4)

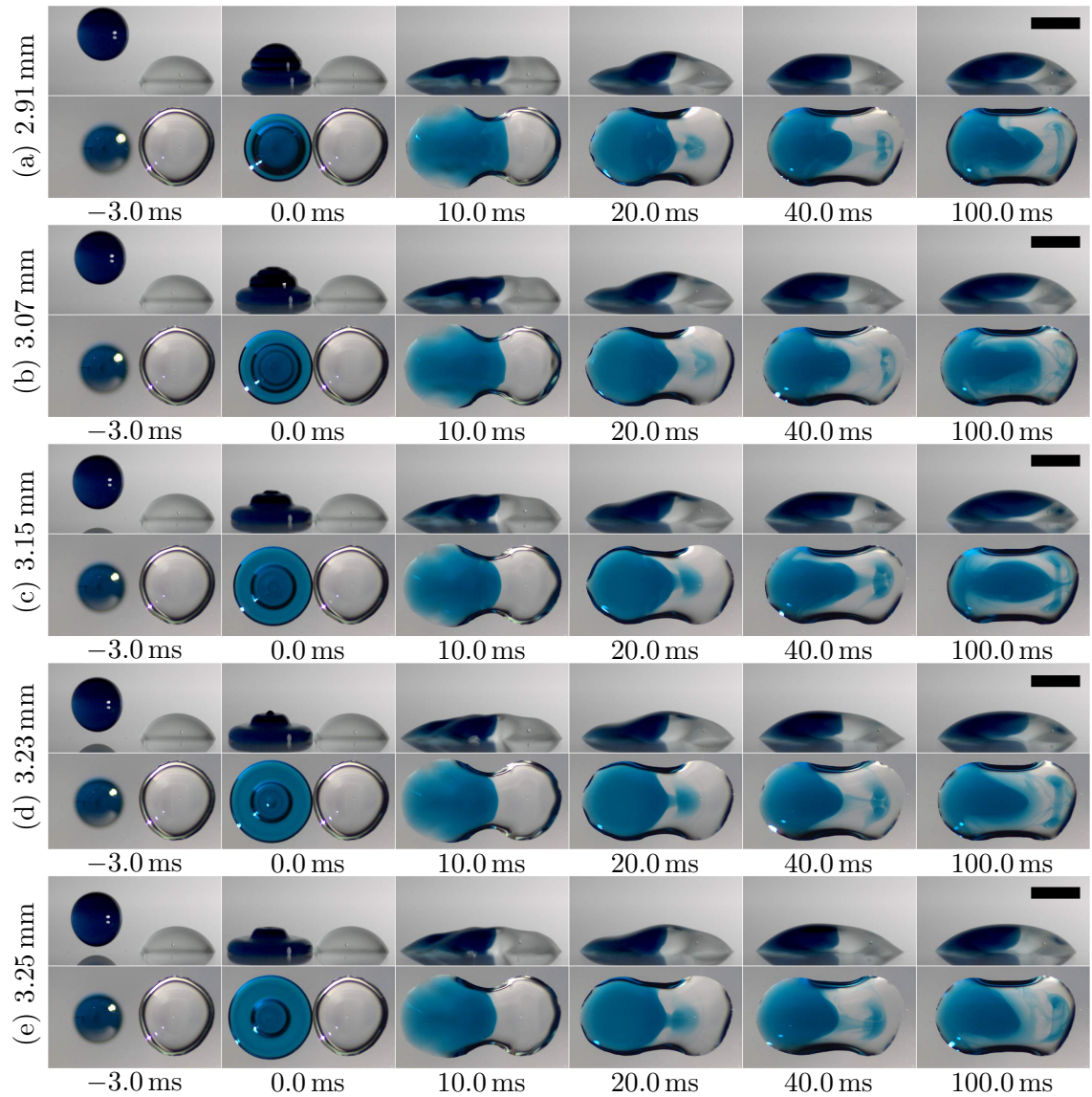


Figure 7.8: Front and bottom views of a dyed impacting droplet coalescing with an undyed sessile droplet of the same fluid (fluid 2; 4.0% ethanol), in which coalescence occurs as the impacting droplet spreads across the substrate into the sessile droplet. The experiment in each panel has a slightly different lateral separation (indicated). All scale bars are 2.0 mm.

is wider for larger lateral separations, whilst the intrusion of dyed fluid into the originally undyed fluid region due to spreading is reduced. Nevertheless, a surface jet materialises for all lateral separations seen in Figure 7.8, with similar internal and free surface dynamics observed, though the precise form of the jet is of course slightly different in each case.

To elucidate the effect of lateral separation on surface jet propagation, the position of the leading edges for the case with a lateral separation of 3.23 mm (Figure 7.8d) is shown in Figure 7.7b, alongside that for the case from Figure 7.3/7.8a in Figure 7.7a. It can be seen that the increase in lateral separation shifts the position of the bulk fluid interface towards the point of coalescence, and jet formation to an earlier time. However, the propagation of the surface jet is hardly affected. Consequently, the formation and propagation of the surface jet is robust to lateral separation in the case that the impacting droplet is deposited on the substrate before spreading into the sessile droplet.

7.4 Droplets of different surface tension

In this section, a surface tension difference is introduced between the coalescing droplets to initiate Marangoni flow and thereby influence surface jet formation.

7.4.1 Surface flow control

Surface jet enhancement

The coalescence of a dyed impacting droplet (fluid 3, $\sigma = 50.5 \text{ mN m}^{-1}$) with an undyed sessile droplet of higher surface tension (fluid 2, $\sigma = 58.0 \text{ mN m}^{-1}$) is shown in Figure 7.9b. Here, a Marangoni flow arises to reduce the surface area of the undyed fluid, which minimises surface energy. Initially, the Marangoni flow entrains a thin layer of dyed fluid onto the free surface around the outside of the undyed fluid (in the plane of the bottom view), which is visible within 3.0 ms of coalescence. Since the two fluids are miscible, the small volume of dyed fluid in the film quickly mixes with the undyed fluid it covers and the surface tension in this region of the free surface does not change appreciably. The free surface dynamics meanwhile are similar to the equal surface tension case (Figure 7.3, repeated in Figure 7.9a), with the formation of a travelling wave precipitating a rapid rise in the free surface of the coalesced droplet. In particular, a surface jet emanates from the dyed fluid region and travels towards the right contact line. However, the induced Marangoni flow also spreads the lower surface tension dyed fluid constituting the jet in all directions across the free surface of the undyed fluid. Hence, Marangoni flow dissipates the inertia of the surface jet, which causes it to stall before reaching the right contact line.

The interruption to jet propagation is clear from Figure 7.10b, in which the maximum penetration of the jet is much less than the corresponding case for droplets of equal fluid

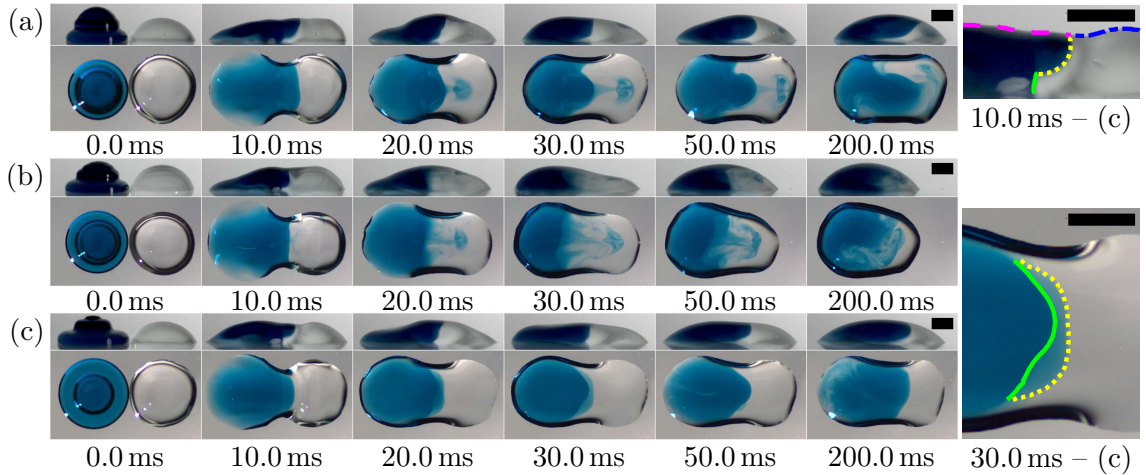


Figure 7.9: Front and bottom views of a dyed impacting droplet coalescing with an undyed sessile droplet, with both precursor droplet fluid properties varied between the panels. (a) A droplet of fluid 2 (4.0% ethanol) impacts a sessile droplet of the same fluid. (b) A droplet of fluid 3 (8.0% ethanol) impacts a sessile droplet of fluid 2 (4.0% ethanol). (c) A droplet of fluid 2 (4.0% ethanol) impacts a sessile droplet of fluid 3 (8.0% ethanol). The impacting droplet is always dyed (blue). All scale bars are 1.0 mm.

properties (Figure 7.10a, which is replotted here from Figure 7.7a). The initial speed of the jet is similar though, before it abruptly slows and stalls. With the increased volume of dyed fluid being transported along the free surface due to Marangoni flow, Figure 7.10b shows that the bulk fluid interface rapidly retracts due to mass conservation, in addition to the internal flow as identified in the equal fluid properties case. This surface flow induces an internal flow that causes the right contact line to retract, whilst the left contact line remains pinned. Marangoni flow also generates additional mixing near the free surface. Hence, the jet penetrates deeper into the coalesced droplet, as visible at $t = 50.0$ ms in the front view, with the head of the jet forming a toroidal section. Increased mixing on a short time scale is therefore observed due to the surface tension difference.

Surface jet suppression

To investigate the influence of deposition order, the fluids are swapped between the precursor droplets in Figure 7.9c compared to Figure 7.9b, though the dye remains in the impacting droplet. Hence, the sessile droplet has a lower surface tension (fluid 3, $\sigma = 50.5 \text{ mN m}^{-1}$) than the impacting droplet (fluid 2, $\sigma = 58.0 \text{ mN m}^{-1}$). Marangoni flow therefore opposes the surface flow that typically generates the surface jet. However, the external dynamics are consistent with those in the other panels of Figure 7.9. Furthermore, the overturning internal flow still arises, which leads to a deformed bulk fluid interface as seen from the image-processed edges also displayed in Figure 7.9. The solid green edges indicate where the internal flow is directed towards the left contact line, whereas the dotted yellow edges indicate the depths at which the internal flow (generated by the travelling wave) is towards the right contact line. The internal dynamics are

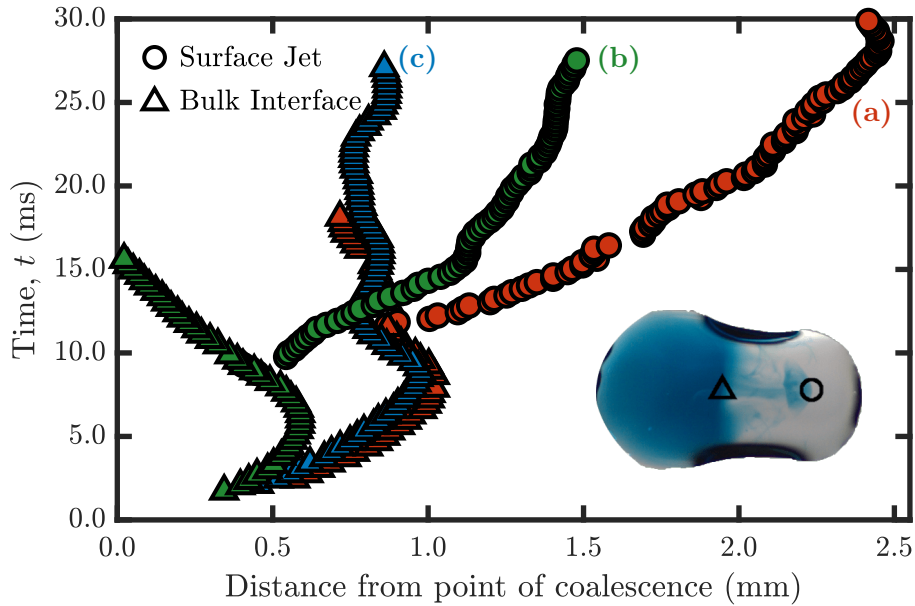


Figure 7.10: Horizontal position of the bulk and (if applicable) jet leading edges, as indicated on the inset frame from case (b), determined from the bottom view frames. Each colour (labelled) corresponds to a different fluid configuration: (a) Fluid 2 (4.0% ethanol) spreads into a droplet of the same fluid, corresponding to Figure 7.9a. (b) Fluid 3 (8.0% ethanol) spreads into a droplet of fluid 2 (4.0% ethanol), corresponding to Figure 7.9b. (c) Fluid 2 (4.0% ethanol) spreads into a droplet of fluid 3 (8.0% ethanol), corresponding to Figure 7.9c.

therefore such that a surface jet could form, but it does not as a result of the opposing Marangoni flow. The suppressed surface flow leaves a distinct, well-defined bulk fluid interface which oscillates around a given horizontal position (Figure 7.10c).

This result demonstrates the influence of deposition order on the internal dynamics when the precursor droplets have different fluid properties, and supports the physical arguments surrounding the internal and surface flows made above. It may also be the physical mechanism underpinning reduced colour bleeding previously observed between inkjet-printed droplets of different surface tension (Oyanagi, 2003).

7.4.2 Time scale analysis

The results in section above can be elucidated by considering the relative time scales of the inertial and Marangoni flows. Due to the low viscosity and high surface tension of the droplets, coalescence proceeds in the inertial regime after the earliest (sub-microsecond) stage of coalescence here (Zhang et al., 2015). Recall from Chapter 2 that the inertial time scale associated with surface-tension-driven flow here is

$$\tau_{\sigma} = \sqrt{\frac{\rho_d r_f^3}{\sigma}},$$

where ρ_d , r_f and σ are droplet density, radius and surface tension, respectively. For a typical droplet in this work (defined in Section 7.2), $\tau_\sigma \approx 4.5$ ms. Note that the inertial time scale relates to the growth of the meniscus bridge between the precursor droplets rather than the dynamics induced by impact and spreading, but it nevertheless provides an indication of the typical inertial time scale and is consistent with the experiments reported. Meanwhile, the time scale associated with Marangoni flow is

$$\tau_m = \frac{(\mu_o + \mu_d)r_f}{\Delta\sigma},$$

where μ_o is the viscosity of the surrounding air. For Figures 7.9b and 7.9c, $\Delta\sigma \approx 8$ mN m⁻¹ and $\mu_o \approx 10^{-5}$ Pa s so the corresponding Marangoni time scale is $\tau_m \approx 0.1$ ms. That is, the Marangoni time scale is at least one order of magnitude shorter than the inertial time scale for the prevailing surface tension difference here, which indicates that the action of Marangoni flow is faster and thus prevents the formation of a surface jet in Figure 7.9c.

Note that the inertial and Marangoni time scales are similar ($\tau_\sigma \approx \tau_m$) if

$$\Delta\sigma \approx (\mu_d + \mu_o) \sqrt{\frac{\sigma}{\rho_d r_f}} \approx 0.3 \text{ mN m}^{-1}. \quad (7.1)$$

Therefore, Marangoni flow can become important in acting as fast as surface tension generated inertial flows for remarkably small surface tension differences. However, for such small surface tension differences the flow induced may not be strong enough to influence the dynamics despite being able to act quickly, especially if there is another influence on the flow, such as the travelling wave in this work. Equation (7.1) nevertheless demonstrates the potential for small surface tension differences to influence internal flows, which could be utilised in the design of devices where larger changes to fluid properties may be undesirable, such as open-surface microfluidics.

7.4.3 Regime map

To elucidate the conditions in which the previously discussed flow structures arise, Figure 7.11 presents a regime map which displays the early time flow structures observed at various lateral separations between the precursor droplets, s normalised by the impacting droplet radius, r_f . Denoting the sessile droplet surface tension as σ_s , the formation of a surface jet depends on the surface tension ratio σ_s/σ and Ohnesorge number (based upon the impacting droplet properties, so $\text{Oh} \propto \sigma^{-1/2}$). Hence, the fluid properties can be adequately characterised by the modified Ohnesorge number $(\sigma_s/\sigma)\text{Oh} \propto \sigma_s \sigma^{-3/2}$ which accounts for both the dominance of surface tension and its difference between the precursor droplets. Each plotted point represents a typical example from at least three repeated experiments of the same case, with the qualitative flow consistent between each repeat.

For $\sigma_s \gg \sigma$, vigorous Marangoni flow is quickly induced at all lateral separations, as indicated by Equation (2.20), preventing larger organised flow structures (e.g. recir-

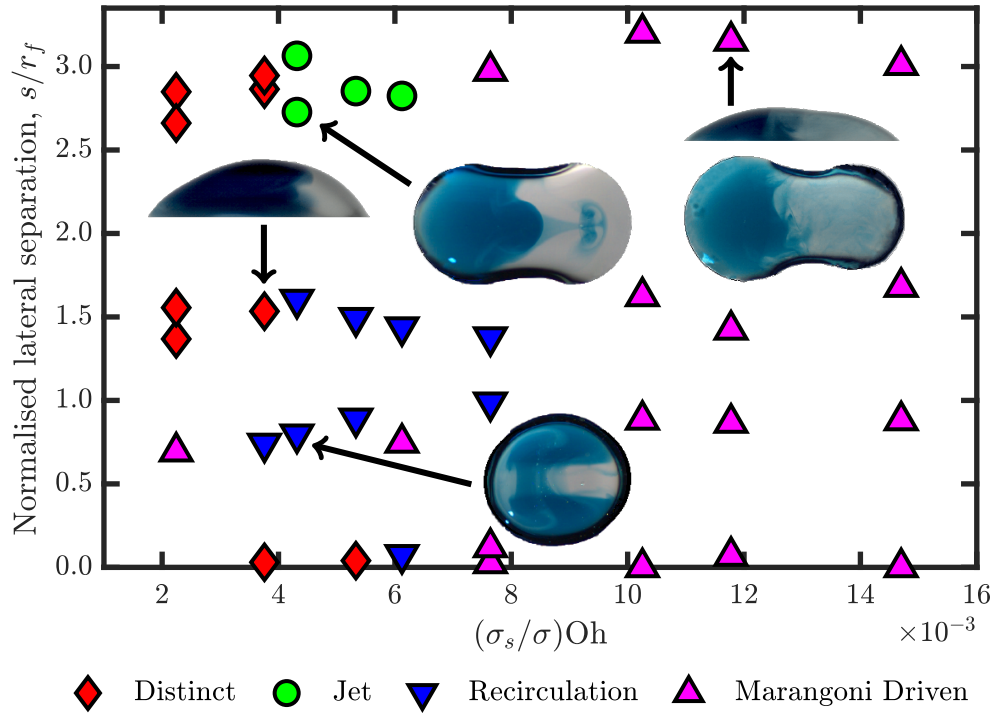


Figure 7.11: Regime map for the early time flow structures seen during the coalescence of impacting and sessile droplets, at various lateral separations and for different relative droplet fluid properties, characterised by a dimensionless group involving the Ohnesorge number (of the impacting droplet) and the surface tension ratio.

culation) from developing. Such cases are described as *Marangoni driven* and typically result in rapid mixing throughout the coalesced droplet, as will be discussed in Section 7.5, and further in Chapter 8. Organised flow structures rely on surface tension dominated flow (i.e. low Ohnesorge number) in addition to a lower surface tension ratio, so typically appear at lower values of $(\sigma_s/\sigma)Oh$. For $\sigma_s \approx \sigma$, the surface jet appears only at the largest lateral separations (when the impacting droplet hits the substrate before spreading into the sessile droplet). The flow is dominated by recirculation (see Figure 7.2) if the lateral separation is smaller for all Ohnesorge numbers studied, as seen in Figure 7.11 by the clustering of blue triangles. A *distinct* interface is maintained between the dyed and undyed fluids (such as in Figure 7.9c) for cases where the sessile droplet surface tension is lower than that of the impacting droplet ($\sigma_s < \sigma$), as explained above, shown as red diamonds (at low values of the modified Ohnesorge number). Whilst there is rapid mixing driven by a local Marangoni flow in the region of the fluid interface in such cases, the interface itself remains sharp due to the suppressed surface flow, without mixing across the whole droplet which occurs in the Marangoni driven cases. A distinct interface can also materialise without surface tension differences for axisymmetric droplet-on-droplet impact ($s/r_f = 0$), as seen in Figure 7.11.

7.5 Long term dynamics and advective mixing

The flows considered so far in this chapter occur on a very short time scale. For example, in Figure 7.3 the surface jet reaches the right contact line less than 30.0 ms after coalescence. Such short term dynamics determine the initial distribution of fluid from each precursor droplet and thus define the initial condition for the longer time scale dynamics which ultimately homogenise the coalesced droplet by molecular diffusion. These longer time scale dynamics are discussed in this section.

Figure 7.12 presents the coalescence of a dyed impacting droplet with an undyed sessile droplet, of various relative fluid properties, to elucidate the effect of surface tension gradients on the long term dynamics and mixing efficiency. Only the fluid properties of the droplets are varied between each panel in Figure 7.12.

In Figure 7.12a, the impacting droplet (fluid 3, $\sigma = 50.5 \text{ mN m}^{-1}$) has a lower surface tension than the sessile droplet (fluid 1, $\sigma = 72.4 \text{ mN m}^{-1}$). A surface flow is visible at $t = 15.0 \text{ ms}$, but the large surface tension difference causes dyed fluid to spread over the sessile droplet, arresting the surface flow and preventing the formation of a well-defined surface jet. After 100.0 ms, the coalesced droplet is comprehensively covered by dyed fluid with significant mixing near the free surface. The bulk is however not fully mixed as indicated by the non-uniform hue across the droplet in the bottom view. After 800.0 ms, the coalesced droplet appears almost homogeneous and is well mixed. For micrometric droplets ($r \approx 25 \text{ }\mu\text{m}$) with the same fluid properties, complete mixing by diffusion alone is expected after a similar time (see Chapter 2). For the millimetric droplets shown in Figure 7.12a, the surface tension gradient drives vigorous internal flow, which improves the efficiency of diffusion to homogenise the coalesced droplet. The fluids are swapped between the precursor droplets in Figure 7.12b compared to Figure 7.12a, with the dye remaining in the impacting droplet. The surface tension gradient suppresses the surface flow, but the overturning internal flow characterised by the deformed bulk interface appears (see also Figure 7.9). The internal fluid interface remains sharp, but rapid mixing (due to the surface tension gradient) causes it to advance rapidly through the droplet over the 600.0 ms shown. However, the extent of undyed fluid infiltration into the dyed fluid region is unclear. Compared to Figure 7.12a, there is significantly less mixing after 600.0 ms, which demonstrates that the order of deposition influences the long term dynamics when the precursor droplets have different fluid properties. In particular, the short term dynamics have a considerable influence on the long term mixing efficiency.

The surface tension of the impacting droplet is progressively decreased through the remaining panels of Figure 7.12, whilst maintaining a consistent sessile droplet of fluid 3 ($\sigma = 50.5 \text{ mN m}^{-1}$). In Figure 7.12c, the impacting droplet consists of fluid 2 ($\sigma = 58.0 \text{ mN m}^{-1}$), as in Figure 7.9c. The dynamics are similar to Figure 7.12b, but there is a reduced surface tension difference so Marangoni flow is less prominent, which results in slower and reduced mixing around the fluid interface. There is also evidence of pattern-

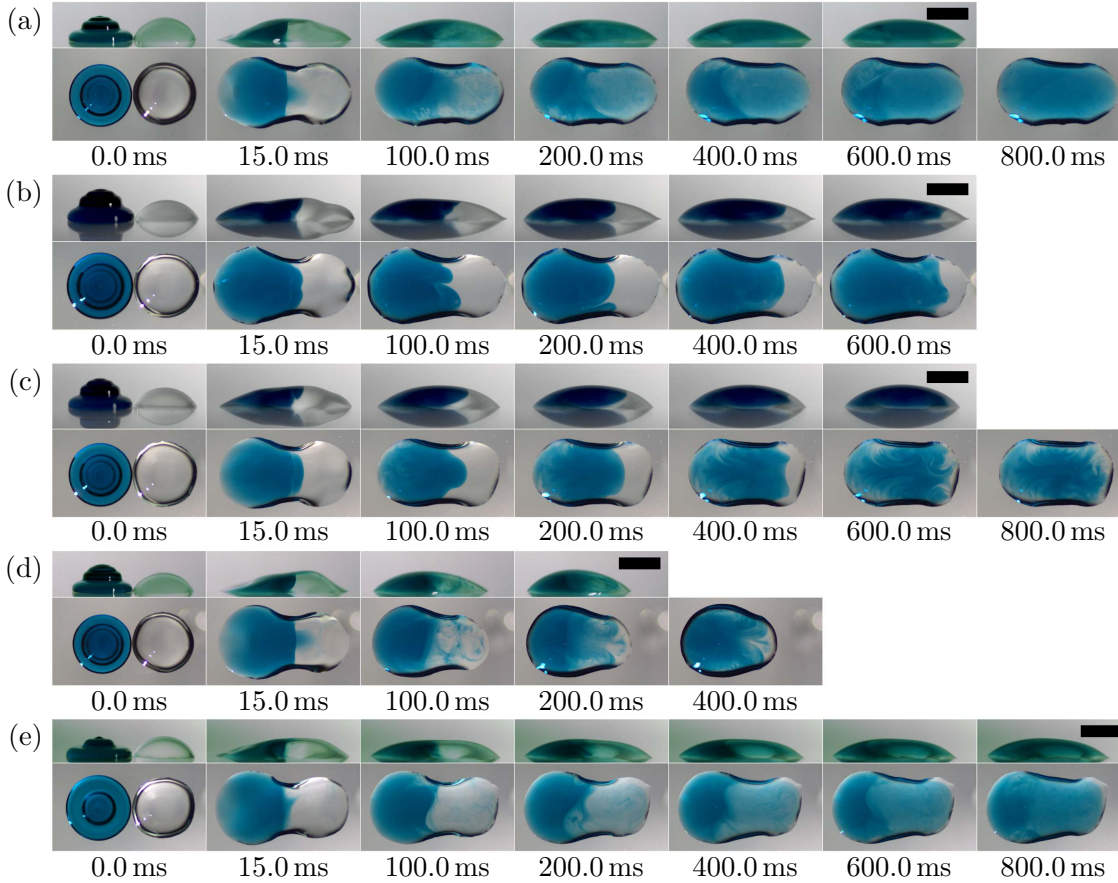


Figure 7.12: Front and bottom views of a dyed droplet impacting droplet coalescing with an undyed sessile droplet, with the fluid properties varied between the panels. (a) A droplet of fluid 3 (8.0% ethanol, $\sigma = 50.5 \text{ mN m}^{-1}$) impacts a sessile droplet of fluid 1 (water, $\sigma = 72.4 \text{ mN m}^{-1}$). (b) A droplet of fluid 1 (water) impacts a sessile droplet of fluid 3 (8.0% ethanol). (c) A droplet of fluid 2 (4.0% ethanol, $\sigma = 58.0 \text{ mN m}^{-1}$) impacts a sessile droplet of fluid 3 (8.0% ethanol). (d) A droplet of fluid 3 (8.0% ethanol) impacts a sessile droplet of the same fluid. (e) A droplet of fluid 4 (18.0% ethanol, $\sigma = 39.9 \text{ mN m}^{-1}$) impacts a sessile droplet of fluid 3 (8.0% ethanol). All scale bars are 2.0 mm.

ing in the dyed fluid at later times as undyed fluid moves towards the left contact line, which is not apparent for larger surface tension differences where Marangoni flow rapidly homogenises the fluid in these regions. In Figure 7.12d, the impacting droplet has the same fluid properties as the sessile droplet (fluid 3, $\sigma = 50.5 \text{ mN m}^{-1}$). A weak surface jet forms that reaches the right contact line, but the surface flow also transports additional dyed fluid across the undyed fluid free surface, as seen at $t = 100.0 \text{ ms}$. Note that this transport of fluid is not spreading due to a Marangoni flow, for which a more uniform film would be expected, such as seen in Figures 7.12a and 7.12e. Instead, the central surface flow observed in other image sequences (see those in Figure 7.8) becomes wider and less distinct due to the lower surface tension, which transports dyed fluid across a greater proportion of the undyed fluid's free surface. Nevertheless, the distribution of dyed fluid after 200.0 ms indicates recirculation of fluid in a jet-like manner on the free surface, with associated retraction of the right contact line. This result shows that the surface jet becomes narrower and stronger as surface tension increases. While dyed fluid is visible throughout

most of the droplet at $t = 400.0$ ms, it mostly resides near the free surface in the originally undyed fluid region with relatively little fluid mixing materialising.

In Figure 7.12e, the impacting droplet has a lower surface tension (fluid 4, $\sigma = 39.9 \text{ mN m}^{-1}$) than the sessile droplet. Hence, a thin film of dyed fluid spreads across the free surface of the undyed fluid due to Marangoni flow, visible at $t = 15.0$ ms, but the surface flow generated by impact is not sufficient to transport dyed fluid a significant distance or form a surface jet. Compared to Figure 7.12a, the flow is less surface tension dominated which reduces the strength of the surface flow generated by impact. Therefore Marangoni-driven spreading becomes more important and dyed fluid is spread rather than propelled across the free surface. The efficiency of mixing in the coalesced droplet is also reduced due to the lower surface tension, reducing the velocity of the Marangoni-induced internal flow and resulting in the droplet being only partially mixed after 800.0 ms.

These results demonstrate that the relative surface tension between precursor droplets influences the long term dynamics and extent of fluid mixing, in addition to the short term dynamics. Mixing efficiency tends to be greatest when the impacting droplet has a lower surface tension than the sessile droplet, since Marangoni flow augments the surface flow initiated by impact and increases the efficiency of molecular diffusion by extending the internal fluid interface. Comparing Figures 7.12a and 7.12e, the mixing efficiency increases and the surface flow becomes stronger as the flow becomes more surface tension dominated. The final droplet footprint is also influenced by the relative precursor droplet fluid properties, which may be important in applications requiring precise droplet placement.

7.6 Discussion and summary

In this chapter, flows generated within impacting and coalescing droplets of equal and distinct surface tension, with various lateral separations between the precursor droplets, have been explored in detail. The fluids used have a high surface tension and low viscosity, leading to surface tension dominated flows exhibiting intricate internal and interfacial dynamics. For precursor droplets of the same fluid properties with small lateral separations, the internal flow within the coalesced droplet is dominated by bulk recirculation due to the impact. However, increasing the lateral separation, such that the impacting droplet first contacts the substrate then spreads into the sessile droplet, results in more complicated internal dynamics and can generate a well-defined surface jet. The surface jet is a robust, repeatable phenomenon that is caused by a reflected wave from the contact line, and the capillary ridge that develops there, for sufficiently large advancing contact angles. This travelling wave produces an internal and surface flow, transporting fluid from the impacting droplet towards the sessile droplet. While the internal flow is rapidly damped by viscosity, the lower resistance at the free surface allows the flow there to continue and generate a surface jet, which travels at roughly constant speed towards the opposite side of the coalesced droplet.

The unequivocal identification of the surface jet was only possible by the combination of front and bottom views, since the bottom view only reveals the presence of a jet but not its depth within the droplet. This observation illustrates the need for caution when assessing internal flows and advective mixing from only one view. Whilst confocal microscopy has successfully resolved internal flows and advective mixing at different depths in far more quiescent cases (e.g. Lai et al., 2010), the time scales of the surface tension dominated flows considered in this work are too short to support its use currently.

By modifying the surface tension difference between coalescing droplets, this chapter shows that surface jets can either be enhanced or suppressed depending on the direction of the resulting Marangoni flow, supported by the derived inertial and Marangoni time scales. Several early-time flow structures are seen, including a sustained distinct separation of the fluid originating in the precursor droplets, or surface jet formation when the surface tension difference is small. For larger surface tension differences, Marangoni flow results in vigorous internal flow which drives different fluids together within the coalesced droplet and contributes to efficient mixing. The conditions for the different flow structures are identified in a regime map expressed in terms of a normalised lateral droplet separation and a modified Ohnesorge number representing the relative droplet fluid properties.

Since the early dynamics determine the distribution of fluid from which longer term mixing dynamics evolve, the order of deposition for droplets of different surface tension is critical for determining the ensuing internal flows and extent of fluid mixing in passively mixed systems. Depositing the higher surface tension droplet first, so that the droplet inertia is not opposed by Marangoni flow, generally improves mixing efficiency. The final droplet footprint on the substrate can also be affected by the deposition order. These results indicate clear practical implications for printing applications where fluid mixing within droplets is either required or undesired.

Chapter 8

Droplet mixing

Previous chapters have generally focused on internal dynamics rather than mixing per se. In this chapter, the mixing dynamics of impacting and coalescing droplets (using the same experimental configuration as was considered in Chapter 7) are of primary interest. The results contained within this chapter are, at the time of writing, unpublished.

8.1 Introduction to colour-change reactions

In previous chapters, as well as in much of the literature (e.g. Lai et al., 2010; Nilsson and Rothstein, 2011; Nowak et al., 2017), an assessment of advective mixing due to surface tension differences was made based on visualising internal flows with an inert dye. As explained in Chapters 2 and 7 though, inert dyes do not allow those regions that are mixed on a molecular level (i.e. *diffusively mixed*) to be identified. However, the extent of diffusive mixing is the primary interest for applications relying on blends of biochemical reagents or reactants generated by coalescence. Instead, with a colour-change reaction, mixed regions attain a different colour from those regions that remain unmixed, due to a modification in the chemical properties of the fluid engendered by mixing. The change in fluid properties concerned is typically a change in pH, thus enabling pH indicators to be used in order to assess the extent of diffusive mixing in coalescing droplets.

One such pH indicator that can partake in a colour-change reaction is phenolphthalein (phph), which is commonly used in acid–base titrations. In solution at acidic or near-neutral pH values, phph exists in a neutral form that appears colourless. Above a pH of approximately 8, phph loses two protons (Le Chatelier’s principle) to OH^- ions to exist in a doubly-deprotonated form (Berger, 1981). This ionisation of phph leads to increased delocalisation of electrons, and the solution appears pink. In strongly basic conditions, the colour fades and phph becomes colourless again, though the conditions and time scales for which this secondary transition occurs means that it is not seen in this work.

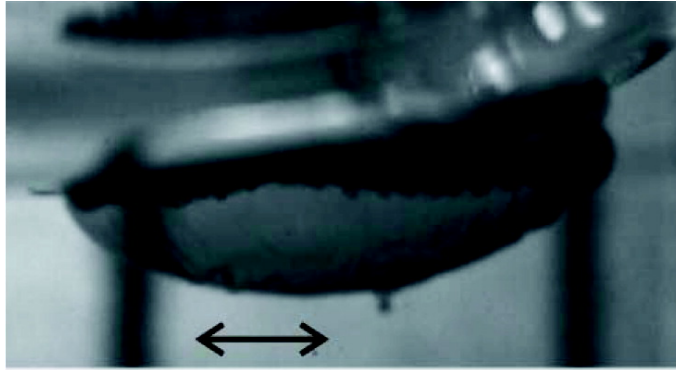


Figure 8.1: Front view of an ethanol-water mixture (20 vol% ethanol) impacting droplet, containing bromothymol blue indicator, coalescing with a 0.1 M NaOH (aqueous) pool, at $t = 1.5$ ms. The double-headed arrow is a 1.0 mm scale bar. The dark band (due to indicator colour change) seen just below the free surface indicates the mixed region. Reprinted (adapted) with permission from Tsuji and Müller (2012). Copyright (2012), American Chemical Society.

Whilst such colour-change reactions have been used to study mixing previously, in both droplet and non-droplet configurations (e.g. Liu et al., 2000; Chainani et al., 2014; Takano et al., 2015; Davanlou and Kumar, 2015), the effect of the colour-change reaction on the dynamics (if any) has been the subject of some ambiguity. Tsuji and Müller (2012) used bromothymol blue (another indicator, with similar action to phph) to observe mixing during the impact of an ethanol-water mixture droplet onto a 0.1 M NaOH pool. Unexpectedly, a colour change (i.e. mixing) was not observed at the maximum penetration depth of the impacting droplet in the pool, but around an ‘equatorial band’ at or near the free surface instead, as seen in Figure 8.1. Moreover, the mixing seen appeared in fingers formed on a millisecond time scale. The lack of observed mixing at the maximum penetration depth was put down to the slow nature of diffusion, whilst the flow generated due to impact engendered the mixing observed in the equatorial band. The origin of the fingers seen is unclear, though it has been shown that an exceptionally wide array of buoyancy-driven instabilities can occur near reaction fronts in which two reactants form a product ($A + B \rightarrow C$ reactions), due to density variations (Trevelyan et al., 2015). Fingers can also be generated in acid-base reactions, such as between HCl and NaOH, in which a NaCl salt is produced (Almarcha et al., 2010). Tsuji and Müller suggest that the fingers seen in their work may be generated by heat diffusion, but it is not clear whether deprotonation of an indicator can produce sufficient heat for this mechanism to be the cause of the fingers/instability seen.

Yeh et al. (2015) conducted an experiment using a similar philosophy to Tsuji and Müller, but for coalescing sessile droplets mobilised by a wettability gradient, using phph as an indicator instead of bromothymol blue. In particular, a 0.1 M (aqueous) NaOH sessile droplet was coalesced with another containing ethanol (potentially a 50.0% ethanol-water mixture based on the reported surface tension¹) and phph. Visualising the dynamics with

¹The original work only says that this droplet was “prepared from phph dissolved in ethanol”, but the reported surface tension of 29.52 mN m^{-1} is roughly consistent with a 50.0% ethanol-water mixture.

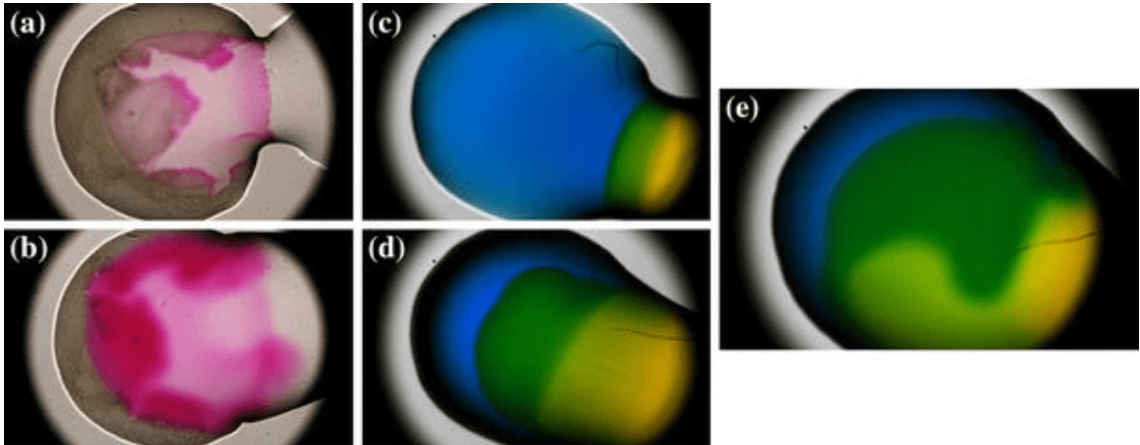


Figure 8.2: Left: Bottom view of a droplet containing ethanol and phph coalescing with a 0.1 M NaOH droplet, after (a) 1.875 ms and (b) 20.000 ms. Mixed regions appear pink. Centre and right: an equivalent case showing a blue droplet coalescing with a yellow droplet of unstated fluid properties, after (c) 1.875 ms, (d) 20.000 ms, and (e) 2000 ms. Mixed regions appear green. In all cases, the precursor droplet volumes are 0.2 μL . Reprinted by permission from Springer Nature Customer Service Centre GmbH: Yeh et al. (2015), Copyright (2015).

only a bottom view, the rate and extent of colour change appeared much faster than in a control experiment of blue and yellow coalescing sessile droplets in which the mixed regions appeared green, as seen in Figure 8.2. Based on the extent of colour change observed from the bottom view after 20 ms for the phph droplets being greater than after 2000 ms in the control experiment (panels (b) and (e) in Figure 8.2), Yeh et al. suggested that the colour-change reaction induced mixing “100 times as efficient as for unreactive fluids mixing inside the coalesced droplet”. As first pointed out by Wilson et al. (2018), the apparent increase in mixing efficiency seen in the phph case may be due to material (in particular, surface tension) differences between the coalescing droplets that could induce Marangoni, Laplace-pressure-driven or density-gradient-driven flows. Moreover, since the dynamics were only observed from below, surface and internal flows can not be distinguished, as was the case for the surface jet in Chapter 7 (see Figure 7.3 in particular). It is therefore not clear that the coalesced droplets were completely mixed in the colour-changed areas, or whether mixing occurred only at one depth (e.g. in a thin film on top of the droplet, as in Figure 7.12 for example). Furthermore, it is not clear whether the fluid properties of the blue/yellow droplets were the same as the colour-change reaction case in Figure 8.2.

Note that chemical reactions *in general* between coalescing droplets can clearly have a significant effect on the internal and mixing dynamics. For example, Khaw et al. (2018) demonstrated an approximate ten-fold increase in mixing rate for magnetically-actuated droplets involving an exothermic acid-base neutralisation reaction between iron oxide and hydrochloric acid, compared to controlled non-reactive droplets. Moreover, reactions involving the production of materials with different physical properties (precipitation, solidification, etc.) may well influence internal and mixing dynamics too. However, the

Table 8.1: Impacting droplet radius, r_f and velocity, u of the ethanol-water mixtures used in the study of mixing via colour-change reactions.

Ethanol Mass %	r_f (mm)	u (m s^{-1})
0.0	1.16 ± 0.02	0.50 ± 0.04
4.0	1.07 ± 0.02	0.51 ± 0.06
8.0	1.02 ± 0.02	0.50 ± 0.04
50.0	0.87 ± 0.02	0.54 ± 0.03
100.0	0.85 ± 0.02	0.51 ± 0.07

hypothesis considered in this chapter is that the observations with respect to internal flows and mixing involving *colour-change reactions* previously made in the literature can be explained by Marangoni flow, due to the different surface tensions of the precursor fluids used in those works.

In particular, it is important to determine whether a colour-change reaction itself has a significant effect on surface tension driven flows such as droplet coalescence – in the case that it does, such a visualisation technique clearly cannot be used to passively monitor internal flows and mixing efficiency. It is also desirable to elucidate the results of both Tsuji and Müller and Yeh et al., which exhibit interesting physics to explore. In this chapter, similar experiments to those in Chapter 7 (impacting and coalescing droplets) are reported, where phph was used to engender a colour-change in mixed regions, in addition to an inert dye (as a control) to visualise the internal flows/advective mixing, and thus conclusively determine the influence of colour-change reactions on internal flows. Moreover, a colour-change reaction is used to monitor mixing in configurations with surface tension differences between coalescing droplets, studying the effect of lateral separation to identify mechanisms of mixing due to Marangoni flow.

8.2 Experimental details

The experiments discussed in this chapter are very similar to those found in Chapter 7, but with a slightly wider range of ethanol-water mixtures deployed. The full range of ethanol-water mixtures used are reported in Table 8.1, along with the velocity and radius of the resulting impacting droplet. Furthermore, phenolphthalein (phph) is used to achieve the desired colour change, as discussed in Chapter 3. Full details of the experimental setup can be found in Section 3.5, with the appropriate approximate dimensionless numbers given in Section 7.2.

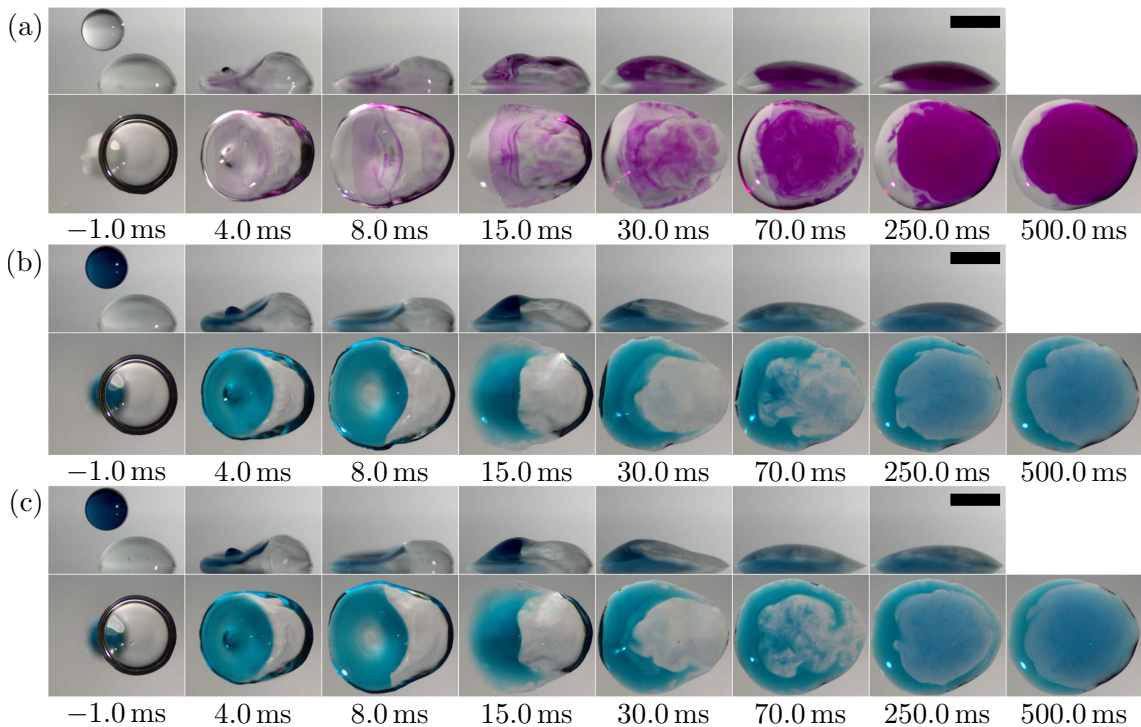


Figure 8.3: Front and bottom views of a 50.0% ethanol-water mixture impacting droplet coalescing with a 0.1 M NaOH sessile droplet in a non-axisymmetric configuration, at a lateral separation such that the impacting droplet hits the sessile droplet before the substrate. (a) The impacting droplet contains phph at a concentration of 5.0 g L^{-1} , so mixed regions appear pink. (b) The impacting droplet contains an inert dye. (c) A repeat of the experiment shown in panel (b). All scale bars are 2.0 mm.

8.3 Effect of colour-change reactions

8.3.1 Non-axisymmetric impact

The non-axisymmetric coalescence of a 50.0% ethanol-water mixture impacting droplet with a 0.1 M NaOH (aqueous) sessile droplet is shown in Figure 8.3. Unlike for impacting droplets of higher surface tension, no delay is seen between impact and coalescence (cf. Section 7.3.1). In Figure 8.3a, mixing is visualised using phph, so mixed areas appear pink. After 4.0 ms, some mixing has occurred, but the front view confirms that it is localised to the narrow interface between the two fluids. With this initial configuration, both inertia and the induced Marangoni flow act to spread the impacting droplet across the higher surface tension fluid of the originally sessile droplet, leading to significant mixing near the free surface (front view at $t = 15.0 \text{ ms}$), but there is little mixing in the bulk. However, in the bottom view most of the droplet has experienced a colour change by this point, despite significant mixing only occurring near the free surface. Colour-change area itself (in the bottom view at least) is evidently not a good indicator of the extent of mixing.

The large initial surface tension difference between the coalescing droplets in Figure 8.3 leads to vigorous Marangoni flow (‘Marangoni ripples’ are clearly visible at $t =$

4.0 ms), which primarily circulates fluid around the free surface to the right (with respect to the bottom view) and back through the middle of the droplet. The majority of the fluid volume appears completely mixed after 250.0 ms, though there is a small volume of fluid (from the impacting droplet) near the left contact line that remains unmixed even 500.0 ms after impact. The lack of mixing there is perhaps unsurprising since there is no mechanism driving fluid from the originally sessile droplet to the left contact line. As determined in Section 7.4.1, depositing the higher surface tension droplet first (as is the case in Figure 8.3) is generally beneficial for mixing, so the lack of mixing near the left contact line seen here may be a persistent undesirable feature of non-axisymmetric coalescence featuring droplets of different surface tension.

The experiment seen in Figure 8.3b has the phph replaced by an inert dye (Malachite green), compared to Figure 8.3a, in order to remove any influence that the colour-change reaction might have on the flow. Whilst only advective mixing can be directly perceived with the inert dye, the internal flow structures seen are clearly very similar to those in Figure 8.3a. In particular, the interface between the dyed and undyed fluids has the same structure as seen with phph, which is especially clear at $t = 8.0$ ms and $t = 15.0$ ms. At later times ($t = 250.0$ ms and $t = 500.0$ ms) by comparing the different ‘shades’ (i.e. hues) of the dye in the bottom view it is clear that the region near the left contact line is unmixed, as identified with easily using phph. The dye is darker in the unmixed regions, but appears as a pastel colour where the droplet is well-mixed at all depths (towards the right). Note that the front view becomes beset by reflections at later times (i.e. $t = 250.0$ ms) when the contact angles and overall droplet height are low, though the extent of mixing is much clearer with phph. Figure 8.3c is a repeat of the experiment shown in Figure 8.3b with a slightly smaller lateral separation. Whilst the precise details of the flows seen in the two panels are slightly different, the general dynamics are remarkably similar. That is, these experiments are repeatable.

The crucial conclusion that can be drawn from Figure 8.3 is that the presence of phph, and the consequent colour-change reaction, does not significantly alter either the internal dynamics or mixing efficiency, otherwise considerable differences in dynamics would be expected between Figure 8.3a and Figure 8.3b/8.3c. Whilst a minor effect due to the colour-change reaction cannot be ruled out, which may be exothermic (as phph/NaOH represents a Brønsted–Lowry acid-base pair), it evidently does not greatly influence the internal dynamics. Hence, these results strongly suggest that colour-change reactions utilising phph can be employed as a faithful passive (with respect to the flow) indicator of mixing. In particular, no significant increase in mixing rate, or change in the internal dynamics, due to the colour-change reaction is expected from the observations made here.

Similar experiments to those in Figure 8.3 are shown in Figure 8.4, where the impacting droplet fluid is 100% ethanol, which has a lower surface tension (by 6.0 mN m^{-1}) than the 50.0% ethanol-water mixture used in the former figure. Two different lateral separations are shown: 1.8 mm in Figure 8.4a and 3.5 mm in Figure 8.4b. Excessive evaporation

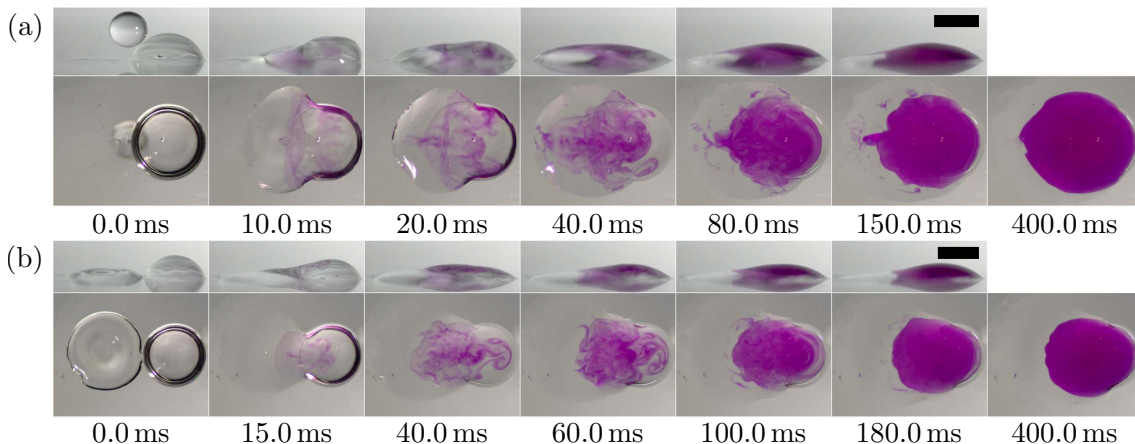


Figure 8.4: Front and bottom views of a pure ethanol impacting droplet coalescing with a 0.1 M NaOH sessile droplet, at two different non-zero lateral separations: (a) 1.8 mm; (b) 3.5 mm. In both cases, the impacting droplet contains phph at a concentration of 5.0 g L^{-1} , so mixed regions appear pink. All scale bars are 2.0 mm.

of the ethanol droplet made this experiment very challenging; some ethanol deposits on ‘dry’ areas of the substrate are visible in the figure, which have a negligible effect on spreading of both the impacting and coalesced droplets, but were found to be virtually unavoidable. However, the main aim of this figure is to confirm whether the dynamics with a 100% ethanol impacting droplet are similar to those with a 50.0% ethanol-water mixture (no preferential evaporation occurs in the former case), which would be expected due to the similar surface tension differences with respect to the consistent sessile droplet. Note that the time scales on which density-driven flows act are larger than both the inertial and Marangoni time scales (Zhang et al., 2015), and so the increased density difference between the precursor droplets with the 100% ethanol impacting droplet is inconsequential. Comparing Figures 8.3 and 8.4, similar internal and mixing dynamics are indeed seen, supporting the conclusions made above.

8.3.2 Sodium hydroxide

The only difference between the colour-change ‘reactive’ and inert dye ‘unreactive’ cases above was the presence of phph in the former and Malachite green in the latter, in an effort to isolate the role of phph. In particular, the fluids were not changed, so in both cases one droplet consisted of 0.1 M NaOH solution, whilst the other was an ethanol-water mixture. This is acceptable with respect to elucidating the role of the colour-change reaction, since no chemical reaction occurs between these two fluids, including between ethanol and aqueous sodium hydroxide. Indeed, the proposed reaction would be



but since ethanol ($\text{CH}_3\text{CH}_2\text{OH}$) is a weaker acid than water and the Na^+ & OH^- ions are mobile in solution, such a reaction does not occur.

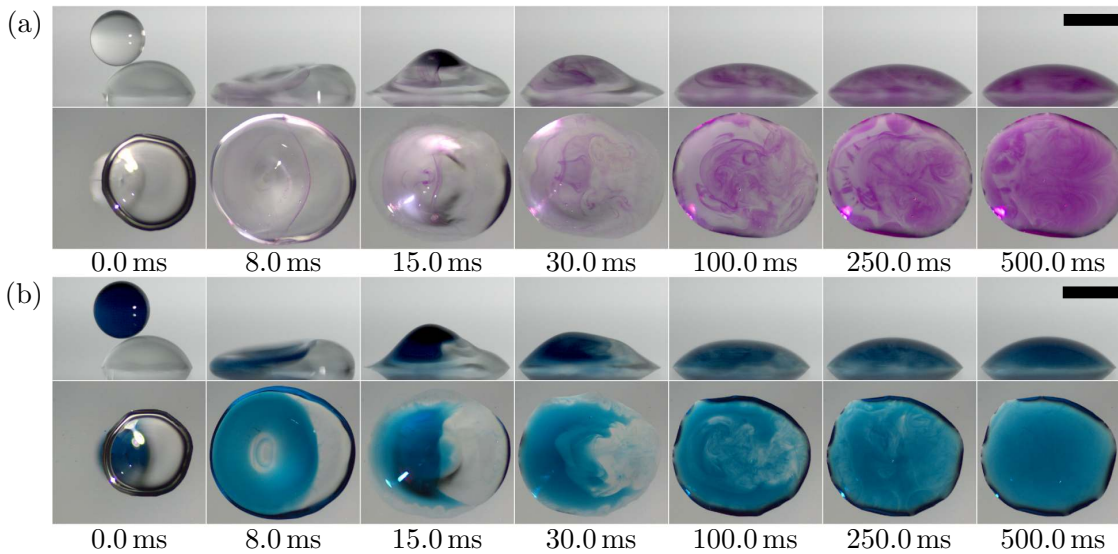


Figure 8.5: Front and bottom views of a 18.0% ethanol-water mixture impacting droplet coalescing with a 4.0% ethanol-water mixture sessile droplet in a non-axisymmetric configuration. (a) The impacting droplet contains phph at a concentration of 3.0 g L^{-1} , whilst the sessile droplet contains NaOH with molarity 0.01 M, so mixed regions appear pink. (b) The impacting droplet contains an inert dye. All scale bars are 2.0 mm.

In the interest of completeness however, Figure 8.5 exhibits the non-axisymmetric coalescence of an impacting droplet consisting of an 18.0% ethanol-water mixture and a sessile droplet consisting of a 4.0% ethanol-water mixture. In panel (a), the impacting droplet contains phph at a concentration of 3.0 g L^{-1} , whilst the sessile droplet contains 0.01 M NaOH. Note that the pink colour of the phph in mixed regions is less intense here than in the figures above, since the concentration of phph used is reduced as the proportion of ethanol is not sufficient to dissolve phph to the 5.0 g L^{-1} concentration used above. In panel (b), the impacting droplet contains an inert dye (Malachite green). In particular, neither NaOH nor phph are present in the experiment shown in Figure 8.5b. As seen, the dynamics in both panels of Figure 8.5 are very similar, which suggests that the presence of NaOH does not have any significant effect on the dynamics (as already confirmed for phph above). Hence, it appears that colour-change reactions can be used to study mixing without any significant influence on the dynamics, i.e. as a dynamically-passive indicator of diffusive mixing.

8.3.3 Reassessment of colour-change reactions

The results above indicate that colour-change reactions do not have a significant effect on the dynamics of coalescence. Given this inference, and with the knowledge of the mixing mechanisms identified above, the flows seen in the works of Yeh et al. (2015) and Tsuji and Müller (2012) are now elucidated.

In the case of Yeh et al. (for the phph sessile droplet coalescence configuration),

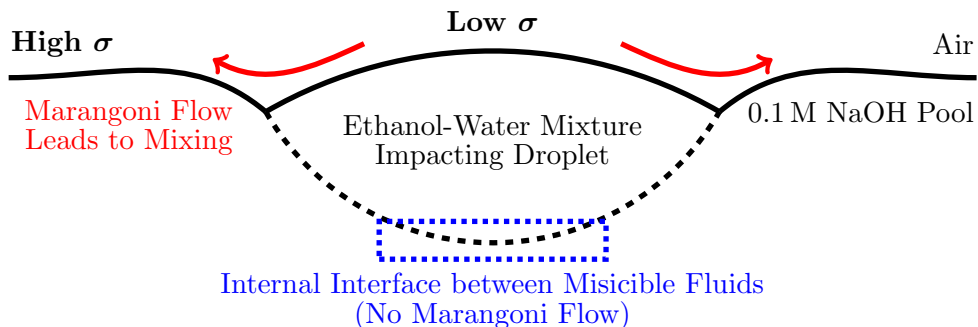


Figure 8.6: Sketch of mixing mechanisms during the impact of an ethanol-water mixture droplet onto a NaOH pool, consistent with the work of Tsuji and Müller (2012) – see Figure 8.1. The red arrows indicate Marangoni flow. The black dashed line indicates the nominal internal interface between the miscible fluids.

surface tension differences between the coalescing droplets may play the dominant role in the dynamics observed. Indeed, the difference in surface tension between the fluids is likely to cause the fluid of the lower surface tension coalescing droplet to spread over that of the other due to Marangoni flow, with mixing occurring only near the free surface of the coalesced droplet, as in Figure 8.3 on short time scales. The smooth circular front and internal fingers identified by Yeh et al. are also characteristic of Marangoni-driven spreading (Keiser et al., 2017). It is thus expected that the provision of a front view for Figure 8.2 would display colourless (i.e. unmixed) fluid in most of the bulk, and so minimal mixing after 20.0 ms that belies the bottom view of the dynamics. This inference is supported by any colour change only being seen within the region of one precursor droplet in Figure 8.2a, as Marangoni flow would only act to drive flow in one direction in order to cover the higher surface tension fluid and so minimise surface energy – the droplet on the LHS therefore appears to have a higher surface tension. Hence, the dynamics appear to be similar to those of impacting and coalescing droplets elucidated above.

With regard to the control experiment carried out by Yeh et al. featuring blue and yellow dyes, since these dyes are not colourless any spreading of either fluid over the other may not necessarily be visible (e.g. in Figure 8.2c). Moreover, the fact that the droplets are not fully mixed (i.e. appear wholly yellow) after 2.0 s in Figure 8.2e despite the small droplet volumes ($0.2\ \mu\text{L}$ for each precursor droplet) suggests that there is no significant Marangoni flow in the control experiment, which as shown above (see Section 7.5) tends to engender fast mixing in low-viscosity ethanol-water mixtures. Thus, the differences seen between the ‘reactive’ and ‘unreactive’ cases shown in Figure 8.2 are likely due to fluid properties rather than an active effect of the colour-change reaction.

Marangoni flow may also play a significant role in the experiment considered by Tsuji and Müller. In that case, a low surface tension droplet impacts a pool of higher surface tension, so Marangoni flow is expected from the impacting droplet fluid outwards along the free surface of the pool (again, to minimise surface energy). This process is depicted in Figure 8.6, which is a sketch representing an idealised vertical cross-section through

the axis of symmetry shortly after impact. At the nominal intersection of the pool and droplet fluids free surfaces, the red arrows identify the direction of Marangoni flow, with the droplet fluid being spread across the pool fluid. Of course, droplet impact is a dynamic situation, which is likely to propel the droplet fluid outward near the free surface, leading to ‘retraction’ of the droplet-pool-air triple-line (akin to a contact line on a substrate) towards the equilibrium height of the pool, from a depressed position due to impact. These factors (Marangoni flow and mass transfer due to the impact dynamics) may be the cause of the mixing in the equatorial band identified by Tsuji and Müller. Moreover, the lack of mixing at the maximum penetration depth of the impacting droplet on short time scales may be due to the lack of such factors, as the two fluids in question are miscible, so there is no internal interface for Marangoni flow to act on. Thus, mixing there relies on diffusion and other effects (e.g. density/viscosity differences) not apparent on short time scales, leading to a lack of mixing there seen in Figure 8.1, which shows the situation only 1.5 ms after impact.

Both the new work for impacting and coalescing droplets presented here, and the existing works of Yeh et al. and Tsuji and Müller, demonstrate that coalescence and mixing of droplets is a complex process that can be significantly influenced by surface tension differences, which give rise to Marangoni flow. Moreover, with the benefit of multiple views of the dynamics and careful consideration of fluid properties, the analysis presented here strongly suggests that such mixing processes can be well studied using colour-change reactions without a significant influence on the dynamics, i.e. colour-change reactions effectively act passively with respect to the dynamics.

8.4 Mixing in different droplet configurations

8.4.1 Axisymmetric impact and coalescence

Having verified the utility of colour-change reactions to assess mixing above, phph is used in Figure 8.7a to study the axisymmetric coalescence of a 50.0% ethanol-water mixture impacting droplet with a 0.1 M NaOH sessile droplet. An equivalent experiment using an inert dye for visualisation is shown in Figure 8.7b. After 10.0 ms, mixing is seen across the whole droplet in the bottom view, though it is clearly localised to a thin layer near the interface of the two precursor droplet fluids based on the front view. By $t = 40.0$ ms, significant mixing near the contact line of the coalesced droplet is evident in Figure 8.7a, with circular pink regions in the bottom view highlighting the location of the vortices there, which is not conspicuous when using only an inert dye to visualise the internal dynamics, i.e. in Figure 8.7b. Meanwhile, the bulk is poorly mixed at this time. The vortices identified are likely to be primarily due to internal flow generated by the impact dynamics (i.e. down and outwards toward the contact line in the coalesced droplet), but earlier frames in Figure 8.7 indicate asymmetric spreading of the impacting droplet

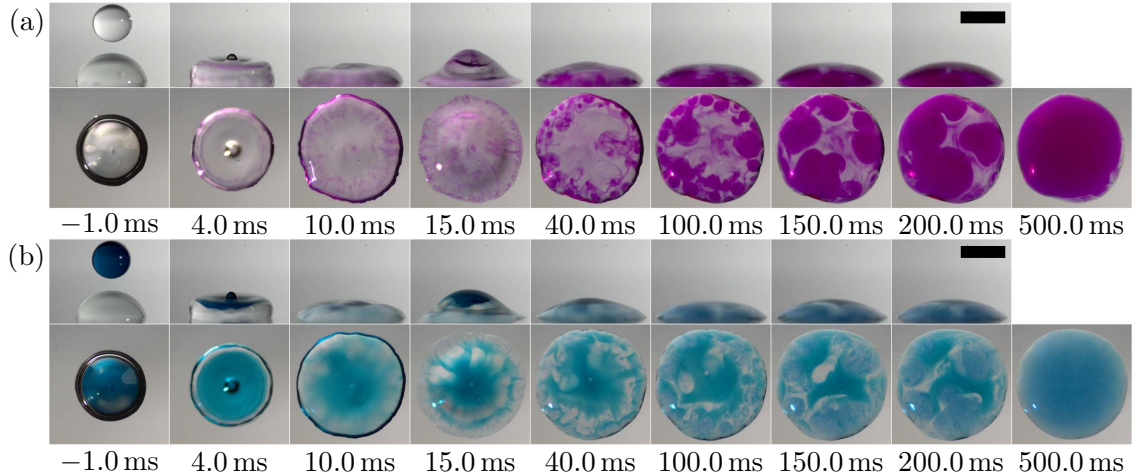


Figure 8.7: Front and bottom views of a 50.0% ethanol-water mixture impacting droplet coalescing with a 0.1 M NaOH (aqueous) sessile droplet in an axisymmetric configuration. (a) The impacting droplet contains phph at a concentration of 5.0 g L^{-1} , so mixed regions appear pink. (b) The impacting droplet contains an inert dye. All scale bars are 2.0 mm.

fluid across the free surface of the originally sessile droplet fluid, which contributes to the asymmetry in the mixing dynamics seen.

The well-mixed vortices subsequently merge and ‘erupt’ away from the contact line, as is already visible in the 40.0 ms frame of Figure 8.7a, leading to the formation of several well-mixed (likely through the whole droplet depth) ‘cores’ by $t = 150.0 \text{ ms}$ (especially visible in the bottom view). This means of mixing is very interesting since the length scale of the cores is much smaller than that of the whole coalesced droplet, thus enabling more efficient mixing within each core before they merge together to yield a homogeneous coalesced droplet 500.0 ms after coalescence. Whilst repeated experiments showed deviations in the precise number and structure of vortices and cores seen (as can be perceived by comparing Figures 8.7a and 8.7b), these structures are a persistent feature of repeated experiments, of which the two shown in Figure 8.7 are typical. Since the cores expand from vortices in the contact line, the latter being primarily due to the impact dynamics, it is expected that such internal dynamics would be robust to modest variations in fluid properties. However, the rapid mixing seen in Figure 8.7 is clearly enabled by vigorous Marangoni flow due to the large surface tension difference ($\geq 40 \text{ mN m}^{-1}$) between the precursor droplets. Moreover, between Figures 8.3 and 8.7 the only difference is the lateral separation, yet no unmixed regions at $t = 500.0 \text{ ms}$ are seen in the latter. Hence, the axisymmetric configuration leads to improved mixing efficiency here.

8.4.2 Non-zero lateral separation

Finally, the effect of varying lateral separation on mixing is considered for a case with a lower surface tension difference than that considered above, thus yielding less vigorous Marangoni flow and so enabling inertia-driven flow structures to be more clearly identified.

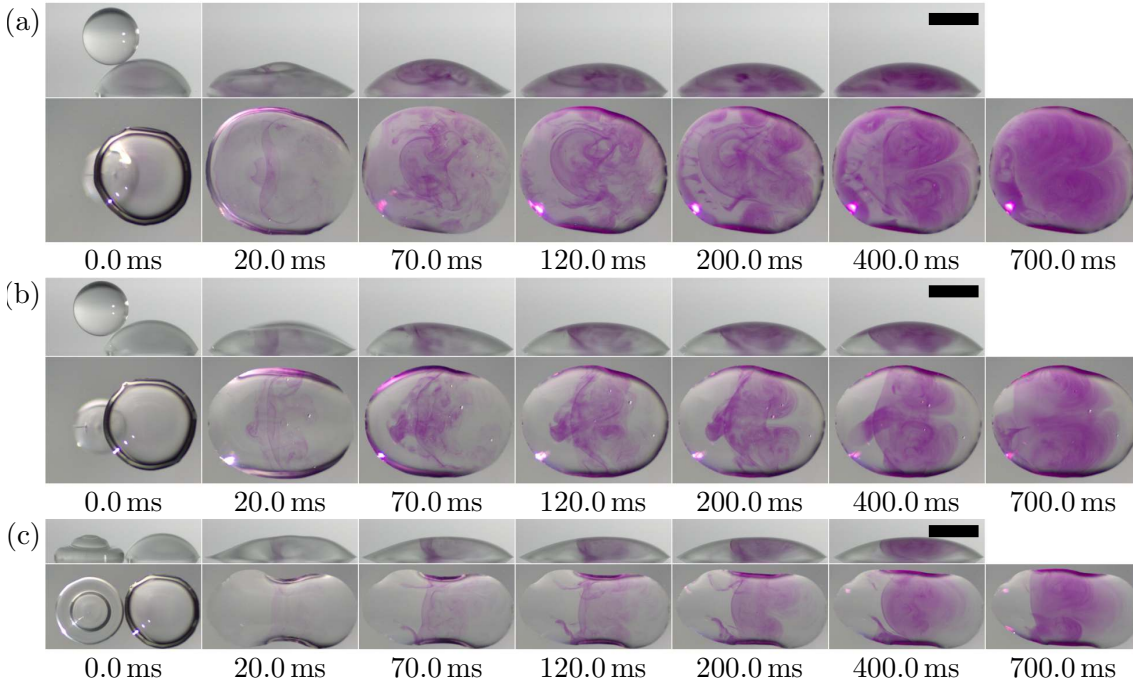


Figure 8.8: Front and bottom views of a 18.0% ethanol-water mixture impacting droplet (containing phph at a concentration of 3.0 g L^{-1}) coalescing with a 4.0% ethanol-water mixture sessile droplet containing NaOH with molarity 0.01 M. Only mixed regions appear pink. The lateral separation is varied between panels: (a) 1.2 mm; (b) 1.8 mm; (c) 3.2 mm. All scale bars are 2.0 mm.

Indeed, Figure 8.8 displays the non-axisymmetric coalescence of a 18.0% ethanol-water mixture impacting droplet (containing 3.0 g L^{-1} phph) with a 0.01 M NaOH 4.0% ethanol-water mixture sessile droplet, at three different lateral separations: 1.2 mm in Figure 8.8a, 1.8 mm in Figure 8.8b, and 3.2 mm in Figure 8.8c.

For the smallest lateral separation considered (1.2 mm in Figure 8.8a), mixing is confined to the free surface in the central region of the coalesced droplet (roughly coinciding with the droplet overlap at $t = 0.0 \text{ ms}$) at early times ($t \lesssim 100.0 \text{ ms}$), after which recirculatory flow develops that is directed around the outside of the droplet to the right, and returns back through its centre. Such recirculatory flow was seen for equal surface tension droplets at a similar lateral separation in the previous chapter (see Figure 7.2). The recirculatory and Marangoni flows are not particularly strong though, so even after 700.0 ms the droplet is not fully mixed, especially toward the LHS of the droplet and near the contact line. The lack of mixing in the LHS of the droplet is to be expected, as the primary flow due to impact is to the right.

The lateral separation is increased in the other panels compared to Figure 8.8a such that the impacting droplet either just collides with the sessile droplet before the substrate (Figure 8.8b), or strikes the substrate first (Figure 8.8c). For both of these larger lateral separations, mixing is seen in the centre of the droplet as in Figure 8.8a, but appears to be only near the free surface for early times ($t \lesssim 150.0 \text{ ms}$). However, in these cases the impact

dynamics somewhat partition the coalesced droplet into three regions: a central region in which mixing is seen, and two outer regions (left and right with respect to the front view) that remain unmixed even at $t = 700.0$ ms (especially for the lateral separation prevalent in Figure 8.8c). Indeed, the fluids from each precursor droplet are only brought into close proximity near the point of coalescence (which becomes the central region of the coalesced droplet), whilst the impact dynamics generally transport the fluids outwards (i.e. away from the other) towards the extremities of the coalesced droplet. Moreover, there is neither an impact-generated internal flow structure (e.g. bulk recirculation) to transport either fluid across the central region and towards the other in order to mix the outer regions, nor sufficiently strong Marangoni flow to dominate the impact-generated internal flow and engender good mixing in the extremities. As expected due to reduced initial overlap of the droplets, for larger lateral separations the extent of the unmixed outer regions is greater, whilst poorer mixing is seen in the centre (comparing Figures 8.8b and 8.8c).

Such a lack of mixing in the outer regions of the coalesced droplet for the larger lateral separations in Figure 8.8 would clearly be an issue in applications for which good mixing and a homogeneous coalesced droplet is required. However, good mixing in the centre is seen and unmixed side regions are made up of fluid consistent with the initial configuration (i.e. impacting droplet fluid on the left; sessile droplet fluid on the right). Hence, good mixing might be expected if multiple droplets were sequentially deposited with non-zero lateral separation (i.e. line printing) and the fluids alternated. Such a configuration could avoid unmixed outer regions by bringing the other fluid into close contact with it via a newly deposited droplet to transform the as-yet unmixed outer region into a new central region in which good mixing would be expected. Moreover, for increased lateral separations (especially when the impacting droplet spreads into the sessile droplet as in Figure 8.8c), as both outer regions are unmixed there would be no significant risk of ‘trapping’ newly deposited (unmixed) fluid between the premixed region on one side and the subsequently deposited droplet of the other fluid on the other side. Such line printing is typically utilised in additive manufacturing to build-up structures sequentially in layers, or to print conductive circuits (e.g. Li et al., 2009), with Figure 8.8 suggesting that a careful choice of lateral offset appropriate to the fluid properties utilised could lead to good mixing and thus a homogeneous line via droplets of different fluids, as is required in reactive inkjet printing for additive manufacturing applications.

8.5 Discussion and summary

This chapter has considered the dynamics of mixing within impacting and coalescing droplets of non-equal surface tension. The fluids used were all derivatives of ethanol-water mixtures, thus exhibiting surface tension dominated flow at low Ohnesorge number. Whilst Chapter 7 showed that inert dyes are excellent for studying internal dynamics in general, this chapter has demonstrated the efficacy of colour-change reactions for studying mixing, in which a colour change is only seen in mixed regions. Through a careful and

extensive comparison to equivalent cases without a colour-change reaction, it was confirmed that a colour-change reaction itself does not have a significant influence on droplet dynamics. Moreover, previous unexplained observations regarding mixing during both droplet-pool and sessile-sessile-droplet coalescence were shown to be consistent with the effects of Marangoni flow, which is supported by and builds upon the results of Chapter 7.

The use of a colour-change reaction uncovered that large surface tension differences can lead to efficient mixing, especially for small lateral separations. In the axisymmetric case, an interesting mechanism of mixing was identified in which mixing occurs around vortices near the contact line, which expand to form several well-mixed ‘cores’ that subsequently merge to yield a homogenous droplet on a desirably short time scale. For smaller surface tension differences at non-zero lateral separations, good mixing is typically seen in the central region of the coalesced droplet, whilst outer regions remain unmixed. However, by depositing multiple droplets sequentially and alternating the droplet fluid between each deposition, a homogenous (i.e. well-mixed) structured deposit could be expected via droplets of different fluids, as is required in applications such as reactive inkjet printing for additive manufacturing.

Chapter 9

Conclusions

9.1 Summary of the work

The internal dynamics of coalescing droplets determine the extent of advective mixing within the coalesced droplet, and hence the efficiency of molecular diffusion to homogenise the fluid. Efficient droplet mixing is required in a wide range of applications, from inkjet-based technologies (e.g. reactive inkjet printing) to microfluidics (e.g. lab-on-a-chip), and especially where a chemical reaction is intended to take place between the fluids from each droplet. Many of these applications involve droplets on substrates, though the effect of substrates on internal flows has received limited attention. A better understanding of internal flows in such configurations is vital for controlling the efficiency and extent of fluid mixing within the coalesced droplet.

This work has elucidated internal flows within coalescing droplets in multiple configurations, but with a common theme of a substrate and its properties being an important factor. Both high-speed imaging experiments and OpenFOAM numerical simulations were used to study such flows, often working in complementary ways in order to fully explore and understand the mechanisms underpinning dynamics observed. In particular, two experimental setups (detailed in Chapter 3) were used to visualise internal flows ensuing between either initially-static free and sessile coalescing droplets in an axisymmetric configuration, or impacting and sessile coalescing droplets with various lateral separations. Both setups acquire a front view of the dynamics, but the latter also features a bottom view enabling a thorough assessment of mixing to be made. Moreover, numerical simulations were carried out using an OpenFOAM solver that was customised during the course of this work. The modifications included the addition of the Kistler dynamic contact angle model to capture substrate wettability and the transport of an additional bounded passive scalar used to assess advective mixing. Extensive validation of the solver was provided, plus examples of free droplet coalescence considered, in Chapter 4.

The results derived from the high-speed imaging experiments and numerical sim-

ulations are summarised in the next section, whilst a more detailed discussion of the conclusions can be found in the last section of each respective primary results chapter.

9.2 Key results

In Chapter 6, both high-speed imaging and numerical simulations were deployed to study internal jet formation during the coalescence of an initially-static free droplet with a sessile droplet in an axisymmetric configuration. Qualitative and quantitative validation of the numerical simulations against the image-processed experiments was achieved. The Kistler dynamic contact angle model was separately shown to match the experimentally-measured contact angles with respect to the contact line speed too, confirming that its use was appropriate in this work. A mechanism of internal jet formation was identified, which relies on the formation of a thinning neck at the top of the coalesced droplet to generate a ‘tip’ with high curvature (and thus high pressure) that accelerates downward flow towards the substrate, imparting significant momentum into the bulk. This mechanism is distinct to that leading to internal jet formation in free droplets, with jets seen at very different volume ratios between the two configurations. In particular, it was demonstrated that the formation of the tip depends on reflected capillary waves, and thus on substrate wettability principally through the receding contact angle. Hence, substrate wettability directly affects jet formation and mixing efficiency in coalescing droplets. Moreover, the dependence on wettability was systematically demonstrated via regime maps concerning the advancing and receding contact angles, volume ratio and droplet viscosity, which show that contact angle hysteresis is not necessarily an accurate predictor of internal jet formation, indicating a more nuanced relationship between substrate wettability and mixing than has been appreciated previously.

In Chapter 7, high-speed imaging was used to study internal flows during the coalescence of impacting and sessile droplets at various lateral separations. For droplets of equal surface tension at large lateral separation such that the impacting droplet struck the substrate before spreading into the sessile droplet to initiate coalescence, a *surface jet* atop the originally sessile droplet was identified, through the provision of two camera views. By quantitative image processing, the mechanism of jet formation in this configuration was determined to be a reflected capillary wave from the contact line that gave rise to a travelling wave across the coalesced droplet, engendering both an internal and surface flow to transport fluid in the direction of wave propagation. By introducing a difference in surface tension between the droplets, surface jet formation and mixing was controlled via Marangoni flow according to the direction of the surface tension gradient. A simple time scale analysis showed that the Marangoni and inertial time scales were similar for remarkably small surface tension differences, from which the precise influence of Marangoni flow on such internal dynamics was elucidated with respect to the surface jet formation mechanism. Either enhanced mixing (via the surface flow) or fluid separation was seen depending on the order of deposition. For higher surface tension differences, Marangoni flow

was shown to result in vigorous internal flow and efficient fluid mixing in a wide variety of configurations, with the conditions required for the various flow structures elucidated with respect to lateral separation and a modified Ohnesorge number.

In Chapter 8, a similar droplet configuration to that in Chapter 7 was considered, but with larger surface tension differences and the focus being on mixing, using a colour-change reaction to identify mixed regions. Careful comparisons to cases with inert dyes to visualise internal flows showed that colour-change reactions have no significant influence on the dynamics of surface-tension-driven flow. Moreover, certain observations made in the literature with respect to colour-change reactions within coalescing droplets were shown to be consistent with the effects of Marangoni flow, with this work thus providing important clarification of some key results in the literature. Different mechanisms of mixing were identified when droplets with larger surface tension differences were in a (nearly) axisymmetric configuration, compared to when the lateral separation between the droplets was greater. Good mixing was shown to be possible in the former case, which is generally not expected for droplets of equal surface tension, whilst undesirable areas of unmixed fluid were seen near the contact lines in the latter. These observations emphasise the influence of Marangoni flow in coalescence mixing dynamics, but also the importance of the direction in which it acts with respect to the impact dynamics and initial droplet configuration.

9.3 Implications of the results

Whilst there are a wide variety of important fundamental conclusions to be taken from this work as mentioned above, there are also several practical implications with respect to droplet mixing in applications.

First, substrate wettability can have a significant influence on the internal and mixing dynamics of coalescing droplets, which seems to have gone relatively unappreciated in practice. In particular, substrates can either enhance or suppress mixing depending on their properties. Hence, it is important to characterise the effect of substrates in applications which rely on certain mixing behaviour. This observation is particularly important for applications in which the substrate evolves in time, such as additive manufacturing in which the product is built-up in layers. Here, the changing substrate properties (e.g. of the support structure and the printed material at different stages of drying/curing) could potentially lead to different mixing dynamics throughout the printing process. As a general rule, low hysteresis substrates give rise to improved mixing efficiency, though the precise influence of substrate wettability is far more nuanced.

Furthermore, surface tension differences can either enhance or suppress coalescence-induced mixing depending on the order of deposition of the droplets, i.e. the direction of the resultant Marangoni flow. As a general rule, it is better to deposit the higher surface

tension fluid first in non-axisymmetric configurations, so that Marangoni flow does not directly oppose the flow due to impact. Moreover, even for relatively small surface tension differences, Marangoni flow can have a significant effect on mixing due to the short time scale (especially compared to the inertial time scale) on which it acts. Indeed, applications involving coalescence between droplets of different fluid properties (not only different surface tensions) are becoming increasingly prevalent with the emergence of technologies such as reactive inkjet printing. In such cases, the effect of the resultant Marangoni flow must be carefully considered due to its likely significant influence on the dynamics, including but not limited to those of mixing.

9.4 Contributions to the literature

The most important contributions to the body of scientific research on the internal dynamics of coalescing droplets made by this work are concisely declared in this section. Specific contributions to scientific methods for studying such internal flows are:

- A quantitatively-validated customised numerical simulation code, implemented within the flexible framework of OpenFOAM, that is suitable for the study of advective mixing in coalescing droplets on substrates, with substrate wettability captured by an accurate dynamic contact angle model.
- A means of generating a truly-free effectively-static droplet with which to study internal flows during the coalescence of initially-static free and sessile droplets.
- An experimental setup featuring two synchronised colour high-speed cameras suitable for assessing advective mixing between impacting and coalescing droplets with variable lateral separation (from axisymmetric to coalescence being initiated by spreading of the impacting droplet across the substrate).
- Careful analysis of colour-change reactions demonstrated that they can be used to passively assess diffusive mixing in coalescing droplets, clarifying several key results in the literature.

The primary novel results claimed are:

- Determination and explanation of a mechanism of internal jet formation in coalescing droplets on a substrate, where jet formation arises at very different droplet volume ratios compared to free droplets.
- Systematic demonstration of the influence of substrate wettability on advective mixing in coalescing droplets on a substrate, comprising various specific results.
- Discovery of *surface jets* between impacting and sessile coalescing droplets of equal fluid properties with non-zero lateral separation, elucidation of the mechanism of

their formation and control of such jets via Marangoni flow for droplets with non-equal fluid properties.

- Elucidation of various mixing mechanisms in impacting and coalescing droplets of different surface tension, where mixing was visualised using colour-change reactions. This includes the demonstration of the effects of Marangoni flow.

9.5 Outlook for future work

There is a wide variety of ways in which the research presented here could be continued and extended, many of which have been mentioned already. Moreover, a better understanding of the internal dynamics of coalescing droplets in non-classical droplet configurations, such as those considered in this work, is highly-desirable given that droplet mixing is key feature of an increasing number of applications.

Due to current experimental limitations in visualising mixing in micrometric coalescing droplets (see Chapter 2), the droplets considered in this work were millimetric. However, applications such as RIJ utilise micrometric droplets, so it is desirable to understand internal flows at this smaller scale. It is important to realise that matching the Weber and Ohnesorge numbers to smaller length scales can not give a complete picture of micrometric droplet dynamics derived from millimetric data due to the effect of molecular diffusion – the Péclet number must be matched too. Using numerical simulations (including molecular diffusion), coalescence at smaller scales could be studied, thus opening a window into the as yet unexplored micrometric world of droplet mixing dynamics. In particular, it would be preferable to systematically scale down from a well-studied, validated millimetric configuration to understand how, and at which scale, the dynamics significantly change, especially in relation to the importance of molecular diffusion. As described in Chapter 2, advances in technologies such as confocal microscopy may make such a study experimentally feasible in the next few years; preliminary work with a front-lit high-speed imaging setup (not discussed here) has highlighted the challenging nature of studying micrometric droplet mixing using a traditional visualisation setup.

This work (especially Chapter 6) has demonstrated the complex ways in which substrate properties can affect mixing, but only for dry solid substrates with relatively high contact angle hysteresis and $\theta_{\text{eq}} \approx 90^\circ$ (as placed). As the set of applications requiring efficient mixing between coalescing droplets diversifies, coalescence on a wider variety of substrates is likely to arise. Hence, it is important to understand their effect on the internal dynamics of coalescing droplets, both from a practical and a fundamental point of view. Particularly interesting examples of different substrates that could be considered include very low hysteresis substrates (e.g. SLIPS), soft substrates, substrates with pre-deposited fluid (perhaps an evaporating layer) and (for the configurations studied in this work) substrates with a wettability gradient.

In addition to being suitable for deriving the physical conclusions outlined above, the rationale behind the choice of an OpenFOAM numerical framework was to develop a flexible quantitatively-validated code suitable for studying a wide range of droplet (mixing) dynamics. Indeed, the customised solver described in Chapter 4 could be used to study coalescing droplets in a much wider variety of configurations than reported in this work, such as non-axisymmetric initially-static free and sessile droplets, impacting and coalescing droplets (as for the equal surface tension experiments in Chapter 7) or jumping droplets, i.e. with superhydrophobic substrates. Moreover, the code could easily be extended to support droplets of different fluid properties (e.g. surface tension) or additional physics such as heat transfer, with most practical issues regarding handling droplet coalescence on substrates in OpenFOAM having already been overcome in this work. The latter addition would enable droplet-based thermal management technologies to be studied, perhaps to improve their efficiency via an improved understanding of the internal dynamics and formal optimisation.

Returning to a key motivator of this work, in RIJ (discussed in Chapter 1) there is a complex two-way coupling between mixing and the reaction kinetics (exothermic/endothermic reactions), which needs to be tackled in tandem to fully elucidate mixing in such applications. Hence, an extension of this work to include application-relevant chemical reactions would surely provide a significant leap forward in the understanding of mixing in exciting emerging technologies involving reacting flows in coalescing droplets.

Appendices

Appendix A

Sessile droplet geometry derivations

Here, extended derivations of spherical cap geometry formulations noted in Section 2.2.6 are provided.

A.1 Droplet height in terms of contact angle

In this section, it is desired to express the droplet height, h in terms of the contact angle, θ and spread length, s as in Equation (2.9) and rewritten here:

$$h = \frac{s}{2} \tan\left(\frac{\theta}{2}\right).$$

First, eliminating R between Equations (2.7) and (2.8) yields

$$h = \frac{s}{2} \cdot \frac{1 - \cos\theta}{\sin\theta} = \frac{s}{2} \left(\frac{1}{\sin\theta} - \frac{\cos\theta}{\sin\theta} \right). \quad (\text{A.1})$$

Now, it is already known by elementary trigonometric identities that

$$\frac{1}{\tan\theta} = \frac{\cos\theta}{\sin\theta} = \frac{1 - \tan^2\left(\frac{\theta}{2}\right)}{2 \tan\left(\frac{\theta}{2}\right)}. \quad (\text{A.2})$$

Therefore, it only remains to express $\sin\theta$ in terms of $\tan\left(\frac{\theta}{2}\right)$ in order to eliminate $\cos\theta$ and $\sin\theta$ from Equation (A.1). Indeed, since $\sin^2\theta + \cos^2\theta = 1$, $\tan\theta$ can be expressed as

$$\tan\theta = \frac{\sin\theta}{\sqrt{1 - \sin^2\theta}}.$$

Eliminating $\tan \theta$ between this equation and Equation (A.2),

$$\sin^2 \theta \left(1 - \tan^2 \left(\frac{\theta}{2} \right) \right)^2 = 4(1 - \sin^2 \theta) \tan^2 \left(\frac{\theta}{2} \right).$$

Rewriting this equation in terms of $\sin^2 \theta$,

$$\sin^2 \theta = \frac{4 \tan^2 \left(\frac{\theta}{2} \right)}{\left(1 - \tan^2 \left(\frac{\theta}{2} \right) \right)^2 + 4 \tan^2 \left(\frac{\theta}{2} \right)} = \frac{\left(2 \tan \left(\frac{\theta}{2} \right) \right)^2}{\left(1 + \tan^2 \left(\frac{\theta}{2} \right) \right)^2}.$$

Taking the positive square root,

$$\sin \theta = \frac{2 \tan \left(\frac{\theta}{2} \right)}{1 + \tan^2 \left(\frac{\theta}{2} \right)}.$$

Hence by substitution of this equation for $\sin \theta$ and Equation (A.2) into Equation (A.1),

$$h = \frac{s}{2} \left(\frac{1}{\sin \theta} - \frac{\cos \theta}{\sin \theta} \right) = \frac{s}{2} \left(\frac{1 + \tan^2 \left(\frac{\theta}{2} \right)}{2 \tan \left(\frac{\theta}{2} \right)} - \frac{1 - \tan^2 \left(\frac{\theta}{2} \right)}{2 \tan \left(\frac{\theta}{2} \right)} \right) = \frac{s}{2} \tan \left(\frac{\theta}{2} \right)$$

as required.

A.2 Droplet volume in terms of contact angle

In this section, it is desired to calculate the droplet volume. To do so, it is required to integrate a horizontal circular cross-section between the apex of the droplet, $z = R$ and the substrate, $z = R - h$. Hence the volume is given by

$$V = \int_{R-h}^R \pi r^2 \, dz,$$

where r is the radius of the cross-section. But by Pythagoras' theorem,

$$r^2 + z^2 = R^2$$

so

$$V = \int_{R-h}^R \pi(R^2 - z^2) \, dz = \left[\pi R^2 z - \frac{\pi}{3} z^3 \right]_{z=R-h}^R = \frac{\pi h^2}{3} (3R - h).$$

Finally, substituting Equation (2.7) yields

$$V = \frac{\pi}{3} R^2 (1 - \cos \theta)^2 [3R - R(1 - \cos \theta)] = \frac{\pi}{3} R^3 (2 - 3 \cos \theta + \cos^3 \theta)$$

as required.

Appendix B

Contact angle implementation as a boundary condition within VOF

The derivation of the correction to the free surface normal at the contact line (Equation (4.18)) which is required to implement the substrate boundary condition on the volume fraction, α and passive scalar, β is elucidated in this appendix. Within the framework of FVM, the correction is applied to the free surface normal for each cell with a face coinciding with the substrate boundary – face notation is omitted here for simplicity.

Recall from Section 4.3 that $\hat{n}_{0,i}$ denotes the outward-pointing free surface unit normal at the contact line emerging from the fluid flow on each time step, which needs to be corrected to $\hat{n}_{c,i}$ in order to satisfy the boundary condition imposed by the dynamic contact angle model, Equations (4.15) to (4.17). Further, $\hat{n}_{s,i}$ denotes the unit normal to the substrate. Since $\hat{n}_{0,i}$ is rotated to $\hat{n}_{c,i}$ within the plane indicated by the normal to the substrate, $\hat{n}_{c,i}$ must lie in the plane spanned by $\hat{n}_{0,i}$ and $\hat{n}_{s,i}$ (Kunkelmann, 2011). Hence, $\hat{n}_{c,i}$ is a linear combination of $\hat{n}_{0,i}$ and $\hat{n}_{s,i}$ as expressed in Equation (4.18) and reprinted here for convenience:

$$\hat{n}_{c,i} = a \hat{n}_{s,i} + b \hat{n}_{0,i}, \quad (4.18)$$

where $a, b \in \mathbb{R}$ are scalars which will now be determined.

First, the cosine of the uncorrected contact angle, θ_0 is by definition given by the inner product of $\hat{n}_{s,i}$ and $\hat{n}_{0,i}$, so

$$\hat{n}_{0,i} \hat{n}_{s,i} = \cos \theta_0. \quad (B.1)$$

Similarly, the updated contact angle derived from the dynamic contact angle model, θ_d satisfies

$$\hat{n}_{c,i} \hat{n}_{s,i} = \cos \theta_d. \quad (B.2)$$

Taking the inner product of Equation (4.18) with $\hat{n}_{s,i}$ yields

$$\hat{n}_{c,j}\hat{n}_{s,j} = a\hat{n}_{s,j}\hat{n}_{s,j} + b\hat{n}_{0,j}\hat{n}_{s,j} = a + b\cos\theta_0,$$

using Equation (B.1) and noting that both $\hat{n}_{0,i}$ and $\hat{n}_{s,i}$ are unit vectors. Equating this equation and Equation (B.2) yields

$$\cos\theta_d = a + b\cos\theta_0, \quad (\text{B.3})$$

which is the first of two simultaneous equations for a and b . Note that θ_d is prescribed by the dynamic contact angle model and θ_0 is the uncorrected contact angle which is calculable from Equation (B.1). Therefore, only a and b are unknown in Equation (B.3).

Now, taking the inner product of equation (4.18) with $\hat{n}_{c,i}$ instead yields

$$\hat{n}_{c,j}\hat{n}_{c,j} = a\hat{n}_{s,j}\hat{n}_{c,j} + b\hat{n}_{0,j}\hat{n}_{c,j} = a\cos\theta_d + b\hat{n}_{0,j}\hat{n}_{c,j},$$

using equation (B.2). But since $\hat{n}_{c,j}$ is a unit vector, this equation reduces to

$$1 = a\cos\theta_d + b\hat{n}_{c,j}\hat{n}_{0,j}, \quad (\text{B.4})$$

so it only remains to eliminate $\hat{n}_{c,j}\hat{n}_{0,i}$ in order to have a second simultaneous equation for a and b . Indeed, taking the inner product of Equation (4.18) with the third and final unit normal, $\hat{n}_{0,i}$ yields

$$\hat{n}_{c,j}\hat{n}_{0,j} = a\hat{n}_{s,j}\hat{n}_{0,j} + b\hat{n}_{0,j}\hat{n}_{0,j} = a\cos\theta_0 + b, \quad (\text{B.5})$$

using Equation (B.1) and noting that $\hat{n}_{0,i}$ is a unit vector. Substituting Equation (B.5) into Equation (B.4) yields

$$1 = a\cos\theta_d + b(a\cos\theta_0 + b) = b^2 + a(\cos\theta_d + b\cos\theta_0), \quad (\text{B.6})$$

which is a second simultaneous equation for a and b .

Equations (B.3) and (B.6) can thus be solved simultaneously to find expressions for a and b . Eliminating a ,

$$1 = b^2 + (\cos\theta_d - b\cos\theta_0)(\cos\theta_d + b\cos\theta_0) = b^2(1 - \cos^2\theta_0) + \cos^2\theta_d.$$

Rearranging for an explicit equation for b^2 ,

$$b^2 = \frac{1 - \cos^2\theta_d}{1 - \cos^2\theta_0} = \frac{(1 - \cos^2\theta_d)(1 - \cos^2\theta_0)}{(1 - \cos^2\theta_0)^2}. \quad (\text{B.7})$$

Using standard trigonometric identities, the numerator of the last expression can be rewrit-

ten as

$$(1 - \cos^2 \theta_d)(1 - \cos^2 \theta_0) = (\sin \theta_0 \sin \theta_d)^2 = (\cos(\theta_0 - \theta_d) - \cos \theta_0 \cos \theta_d)^2.$$

Substituting this equation into Equation (B.7) and taking the positive square root, the equation for b reads

$$b = \frac{\cos(\theta_0 - \theta_d) - \cos \theta_0 \cos \theta_d}{1 - \cos^2 \theta_0}. \quad (\text{B.8})$$

Finally, eliminating b between Equations (B.3) and (B.8) gives an equation for a which reads

$$a = \frac{\cos \theta_d - \cos \theta_0 \cos(\theta_0 - \theta_d)}{1 - \cos^2 \theta_0}. \quad (\text{B.9})$$

Hence, using Equations (4.18), (B.8) and (B.9) together, the free surface normal at the contact line can be corrected to satisfy the boundary condition on α and β imposed by the dynamic contact angle model.

Of course, Equations (B.8) and (B.9) can be simplified but the form given here is the most useful for numerical implementation. Indeed, only θ_d is explicitly computed within the OpenFOAM implementation before a and b are, whereas θ_0 is only known implicitly via Equation (B.1). In particular, the exact equations implemented within OpenFOAM to compute a and b are

$$a = \frac{\cos \theta_d - (\hat{n}_{0,j} \hat{n}_{s,j}) \cos(\arccos(\hat{n}_{0,j} \hat{n}_{s,j}) - \theta_d)}{1 - (\hat{n}_{0,j} \hat{n}_{s,j})^2} \quad (\text{B.10})$$

and

$$b = \frac{\cos(\arccos(\hat{n}_{0,j} \hat{n}_{s,j}) - \theta_d) - (\hat{n}_{0,j} \hat{n}_{s,j}) \cos \theta_d}{1 - (\hat{n}_{0,j} \hat{n}_{s,j})^2}. \quad (\text{B.11})$$

Equations (4.18), (B.10) and (B.11) together are implemented in a private member function (`correctContactAngle`) contained within the `interfaceProperties.C` file of the OpenFOAM source code, to ensure that the free surface normal at the contact line is consistent with the dynamic contact angle model-imposed boundary condition during the computation of the free surface curvature, κ (i.e. `correctContactAngle` is called within the `calculateK` function) on each time step.

Appendix C

Iterative algorithms and parameters

The full details of the algorithms used for the solution of the system of linear equations, resulting from the discretisation of the PDEs, within the OpenFOAM PISO solution algorithm are given in this appendix. Details of the solution procedure itself, which is based on the PISO algorithm, are given in Section 4.4.5.

For all such algorithms, the residual tolerance was set very low to ensure convergence at each time step, thus favouring accuracy over speed. The relative tolerance was always set to zero (i.e. its influence was rescinded) to ensure that the prescribed tolerance was reached. Whilst a maximum number of iterations was set, the value was chosen to be very large so that it was not an effective constraint.

Subcycling of advection-diffusion equations is often performed in OpenFOAM simulations in order to relax the strict Courant number limit on the time step. However, in this work it was preferred to maintain a strict Courant number limit (see Section 4.4.8)

Table C.1: OpenFOAM solver settings for α . Equivalent settings are used for β .

Option	Value	Notes
<code>nAlphaCorr</code>	1	
<code>nAlphaSubCycles</code>	1	Time step tightly controlled instead of subcycling.
<code>cAlpha</code>	1	Small to avoid too much interface compression.
<code>MULESCorr</code>	no	Keep MULES explicit rather than semi-implicit.
<code>nLimiterIter</code>	1	One MULES iteration over the limiter.
Preconditioner	DIC	
Solver	PCG	
Tolerance	1×10^{-9}	Set low to ensure convergence.
Rel. Tolerance	0	Forces solution to converge to the tolerance above.
Min. Iterations	50	Ensure stable converged solution each time step.
Max. Iterations	1000	Set high so as not to be an effective constraint.

Table C.2: OpenFOAM solver settings for `p_rgh` – the modified pressure, p' .

Option	Value	Notes
Smoother	Gauss-Seidel	
Solver	GAMG	More efficient (far fewer iterations) than, e.g., PCG.
Tolerance	1×10^{-7}	The final iteration tolerance is 1×10^{-8} .
Rel. Tolerance	0	Forces solution to converge to the tolerance above.
Min. Iterations	2	
Max. Iterations	1000	Set high so as not to be an effective constraint.

Table C.3: OpenFOAM solver settings for `pcorr` – the pressure correction required for the adaptive mesh refinement algorithm.

Option	Value	Notes
Smoother	Gauss-Seidel	
Solver	GAMG	More efficient (far fewer iterations) than, e.g., PCG.
Tolerance	1×10^{-8}	Set low to ensure convergence.
Rel. Tolerance	0	Forces solution to converge to the tolerance above.
Min. Iterations	2	
Max. Iterations	1000	Set high so as not to be an effective constraint.

Table C.4: OpenFOAM solver settings for `U` – the velocity, u_i .

Option	Value	Notes
Preconditioner	DILU	
Solver	PBiCG	Computational cost not enough to warrant GAMG.
Tolerance	1×10^{-10}	Set low to ensure full convergence.
Rel. Tolerance	0	Forces solution to converge to the tolerance above.
Min. Iterations	5	
Max. Iterations	1000	Set high so as not to be an effective constraint.

for the contact angle model implementation. Therefore, no subcycling was carried out. An explicit version of the MULES FCT solver (see Section 4.4.6 for details of FCT and MULES) was maintained for the bounded scalars, as seen in Table C.1 which contains the settings pertinent to α (equivalently β).

Details for the modified pressure, p' (called `p_rgh` in OpenFOAM) are given in Table C.2. Meanwhile, Table C.3 give details of the algorithm for the pressure correction required for the adaptive mesh. The velocity is determined from the updated pressure in each time step with the settings seen in Table C.4. A momentum predictor step was employed at the beginning of each time step (see Table 4.2).

References

Citing pages are listed after each entry.

- Acheson, D. J. 1990. *Elementary fluid dynamics*. Oxford: Oxford University Press. Cited on pp. 10, 72, and 81.
- Afkhami, S., Zaleski, S., and Bussmann, M. 2009. A mesh-dependent model for applying dynamic contact angles to VOF simulations. *J. Comput. Phys.* **228**(15), pp. 5370–5389. Cited on p. 77.
- Ahmad, S., Tang, H., and Yao, H. 2018. Oblique impact of two successive droplets on a flat surface. *Int. J. Heat Mass Transfer.* **119**, pp. 433–445. Cited on p. 95.
- Al-Dirawi, K. H. and Bayly, A. E. 2019. A new model for the bouncing regime boundary in binary droplet collisions. *Phys. Fluids.* **31**(2), pp. 027105. Cited on pp. 1 and 115.
- Al-Dirawi, K. H. and Bayly, A. E. 2020. An experimental study of binary collisions of miscible droplets with non-identical viscosities. *Exp. Fluids.* **61**(2), pp. 50. Cited on p. 20.
- Al-Ghaithi, K. H. A., Harlen, O. G., Kapur, N., and Wilson, M. C. T. 2020. Morphologies and dynamics of micro-droplet impact onto an idealised scratch. arXiv:2007.01727 [physics.flu-dyn]. Cited on p. 42.
- Albadawi, A., Donoghue, D. B., Robinson, A. J., Murray, D. B., and Delauré, Y. M. C. 2013. Influence of surface tension implementation in volume of fluid and coupled volume of fluid with level set methods for bubble growth and detachment. *Int. J. Multiphase Flow.* **53**, pp. 11–28. Cited on pp. 79 and 80.
- Almarcha, C., Trevelyan, P. M. J., Grosfils, P., and De Wit, A. 2010. Chemically driven hydrodynamic instabilities. *Phys. Rev. Lett.* **104**(4), pp. 044501. Cited on p. 166.
- Andersen, N. K. and Taboryski, R. 2017. Drop shape analysis for determination of dynamic contact angles by double sided elliptical fitting method. *Meas. Sci. Technol.* **28**(4), pp. 047003. Cited on pp. 63 and 64.

- Angelopoulos, I., Allenby, M. C., Lim, M., and Zamorano, M. 2020. Engineering inkjet bioprinting processes toward translational therapies. *Biotechnol. Bioeng.* **117**(1), pp. 272–284. Cited on p. 3.
- Anilkumar, A. V., Lee, C. P., and Wang, T. G. 1991. Surface-tension-induced mixing following coalescence of initially stationary drops. *Phys. Fluids A: Fluid Dyn.* **3**(11), pp. 2587–2591. Cited on pp. 26, 34, 37, 39, and 113.
- Antonopoulou, E., Harlen, O. G., Walkley, M. A., and Kapur, N. 2020. Jetting behavior in drop-on-demand printing: Laboratory experiments and numerical simulations. *Phys. Rev. Fluids.* **5**(4), pp. 043603. Cited on p. 3.
- Arkles, B., Pan, Y., and Kim, Y. M. 2009. The role of polarity in the structure of silanes employed in surface modification. In: Mittal, K. L. ed. *Silanes and Other Coupling Agents*. Leiden: Koninklijke Brill NV, pp. 51–64. Cited on p. 51.
- Ashgriz, N. and Poo, J. Y. 1990. Coalescence and separation in binary collisions of liquid drops. *J. Fluid Mech.* **221**, pp. 183–204. Cited on p. 39.
- Atefi, E., Mann Jr, J. A., and Tavana, H. 2013. A robust polynomial fitting approach for contact angle measurements. *Langmuir.* **29**(19), pp. 5677–5688. Cited on p. 64.
- Bain, C. D., Burnett-Hall, G. D., and Montgomerie, R. R. 1994. Rapid motion of liquid drops. *Nature.* **372**(6505), pp. 414–415. Cited on p. 12.
- Balch, K. 1997. High speed videography. In: Ray, S. F. ed. *High Speed Photography and Photonics*. Oxford: Focal Press, pp. 99–123. Cited on p. 54.
- Bao, B., Li, M., Li, Y., et al. 2015. Patterning fluorescent quantum dot nanocomposites by reactive inkjet printing. *Small.* **11**(14), pp. 1649–1654. Cited on p. 5.
- Basařová, P., Váchová, T., and Bartovská, L. 2016. Atypical wetting behaviour of alcohol–water mixtures on hydrophobic surfaces. *Colloids Surf., A.* **489**, pp. 200–206. Cited on p. 47.
- Basařová, P., Pišlová, J., Mills, J., and Orvalho, S. 2018. Influence of molecular structure of alcohol–water mixtures on bubble behaviour and bubble surface mobility. *Chem. Eng. Sci.* **192**, pp. 74–84. Cited on p. 48.
- Battal, T., Bain, C. D., Weiß, M., and Darton, R. C. 2003. Surfactant adsorption and Marangoni flow in liquid jets: I. Experiments. *J. Colloid Interface Sci.* **263**(1), pp. 250–260. Cited on p. 11.
- Bayer, B. E. 1976. *Color imaging array*. Patent: US3971065A. Assignee: Eastman Kodak Co. Cited on p. 54.
- Berberović, E., van Hinsberg, N. P., Jakirlić, S., Roisman, I. V., and Tropea, C. 2009. Drop impact onto a liquid layer of finite thickness: Dynamics of the cavity evolution. *Phys. Rev. E.* **79**(3), pp. 036306. Cited on p. 71.

- Berger, S. 1981. The pH dependence of phenolphthalein: A ^{13}C NMR study. *Tetrahedron*. **37**(8), pp. 1607–1611. Cited on p. 165.
- Berry, J. D. and Dagastine, R. R. 2017. Mapping coalescence of micron-sized drops and bubbles. *J. Colloid Interface Sci.* **487**, pp. 513–522. Cited on p. 115.
- Berry, J. D., Neeson, M. J., Dagastine, R. R., Chan, D. Y. C., and Tabor, R. F. 2015. Measurement of surface and interfacial tension using pendant drop tensiometry. *J. Colloid Interface Sci.* **454**, pp. 226–237. Cited on pp. x, 46, and 47.
- Berthier, J. 2013. *Micro-drops and digital microfluidics*. 2nd ed. Waltham, MA: William Andrew. Cited on pp. 9, 10, 11, 15, and 20.
- Biscay, F., Ghoufi, A., and Malfreyt, P. 2011. Surface tension of water–alcohol mixtures from Monte Carlo simulations. *J. Chem. Phys.* **134**(4), pp. 044709. Cited on p. 47.
- Blake, T. D. 2006. The physics of moving wetting lines. *J. Colloid Interface Sci.* **299**(1), pp. 1–13. Cited on pp. x, 29, 30, and 31.
- Blake, T. D. and Haynes, J. M. 1969. Kinetics of liquid/liquid displacement. *J. Colloid Interface Sci.* **30**(3), pp. 421–423. Cited on p. 30.
- Blake, T. D., Bracke, M., and Shikhmurzaev, Y. D. 1999. Experimental evidence of nonlocal hydrodynamic influence on the dynamic contact angle. *Phys. Fluids*. **11**(8), pp. 1995–2007. Cited on p. 29.
- Blanchette, F. 2010. Simulation of mixing within drops due to surface tension variations. *Phys. Rev. Lett.* **105**(7), pp. 074501. Cited on pp. 13, 23, 39, and 40.
- Blanchette, F. and Bigioni, T. P. 2006. Partial coalescence of drops at liquid interfaces. *Nat. Phys.* **2**(4), pp. 254–257. Cited on pp. 127 and 128.
- Blanchette, F. and Bigioni, T. P. 2009. Dynamics of drop coalescence at fluid interfaces. *J. Fluid Mech.* **620**, pp. 333–352. Cited on p. 39.
- Blanchette, F., Messio, L., and Bush, J. W. M. 2009. The influence of surface tension gradients on drop coalescence. *Phys. Fluids*. **21**(7), pp. 072107. Cited on pp. 24, 39, 40, and 143.
- Boelens, A., Latka, A., and de Pablo, J. 2018. Observation of the pressure effect in simulations of droplets splashing on a dry surface. *Phys. Rev. Fluids*. **3**(6), pp. 063602. Cited on pp. 71 and 78.
- Bonn, D., Eggers, J., Indekeu, J., Meunier, J., and Rolley, E. 2009. Wetting and spreading. *Rev. Mod. Phys.* **81**(2), pp. 739–805. Cited on pp. 14 and 149.
- Boris, J. P. and Book, D. L. 1973. Flux-corrected transport. I. SHASTA, a fluid transport algorithm that works. *J. Comput. Phys.* **11**(1), pp. 38–69. Cited on p. 87.

- Bormashenko, E. 2013a. Wetting of real solid surfaces: new glance on well-known problems. *Colloid Polym. Sci.* **291**(2), pp. 339–342. Cited on pp. 14, 16, and 17.
- Bormashenko, E. Y. 2013b. *Wetting of Real Surfaces*. Berlin: De Gruyter. Cited on pp. 9, 13, 16, and 18.
- Brackbill, J. U., Kothe, D. B., and Zemach, C. 1992. A continuum method for modeling surface tension. *J. Comput. Phys.* **100**(2), pp. 335–354. Cited on p. 73.
- Brockmeier, A., Rodriguez, F. J. S., Harrison, M., and Hilleringmann, U. 2012. Surface tension and its role for vertical wet etching of silicon. *J. Micromech. Microeng.* **22**(12), pp. 125012. Cited on p. 48.
- Bruning, M. A., Costalonga, M., Karpitschka, S., and Snoeijer, J. H. 2018. Delayed coalescence of surfactant containing sessile droplets. *Phys. Rev. Fluids.* **3**(7), pp. 073605. Cited on p. 143.
- Carrier, O. and Bonn, D. 2015. Liquid spreading. In: Brutin, D. ed. *Droplet Wetting and Evaporation: From Pure to Complex Fluids*. Academic Press, pp. 3–13. Cited on p. 14.
- Castrejón-Pita, A. A., Castrejón-Pita, J. R., and Hutchings, I. M. 2012. Experimental observation of von Kármán vortices during drop impact. *Phys. Rev. E.* **86**(4), pp. 045301. Cited on p. 34.
- Castrejón-Pita, J. R., Betton, E. S., Kubiak, K. J., Wilson, M. C. T., and Hutchings, I. M. 2011. The dynamics of the impact and coalescence of droplets on a solid surface. *Biomicrofluidics.* **5**(1), pp. 014112. Cited on pp. 36 and 51.
- Castrejón-Pita, J. R., Kubiak, K. J., Castrejón-Pita, A. A., Wilson, M. C. T., and Hutchings, I. M. 2013. Mixing and internal dynamics of droplets impacting and coalescing on a solid surface. *Phys. Rev. E.* **88**(2), pp. 023023. Cited on pp. x, 6, 15, 25, 33, 39, 42, 58, 59, 61, 114, and 146.
- Castrejón-Pita, J. R., Muñoz-Sánchez, B. N., Hutchings, I. M., and Castrejón-Pita, A. A. 2016. Droplet impact onto moving liquids. *J. Fluid Mech.* **809**, pp. 716–725. Cited on p. 34.
- Cha, H., Xu, C., Sotelo, J., et al. 2016. Coalescence-induced nanodroplet jumping. *Phys. Rev. Fluids.* **1**(6), pp. 064102. Cited on p. 1.
- Chainani, E. T., Choi, W.-H., Ngo, K. T., and Scheeline, A. 2014. Mixing in colliding, ultrasonically levitated drops. *Anal. Chem.* **86**(4), pp. 2229–2237. Cited on p. 166.
- Chaudhury, M. K. and Whitesides, G. M. 1992. How to make water run uphill. *Science.* **256**(5063), pp. 1539–1541. Cited on p. 15.
- Chen, G., Xiong, Q., Morris, P. J., et al. 2014. OpenFOAM for computational fluid dynamics. *Not. Am. Math. Soc.* **61**(4), pp. 354–363. Cited on p. 70.

-
- Chen, S. and Doolen, G. D. 1998. Lattice Boltzmann method for fluid flows. *Annu. Rev. Fluid Mech.* **30**(1), pp. 329–364. Cited on p. 41.
- Chen, X., Sun, Y., Xue, C., Yu, Y., and Hu, G. 2017. Tunable structures of compound droplets formed by collision of immiscible microdroplets. *Microfluid. Nanofluid.* **21**(6), pp. 109. Cited on pp. 39 and 142.
- Chu, F., Li, S., Ni, Z., and Wen, D. 2020. Departure velocity of rolling droplet jumping. *Langmuir.* **36**(14), pp. 3713–3719. Cited on pp. 32 and 71.
- Chubynsky, M. V., Belousov, K. I., Lockerby, D. A., and Sprittles, J. E. 2020. Bouncing off the walls: The influence of gas-kinetic and van der Waals effects in drop impact. *Phys. Rev. Lett.* **124**(8), pp. 084501. Cited on p. 14.
- Cox, R. G. 1986. The dynamics of the spreading of liquids on a solid surface. Part 1. Viscous flow. *J. Fluid Mech.* **168**, pp. 169–194. Cited on p. 29.
- Cresswell, R. W. and Morton, B. R. 1995. Drop-formed vortex rings—the generation of vorticity. *Phys. Fluids.* **7**(6), pp. 1363–1370. Cited on p. 24.
- Cristini, V. and Tan, Y.-C. 2004. Theory and numerical simulation of droplet dynamics in complex flows – a review. *Lab Chip.* **4**(4), pp. 257–264. Cited on p. 2.
- Cussler, E. L. 2009. *Diffusion: Mass Transfer in Fluid Systems*. 3rd ed. Cambridge University Press. Cited on p. 21.
- Daly, R., Harrington, T. S., Martin, G. D., and Hutchings, I. M. 2015. Inkjet printing for pharmaceuticals – A review of research and manufacturing. *Int. J. Pharm.* **494**(2), pp. 554–567. Cited on p. 6.
- Davanlou, A. and Kumar, R. 2015. Passive mixing enhancement of microliter droplets in a thermocapillary environment. *Microfluid. Nanofluid.* **19**(6), pp. 1507–1513. Cited on pp. 36 and 166.
- de Gennes, P.-G. 1985. Wetting: statics and dynamics. *Rev. Mod. Phys.* **57**(3), pp. 827–863. Cited on pp. 14 and 16.
- Deegan, R. D., Bakajin, O., Dupont, T. F., et al. 1997. Capillary flow as the cause of ring stains from dried liquid drops. *Nature.* **389**(6653), pp. 827–829. Cited on p. 1.
- Deka, H., Ray, B., Biswas, G., et al. 2017. The regime of large bubble entrapment during a single drop impact on a liquid pool. *Phys. Fluids.* **29**(9), pp. 092101. Cited on p. 92.
- Deka, H., Biswas, G., Chakraborty, S., and Dalal, A. 2019. Coalescence dynamics of unequal sized drops. *Phys. Fluids.* **31**(1), pp. 012105. Cited on pp. 41, 78, 117, 127, 128, 135, and 137.
- Derby, B. 2010. Inkjet printing of functional and structural materials: fluid property requirements, feature stability, and resolution. *Annu. Rev. Mater. Res.* **40**, pp. 395–414. Cited on p. 26.

- Deshpande, S. S., Anumolu, L., and Trujillo, M. F. 2012. Evaluating the performance of the two-phase flow solver interFoam. *Comput. Sci. Discovery*. **5**, pp. 014016. Cited on pp. 41, 71, 80, and 84.
- Dettre, R. H. and Johnson Jr., R. E. 1964. Contact Angle Hysteresis. II. Contact angle measurements on rough surfaces. In: Fowkes, F. M. ed. *Contact Angle, Wettability, and Adhesion*. Washington DC: American Chemical Society, pp. 136–144. Cited on p. 16.
- Diddens, C. 2017. Detailed finite element method modeling of evaporating multi-component droplets. *J. Comput. Phys.* **340**, pp. 670–687. Cited on p. 38.
- Dong, H., Carr, W. W., Bucknall, D. G., and Morris, J. F. 2007. Temporally-resolved inkjet drop impaction on surfaces. *AIChE J.* **53**(10), pp. 2606–2617. Cited on p. 39.
- Drelich, J., Fang, C., and White, C. L. 2002. Measurement of interfacial tension in fluid-fluid systems. In: Somasundaran, P. ed. *Encyclopedia of Surface and Colloid Science*. New York: Marcel Dekker Press, pp. 3152–3166. Cited on p. 46.
- Duchemin, L., Eggers, J., and Josserand, C. 2003. Inviscid coalescence of drops. *J. Fluid Mech.* **487**, pp. 167–178. Cited on pp. 92 and 105.
- Dussan V., E. B. 1979. On the spreading of liquids on solid surfaces: static and dynamic contact lines. *Annu. Rev. Fluid Mech.* **11**(1), pp. 371–400. Cited on pp. 15, 27, and 30.
- Dussan V., E. B. and Davis, S. H. 1974. On the motion of a fluid-fluid interface along a solid surface. *J. Fluid Mech.* **65**(1), pp. 71–95. Cited on pp. 27 and 28.
- Edwards, A. M. J., Atkinson, P. S., Cheung, C. S., et al. 2018. Density-driven flows in evaporating binary liquid droplets. *Phys. Rev. Lett.* **121**(18), pp. 184501. Cited on p. 18.
- Eggers, J. 2004. Toward a description of contact line motion at higher capillary numbers. *Phys. Fluids*. **16**(9), pp. 3491–3494. Cited on p. 28.
- Eggers, J., Lister, J. R., and Stone, H. A. 1999. Coalescence of liquid drops. *J. Fluid Mech.* **401**, pp. 293–310. Cited on p. 20.
- Eiswirth, R. T., Bart, H.-J., Ganguli, A. A., and Kenig, E. Y. 2012. Experimental and numerical investigation of binary coalescence: Liquid bridge building and internal flow fields. *Phys. Fluids*. **24**(6), pp. 062108. Cited on pp. 2, 37, 39, 41, 83, 96, and 113.
- Ersoy, N. E. and Eslamian, M. 2019. Capillary surface wave formation and mixing of miscible liquids during droplet impact onto a liquid film. *Phys. Fluids*. **31**(1), pp. 012107. Cited on pp. 33 and 141.
- Eötvös, R. 1886. Ueber den zusammenhang der oberflächenspannung der flüssigkeiten mit ihrem molecularvolumen. *Ann. Phys.* **263**(3), pp. 448–459. Cited on p. 11.

- Farhangi, M. M., Graham, P. J., Choudhury, N. R., and Dolatabadi, A. 2012. Induced detachment of coalescing droplets on superhydrophobic surfaces. *Langmuir*. **28**(2), pp. 1290–1303. Cited on pp. 71 and 76.
- Fathi, S. and Dickens, P. 2013. Challenges in drop-on-drop deposition of reactive molten nylon materials for additive manufacturing. *J. Mater. Process. Tech.* **213**(1), pp. 84–93. Cited on pp. 5, 34, and 142.
- Feng, J. Q. 2017. A computational study of high-speed microdroplet impact onto a smooth solid surface. *J. Appl. Fluid Mech.* **10**(1), pp. 243–256. Cited on pp. 71 and 77.
- Focke, C. and Bothe, D. 2011. Computational analysis of binary collisions of shear-thinning droplets. *J. Non-Newtonian Fluid Mech.* **166**(14-15), pp. 799–810. Cited on p. 39.
- Frenkel, M. 2009. Tailoring substrates for inkjet printing. In: Magdassi, S. ed. *The Chemistry of Inkjet Inks*. Singapore: World Scientific Publishing, pp. 73–97. Cited on p. 3.
- Frohn, A. and Roth, N. 2000. *Dynamics of Droplets*. Berlin, Heidelberg: Springer-Verlag. Cited on pp. 10, 12, and 14.
- Gao, M., Li, L., and Song, Y. 2017. Inkjet printing wearable electronic devices. *J. Mater. Chem. C*. **5**(12), pp. 2971–2993. Cited on p. 3.
- Geng, X., Yu, M., Zhang, W., et al. 2019. Slip length and structure of liquid water flowing past atomistic smooth charged walls. *Sci. Rep.* **9**(1), pp. 18957. Cited on p. 77.
- Geyer, F., D’Acunzi, M., Sharifi-Aghili, A., et al. 2020. When and how self-cleaning of superhydrophobic surfaces works. *Sci. Adv.* **6**(3), pp. eaaw9727. Cited on p. 15.
- Ghaffari, A., Hashemabadi, S. H., and Bazmi, M. 2015. CFD simulation of equilibrium shape and coalescence of ferrofluid droplets subjected to uniform magnetic field. *Colloids Surf., A*. **481**, pp. 186–198. Cited on p. 71.
- Göhl, J., Mark, A., Sasic, S., and Edelvik, F. 2018. An immersed boundary based dynamic contact angle framework for handling complex surfaces of mixed wettabilities. *Int. J. Multiphase Flow*. **109**, pp. 164–177. Cited on pp. 29 and 38.
- González, B., Calvar, N., Gómez, E., and Domínguez, Á. 2007. Density, dynamic viscosity, and derived properties of binary mixtures of methanol or ethanol with water, ethyl acetate, and methyl acetate at T=(293.15, 298.15, and 303.15) K. *J. Chem. Thermodynamics*. **39**(12), pp. 1578–1588. Cited on pp. 45 and 46.
- Gonzalez, R. C., Woods, R. E., and Eddin, S. L. 2004. *Digital Image Processing Using MATLAB*. Upper Saddle River, NJ: Pearson/Prentice Hall. Cited on p. 63.
- Graham, P. J., Farhangi, M. M., and Dolatabadi, A. 2012. Dynamics of droplet coalescence in response to increasing hydrophobicity. *Phys. Fluids*. **24**(11), pp. 112105. Cited on p. 32.

- Gregory, D. A., Zhang, Y., Smith, P. J., Zhao, X., and Ebbens, S. J. 2016. Reactive inkjet printing of biocompatible enzyme powered silk micro-rockets. *Small*. **12**(30), pp. 4048–4055. Cited on p. 5.
- Guan, J. H. 2017. *Droplets on low friction surfaces*. PhD thesis, Northumbria University. Cited on p. 30.
- Guan, J. H., Wells, G. G., Xu, B., et al. 2015. Evaporation of sessile droplets on slippery liquid-infused porous surfaces (SLIPS). *Langmuir*. **31**(43), pp. 11781–11789. Cited on p. 16.
- Guo, Y., Patanwala, H. S., Bognet, B., and Ma, A. W. K. 2017. Inkjet and inkjet-based 3D printing: Connecting fluid properties and printing performance. *Rapid Prototyp. J.* **23**(3), pp. 562–576. Cited on p. 3.
- Harbottle, D., Bueno, P., Isaksson, R., and Kretzschmar, I. 2011. Coalescence of particle-laden drops with a planar oil–water interface. *J. Colloid Interface Sci.* **362**(1), pp. 235–241. Cited on pp. 1 and 33.
- He, Y., Foerster, A., Begines, B., et al. 2018. Reactive inkjet printing for additive manufacturing. In: Smith, P. J. and Morrin, A. eds. *Reactive Inkjet Printing: A Chemical Synthesis Tool*. The Royal Society of Chemistry, pp. 202–221. Cited on p. 5.
- Hessel, V., Löwe, H., and Schönfeld, F. 2005. Micromixers – a review on passive and active mixing principles. *Chem. Eng. Sci.* **60**(8-9), pp. 2479–2501. Cited on p. 23.
- Hirt, C. W. and Nichols, B. D. 1981. Volume of fluid (VOF) method for the dynamics of free boundaries. *J. Comput. Phys.* **39**(1), pp. 201–225. Cited on p. 40.
- Hoang, D. A., van Steijn, V., Portela, L. M., Kreutzer, M. T., and Kleijn, C. R. 2013. Benchmark numerical simulations of segmented two-phase flows in microchannels using the volume of fluid method. *Comput. Fluids*. **86**, pp. 28–36. Cited on p. 38.
- Hoepffner, J. and Paré, G. 2013. Recoil of a liquid filament: Escape from pinch-off through creation of a vortex ring. *J. Fluid Mech.* **734**, pp. 183–197. Cited on p. 24.
- Hoffman, R. L. 1975. A study of the advancing interface. I. Interface shape in liquid-gas systems. *J. Colloid Interface Sci.* **50**(2), pp. 228–241. Cited on pp. x, 29, 31, and 32.
- Hood, L. 2008. A personal journey of discovery: Developing technology and changing biology. *Annu. Rev. Anal. Chem.* **1**, pp. 1–43. Cited on p. 3.
- Hou, T. Y., Lowengrub, J. S., and Shelley, M. J. 2001. Boundary integral methods for multicomponent fluids and multiphase materials. *J. Comput. Phys.* **169**(2), pp. 302–362. Cited on p. 37.
- Hsiao, W.-K. and Betton, E. S. 2016. Coalescence and line formation. In: Hoath, S. D. ed. *Fundamentals of Inkjet Printing: The Science of Inkjet and Droplets*. Wiley-VCH, pp. 219–250. Cited on p. 147.

- Hu, H. and Larson, R. G. 2002. Evaporation of a sessile droplet on a substrate. *J. Phys. Chem. B.* **106**(6), pp. 1334–1344. Cited on p. 49.
- Hu, H. and Larson, R. G. 2005. Analysis of the effects of Marangoni stresses on the microflow in an evaporating sessile droplet. *Langmuir.* **21**(9), pp. 3972–3980. Cited on p. 22.
- Hu, H. and Larson, R. G. 2006. Marangoni effect reverses coffee-ring depositions. *J. Phys. Chem. B.* **110**(14), pp. 7090–7094. Cited on p. 12.
- Huang, H., Sukop, M., and Lu, X. 2015. *Multiphase lattice Boltzmann methods: Theory and application*. Chichester: John Wiley & Sons. Cited on p. 42.
- Huh, C. and Scriven, L. E. 1971. Hydrodynamic model of steady movement of a solid/liquid/fluid contact line. *J. Colloid Interface Sci.* **35**(1), pp. 85–101. Cited on p. 27.
- Hutchings, I. M., Martin, G. D., and Hoath, S. D. 2016. Introductory remarks. In: Hoath, S. D. ed. *Fundamentals of Inkjet Printing: The Science of Inkjet and Droplets*. Wiley-VCH, pp. 1–12. Cited on p. 3.
- Issa, R. I. 1986. Solution of the implicitly discretised fluid flow equations by operator-splitting. *J. Comput. Phys.* **62**(1), pp. 40–65. Cited on p. 85.
- Jadidbonab, H., Mitroglou, N., Karathanassis, I., and Gavaises, M. 2018. Experimental study of diesel-fuel droplet impact on a similarly sized polished spherical heated solid particle. *Langmuir.* **34**(1), pp. 36–49. Cited on p. 63.
- James, E. 2018. *Wetting and spreading of viscous droplets: a critical assessment of fluid and surface properties*. PhD thesis, University of Leeds. Cited on p. 51.
- Jehannin, M., Charton, S., Karpitschka, S., et al. 2015. Periodic precipitation patterns during coalescence of reacting sessile droplets. *Langmuir.* **31**(42), pp. 11484–11490. Cited on p. 143.
- Jia, F., Sun, K., Zhang, P., Yin, C., and Wang, T. 2020. Marangoni effect on the impact of droplets onto a liquid-gas interface. *Phys. Rev. Fluids.* **5**(7), pp. 073605. Cited on p. 39.
- Jiang, T.-S., Soo-Gun, O. H., and Slattery, J. C. 1979. Correlation for dynamic contact angle. *J. Colloid Interface Sci.* **69**(1), pp. 74–77. Cited on p. 31.
- Jiao, L., Li, D., Li, W., et al. 2019. Light-actuated droplets coalescence and ion detection on the CAHTs-assisted superhydrophobic surface. *Sens. Actuat. B-Chem.* **282**, pp. 469–481. Cited on p. 142.
- Kapur, N. and Gaskell, P. H. 2007. Morphology and dynamics of droplet coalescence on a surface. *Phys. Rev. E.* **75**(5), pp. 056315. Cited on p. 145.
- Kazuhide, K. and Toshiyuki, M. 2000. *Ink composition for ink jet recording and recording*. Patent: JP2000-063719A. Assignee: Seiko Epson Corp. Cited on p. 4.

- Keiser, L., Bense, H., Colinet, P., Bico, J., and Reyssat, E. 2017. Marangoni bursting: evaporation-induced emulsification of binary mixtures on a liquid layer. *Phys. Rev. Lett.* **118**(7), pp. 074504. Cited on pp. 143 and 173.
- Keshavarzi, G., Yeoh, G. H., and Barber, T. 2013. Comparison of the VOF and CLSVOF methods in interface capturing of a rising bubble. *J. Comput. Multiphase Flows.* **5**(1), pp. 43–55. Cited on p. 41.
- Khatir, Z., Kubiak, K. J., Jimack, P. K., and Mathia, T. G. 2016. Dropwise condensation heat transfer process optimisation on superhydrophobic surfaces using a multi-disciplinary approach. *Appl. Therm. Eng.* **106**, pp. 1337–1344. Cited on pp. 1 and 71.
- Khattab, I. S., Bandarkar, F., Fakhree, M. A. A., and Jouyban, A. 2012. Density, viscosity, and surface tension of water+ethanol mixtures from 293 to 323K. *Korean J. Chem. Eng.* **29**(6), pp. 812–817. Cited on pp. 45 and 46.
- Khaw, M.-K., Mohd-Yasin, F., and Nguyen, N.-T. 2018. Magnetically-actuated mixing and merging of acid-base micro-droplets on open surfaces: Preliminary study. *Sensors.* **18**(6), pp. 1767. Cited on pp. 36 and 167.
- Kirkpatrick, M. P. and Armfield, S. W. 2009. Open boundary conditions in numerical simulations of unsteady incompressible flow. *ANZIAM J.* **50**, pp. C760–C773. Cited on p. 77.
- Kistler, S. F. 1993. Hydrodynamics of wetting. In: Berg, J. C. ed. *Wettability*. New York: Dekker, pp. 311–429. Cited on p. 31.
- Koldeweij, R. B. J., van Capelleveen, B. F., Lohse, D., and Visser, C. W. 2019. Marangoni-driven spreading of miscible liquids in the binary pendant drop geometry. *Soft Matter.* **15**(42), pp. 8525–8531. Cited on p. 147.
- Kooij, S., Sijs, R., Denn, M. M., Villermaux, E., and Bonn, D. 2018. What determines the drop size in sprays? *Phys. Rev. X.* **8**(3), pp. 031019. Cited on p. 44.
- Kovalchuk, N. M., Reichow, M., Frommweiler, T., Vigolo, D., and Simmons, M. J. H. 2019. Mass transfer accompanying coalescence of surfactant-laden and surfactant-free drop in a microfluidic channel. *Langmuir.* **35**(28), pp. 9184–9193. Cited on pp. 13, 26, 36, and 142.
- Kröber, P., Delaney, J. T., Perelaer, J., and Schubert, U. S. 2009. Reactive inkjet printing of polyurethanes. *J. Mater. Chem.* **19**(29), pp. 5234–5238. Cited on pp. 5 and 35.
- Kunkelmann, C. 2011. *Numerical modeling and investigation of boiling phenomena*. PhD thesis, Technische Universität Darmstadt. Cited on pp. 71, 80, and 189.
- Kwon, K. S., Yang, L., Martin, G. D., et al. 2016. Visualization and measurement. In: Hoath, S. D. ed. *Fundamentals of Inkjet Printing: The Science of Inkjet and Droplets*. Wiley-VCH, pp. 313–337. Cited on p. 54.

- Lai, Y.-H., Hsu, M.-H., and Yang, J.-T. 2010. Enhanced mixing of droplets during coalescence on a surface with a wettability gradient. *Lab Chip*. **10**(22), pp. 3149–3156. Cited on pp. 35, 114, 143, 164, and 165.
- Larsen, B. E., Fuhrman, D. R., and Roenby, J. 2019. Performance of interFoam on the simulation of progressive waves. *Coastal Eng. J.* **61**(3), pp. 380–400. Cited on p. 80.
- Lautrup, B. 2011. *Physics of continuous matter: exotic and everyday phenomena in the macroscopic world*. 2nd ed. Boca Raton, FL: CRC press. Cited on p. 18.
- Law, C. K. 2012. Fuel options for next-generation chemical propulsion. *AIAA J.* **50**(1), pp. 19–36. Cited on pp. 2 and 39.
- Lee, J. H., Hong, S. K., Hur, H. C., and Choi, Y. J. 2009. Improvement of the resolution in direct membrane integrity test by controlling solution surface tension. *Water Sci. Technol.* **59**(11), pp. 2205–2211. Cited on p. 48.
- Li, D., Sutton, D., Burgess, A., Graham, D., and Calvert, P. D. 2009. Conductive copper and nickel lines via reactive inkjet printing. *J. Mater. Chem.* **19**(22), pp. 3719–3724. Cited on pp. 5 and 177.
- Li, X., Chen, J., Liu, B., et al. 2018. Inkjet printing for biofabrication. In: Ovsianikov, A., Yoo, J., and Mironov, V. eds. *3D Printing and Biofabrication*. Springer International Publishing, pp. 283–301. Cited on p. 3.
- Li, X. G. and Fritsching, U. 2011. Numerical investigation of binary droplet collisions in all relevant collision regimes. *J. Comput. Multiphase Flows.* **3**(4), pp. 207–224. Cited on p. 71.
- Li, Y., Diddens, C., Lv, P., et al. 2019. Gravitational effect in evaporating binary micro-droplets. *Phys. Rev. Lett.* **122**(11), pp. 114501. Cited on p. 18.
- Lindken, R., Rossi, M., Große, S., and Westerweel, J. 2009. Micro-particle image velocimetry (μ PIV): recent developments, applications, and guidelines. *Lab Chip*. **9**(17), pp. 2551–2567. Cited on p. 36.
- Liu, C.-Y., Carvalho, M. S., and Kumar, S. 2019. Dynamic wetting failure in curtain coating: Comparison of model predictions and experimental observations. *Chem. Eng. Sci.* **195**, pp. 74–82. Cited on p. 29.
- Liu, D., Guo, Y.-C., and Lin, W.-Y. 2013a. Surface tension gradients on mixing processes after coalescence of binary equal-sized droplets. *Chin. Phys. Lett.* **30**(7), pp. 074701. Cited on p. 142.
- Liu, D., Zhang, P., Law, C. K., and Guo, Y. 2013b. Collision dynamics and mixing of unequal-size droplets. *Int. J. Heat Mass Transfer.* **57**(1), pp. 421–428. Cited on p. 113.
- Liu, R. H., Stremmer, M. A., Sharp, K. V., et al. 2000. Passive mixing in a three-dimensional serpentine microchannel. *J. Microelectromech. Syst.* **9**(2), pp. 190–197. Cited on p. 166.

- Lohse, D. and Zhang, X. 2020. Physicochemical hydrodynamics of droplets out of equilibrium: a perspective review. arXiv:2005.03782 [physics.flu-dyn]. Cited on p. 11.
- López-Herrera, J., Ganan-Calvo, A. M., Popinet, S., and Herrada, M. A. 2015. Electrokinetic effects in the breakup of electrified jets: A volume-of-fluid numerical study. *Int. J. Multiphase Flow.* **71**, pp. 14–22. Cited on p. 70.
- Ludwicki, J. M. and Steen, P. H. 2020. Sweeping by sessile drop coalescence. arXiv:2005.06977 [physics.flu-dyn]. Cited on pp. 41 and 76.
- Luo, X., Yin, H., Ren, J., et al. 2019. Enhanced mixing of binary droplets induced by capillary pressure. *J. Colloid Interface Sci.* **545**, pp. 35–42. Cited on pp. 114 and 142.
- Lupo, G., Ardekani, M. N., Brandt, L., and Duwig, C. 2019. An immersed boundary method for flows with evaporating droplets. *Int. J. Heat Mass Transfer.* **143**, pp. 118563. Cited on p. 38.
- Ma, Y., Cao, X., Feng, X., Ma, Y., and Zou, H. 2007. Fabrication of super-hydrophobic film from PMMA with intrinsic water contact angle below 90°. *Polymer.* **48**(26), pp. 7455–7460. Cited on p. 51.
- Margarinos, I., Nikolopoulos, N., Marengo, M., Antonini, C., and Gavaises, M. 2014. VOF simulations of the contact angle dynamics during the drop spreading: Standard models and a new wetting force model. *Adv. Colloid Interface Sci.* **212**, pp. 1–20. Cited on p. 28.
- Marangoni, C. 1871. Ueber die ausbreitung der tropfen einer flüssigkeit auf der oberfläche einer anderen. *Ann. Phys.* **219**(7), pp. 337–354. Cited on p. 11.
- Márquez Damián, S. 2013. *An extended mixture model for the simultaneous treatment of short and long scale interfaces*. PhD thesis, Universidad Nacional del Litoral. Cited on pp. 88 and 90.
- Mazutis, L. and Griffiths, A. D. 2012. Selective droplet coalescence using microfluidic systems. *Lab Chip.* **12**(10), pp. 1800–1806. Cited on p. 20.
- McKinley, G. H. 2005. Dimensionless groups for understanding free surface flows of complex fluids. *Society of Rheology, Rheology Bulletin.* **74**(2), pp. 6–9. Cited on p. 26.
- Mikami, H., Harmon, J., Kobayashi, H., et al. 2018. Ultrafast confocal fluorescence microscopy beyond the fluorescence lifetime limit. *Optica.* **5**(2), pp. 117–126. Cited on p. 35.
- Mirzaei, M. 2017. A new method for measuring the contact angles from digital images of liquid drops. *Micron.* **102**, pp. 65–72. Cited on pp. 64 and 65.
- Mizuno, K., Miyashita, Y., Shindo, Y., and Ogawa, H. 1995. NMR and FT-IR studies of hydrogen bonds in ethanol-water mixtures. *J. Phys. Chem.* **99**(10), pp. 3225–3228. Cited on p. 44.

- Moghtadernejad, S., Tembely, M., Jadidi, M., Esmail, N., and Dolatabadi, A. 2015. Shear driven droplet shedding and coalescence on a superhydrophobic surface. *Phys. Fluids*. **27**(3), pp. 032106. Cited on p. 76.
- Moukalled, F., Mangani, L., and Darwish, M. 2016. *The finite volume method in computational fluid dynamics: an advanced introduction with OpenFOAM and MATLAB*. Switzerland: Springer International Publishing. Cited on pp. 80 and 85.
- Mukherjee, S. and Abraham, J. 2007. Investigations of drop impact on dry walls with a lattice-Boltzmann model. *J. Colloid Interface Sci.* **312**(2), pp. 341–354. Cited on p. 32.
- Mulla, M. A., Yow, H. N., Zhang, H., Cayre, O. J., and Biggs, S. 2016. Colloid particles in ink formulations. In: Hoath, S. D. ed. *Fundamentals of Inkjet Printing: The Science of Inkjet and Droplets*. Wiley-VCH, pp. 141–168. Cited on p. 11.
- Nabil, M. and Rattner, A. S. 2016. interThermalPhaseChangeFoam – A framework for two-phase flow simulations with thermally driven phase change. *SoftwareX*. **5**, pp. 216–226. Cited on p. 77.
- Napadensky, E. 2009. Tailoring substrates for inkjet printing. In: Magdassi, S. ed. *The Chemistry of Inkjet Inks*. Singapore: World Scientific Publishing, pp. 73–97. Cited on p. 5.
- Narhe, R., Beysens, D., and Nikolayev, V. S. 2004. Contact line dynamics in drop coalescence and spreading. *Langmuir*. **20**(4), pp. 1213–1221. Cited on p. 114.
- Nash, J. J., Spicer, P. T., and Erk, K. A. 2018. Controllable internal mixing in coalescing droplets induced by the solutal Marangoni convection of surfactants with distinct headgroup architectures. *J. Colloid Interface Sci.* **529**, pp. 224–233. Cited on pp. 11 and 142.
- Ng, V.-V., Sellier, M., and Nock, V. 2017. Marangoni-improved mixing in a two-droplet system. *Interf. Phenom. Heat Transf.* **5**(1), pp. 81–95. Cited on p. 143.
- Nikolopoulos, N., Nikas, K.-S., and Bergeles, G. 2009. A numerical investigation of central binary collision of droplets. *Comput. Fluids*. **38**(6), pp. 1191–1202. Cited on p. 20.
- Nilsson, M. A. and Rothstein, J. P. 2011. The effect of contact angle hysteresis on droplet coalescence and mixing. *J. Colloid Interface Sci.* **363**(2), pp. 646–654. Cited on pp. 114, 136, and 165.
- Nito, Y. and Hakamada, S. 2009. *Reaction liquid, set of ink composition and reaction liquid, and image recording method*. Patent: US7537329B2. Assignee: Canon Inc. Cited on p. 4.
- Nobari, M. R. and Tryggvason, G. 1994. *The flow induced by the coalescence of two initially stationary drops*. NASA Technical Memorandum 106752, NASA. Cited on pp. 39, 40, 97, and 113.

- Nowak, E., Kovalchuk, N. M., Che, Z., and Simmons, M. J. H. 2016. Effect of surfactant concentration and viscosity of outer phase during the coalescence of a surfactant-laden drop with a surfactant-free drop. *Colloids Surf. A*. **505**, pp. 124–131. Cited on pp. 110 and 142.
- Nowak, E., Xie, Z., Kovalchuk, N. M., Matar, O. K., and Simmons, M. J. H. 2017. Bulk advection and interfacial flows in the binary coalescence of surfactant-laden and surfactant-free drops. *Soft Matter*. **13**(26), pp. 4616–4628. Cited on pp. x, 13, 25, 33, 37, 38, 39, 56, 114, and 165.
- Olcay, A. B. and Krueger, P. S. 2008. Measurement of ambient fluid entrainment during laminar vortex ring formation. *Exp. Fluids*. **44**(2), pp. 235–247. Cited on pp. x and 24.
- Oyanagi, T. 2003. *Aqueous Pigment-Based Ink Set*. Patent: US6536891B2. Assignee: Seiko Epson Corp. Cited on pp. 3 and 158.
- Paik, P., Pamula, V. K., Pollack, M. G., and Fair, R. B. 2003. Electrowetting-based droplet mixers for microfluidic systems. *Lab Chip*. **3**(1), pp. 28–33. Cited on pp. 23, 61, and 147.
- Patankar, S. V. 1980. *Numerical heat transfer and fluid flow*. Washington, DC: Hemisphere Publishing Corporation. Cited on p. 78.
- Paulsen, J. D., Burton, J. C., and Nagel, S. R. 2011. Viscous to inertial crossover in liquid drop coalescence. *Phys. Rev. Lett.* **106**(11), pp. 114501. Cited on p. 20.
- Pavlidis, D., Gomes, J. L. M. A., Xie, Z., et al. 2016. Compressive advection and multi-component methods for interface-capturing. *Int. J. Numer. Methods Fluids*. **80**(4), pp. 256–282. Cited on p. 39.
- Perumanath, S., Borg, M. K., Chubynsky, M. V., Sprittles, J. E., and Reese, J. M. 2019. Droplet coalescence is initiated by thermal motion. *Phys. Rev. Lett.* **122**(10), pp. 104501. Cited on pp. 1 and 20.
- Qian, J. and Law, C. K. 1997. Regimes of coalescence and separation in droplet collision. *J. Fluid Mech.* **331**, pp. 59–80. Cited on pp. 20 and 39.
- Quéré, D. 2008. Wetting and roughness. *Annu. Rev. Mater. Res.* **38**, pp. 71–99. Cited on p. 15.
- Quetzeri-Santiago, M. A., Yokoi, K., Castrejón-Pita, A. A., and Castrejón-Pita, J. R. 2019. Role of the dynamic contact angle on splashing. *Phys. Rev. Lett.* **122**(22), pp. 228001. Cited on p. 114.
- Quetzeri-Santiago, M. A., Castrejón-Pita, J. R., and Castrejón-Pita, A. A. 2020. On the analysis of the contact angle for impacting droplets using a polynomial fitting approach. *Exp. Fluids*. **61**(143), pp. 143. Cited on p. 64.

- Raman, K. A. 2016. *A numerical study on the dynamics of droplet-wall interactions*. PhD thesis, National University of Singapore. Cited on p. 38.
- Raman, K. A. 2018. Dynamics of simultaneously impinging drops on a dry surface: Role of inhomogeneous wettability and impact shape. *J. Colloid Interface Sci.* **516**, pp. 232–247. Cited on pp. 39, 114, and 141.
- Raman, K. A., Jaiman, R. K., Lee, T.-S., and Low, H.-T. 2016. Lattice Boltzmann study on the dynamics of successive droplets impact on a solid surface. *Chem. Eng. Sci.* **145**, pp. 181–195. Cited on pp. 39, 95, 114, and 141.
- Raman, K. A., Jaiman, R. K., Lee, T.-S., and Low, H.-T. 2017. Dynamics of simultaneously impinging drops on a dry surface: Role of impact velocity and air inertia. *J. Colloid Interface Sci.* **486**, pp. 265–276. Cited on pp. 39 and 42.
- Rattner, A. S. and Garimella, S. 2014. Simple mechanistically consistent formulation for volume-of-fluid based computations of condensing flows. *J. Heat Transfer.* **136**(7), pp. 071501. Cited on p. 77.
- Ray, S. F. 1997. *High Speed Photography and Photonics*. Oxford: Focal Press. Cited on p. 53.
- Ren, W. and E, W. 2007. Boundary conditions for the moving contact line problem. *Phys. Fluids.* **19**(2), pp. 022101. Cited on p. 27.
- Rioboo, R., Tropea, C., and Marengo, M. 2001. Outcomes from a drop impact on solid surfaces. *Atomization. Spray.* **11**(2), pp. 155–165. Cited on pp. 60 and 148.
- Ristenpart, W. D., McCalla, P. M., Roy, R. V., and Stone, H. A. 2006. Coalescence of spreading droplets on a wettable substrate. *Phys. Rev. Lett.* **97**(6), pp. 064501. Cited on p. 149.
- Roisman, I. V., Rioboo, R., and Tropea, C. 2002. Normal impact of a liquid drop on a dry surface: model for spreading and receding. *Proc. R. Soc. London, Ser. A.* **458**(2022), pp. 1411–1430. Cited on p. 32.
- Rusche, H. 2002. *Computational fluid dynamics of dispersed two-phase flows at high phase fractions*. PhD thesis, Imperial College, University of London. Cited on pp. 72 and 80.
- Saha, A., Wei, Y., Tang, X., and Law, C. K. 2019. Kinematics of vortex ring generated by a drop upon impacting a liquid pool. *J. Fluid Mech.* **875**, pp. 842–853. Cited on pp. 24, 114, and 141.
- Saha, A. A. and Mitra, S. K. 2009. Effect of dynamic contact angle in a volume of fluid (VOF) model for a microfluidic capillary flow. *J. Colloid Interface Sci.* **339**(2), pp. 461–480. Cited on p. 77.
- Scardovelli, R. and Zaleski, S. 1999. Direct numerical simulation of free-surface and interfacial flow. *Annu. Rev. Fluid Mech.* **31**(1), pp. 567–603. Cited on pp. 40 and 41.

- Schrödinger, E. 1915. Notiz über den kapillardruck in gasblasen. *Ann. Phys.* **351**(3), pp. 413–418. Cited on p. 46.
- Schuster, F., Hirth, T., and Weber, A. 2019. Reactive inkjet printing of polyethylene glycol and isocyanate based inks to create porous polyurethane structures. *J. Appl. Polym. Sci.* **136**(3), pp. 46977. Cited on p. 5.
- Seppecher, P. 1996. Moving contact lines in the Cahn-Hilliard theory. *Int. J. Eng. Sci.* **34**(9), pp. 977–992. Cited on p. 27.
- Shikhmurzaev, Y. D. 1993. The moving contact line on a smooth solid surface. *Int. J. Multiphase Flow.* **19**(4), pp. 589–610. Cited on p. 28.
- Shikhmurzaev, Y. D. 2008. *Capillary flows with forming interfaces*. Boca Raton, FL: Chapman & Hall/CRC. Cited on pp. 14, 27, and 28.
- Shim, S. and Stone, H. A. 2017. Damped coalescence cascade of liquid drops. *Phys. Rev. Fluids.* **2**(4), pp. 044001. Cited on p. 143.
- Šikalo, Š., Wilhelm, H.-D., Roisman, I., Jakirlić, S., and Tropea, C. 2005. Dynamic contact angle of spreading droplets: Experiments and simulations. *Phys. Fluids.* **17**(6), pp. 062103. Cited on p. 32.
- Smith, P. J. and Morrin, A. 2012. Reactive inkjet printing. *J. Mater. Chem.* **22**(22), pp. 10965–10970. Cited on pp. 4 and 5.
- Smith, P. J. and Morrin, A. 2018. Reactive inkjet printing – an introduction. In: Smith, P. J. and Morrin, A. eds. *Reactive Inkjet Printing: A Chemical Synthesis Tool*. The Royal Society of Chemistry, pp. 1–11. Cited on p. 4.
- Snoeijer, J. H. and Andreotti, B. 2013. Moving contact lines: Scales, regimes, and dynamical transitions. *Annu. Rev. Fluid Mech.* **45**, pp. 269–292. Cited on pp. 28 and 29.
- Sprittles, J. E. and Shikhmurzaev, Y. D. 2012a. The dynamics of liquid drops and their interaction with solids of varying wettabilities. *Phys. Fluids.* **24**(8), pp. 082001. Cited on p. 29.
- Sprittles, J. E. and Shikhmurzaev, Y. D. 2012b. Coalescence of liquid drops: Different models versus experiment. *Phys. Fluids.* **24**(12), pp. 122105. Cited on pp. 92 and 105.
- Sprittles, J. E. and Shikhmurzaev, Y. D. 2014a. A parametric study of the coalescence of liquid drops in a viscous gas. *J. Fluid Mech.* **753**, pp. 279–306. Cited on p. 92.
- Sprittles, J. E. and Shikhmurzaev, Y. D. 2014b. Dynamics of liquid drops coalescing in the inertial regime. *Phys. Rev. E.* **89**(6), pp. 063008. Cited on p. 21.
- Stone, H. A., Stroock, A. D., and Ajdari, A. 2004. Engineering flows in small devices: Microfluidics toward a lab-on-a-chip. *Annu. Rev. Fluid Mech.* **36**, pp. 381–411. Cited on pp. 2 and 23.

- Subramanian, R. S., Moumen, N., and McLaughlin, J. B. 2005. Motion of a drop on a solid surface due to a wettability gradient. *Langmuir*. **21**(25), pp. 11844–11849. Cited on p. 15.
- Sui, Y., Ding, H., and Speltz, P. D. M. 2014. Numerical simulations of flows with moving contact lines. *Annu. Rev. Fluid Mech.* **46**(1), pp. 97–119. Cited on p. 41.
- Sun, K., Jia, M., and Wang, T. 2014. Numerical investigation on the head-on collision between unequal-sized droplets with multiple-relaxation-time lattice Boltzmann model. *Int. J. Heat Mass Transfer*. **70**, pp. 629–640. Cited on p. 39.
- Sun, K., Wang, T., Zhang, P., and Law, C. K. 2015a. Non-Newtonian flow effects on the coalescence and mixing of initially stationary droplets of shear-thinning fluids. *Phys. Rev. E*. **91**(2), pp. 023009. Cited on pp. 39, 42, and 142.
- Sun, K., Zhang, P., Law, C. K., and Wang, T. 2015b. Collision dynamics and internal mixing of droplets of non-Newtonian liquids. *Phys. Rev. Appl.* **4**(5), pp. 054013. Cited on p. 39.
- Sun, K., Zhang, P., Che, Z., and Wang, T. 2018a. Marangoni-flow-induced partial coalescence of a droplet on a liquid/air interface. *Phys. Rev. Fluids*. **3**(2), pp. 023602. Cited on p. 143.
- Sun, K., Zhang, P., Jia, M., and Wang, T. 2018b. Collision-induced jet-like mixing for droplets of unequal-sizes. *Int. J. Heat Mass Transfer*. **120**, pp. 218–227. Cited on p. 39.
- Sun, Z., Xi, G., and Chen, X. 2009. Mechanism study of deformation and mass transfer for binary droplet collisions with particle method. *Phys. Fluids*. **21**(3), pp. 032106. Cited on p. 38.
- Sykes, T. C., Castrejón-Pita, A. A., Castrejón-Pita, J. R., et al. 2020a. Surface jets and internal mixing during the coalescence of impacting and sessile droplets. *Phys. Rev. Fluids*. **5**(2), pp. 023602. Cited on pp. ii, 8, and 141.
- Sykes, T. C., Harbottle, D., Khatir, Z., Thompson, H. M., and Wilson, M. C. T. 2020b. Substrate wettability influences internal jet formation and mixing during droplet coalescence. *Langmuir*. **36**(32), pp. 9596–9607. Cited on pp. 8 and 113.
- Taherian, F., Marcon, V., Bonaccorso, E., and van der Vegt, N. F. A. 2016. Vortex formation in coalescence of droplets with a reservoir using molecular dynamics simulations. *J. Colloid Interface Sci.* **479**, pp. 189–198. Cited on p. 143.
- Takano, Y., Kikkawa, S., Suzuki, T., and Kohno, J.-Y. 2015. Coloring rate of phenolphthalein by reaction with alkaline solution observed by liquid-droplet collision. *J. Phys. Chem. B*. **119**(23), pp. 7062–7067. Cited on pp. 36 and 166.
- Talbot, E., Bain, C., De Dier, R., Sempels, W., and Vermant, J. 2016. Droplets drying on surfaces. In: Hoath, S. D. ed. *Fundamentals of Inkjet Printing: The Science of Inkjet and Droplets*. Wiley-VCH, pp. 251–280. Cited on p. 12.

- Tang, C., Zhao, J., Zhang, P., Law, C. K., and Huang, Z. 2016. Dynamics of internal jets in the merging of two droplets of unequal sizes. *J. Fluid Mech.* **795**, pp. 671–689. Cited on pp. 39 and 113.
- Tang, Z., Fang, K., Bukhari, M. N., Song, Y., and Zhang, K. 2020. Effects of viscosity and surface tension of a reactive dye ink on droplet formation. *Langmuir.* **36**(32), pp. 9481–9488. Cited on p. 4.
- Tanner, L. H. 1979. The spreading of silicone oil drops on horizontal surfaces. *J. Phys. D: Appl. Phys.* **12**(9), pp. 1473. Cited on p. 29.
- Teh, S.-Y., Lin, R., Hung, L.-H., and Lee, A. P. 2008. Droplet microfluidics. *Lab Chip.* **8**(2), pp. 198–220. Cited on p. 2.
- Teraoka, H., Takizawa, Y., Takada, Y., and Yakushigawa, Y. 2003. *Color ink-jet recording ink set, ink-jet recording method, recording unit, ink-cartridge, ink-jet recording apparatus and bleeding reduction method*. Patent: US6530656B1. Assignee: Canon Inc. Cited on p. 4.
- Theobald, D. W., Hanson, B., Fairweather, M., and Heggs, P. J. 2020. Implications of hydrodynamics on the design of pulsed sieve-plate extraction columns: A one-fluid multiphase CFD model using the volume of fluid method. *Chem. Eng. Sci.* **221**, pp. 115640. Cited on p. 86.
- Thoroddsen, S. T. and Takehara, K. 2000. The coalescence cascade of a drop. *Phys. Fluids.* **12**(6), pp. 1265–1267. Cited on p. 1.
- Thoroddsen, S. T., Takehara, K., and Etoh, T. G. 2005. The coalescence speed of a pendent and a sessile drop. *J. Fluid Mech.* **527**, pp. 85–114. Cited on pp. 20, 37, 39, and 136.
- Trevelyan, P. M. J., Almarcha, C., and De Wit, A. 2015. Buoyancy-driven instabilities around miscible $A + B \rightarrow C$ reaction fronts: A general classification. *Phys. Rev. E.* **91**(2), pp. 023001. Cited on p. 166.
- Tribble, M. K. 2014. *Application of consumer color cameras as three-color pyrometers*. MSc thesis, New Mexico Institute of Mining and Technology. Cited on p. 55.
- Trujillo-Pino, A., Krissian, K., Alemán-Flores, M., and Santana-Cedrés, D. 2013. Accurate subpixel edge location based on partial area effect. *Image Vision Comput.* **31**(1), pp. 72–90. Cited on p. 63.
- Tse, C. 2015. *Utilising inkjet printing for tissue engineering*. PhD thesis, University of Sheffield. Cited on p. 5.
- Tsuji, K. and Müller, S. C. 2012. Chemical reaction evolving on a droplet. *J. Phys. Chem. Lett.* **3**(8), pp. 977–980. Cited on pp. xiii, 166, 168, 172, 173, and 174.

- Tu, J., Yeoh, G. H., and Liu, C. 2013. *Computational fluid dynamics: a practical approach*. 2nd ed. Amsterdam: Butterworth-Heinemann. Cited on p. 80.
- Unverdi, S. O. and Tryggvason, G. 1992a. A front-tracking method for viscous, incompressible, multi-fluid flows. *J. Comput. Phys.* **100**(1), pp. 25–37. Cited on pp. 39 and 40.
- Unverdi, S. O. and Tryggvason, G. 1992b. Computations of multi-fluid flows. *Physica D: Nonlinear Phenomena*. **60**(1-4), pp. 70–83. Cited on pp. 39 and 40.
- van Leer, B. 1979. Towards the ultimate conservative difference scheme. V. A second-order sequel to Godunov’s method. *J. Comput. Phys.* **32**(1), pp. 101–136. Cited on p. 80.
- Vazquez, G., Alvarez, E., and Navaza, J. M. 1995. Surface tension of alcohol + water from 20 to 50°C. *J. Chem. Eng. Data*. **40**(3), pp. 611–614. Cited on pp. 44 and 47.
- Versteeg, H. K. and Malalasekera, W. 1995. *An introduction to computational fluid dynamics: the finite volume method*. Harlow: Addison-Wesley-Longman. Cited on pp. 78, 79, and 85.
- Viswanathan, H. 2019. Breakup and coalescence of drops during transition from dripping to jetting in a Newtonian fluid. *Int. J. Multiphase Flow*. **112**, pp. 269–285. Cited on p. 92.
- Voinov, O. V. 1976. Hydrodynamics of wetting. *Fluid Dyn.* **11**(5), pp. 714–721. Cited on p. 29.
- Wang, H., Liao, Q., Zhu, X., Li, J., and Tian, X. 2010. Experimental studies of liquid droplet coalescence on the gradient surface. *J Supercond. Nov. Magn.* **23**(6), pp. 1165–1168. Cited on p. 51.
- Wang, L. and Sun, J. 2018. Lattice Boltzmann modeling for the coalescence between a free droplet in gases and a sessile droplet on wettable substrate with contact angle hysteresis. *Proc. Inst. Mech. Eng. C*. **232**(3), pp. 431–444. Cited on p. 123.
- Wang, Y. and Bourouiba, L. 2018. Non-isolated drop impact on surfaces. *J. Fluid Mech.* **835**, pp. 24–44. Cited on p. 60.
- Wasserfall, J., Figueiredo, P., Kneer, R., Rohlfs, W., and Pischke, P. 2017. Coalescence-induced droplet jumping on superhydrophobic surfaces: Effects of droplet mismatch. *Phys. Rev. Fluids*. **2**(12), pp. 123601. Cited on pp. 71, 78, and 80.
- Wilhelmy, L. 1863. Ueber die abhängigkeit der capillaritäts-constanten des alkohols von substanz und gestalt des benetzten festen körpers. *Ann. Phys.* **195**(6), pp. 177–217. Cited on p. 46.
- Wilson, M. C. T. and Kubiak, K. J. 2016. Simulation of drops on surfaces. In: Hoath, S. D. ed. *Fundamentals of Inkjet Printing: The Science of Inkjet and Droplets*. Wiley-VCH, pp. 281–312. Cited on pp. 28, 30, 32, and 42.

- Wilson, M. C. T., Summers, J. L., Shikhmurzaev, Y. D., Clarke, A., and Blake, T. D. 2006. Nonlocal hydrodynamic influence on the dynamic contact angle: Slip models versus experiment. *Phys. Rev. E*. **73**(4), pp. 041606. Cited on pp. 29 and 31.
- Wilson, M. C. T., Castrejón-Pita, J. R., and Castrejón-Pita, A. A. 2018. Droplet mixing. In: Smith, P. J. and Morrin, A. eds. *Reactive Inkjet Printing: A Chemical Synthesis Tool*. The Royal Society of Chemistry, pp. 38–58. Cited on pp. 2, 6, 22, 23, and 167.
- Wu, J., Ma, R., Wang, Z., and Yao, S. 2011. Do droplets always move following the wettability gradient? *Appl. Phys. Lett.* **98**(20), pp. 204104. Cited on p. 15.
- Wu, M., Cubaud, T., and Ho, C.-M. 2004. Scaling law in liquid drop coalescence driven by surface tension. *Phys. Fluids*. **16**(7), pp. L51–L54. Cited on p. 1.
- Xia, X., He, C., Yu, D., Zhao, J., and Zhang, P. 2017. Vortex-ring-induced internal mixing upon the coalescence of initially stationary droplets. *Phys. Rev. Fluids*. **2**(11), pp. 113607. Cited on pp. 26, 39, 41, 83, 113, 116, 117, and 138.
- Xia, Z., Xiao, Y., Yang, Z., et al. 2019. Droplet impact on the super-hydrophobic surface with micro-pillar arrays fabricated by hybrid laser ablation and silanization process. *Materials*. **12**(5), pp. 765. Cited on p. 51.
- Yang, X., Chhasatia, V. H., and Sun, Y. 2013. Oscillation and recoil of single and consecutively printed droplets. *Langmuir*. **29**(7), pp. 2185–2192. Cited on p. 39.
- Yarnold, G. D. 1938. The motion of a mercury index in a capillary tube. *Proc. Phys. Soc. London*. **50**(4), pp. 540–552. Cited on p. 28.
- Yeh, S.-I., Fang, W.-F., Sheen, H.-J., and Yang, J.-T. 2013. Droplets coalescence and mixing with identical and distinct surface tension on a wettability gradient surface. *Microfluid. Nanofluid.* **14**(5), pp. 785–795. Cited on pp. 35, 36, 114, and 143.
- Yeh, S.-I., Sheen, H.-J., and Yang, J.-T. 2015. Chemical reaction and mixing inside a coalesced droplet after a head-on collision. *Microfluid. Nanofluid.* **18**(5-6), pp. 1355–1363. Cited on pp. xiii, 61, 166, 167, 168, 172, 173, and 174.
- Young, T. 1805. III. An essay on the cohesion of fluids. *Philos. Trans. Royal Soc.* **95**, pp. 65–87. Cited on p. 14.
- Yuan, Y. and Lee, T. R. 2013. Contact angle and wetting properties. In: Bracco, G. and Holst, B. eds. *Surface science techniques*. Springer, pp. 3–34. Cited on pp. x, 10, 14, 15, 16, and 17.
- Zalesak, S. T. 1979. Fully multidimensional flux-corrected transport algorithms for fluids. *J. Comput. Phys.* **31**(3), pp. 335–362. Cited on p. 87.
- Zalesak, S. T. 2005. The design of flux-corrected transport (FCT) algorithms for structured grids. In: Kuzmin, D., Turek, S., and Löhner, R. eds. *Flux-Corrected Transport*. Berlin: Springer, pp. 29–78. Cited on p. 88.

- Zhang, F. H., Li, E. Q., and Thoroddsen, S. T. 2009. Satellite formation during coalescence of unequal size drops. *Phys. Rev. Lett.* **102**(10), pp. 104502. Cited on pp. 1, 37, 115, and 127.
- Zhang, J. and Kwok, D. Y. 2013. Lattice Boltzmann Method (LBM). In: Li, D. ed. *Encyclopedia of Microfluidics and Nanofluidics*. Boston, MA: Springer, pp. 1–8. Cited on p. 42.
- Zhang, Y., Oberdick, S. D., Swanson, E. R., Anna, S. L., and Garoff, S. 2015. Gravity driven current during the coalescence of two sessile drops. *Phys. Fluids.* **27**(2), pp. 022101. Cited on pp. 58, 59, 61, 142, 152, 158, and 171.